Chemical-biological studies of cell division and intracellular organization in bacteria

By

Thiago Monteiro Araújo dos Santos

A dissertation submitted in partial fulfillment of

the requirements for the degree of

Doctor of Philosophy

(Microbiology)

at the

UNIVERSITY OF WISCONSIN–MADISON

2017

Date of final oral examination: 07/07/2017

The dissertation is approved by the following members of the Final Oral Committee:

Briana M. Burton, Assistant Professor, Bacteriology
Patricia J. Kiley, Professor, Biomolecular Chemistry
Jue D. Wang, Associate Professor, Bacteriology
Douglas B. Weibel, Professor, Biochemistry
Rodney A. Welch, Professor, Medical Microbiology and Immunology

TABLE OF CONTENTS

To those who inspire me

Acknowledgements

This is a lesson that I have learned over and over again: No one achieves anything alone. Throughout my entire life, I have received the support and learned from amazingly successful, impactful individuals. As I complete my doctoral degree and embark on another thrilling chapter of my academic journey, I would like to express my sincere appreciation to those who inspired me to become a scientist and those who helped me become one.

I am deeply indebted to my mentor, Prof. Doug Weibel, for his continuous encouragement during this important part of my training and for providing the guidance I needed to succeed in graduate school. I clearly remember my first interaction with Doug: I sent him a long email expressing my interest in joining his research group for my doctoral studies. He immediately replied to my message with an equally long email that I still keep and read when I need inspiration. My first meeting with Doug, after I moved to Madison, was another memorable experience. His keen intellect, creativity, and contagious passion for science captivated me.

Doug fostered my passion for science and my motivation to pursue an academic career. He continuously challenged me to reach beyond my limitations and made me a better scientist. More important, the kindness of his character has impressed me with a sincere respect for him. He has been an exemplary figure to me and he is now a dear friend. Thank you, Doug, for opening so many doors and for allowing me the opportunity to expand my horizons. Your mentorship empowered me to keep pursuing my career goals.

I am also grateful to all my professors and, especially, to those who were (at some point) part of my doctoral committee: Profs. Briana Burton, Marcin Filutowicz, Laura Kiessling, Tricia Kiley, Ned Ruby, Jade Wang, and Rod Welch. The exceptional assistance and insights from my committee members were fundamental to my work and my scientific growth. The imprinting of their collective knowledge and experience is all over the pages of this dissertation. Thank you all for your friendship and support.

All the friends and colleagues I made in the Weibel laboratory had an enormous positive impact on my personal and professional development. Thank you all for making this journey even more enjoyable than I could have ever expected. I am particularly thankful to Katie Brenner, Ye-Jin Eun, Piercen Oliver, Hannah Tuson, and Maoquan Zhou for their constant support and helpful advice. I am extremely grateful to Katie Hurley, Ti-Yu Lin, and Na Yin for all the successful collaborations and the solid friendship. I sincerely hope that we will have many other opportunities to collaborate in the future.

I also thank the outstanding team of undergraduate students I mentored: Samantha Anderson, Brice Blahnik, Endia Blunt, Gabriel Carneiro, Crystal De Jesus, Matt Lammers, Madhu Rajendran, and Ian Sparks. Time and again, they have reinforced my desire to become an educator. Working with this talented group of students was a great privilege and an invaluable learning experience. Thank you, guys, for being part of my training and for letting me be part of yours.

I have made many wonderful friends from all over the world. I cannot possible name them all here, but I am no less grateful for their generosity and friendship. I also received an amazing support from the entire University of Wisconsin-Madison community; especially, the Microbiology Doctoral Training Program, the Department of

Biochemistry, and the International Student Services. Thank you for building and disseminating the positive sense of community that promotes the collective success of this great school.

Finally, I thank the people I love the most; my family. My words cannot adequately express how much I appreciate the unconditional love and support I have always received from my mom, my dad, my little sister, my older brother, and my sister-in-law. A simple acknowledgement is insufficient. My parents were my first mentors and certainly the source of my inspiration. They taught me that a good character goes a long way, and anything is possible if I have determination and a willingness to work hard. It is so comforting to know that I have such caring people surrounding me. Thank you for believing in me and in my dreams. This dissertation is one of my many dreams you made possible.

Chemical-biological studies of cell division and intracellular organization in bacteria

Thiago Monteiro Araújo dos Santos

Under the supervision of Douglas B. Weibel, Ph.D.

Department of Biochemistry

University of Wisconsin–Madison, Madison, WI

Subcellular localization of biomolecules is a fundamental example of biological organization and is critical for the structural and metabolic properties of cells. Despite lacking the complex intracellular compartmentalization characteristic of eukaryotic cells, bacteria have evolved several mechanisms to achieve spatiotemporal organization of biomolecules and maintain spatial compartmentalization of biochemical processes essential for survival and growth. For instance, several bacterial proteins display asymmetric patterns of localization throughout the cell cycle and are enriched at the division site or poles in rod-shaped bacteria. The localization pattern of these proteins is integral to processes such as cell division, morphogenesis, virulence, and chemotaxis. Even small deviations from these highly-regulated localization patterns result in negative physiological outcomes on bacterial fitness. Several hypotheses have been formulated to explain protein localization in bacteria; however, many molecular details underlying these mechanisms remain largely undefined. The research described in this dissertation combines a set of techniques from genetics, biochemistry, chemistry, and materials science to addresses this topic from several different perspectives. Particularly, we investigated cellular features and environmental signals that affect protein localization and cell division in bacteria. First, we studied the mechanism of

polar localization of chemoreceptor clusters in *Escherichia coli*. We discovered that the trans-envelope Tol-Pal complex is a major determinant for chemoreceptor localization and deletion of this multiprotein complex led to motility and chemotaxis defects. Second, we explored the role of iron deprivation on assembly and placement of the bacterial division machinery at the division site. We found that iron deficiency affects recruitment of the division machinery to the division site and arrests late stages of constriction during division. Finally, we characterize a new family of small molecules that block DNA replication and arrest cell division through a mechanism that is distinct from other known inhibitors of DNA replication. The results reported in this dissertation will provide insights into the biochemical underpinnings of bacterial physiology and open doors to understand related processes in other organisms.

CHAPTER 1

Introduction to bacterial intracellular organization

Part of this chapter was adapted from:

Hurley KA[§], Santos TMA[§], Nepomuceno GM, Huynh V, Shaw JT, Weibel DB. Targeting the bacterial division protein FtsZ. *J Med Chem.* 2016; 59: 6975-98.

([§]*Denotes equal contribution*)

ABSTRACT

The absence of complex intracellular compartmentalization is a distinguishing feature of prokaryotic cells. Nonetheless, bacteria have evolved many strategies to achieve spatiotemporal patterns of biomolecular localization and maintain compartmentalization of biochemical processes that regulate cell growth and survival. In this chapter, we review the major molecular mechanisms that bacteria use to establish, maintain and replicate the asymmetric distribution of various proteins and protein complexes inside the cell. We summarize recent findings that support specific mechanisms responsible for polar localization of diverse proteins in rod-shaped bacteria and mechanisms involved in placement of the division machinery (divisome) at the division site. Finally, we discuss unanswered questions in the field and how these molecular mechanisms can be exploited as targets for devising new families of antimicrobial agents.

Organization of intracellular components in bacteria

Eukaryotic cells possess an elaborate endomembrane system and dynamic vesicle trafficking for synthesis, uptake and transport of biomolecules. These cellular innovations represent one of the major evolutionary acquisitions that differentiate eukaryotes and prokaryotes. However, despite lacking complex structural intracellular compartmentalization, bacterial cells have evolved several strategies to achieve spatiotemporal patterns of biomolecular organization and maintain the compartmentalization of biochemical processes essential for cell growth and survival [1-4]. Asymmetric intracellular localization is a distinguishing feature of many bacterial cellular components, including proteins [5-8], lipids [9-11], nucleic acids [12-14], ribosomes [15-17], and metabolites (e.g., ci-di-GMP [18], polyphosphate [19]).

Proteomic and microscopic approaches for identifying and studying the localization and dynamics of intracellular components have expanded our understanding of asymmetric patterns of localization in bacteria [14, 20-24]. The spatiotemporal localization patterns displayed by some of these biomolecules is remarkably complex and change dramatically during the cell cycle. The molecular mechanisms underlying the localization of the majority of these biomolecules are not completely understood; however, many studies have revealed compelling connections between the position of these cellular components and their function. These findings highlight the importance of optimally responding to changes in the metabolic demand, the environmental conditions, or the developmental state of the cell.

A growing number of proteins and protein complexes have been found to localize to the cell poles in rod-shaped bacteria and the division plane, making these regions of the cell attractive targets for studying spatial and temporal biomolecular

organization. Some examples of proteins that are enriched at the poles or the division site throughout the cell cycle or during specific cell-cycle events include components and regulators of the cell division machinery (divisome) [25-27], virulence factors [6, 28], secretion systems [29, 30], surface adhesion apparatus [31], regulators of cell development [32-34], determinants of flagellum biogenesis [33, 35], and chemotaxis apparatus [5, 35-37]. This chapter describes several molecular mechanisms responsible for protein localization in bacteria and the relationship between protein positioning and function, highlights unanswered questions in the field, and discusses the possible use of these localization mechanisms to develop new families of antimicrobial agents.

Molecular mechanisms for protein localization in bacteria

The cell poles in rod-shaped bacteria and the division site exhibit several unique chemical and physical features that bacteria exploit to position proteins and proteins complexes at these subcellular regions [11, 34, 38-40]. Several mechanisms have been formulated to account for the positioning of proteins of protein complexes at these specific cellular regions (Figure 1). In some cases, different mechanisms operate in combination to influence the subcellular localization of these proteins [41-43]. In the next sections, we describe the major themes of mechanisms and highlight some variations to these major themes. Although the mechanism (or mechanisms) controlling the subcellular localization of proteins destined to cell poles or the division site cannot be predicted based on the protein sequence or tridimensional conformation, the choice of mechanism seems to be motivated by intrinsic features of the protein, differences in the cellular context (e.g., nutritional and developmental state of the cell, physiochemical nature of the surrounding environment), or a combination of these factors.

Direct sensing of membrane curvature. A current model to explain the subcellular localization of proteins targeted to the cell poles is based on the intrinsic geometric features of rod-shaped bacteria. The curvature of the cell envelope at the poles is higher than the curvature along the cylindrical region of the cell [39, 40], and one hypothesis suggests that some proteins sense regions of negative curvature (i.e., the concave membrane curvature characteristic of the cell poles) and preferentially accumulate at these locations. This model predicts that protein complexes that exploit this geometric cue for localization need to assemble into large structures that have a length scale sufficient to sense membrane curvature [39, 40, 44].

The classic example of a protein that seems to sense negatively curved regions of the membrane is the protein DivIVA, involved in cell division and sporulation of *Bacillus subtilis* [7, 44] (Figure 1A). The evidence supporting this model for positioning of DivIVA are: (1) DivIVA localizes preferentially to the highly negatively curved incipient division site and secondarily to the less negatively curved cell poles; (2) DivIVA redistributes and becomes more enriched at the cell poles when division is inhibited; (3) DivIVA localizes diffusively in protoplasts [7]; (4) DivIVA of *B. subtilis* localizes to the poles in heterologous rod-shaped host cells such as *Escherichia coli* and *Schizosaccharomyces pombe*, indicating that cell geometry and not a biological cell-specific landmark drives localization [45]; and (5) DivIVA oligomers form higher order assembly [46] that could be sufficient to sense membrane curvature. As we discuss later, the subcellular localization of DivIVA is crucial for the correct positioning of other proteins important for cell division and competence regulation in *B. subtilis*. It is speculated that homologs of DivIVA present in other bacterial groups similarly localize to specific regions of the cell by sensing negatively curved surfaces. One example is the

DivIVA^{Sc} of *Streptomyces coelicolor* that mainly localizes at the hyphal tips to regulate growth and morphogenesis [47, 48].

Recent studies have shown that chemoreceptor clusters of *B. subtilis* [49] and *E. coli* [43] are highly sensitive to membrane curvature and exploit regions of negative curvature to influence their localization. Chemoreceptors form inter-communicating clusters that are ~200-400 nm in diameter [5, 50-55] and these clusters may have a shape that allows curvature sensing [56]. In *B. subtilis*, the intrinsic shape of chemoreceptors favors accumulation at concave regions of membrane at the base of division septa generated during cell division [49] (Figure 1A). This model suggests that high local concentration of complexes promotes the formation of large arrays stabilized by other components of the chemosensory machinery (e.g., the histidine kinase CheA and the adaptor protein CheW) reducing lateral diffusion of chemoreceptors. Consequently, clusters of chemoreceptors remain at the cell poles following division as an inheritance of the division site. Another recent study supports the hypothesis that curvature sensing is an intrinsic property of *E. coli* chemoreceptors [43]. Interestingly, in both examples, optimal localization of chemoreceptors at the cell poles depends on other cellular components [41, 42, 57] and seems to be coordinated with cell division events [41, 49]. Mutations that affect the polar localization of chemoreceptors reduce cell motility and chemotaxis [41].

A similar concept can be extended to explain the subcellular localization of proteins that prefer the convex side of curved membranes. Positive regions of membrane curvature (i.e., the convex geometry of the plasma membrane) and a proline residue located at the N-terminal region seem to be necessary for localization of SpoVM to the membrane that surrounds the developing spore (forespore) during sporulation of

B. subtilis [8, 58] (Figure 1A). Localization of SpoVM to the forespore is required for normal synthesis of spore cortex and coat [58].

Nucleoid occlusion. The nucleoid is the bacterial equivalent of the eukaryotic nucleus and comprises a highly compacted chromosome that lacks a membranous envelope and often fills most of the intracellular space [59]. Some proteins and protein complexes are restricted to the septum and the cell poles by the phenomenon of nucleoid occlusion (or nucleoid exclusion). This mechanism functions as an "anti-landmark" by preventing the localization of proteins to nucleoid-containing regions of the cell (Figure 1B). One of the classic examples of protein localization directed by nucleoid occlusion occurs during cell division. Positioning of the divisome in *B. subtilis* and *E. coli* is restricted to the division site at mid-cell because the nucleoid and nucleoid-associated division inhibitors—Noc in *B. subtilis* [60] and SlmA in *E. coli* [61]—prevent divisome assembly at all sites in the cell except the gap between the two nucleoids at the center of the cell. In addition to assisting divisome positioning, nucleoid occlusion also provides a spatiotemporal checkpoint to delay division until the replication and segregation of the replicated chromosomes is complete. As we will discuss in more details in a separate section of this chapter, bacteria have evolved additional mechanisms to prevent division close to the cell poles (i.e., at the gaps between the ends of nucleoids and the cell poles) during cytokinesis.

An analogous mechanism for nucleoid-occlusion-dependent localization of proteins that does not require nucleoid-associated proteins is based on the idea that the formation of higher-order structures of protein assemblies is energetically favorable outside the crowded cellular environment occupied by the nucleoid. According to this

mechanism, multimeric protein assemblies or protein aggregates are passively placed at the poles because of a volume-exclusion effect. This exclusion effect explains the localization of the multimeric pole-organizing factor PopZ in *Caulobacter crescentus* [34]. Consistent with the proposed model: (1) PopZ forms oligomers and self-assembles into a matrix that localizes to the cell poles and to non-polar DNA-free regions of the cell (e.g., at the gaps between segregated nucleoids of filamented *C. crescentus* cells in which division is blocked) [34, 38, 62]; (2) self-interaction and multimerization of PopZ is necessary for its polar localization [62, 63]; (3) PopZ localizes to the cell poles in heterologous host such as *E. coli* [34, 38, 62]; and (4) PopZ does not rely on membrane curvature for polar localization [34]. As we describe in the next section, polar localization of PopZ mediates polar recruitment of other proteins involved in morphogenesis and cell cycle signaling [34, 38].

A recent study has shown that nucleoid occlusion is also important for promoting polar localization of chemoreceptor clusters in *E. coli* [42]. As we previously discussed, chemoreceptors rely on the geometric features of the cell poles to accumulate there. In Chapter 2 of this dissertation, we describe an additional mechanism for localization of chemoreceptor clusters. We show that the trans-envelope Tol-Pal complex is required to maintain the polar positioning of chemoreceptor clusters in *E. coli*. Our model posits that the Tol-Pal complex restricts the diffusion of chemoreceptor clusters at the cell poles and may be involved in cluster segregation during cell division [41]. These findings suggest that some protein complexes exploit multiple mechanisms to establish and maintain polar localization.

Affinity for polar or septal components of the cell. Another mechanism that accounts

for the positioning of proteins at the bacterial cell poles or the division septa involves recruitment through an interaction with other cellular components (e.g., lipids or other proteins) already present at these cellular regions. Many proteins with reported polar localization exploit this "diffusion-and-capture" mechanism to reach and maintain their polarity. According to this mechanism, a polar or septal cellular component provides a docking site for other proteins that will serve as molecular hubs for a different group of proteins, resulting in a temporal sequence of hierarchical protein-protein interactions (Figure 1C). As mentioned in the previous sections, both DivIVA and PopZ have been demonstrated to serve as molecular landmarks. Localization of DivIVA to the cell poles or the division site is important for recruitment of other proteins in *B. subtilis*, such as the proteins involved in divisome placement MinC and MinD (through recruitment of MinJ) [64, 65], the division inhibitor Maf [66], and the regulator of competence gene expression ComN [67]. Hierarchical dependence for protein localization is also characteristic of the *C. crescentus* cell cycle. PopZ forms a matrix at the cell poles that serves as a polar "hub" for other polarly localized protein partners [15, 34, 38]. The PopZ matrix is necessary for polar attachment of the newly replicated origin region of the chromosome via interaction with ParB and for direct or indirect recruitment of proteins (e.g., CckA, DivJ, SpmX, TipN, MipZ) [15, 34, 68] involved in cell division and major developmental processes. The indication of DivIVA and PopZ serving as a docking site for other protein partners reinforces the notion that multiple mechanisms of localization are interconnected to promote intracellular organization in bacteria.

The diffusion-and-capture mechanism has been also reported in *Vibrio cholerae* for coordinating chromosome segregation, partitioning of the chemotaxis machinery, and flagellar localization/assembly [35, 69]. HubP anchors the ATPases ParA1, ParC

(indirectly), and FlhG to the old cell pole [35]. The periplasmic region of HubP is sufficient for its polar localization, but the detailed mechanism for HubP localization at the *V*. *cholerae* pole is still poorly understood. Genomic and microscopy analyses suggest that a potential interaction between a predicted LysM peptidoglycan-binding domain of HubP and the peptidoglycan contributes to its polar targeting and retention [35]. This relationship of hierarchical dependence for protein localization is a hallmark of the bacterial divisome assembly at the division site, as demonstrated in the *E*. *coli* [70, 71], *B*. *subtilis* [72], and *C*. *crescentus* [73] (Figure 2). The spatiotemporal dynamics of the bacterial divisome will be discussed in more details in a separate section.

Another special illustration of this model is the interaction of proteins with phospholipids that localize at specific regions of the cell. For example, the 2 major anionic phospholipids of *E*. *coli*—phosphatidylglycerol and diphosphatidylglycerol (cardiolipin)—accumulate at the bacterial cell poles [9-11, 74] to stabilize mechanical strain that arises due to membrane curvature [39, 40, 75, 76]. Accumulation of these phospholipids at the cell poles influences the local physicochemical properties of phospholipid bilayers, and positions and regulates several polarly localized membrane-associated proteins in *E*. *coli*, including the osmosensory transporter ProP [77-79], the machanosensistive channel MscS [79], the SecYEG translocon/SecA ATPase [80], the cell-division determinants MinD and MinE [10, 81], and the recombinase RecA [82] (Figure 1C). Interestingly, the role of cardiolipin in regulating membrane-associated proteins has also been reported in mitochondria [83].

Protein localization influenced by proton-motive force. The free energy derived from the oxidation of reducing equivalents in bacteria is converted into a proton-motive force

across the cytoplasmic membrane that is essential to drive synthesis of ATP, flagellar rotation, and the transport of solutes across the cytoplasmic membrane. This proton-motive force is comprised of two components: the electrical difference in charge (membrane potential or $\Delta\Psi$) and the chemical difference in proton concentration (ΔpH) across the cytoplasmic membrane. Recent studies have demonstrated that the localization of some bacterial proteins involved in cell division and anaerobic respiration is regulated by proton-motive force [84, 85] (Figure 1D).

The electrical component of the proton-motive force (i.e., membrane potential or $\Delta\Psi$) is essential for proper subcellular localization of some cell-division proteins, such as MinD and FtsA in *B. subtilis* and *E. coli* [84]. Consistent with this model, ionophores (e.g., CCCP and valinomycin) and bacteriocins (e.g., nisin and colicin N) that cause depolarization of the cell membrane abolish the oscillation of MinD and the mid-cell localization of FtsA [84]. The mechanism underlying $\Delta\Psi$-dependent localization of these membrane proteins is poorly understood, but in vitro experiments suggest that, at least for MinD, the membrane potential stimulates the interaction between the C-terminal amphipathic helix of MinD and the phospholipid bilayer [84]. A reduction in mid-cell localization of FtsZ and ZapA occurs after treating cells with CCCP and this phenomenon is correlated with the mislocalization of FtsA [84], one of the proteins necessary for stabilization of the ring-like structure formed by the cell division protein FtsZ in *E. coli*.

Another study demonstrated that polar localization of nitrate reductase A in *E. coli* is controlled by proton concentration gradient (ΔpH) in response to the metabolic demands of the cell [85]. Nitrate reductase concentrates at the cell poles during

anaerobic respiration in the presence of nitrate and less so in the presence of alternative terminal electron acceptors such as fumarate or trimethylamine [85]. Addition of the electroneutral anion/OH^--exchanger trichlorocarbanilide to *E. coli* cell cultures dissipates ΔpH and significantly affects the polar localization of nitrate reductase complexes [85]. However, valinomycin, a potassium ionophore that reduces only $\Delta\Psi$, has no effect on localization, suggesting that the establishment of a ΔpH is sufficient to promote polar recruitment of the nitrate reductase complex under anoxic conditions [85]. Polar localization of nitrate reductase is not coupled to the cell cycle and is completely prevented in the presence of oxygen [85]. Polar recruitment during anaerobic growth seems to potentiate the electron flux through the respiratory chain allowing cells to produce ATP more efficiently through respiration of nitrate [85].

Growth- and division-associated mechanisms of localization. In addition to exploiting geometric and biological features of the cell poles to direct protein localization, some proteins highjack biosynthetic (e.g., peptidoglycan biosynthesis) or division events to passively accumulate at the cell poles. According to these mechanisms, proteins destined to the cell poles (1) progressively move towards the poles as cells proceed through repeated cycles of growth and division or (2) interact with components localized to mid-cell during division and remain at the pole as an inheritance of the division cycle (Figure 1E).

Asymmetric subcellular localization mediated by lateral growth of the peptidoglycan layer has been proposed to explain the polarized distribution of the virulence factor ActA on the surface of the Gram-positive pathogen *Listeria monocytogenes* [28]. Following infection of a host cell, ActA is translocated through the

cytoplasmic membrane at distinct regions, forming irregular patches upon association with the peptidoglycan layer [86], and becomes homogeneously distributed along the lateral edges of the cell over time [28]. As cell elongation progresses and the older peptidoglycan moves towards the poles, ActA slowly and progressively accumulates at the cell poles and becomes particularly conspicuous at older cell poles after successive rounds of division [28]. This mechanism of localization explains the characteristic unipolar pattern of ActA necessary for the actin-based motility that propels *L. monocytogenes* within the host cell and allows direct spread from cell to cell [87-89]. Other virulence factors of *L. monocytogenes* (e.g., InternalinA) seem to use a similar mechanism to accumulate at the cell poles [28].

Association with the peptidoglycan has also been proposed to account for localization of the division marker MapZ in *Streptococcus pneumoniae* [90]. Fluorescence microscopy revealed that MapZ forms ring-like structures at the equatorial region of the cell, recruits the cell-division protein FtsZ, and moves apart as the cell elongates to mark future division sites [90]. MapZ rings are mechanically pushed apart as peripheral peptidoglycan synthesis occurs and FtsZ remains at the septum to support constriction [90]. Consistent with this proposed model: (1) peripheral peptidoglycan synthesis is responsible for cell elongation in *S. pneumoniae* [91, 92]; (2) the extracellular C-terminal domain of MapZ efficiently binds peptidoglycan [90]; and (3) chemical inhibition of peptidoglycan synthesis prevents proper localization of MapZ and affects proper placement of the division machinery [90]. It is still unclear whether MapZ recognizes peptidoglycan structures specifically localized at mid-cell. In addition to marking the division site and positioning FtsZ, the phosphorylation level of MapZ seems to indirectly modulate cytokinesis [90]. Importantly, MapZ is conserved among

Streptococcaceae and other Lactobacillales [90] and might have a similar role at regulating cell division in other members of these bacterial groups.

A different strategy for polar localization of proteins seems to rely solely on the actual process of cell division. In this case, even proteins that are not associated with cell division localize to mid-cell during divisome assembly and remain associated with the newly-formed cell poles in the progeny cells as an inheritance of the division cycle. An example of asymmetry generated by cell division is proposed for polar localization of the cell-pole organizer/determinant TipN in *C. crescentus* [32, 33]. In the beginning of the cell cycle, TipN is localized at the newer pole (i.e., the pole generated following the previous round of cell division) [32, 33]. As cells engage in division, TipN diffuses away from the new pole and relocalizes at the division site as the divisome assembles [32, 33]. The detailed mechanism for polar delocalization and septal relocalization of TipN during the cell cycle is not completely understood, but the process depends on cell division [32, 33]. Recent studies show that TipN interacts with components of the Tol-Pal complex—a subcomplex of the divisome involved in constriction of the outer membrane in Gram-negative bacteria [71]—and this interaction is necessary for polar localization of TipN [93]. This mechanism of localization demonstrates that division (or the divisiome itself) also functions as a landmark for protein positioning and, in the case of TipN, guarantees that the new poles of progeny cells inherit the necessary information for polar determination.

Polar localization enhanced by proteolysis. One of the classic demonstrations that proteolysis can help promote asymmetric distribution of proteins in bacteria is the polarized localization of IcsA on the surface of the pathogen *Shigella flexneri* [6]. This

virulence factor is the functional counterpart of ActA in *L. monocytogenes* as it allows intracellular actin-based motility of *S. flexneri* inside the host cell [94]. The current model for polar accumulation of IcsA proposes that the protein is targeted to one pole of the bacterial cell even prior to translocation into the outer membrane and, therefore, appears on the cell surface in a polarized distribution [95]. Upon insertion into the outer membrane, IcsA diffuses slowly, but is cleaved by the homogeneously distributed protease IcsP [95] (Figure 1F). The combination of continuous insertion of IcsA at one cell pole and cleavage by IcsP, preventing lateral diffusion of IcsA away from the pole, is sufficient for establishing and maintaining the unipolar distribution of IcsA [95, 96]. It remains largely unclear how this initial unipolar positioning occurs; however, IcsA displays unipolar localization in a variety of heterologous hosts, including *E. coli*, *Salmonella enterica,* and *Yersinia pseudotuberculosis*, and *V. cholerae* [97]. This finding suggests that the mechanism for localization of IcsA might be widely spread among different bacterial groups.

Restricted diffusion of outer membrane proteins (OMPs) that form supramolecular assemblies. Similarly to the cytoplasmic membrane, the outer membrane of Gram-negative bacteria displays remarkable spatial organization of protein complexes. Recent single-molecule fluorescence microscopy studies of outer membrane proteins (OMPs) in *E. coli* and molecular dynamics simulations revealed that the OMPs BtuB (a vitamin B_{12} transporter) and Cir (an iron siderophore transporter) move towards and become confined at the poles [98]. Biogenesis of these OMPs is higher at mid-cell and newly-introduced OMPs form heterogeneous islands of ~0.5 μm in diameter through promiscuous protein-protein interactions [98]. The asymmetric addition of new OMPs

and the restricted diffusion of these OMPs due to formation of supramolecular assemblies through OMP-OMP interactions seem to be sufficient to drive partitioning and influence polar confinement of old OMP islands as cells grow and divide [98] (Figure 1G). It is unclear whether the geometry of the outer membrane poles plays a role in localization of these OMP islands. Importantly, this model highlights that the mechanism underlying polar localization of OMP is linked to OMP turnover and is not a consequence of molecular crowding or association with other outer membrane components such as lipopolysaccharides [98]. In addition, intrinsic to this model is the concept that new cells receive little or no old OMP. This biased partitioning of OMP has major implications in phenotypic heterogeneity of bacterial populations [99]. A recent study showed that the trans-envelope complex AcrAB-TolC—the main multidrug efflux pump of *E. coli* [100]—accumulates at the old pole of "mother" (older) cells as they divide, leading to differences in drug-resistance profile in the population [99]. Polar accumulation of AcrAB-TolC is dependent on the outer membrane component of the complex, TolC [99], suggesting that protein components located in one layer (e.g., outer membrane) of the cell envelope influence the localization of proteins located in a different layer (e.g., cytoplasmic membrane).

Spatiotemporal dynamics of cell division proteins

Bacterial cell division is a complex process that requires accurate identification of the division site, positioning of the division machinery, and coordinated constriction of the cell envelope. In bacteria, with few exceptions [101, 102], this essential process is initiated with the polymerization of the cell-division protein FtsZ into a filamentous, ring-like structure (referred to as the Z ring) that is located in the cytoplasm peripheral

to the membrane and close to the division site [25, 103-105]. Concomitant with and following its polymerization, the Z ring coordinates the recruitment of various auxiliary proteins that perform diverse roles in cell division and cell wall biosynthesis/remodeling [106-109] (Figures 2A and 2B). Depletion of FtsZ in rod-shaped bacteria, such as the *E. coli*, produces long, filamentous cells due to the continued growth of cells that are no longer dividing [110]. Cocci-shaped bacteria, such as the pathogen *Staphylococcus aureus*, increase in volume up to 8-fold when depleted of FtsZ [111]. In both cases, cells are unable to divide; continued growth makes them enlarged and sensitive to changes in the physical properties of their environment, and the cells eventually lyse.

The spatiotemporal regulation of Z ring formation requires a complex and concerted network of proteins that modulate assembly and activity of FtsZ to ensure that the division process is tightly coordinated with DNA replication, chromosome segregation, and cell elongation [112-115]. The molecular details underlying the synchronicity of these processes are not completely understood; however, research over the past 2 decades has elucidated important structural, functional, and regulatory aspects of these mechanisms. In *E. coli*, the division process requires at least 14 major cytoplasmic, membrane, and periplasmic proteins, of which ~10 are essential [70, 108, 109, 116] (Figures 2A and 2B). FtsZ and the other cell division proteins, as well as their regulators, are recruited to mid-cell in a hierarchical order to form the functional divisome, a ring-like multiprotein complex that constricts during the process of division and disappears when the cells separate [70, 107, 108, 117]. The divisome machinery is essential and appears to be widely conserved among bacteria.

E. coli and *B. subtilis* use at least two coordinated systems to accurately position

the Z ring at the mid-cell and ensure that divisome formation is timed to occur at the final stage of the cell cycle: (1) the Min system of proteins prevents aberrant division at regions other than the mid-cell [26, 27] and (2) nucleoid occlusion proteins prevent division from occurring over segregating chromosomes [60, 61] (Figure 2B). Importantly, in the absence of these two negative regulators of Z ring positioning, both *E. coli* and *B. subtilis* still have a bias for Z ring formation at mid-cell [60, 61], suggesting that additional mechanisms may influence FtsZ assembly at the mid-cell and coordinate chromosome segregation and cell division. A recent study provided evidence of an additional positional marker in *E. coli* cells grown in minimal media and lacking functional Min and nucleoid occlusion systems [118]. The replication terminus (Ter) macrodomain region of the chromosome acts as a landmark for the Z ring in the presence of the chromosomal terminus organization protein MatP and the cell division proteins ZapA and ZapB [118].

Much of the mechanistic insight on the spatiotemporal regulation of the Z ring has come from studies of *E. coli* and *B. subtilis*. However, many bacteria lack both canonical systems for positioning FtsZ. For example, spatiotemporal assembly and placement of the Z ring in *C. crescentus* require the ATPase MipZ [68]. MipZ associates with the origin region of chromosomes and (in a manner analogous to the Min system) directly guides FtsZ positioning and polymerization into the Z ring at mid-cell [68] (Figure 2B). As mentioned in a previous section, in *S. pneumoniae*, the single-passage transmembrane MapZ forms a ring-like structure at the division site and guides positioning of the Z ring [90] (Figure 2B). In addition to its dual role in marking the cell division site and positioning FtsZ, the balance between the phosphorylated and dephosphorylated forms of MapZ may be important for controlling Z ring stability and

regulation of constriction [90].

In addition to these specific protein-based systems that control FtsZ dynamics, other positive and negative regulators interact with FtsZ to modulate structure and function of the divisome in response to the nutritional and developmental state of the cell (Table 1). These regulatory systems for positioning of FtsZ have adapted to different environments, cell shapes, and developmental behaviors, and emphasize the importance of coordinating the correct timing of cell division and chromosome segregation. Many studies have indicated that unknown regulators of FtsZ may be awaiting discovery.

Prospects and challenges

Studying the establishment, maintenance, and replication of bacterial subcellular organization is a central step in decoding cell biology. Seminal studies over the past 25 years have uncovered new biology and transformed our view of biomolecular spatiotemporal organization in bacteria; however, many aspects of this fascinating area remain still enigmatic. In this section, we frame some important unanswered questions in the field, consider the possible challenges intrinsic to addressing these questions, and discuss the potential use of these localization mechanisms as target for development of new families of antimicrobial agents.

An evident question in the field is: What other types of mechanism for biomolecule localization exist? It is likely that the examples of mechanisms characterized so far highlight only the most general principles shared among different groups of bacteria. Most localization studies in bacteria focus on uncovering mechanisms of cell polarity or those involved in placement/assembly of the division

machinery at the division site. Recent proteome-scale analysis showed that ~10% of the predicted *C. crescentus* proteome analyzed display distinct localization patterns (e.g., unipolar, bipolar, in the stalk, as a band at mid-cell, as a central focus, in a line) or a combination of these patterns [22]. Some of the reported localization patterns cannot be simply explained by the mechanisms described above. These observations reinforce the significance of intracellular organization for bacterial growth and survival and expand the inventory of mechanisms awaiting to be discovered.

The identification and molecular characterization of mechanisms for the spatial and temporal control of intracellular organization in bacteria lags dramatically behind related studies in eukaryotes. The knowledge accumulated from studies in eukaryotes raises the question: What lessons from eukaryotic cell biology can we translate to bacterial systems? One area that has received momentum in prokaryotic research, perhaps influenced by important findings in eukaryotic cell biology, is the field of RNA localization and the connection between the localization of specific messenger RNAs (mRNAs) and the proteins that they encode [12, 14]. Spatiotemporal localization of proteins guided by mRNA localization adds a new layer of complexity to the theme and will possibly uncover new and interesting biology. Other exciting, emerging areas in the bacterial field include (1) spatial control of proteolysis [119, 120] and (2) control of protein localization by small GTPases [121, 122]. Despite the relative recentness of these fields, we expect that a clear picture of the bacterial mechanisms will provide a starting point for understanding conserved mechanisms in eukaryotic organelles such as mitochondria, which may shed insight into the connection between the dysfunction of this organelle and human diseases.

A strategy that has accelerated the field of protein localization in eukaryotes is the possibility of predicting organelle targeting [123, 124]. Algorithms to predict protein targeting in bacteria rely on the absence or presence of "signals" encoded in the sequence of a nascent protein (e.g., N-terminal signal peptide or secondary structures for membrane insertion) [125]. These computer programs are designed to predict whether a protein will remain in the cytoplasm, be directed to one of the layers of the cell envelope, or be secreted to the extracellular space. A theoretical framework has been developed to address the distribution of some lipids in bacteria [76]. However, at this point, both the choice of localization mechanism and the pattern of intracellular distribution for bacterial proteins are not amenable to computational identification. The emerging picture reveals a substantial amount of diversity and overlap routes for protein localization, which challenges the development of prediction methods. There is no apparent signal encoded in the protein sequence, but the choice of mechanism seems to be motivated by intrinsic features of the protein (e.g., protein folding, the presence of patches that interact with the anionic character of polar membranes, the ability to form multimeric complexes that sense membrane curvature, presence of peptidoglycan-binding domain), differences in the cellular context (e.g., nutritional and developmental state of the cell, physiochemical nature of the surrounding environment), or a combination of these factors.

As we discussed in the previous sections, subcellular organization in bacteria is critical for metabolic and structural properties of the cell. For example, protein localization is essential for bacterial virulence and division. The connection between protein localization and function might have implications for antibiotic discovery. All known clinical antibiotics target DNA replication, transcription, translation,

peptidoglycan biosynthesis, folate biosynthesis or the integrity of the cytoplasmic membrane [126, 127]. An increase of multidrug resistance among pathogenic bacteria and the lack of innovation in the discovery of new antibacterial drugs emphasize the need for new chemotherapeutic strategies. An important, unanswered question is whether additional classes of mechanisms and targets exist for developing new families of antibiotics. The bacterial "localizome" contains multiple targets for which clinical antibiotics have not yet emerged. Strategies for the identification of drugs that target the bacterial divisome and the challenges that accompany the discovery approaches have been recently revisited [128]. In Chapter 3 of this dissertation, we describe the mode of action of synthetic small molecules that chelate iron and arrest cytokinesis by preventing placement of the divisome at the division site [129].

Concluding remarks

Many proteins and other biomolecules of bacterial cells display patterns of localization that challenge the traditional and incorrect interpretation that prokaryotes lack dedicated mechanisms for spatiotemporal control of their cellular components. This intracellular compartmentalization is integral to a variety of physiological processes, including: cell division, virulence, spore formation, cell wall assembly, and chemotaxis. Several proteins and protein complexes are localized to the division plane and the poles in rod-shaped bacteria. Although hypotheses have been formulated to account for their localization, the molecular details underlying these mechanisms remain largely undefined. Understanding how bacteria establish and maintain their intracellular biomolecular organization will provide insight into the biochemical underpinnings of bacterial physiology, and potentially open doors to understand

related processes in other microbes and in eukaryotic organelles. Finally, a clear picture of the complexities that underlie the bacterial “localizome” will guide studies directed at testing whether disruption of protein localization may be a viable mechanism for antimicrobial targeting and development.

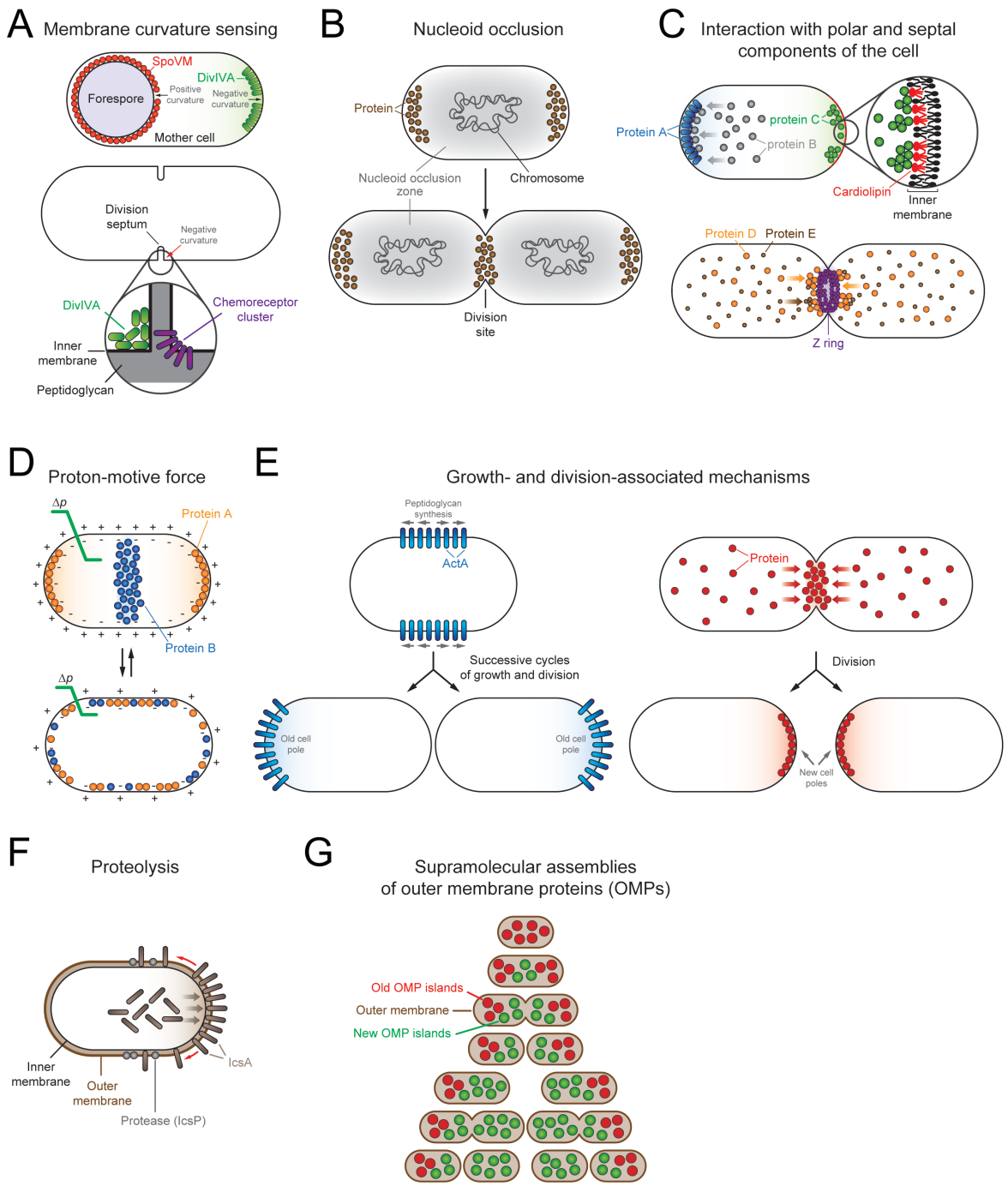

Figure 1. Molecular mechanisms for spatiotemporal localization of polar and septal proteins in bacteria.

(A) Direct sensing of membrane curvature in *B. subtilis*. DivIVA and chemoreceptor clusters sense negatively curved regions of the membrane (i.e., the concave surface of membrane) [7, 44, 49]. SpoVM of *B. subtilis* recognizes the positive curvature (i.e., the convex surface) of the forespore membrane [8, 58].

(B) Nucleoid occlusion. The bacterial nucleoid functions as an anti-landmark and prevents localization of proteins at nucleoid-containing regions of the cell. Formation of large protein assemblies such as higher-order structures (e.g. PopZ in *C. crescentus*) is energetically favored outside the nucleoid region [34, 38, 62].

(C) Affinity for polar or septal components of the cell. *Top left*: A diffusing protein (e.g., hypothetical protein B) is trapped at the cell poles through an interaction with another protein (e.g., hypothetical protein A) that is already localized at the cell poles. *Top right*: Some proteins (e.g., hypothetical protein C [10, 77-82]) interact preferentially with cardiolipin and other anionic phospholipids that are enriched at the cell poles [9-11, 74]. *Bottom*: Hierarchical dependence for protein localization during divisome assembly at the division site [70-73]. See Figure 2 for additional information.

(D) Protein localization influenced by proton-motive force (Δp). The electrical and chemical components of the proton-motive force are important for polar (e.g., hypothetical protein A) and septal (e.g., hypothetical protein B) localization of some bacterial proteins [84, 85]. Decrease in Δp causes mislocalization of these proteins. The detailed underlying mechanism is not completely understood.

(E) Growth- and division-associated mechanisms of localization. *Left*: In *L. monocytogenes*, ActA forms irregular patches upon association with the peptidoglycan [86], and becomes homogeneously distributed along the lateral edges of the cell over time [28]. As cell elongation progresses and the older peptidoglycan moves towards the poles, ActA progressively accumulates at the cell poles after successive rounds of division [28]. *Right*: Some proteins (e.g., TipN in *C. crescentus* [32, 33]) localize to mid-cell during divisome assembly and remain associated with the newly-formed cell poles in the progeny cells as an inheritance of the division cycle.

(F) Protein localization enhanced by proteolysis in *S. flexnery*. IcsA is continuously inserted at one cell pole, but has limited lateral diffusion due to cleavage by the protease IcsP [95, 96].

(G) Restricted diffusion of outer membrane proteins (OMPs) that form supramolecular assemblies. Newly-introduced OMPs form heterogeneous islands at mid-cell through promiscuous protein-protein interactions, which prevents their lateral diffusion. The asymmetric addition of new OMPs at the mid-cell and the restricted diffusion of these OMPs due to formation of supramolecular assemblies result in polar confinement of old OMP islands as cells grow and divide [98].

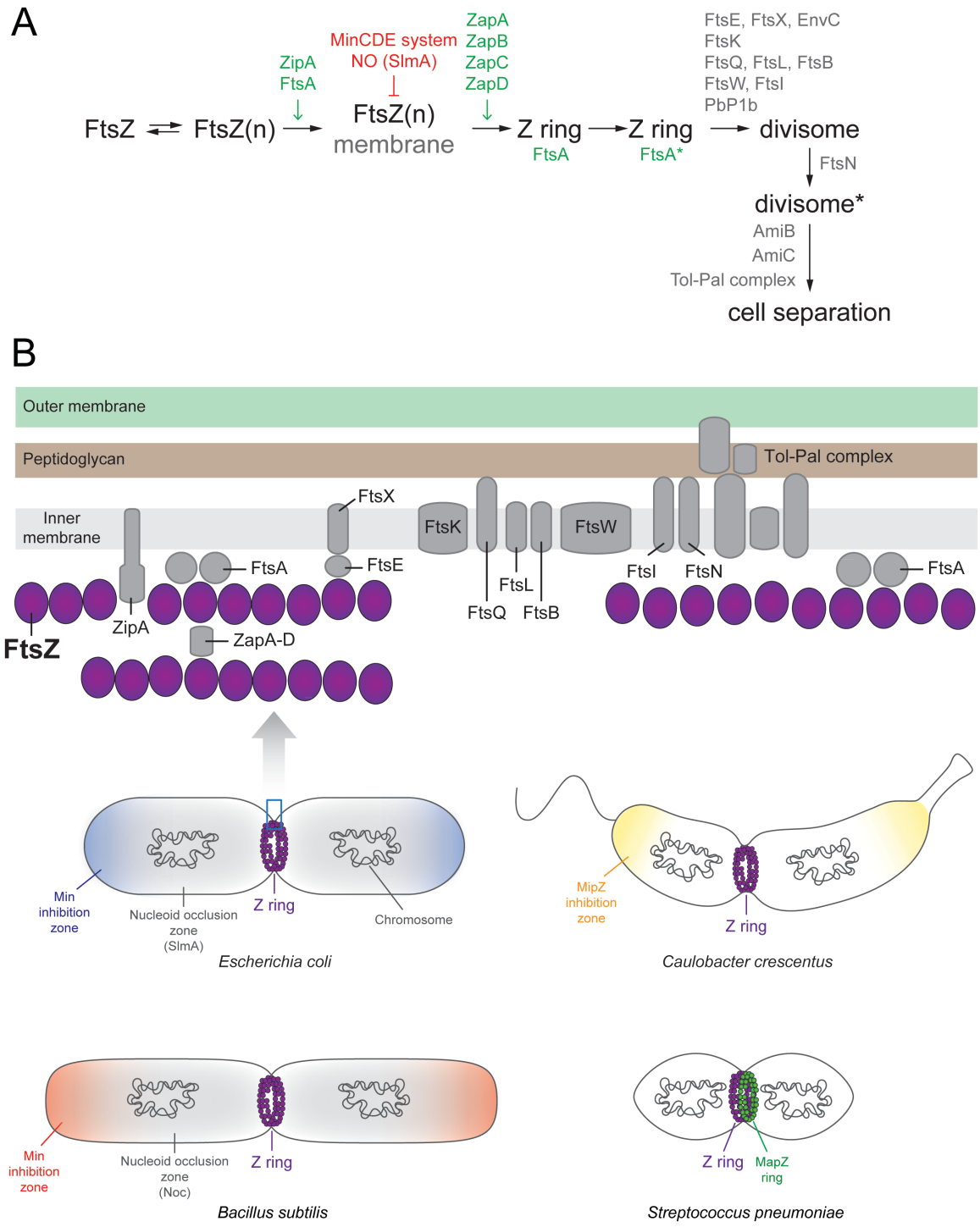

Figure 2. Spatiotemporal regulation of the Z ring in different groups of bacteria.

(A) Diagram summarizing the hierarchical recruitment of cell division proteins in *E. coli*. FtsZ and the early cell division proteins localize to the division site before cell septation starts. The proteins are recruited to the Z ring in a sequential and approximately linear pathway. The requirement of an upstream protein for localization of a downstream protein to the Z ring was deduced from various studies of genetics, biochemistry, and microscopy. Proteins that regulate the assembly of the Z ring are shown in green (positive regulators) and red (negative regulators). This diagram was redrawn from reference [106]. NO, nucleoid occlusion.

(B) *Top*: A cartoon depicting the predicted organization of the *E. coli* divisome. Cell division is initiated with the polymerization of FtsZ into the Z ring onto which the divisome apparatus assembles. The cartoon of the divisome was adapted from references [73] and [130]. *Bottom*: A cartoon illustrating some of the bacterial mechanisms for positioning of the Z ring during cell division. In *E. coli*, Min proteins (MinCDE) oscillate between the cell poles, creating an inhibition zone (blue shaded area) and preventing Z ring (in purple) polymerization near those poles [26, 27]. (For simplicity, the dynamic behavior of the Min system is omitted). In addition, nucleoid occlusion, mediated by the protein SlmA, creates an inhibition zone (gray shaded area) along the cylindrical region of the cell and prevents Z ring assembly over the nucleoid [61]. Similarly, the *B. subtilis* Min system (composed of MinCDJ and DivIVA) creates a zone of inhibition (red shaded area) that prevents Z ring assembly at the cell poles. However, MinCDJ localizes to the cell poles in a DivIVA-dependent manner and does not undergo the characteristic dynamic oscillatory behavior observed in *E. coli* [131]. In addition to the Min system, the protein Noc mediates nucleoid occlusion (gray shaded

area), preventing divisome assembly from occurring over segregating chromosomes [60]. In *C. crescentus*, the protein MipZ (yellow shaded area) coordinates chromosome segregation and cell division in response to both spatial and temporal cues. Assembly of the Z ring is coincident with the subcellular position that exhibits the lowest concentration of MipZ. Prior to chromosome replication, MipZ and FtsZ are localized to the opposite poles of the cell. MipZ forms a complex with proteins involved in chromosome partitioning. Following duplication of the chromosomal origin of replication (oriC), MipZ migrates toward the opposite cell pole creating a bipolar gradient, displacing FtsZ from the pole, and directing formation of the Z ring at mid-cell [68, 132]. In *S. pneumoniae*, the protein MapZ forms a ring-like structure (in green) positioned at mid-cell (and at future division sites), marking the division site and positioning FtsZ [90].

Table 1. Proteins that regulate the formation of the Z ring in different bacterial groups [a].

Positive regulators of Z ring formation	
FtsA [b]	Membrane anchor that supports assembly and stabilization of the Z ring. It is also important for the recruitment of downstream proteins necessary for divisome maturation [133, 134]. Widely conserved.
SsgA, SsgB	Regulates Z ring formation during sporulation-specific cell division in *S. coelicolor* [135].
PomZ	Regulates Z ring formation and cell division in *Myxococcus xanthus* [136].
MapZ	Regulates Z ring formation and positioning at mid-cell in *S. pneumoniae* and possibly in other Lactobacillales. It is also involved in the regulation of cytokinesis [90].
SepF	Required for proper morphology of the divisional septum. It has overlapping roles with FtsA in Z ring assembly [137, 138]. Conserved in Gram-positive bacteria and Cyanobacteria.
ZapA, B, C, D	Mediate additional stabilization of the Z ring [139-142]. ZapA is widely conserved.
ZipA	Secondary membrane anchor that together with FtsA supports assembly of the Z ring [143, 144]. Conserved in Gammaproteobacteria.
Negative regulators of Z ring formation	
ClpX/ClpXP	Helps modulate the equilibrium between the cytoplasmic pool of unassembled FtsZ and polymeric FtsZ through degradation [145]. ClpX chaperone can also inhibit formation of the Z ring in a ClpP-independent fashion by physically blocking the assembly of FtsZ filaments [146, 147]. Widely conserved.
CrgA	Important for coordinating cell growth and division in *S. coelicolor*. It regulates the dynamics of Z ring formation and affects both the timing of FtsZ expression and its turnover [148].
EzrA	Modulates the position of the Z ring during cell division and plays a role in coordinating cell growth and division [149]. Conserved in Gram-positive bacteria with low GC content.

GdhZ	NAD-dependent glutamate dehydrogenase that controls Z ring disassembly by stimulating the GTPase activity of FtsZ in *C. crescentus* [150].
KidO	Coordinates cellular or developmental activities with the availability of NADH in *C. crescentus*. KidO bound to NADH is thought to destabilize lateral interactions between FtsZ protofilaments. It has been recently proposed to work in synergy with GdhZ to trigger Z ring disassembly [150, 151].
OpgH	Glucosyltransferase that functions as a nutrient-dependent antagonist of the Z ring in *E. coli*. OpgH is thought to sequester FtsZ from growing polymers. Blocks Z ring formation to coordinate cell growth and cell division [152].
MciZ	Inhibits Z ring formation by capping the minus end of FtsZ filaments and shortening the filaments [153]. Conserved in *Bacillus* spp..
MinC	Important for positioning the Z ring at mid-cell [26, 27, 154]. Widely conserved.
MipZ	Required for positioning the Z ring at mid-cell in *C. crescentus* [68].
Noc	Inhibits Z ring formation over segregating chromosomes in *B. subtilis* [60].
SlmA	Analogous to Noc, it inhibits Z ring formation over segregating chromosomes in *E. coli* [61]. Widely spread in Betaproteobacteria and Gammaproteobacteria.
SulA	Negative modulator of Z ring expressed in response to DNA damage as part of the SOS system [155, 156]. Conserved in Gammaproteobacteria.
UgtP	Similar to OpgH, this glucosyltransferase inhibits cell division by blocking Z ring formation in a growth rate-dependent fashion. This cellular sensor ensures that cells reach the appropriate mass and complete chromosome segregation prior to cytokinesis [157]. Widely conserved.
YneA	Analogous to SulA, it regulates cell division through the suppression of Z ring formation during the SOS response in *B. subtilis* [158].

[a] Some of these proteins and the molecular systems that they compose are widespread among bacteria. However, some of them are exclusive to specific groups of bacteria [159]. See the text and refer to the cited literature for an additional explanation. The

referencing is not exhaustive for the best-studied proteins listed.

[b] It was recently demonstrated that FtsA has a dual, antagonistic role on the FtsZ filament network. FtsA is involved in recruitment of FtsZ filaments to the membrane, but it also provides a negative regulation by causing fragmentation of FtsZ polymers, allowing the rapid disassembly of FtsZ filaments [134].

REFERENCES

1. Matsumoto K, Kusaka J, Nishibori A, Hara H. Lipid domains in bacterial membranes. *Mol Microbiol*. 2006; 61: 1110-7.
2. Shapiro L, McAdams HH, Losick R. Why and how bacteria localize proteins. *Science*. 2009; 326: 1225-8.
3. Campos M, Jacobs-Wagner C. Cellular organization of the transfer of genetic information. *Curr Opin Microbiol*. 2013; 16: 171-6.
4. Buskila AA, Kannaiah S, Amster-Choder O. RNA localization in bacteria. *RNA Biol*. 2014; 11: 1051-60.
5. Maddock JR, Shapiro L. Polar location of the chemoreceptor complex in the *Escherichia coli* cell. *Science*. 1993; 259: 1717-23.
6. Goldberg MB, Barzu O, Parsot C, Sansonetti PJ. Unipolar localization and ATPase activity of IcsA, a *Shigella* flexneri protein involved in intracellular movement. *J Bacteriol*. 1993; 175: 2189-96.
7. Ramamurthi KS, Losick R. Negative membrane curvature as a cue for subcellular localization of a bacterial protein. *Proc Natl Acad Sci U S A*. 2009; 106: 13541-5.
8. Ramamurthi KS, Lecuyer S, Stone HA, Losick R. Geometric cue for protein localization in a bacterium. *Science*. 2009; 323: 1354-7.
9. Mileykovskaya E, Dowhan W. Visualization of phospholipid domains in *Escherichia coli* by using the cardiolipin-specific fluorescent dye 10-N-nonyl acridine orange. *J Bacteriol*. 2000; 182: 1172-5.
10. Renner LD, Weibel DB. Cardiolipin microdomains localize to negatively curved regions of *Escherichia coli* membranes. *Proc Natl Acad Sci U S A*. 2011; 108: 6264-9.
11. Oliver PM, Crooks JA, Leidl M, Yoon EJ, Saghatelian A, Weibel DB. Localization of anionic phospholipids in *Escherichia coli* cells. *J Bacteriol*. 2014; 196: 3386-98.
12. Montero Llopis P, Jackson AF, Sliusarenko O, Surovtsev I, Heinritz J, Emonet T, et al. Spatial organization of the flow of genetic information in bacteria. *Nature*. 2010; 466: 77-81.
13. Nevo-Dinur K, Nussbaum-Shochat A, Ben-Yehuda S, Amster-Choder O. Translation-independent localization of mRNA in *E. coli*. *Science*. 2011; 331: 1081-4.
14. Moffitt JR, Pandey S, Boettiger AN, Wang S, Zhuang X. Spatial organization shapes the turnover of a bacterial transcriptome. *Elife*. 2016; 5: e13065.
15. Bowman GR, Comolli LR, Gaietta GM, Fero M, Hong SH, Jones Y, et al. *Caulobacter* PopZ forms a polar subdomain dictating sequential changes in pole composition and function. *Mol Microbiol*. 2010; 76: 173-89.
16. Lewis PJ, Thaker SD, Errington J. Compartmentalization of transcription and translation in *Bacillus subtilis*. *EMBO J*. 2000; 19: 710-8.

17. Bakshi S, Siryaporn A, Goulian M, Weisshaar JC. Superresolution imaging of ribosomes and RNA polymerase in live *Escherichia coli* cells. *Mol Microbiol*. 2012; 85: 21-38.

18. Christen M, Kulasekara HD, Christen B, Kulasekara BR, Hoffman LR, Miller SI. Asymmetrical distribution of the second messenger c-di-GMP upon bacterial cell division. *Science*. 2010; 328: 1295-7.

19. Henry JT, Crosson S. Chromosome replication and segregation govern the biogenesis and inheritance of inorganic polyphosphate granules. *Mol Biol Cell*. 2013; 24: 3177-86.

20. Lai EM, Nair U, Phadke ND, Maddock JR. Proteomic screening and identification of differentially distributed membrane proteins in *Escherichia coli*. *Mol Microbiol*. 2004; 52: 1029-44.

21. Kitagawa M, Ara T, Arifuzzaman M, Ioka-Nakamichi T, Inamoto E, Toyonaga H, et al. Complete set of ORF clones of *Escherichia coli* ASKA library (a complete set of *E. coli* K-12 ORF archive): Unique resources for biological research. *DNA Res*. 2005; 12: 291-9.

22. Werner JN, Chen EY, Guberman JM, Zippilli AR, Irgon JJ, Gitai Z. Quantitative genome-scale analysis of protein localization in an asymmetric bacterium. *Proc Natl Acad Sci U S A*. 2009; 106: 7858-63.

23. Li G, Young KD. Isolation and identification of new inner membrane-associated proteins that localize to cell poles in *Escherichia coli*. *Mol Microbiol*. 2012; 84: 276-95.

24. Gahlmann A, Moerner WE. Exploring bacterial cell biology with single-molecule tracking and super-resolution imaging. *Nat Rev Microbiol*. 2014; 12: 9-22.

25. Bi EF, Lutkenhaus J. FtsZ ring structure associated with division in *Escherichia coli*. *Nature*. 1991; 354: 161-4.

26. Hu Z, Mukherjee A, Pichoff S, Lutkenhaus J. The MinC component of the division site selection system in *Escherichia coli* interacts with FtsZ to prevent polymerization. *Proc Natl Acad Sci U S A*. 1999; 96: 14819-24.

27. Raskin DM, de Boer PA. Rapid pole-to-pole oscillation of a protein required for directing division to the middle of *Escherichia coli*. *Proc Natl Acad Sci U S A*. 1999; 96: 4971-6.

28. Rafelski SM, Theriot JA. Mechanism of polarization of *Listeria monocytogenes* surface protein ActA. *Mol Microbiol*. 2006; 59: 1262-79.

29. Carlsson F, Joshi SA, Rangell L, Brown EJ. Polar localization of virulence-related Esx-1 secretion in Mycobacteria. *PLoS Pathog*. 2009; 5: e1000285.

30. Morgan JK, Luedtke BE, Shaw EI. Polar localization of the *Coxiella burnetii* type IVB secretion system. *FEMS Microbiol Lett*. 2010; 305: 177-83.

31. Jain S, van Ulsen P, Benz I, Schmidt MA, Fernandez R, Tommassen J, et al. Polar localization of the autotransporter family of large bacterial virulence proteins. *J Bacteriol*. 2006; 188: 4841-50.

32. Lam H, Schofield WB, Jacobs-Wagner C. A landmark protein essential for establishing and perpetuating the polarity of a bacterial cell. *Cell*. 2006; 124: 1011-23.

33. Huitema E, Pritchard S, Matteson D, Radhakrishnan SK, Viollier PH. Bacterial birth scar proteins mark future flagellum assembly site. *Cell*. 2006; 124: 1025-37.

34. Ebersbach G, Briegel A, Jensen GJ, Jacobs-Wagner C. A self-associating protein critical for chromosome attachment, division, and polar organization in *Caulobacter*. *Cell*. 2008; 134: 956-68.

35. Yamaichi Y, Bruckner R, Ringgaard S, Moll A, Cameron DE, Briegel A, et al. A multidomain hub anchors the chromosome segregation and chemotactic machinery to the bacterial pole. *Genes Dev*. 2012; 26: 2348-60.

36. Alley MR, Maddock JR, Shapiro L. Polar localization of a bacterial chemoreceptor. *Genes Dev*. 1992; 6: 825-36.

37. Gestwicki JE, Lamanna AC, Harshey RM, McCarter LL, Kiessling LL, Adler J. Evolutionary conservation of methyl-accepting chemotaxis protein location in Bacteria and Archaea. *J Bacteriol*. 2000; 182: 6499-502.

38. Bowman GR, Comolli LR, Zhu J, Eckart M, Koenig M, Downing KH, et al. A polymeric protein anchors the chromosomal origin/ParB complex at a bacterial cell pole. *Cell*. 2008; 134: 945-55.

39. Huang KC, Ramamurthi KS. Macromolecules that prefer their membranes curvy. *Mol Microbiol*. 2010; 76: 822-32.

40. Wingreen NS, Huang KC. Physics of intracellular organization in bacteria. *Annu Rev Microbiol*. 2015; 69: 361-79.

41. Santos TM, Lin TY, Rajendran M, Anderson SM, Weibel DB. Polar localization of *Escherichia coli* chemoreceptors requires an intact Tol-Pal complex. *Mol Microbiol*. 2014; 92: 985-1004.

42. Neeli-Venkata R, Startceva S, Annila T, Ribeiro AS. Polar Localization of the serine chemoreceptor of *Escherichia coli* is nucleoid exclusion-dependent. *Biophys J*. 2016; 111: 2512-22.

43. Draper W, Liphardt J. Origins of chemoreceptor curvature sorting in *Escherichia coli*. *Nat Commun*. 2017; 8: 14838.

44. Lenarcic R, Halbedel S, Visser L, Shaw M, Wu LJ, Errington J, et al. Localisation of DivIVA by targeting to negatively curved membranes. *EMBO J*. 2009; 28: 2272-82.

45. Edwards DH, Thomaides HB, Errington J. Promiscuous targeting of *Bacillus subtilis* cell division protein DivIVA to division sites in *Escherichia coli* and fission yeast. *EMBO J*. 2000; 19: 2719-27.

46. Stahlberg H, Kutejova E, Muchova K, Gregorini M, Lustig A, Muller SA, et al. Oligomeric structure of the *Bacillus subtilis* cell division protein DivIVA determined by transmission electron microscopy. *Mol Microbiol*. 2004; 52: 1281-90.

47. Flardh K. Essential role of DivIVA in polar growth and morphogenesis in *Streptomyces coelicolor* A3(2). *Mol Microbiol*. 2003; 49: 1523-36.

48. Holmes NA, Walshaw J, Leggett RM, Thibessard A, Dalton KA, Gillespie MD, et al. Coiled-coil protein Scy is a key component of a multiprotein assembly controlling polarized growth in *Streptomyces*. *Proc Natl Acad Sci U S A*. 2013; 110: E397-406.

49. Strahl H, Ronneau S, Gonzalez BS, Klutsch D, Schaffner-Barbero C, Hamoen LW. Transmembrane protein sorting driven by membrane curvature. *Nat Commun*. 2015; 6: 8728.

50. Bray D, Levin MD, Morton-Firth CJ. Receptor clustering as a cellular mechanism to control sensitivity. *Nature*. 1998; 393: 85-8.

51. Gestwicki JE, Kiessling LL. Inter-receptor communication through arrays of bacterial chemoreceptors. *Nature*. 2002; 415: 81-4.

52. Zhang P, Khursigara CM, Hartnell LM, Subramaniam S. Direct visualization of *Escherichia coli* chemotaxis receptor arrays using cryo-electron microscopy. *Proc Natl Acad Sci U S A*. 2007; 104: 3777-81.

53. Briegel A, Ding HJ, Li Z, Werner J, Gitai Z, Dias DP, et al. Location and architecture of the *Caulobacter crescentus* chemoreceptor array. *Mol Microbiol*. 2008; 69: 30-41.

54. Greenfield D, McEvoy AL, Shroff H, Crooks GE, Wingreen NS, Betzig E, et al. Self-organization of the *Escherichia coli* chemotaxis network imaged with super-resolution light microscopy. *PLoS Biol*. 2009; 7: e1000137.

55. Liu J, Hu B, Morado DR, Jani S, Manson MD, Margolin W. Molecular architecture of chemoreceptor arrays revealed by cryoelectron tomography of *Escherichia coli* minicells. *Proc Natl Acad Sci U S A*. 2012; 109: E1481-8.

56. Endres RG. Polar chemoreceptor clustering by coupled trimers of dimers. *Biophys J*. 2009; 96: 453-63.

57. Shiomi D, Banno S, Homma M, Kawagishi I. Stabilization of polar localization of a chemoreceptor via its covalent modifications and its communication with a different chemoreceptor. *J Bacteriol*. 2005; 187: 7647-54.

58. van Ooij C, Losick R. Subcellular localization of a small sporulation protein in *Bacillus subtilis*. *J Bacteriol*. 2003; 185: 1391-8.

59. Holmes VF, Cozzarelli NR. Closing the ring: Links between SMC proteins and chromosome partitioning, condensation, and supercoiling. *Proc Natl Acad Sci U S A*. 2000; 97: 1322-4.

60. Wu LJ, Errington J. Coordination of cell division and chromosome segregation by a nucleoid occlusion protein in *Bacillus subtilis*. *Cell*. 2004; 117: 915-25.

61. Bernhardt TG, de Boer PA. SlmA, a nucleoid-associated, FtsZ binding protein required for blocking septal ring assembly over chromosomes in *E. coli*. *Mol Cell*. 2005; 18: 555-64.

62. Laloux G, Jacobs-Wagner C. Spatiotemporal control of PopZ localization through cell cycle-coupled multimerization. *J Cell Biol*. 2013; 201: 827-41.

63. Bowman GR, Perez AM, Ptacin JL, Ighodaro E, Folta-Stogniew E, Comolli LR, et al. Oligomerization and higher-order assembly contribute to sub-cellular localization of a bacterial scaffold. *Mol Microbiol*. 2013; 90: 776-95.

64. Bramkamp M, Emmins R, Weston L, Donovan C, Daniel RA, Errington J. A novel component of the division-site selection system of *Bacillus subtilis* and a new mode of action for the division inhibitor MinCD. *Mol Microbiol*. 2008; 70: 1556-69.

65. Patrick JE, Kearns DB. MinJ (YvjD) is a topological determinant of cell division in *Bacillus subtilis*. *Mol Microbiol*. 2008; 70: 1166-79.

66. Briley K, Jr., Prepiak P, Dias MJ, Hahn J, Dubnau D. Maf acts downstream of ComGA to arrest cell division in competent cells of *B. subtilis*. *Mol Microbiol*. 2011; 81: 23-39.

67. dos Santos VT, Bisson-Filho AW, Gueiros-Filho FJ. DivIVA-mediated polar localization of ComN, a posttranscriptional regulator of *Bacillus subtilis*. *J Bacteriol*. 2012; 194: 3661-9.

68. Thanbichler M, Shapiro L. MipZ, a spatial regulator coordinating chromosome segregation with cell division in *Caulobacter*. *Cell*. 2006; 126: 147-62.

69. Ringgaard S, Schirner K, Davis BM, Waldor MK. A family of ParA-like ATPases promotes cell pole maturation by facilitating polar localization of chemotaxis proteins. *Genes Dev*. 2011; 25: 1544-55.

70. Aarsman MEG, Piette A, Fraipont C, Vinkenvleugel TMF, Nguyen-Distèche M, Den Blaauwen T. Maturation of the *Escherichia coli* divisome occurs in two steps. *Mol Microbiol*. 2005; 55: 1631-45.

71. Gerding MA, Ogata Y, Pecora ND, Niki H, de Boer PA. The trans-envelope Tol-Pal complex is part of the cell division machinery and required for proper outer-membrane invagination during cell constriction in *E. coli*. *Mol Microbiol*. 2007; 63: 1008-25.

72. Gamba P, Veening JW, Saunders NJ, Hamoen LW, Daniel RA. Two-step assembly dynamics of the *Bacillus subtilis* divisome. *J Bacteriol*. 2009; 191: 4186-94.

73. Goley ED, Yeh YC, Hong SH, Fero MJ, Abeliuk E, McAdams HH, et al. Assembly of the *Caulobacter* cell division machine. *Mol Microbiol*. 2011; 80: 1680-98.

74. Koppelman CM, Den Blaauwen T, Duursma MC, Heeren RM, Nanninga N. *Escherichia coli* minicell membranes are enriched in cardiolipin. *J Bacteriol*. 2001; 183: 6144-7.

75. Huang KC, Mukhopadhyay R, Wingreen NS. A curvature-mediated mechanism for localization of lipids to bacterial poles. *PLoS Comput Biol*. 2006; 2: e151.

76. Mukhopadhyay R, Huang KC, Wingreen NS. Lipid localization in bacterial cells through curvature-mediated microphase separation. *Biophys J*. 2008; 95: 1034-49.

77. Romantsov T, Helbig S, Culham DE, Gill C, Stalker L, Wood JM. Cardiolipin promotes polar localization of osmosensory transporter ProP in *Escherichia coli*. *Mol Microbiol*. 2007; 64: 1455-65.

78. Romantsov T, Stalker L, Culham DE, Wood JM. Cardiolipin controls the osmotic stress response and the subcellular location of transporter ProP in *Escherichia coli*. *J Biol Chem*. 2008; 283: 12314-23.

79. Romantsov T, Battle AR, Hendel JL, Martinac B, Wood JM. Protein localization in *Escherichia coli* cells: Comparison of the cytoplasmic membrane proteins ProP, LacY, ProW, AqpZ, MscS, and MscL. *J Bacteriol*. 2010; 192: 912-24.

80. Gold VA, Robson A, Bao H, Romantsov T, Duong F, Collinson I. The action of cardiolipin on the bacterial translocon. *Proc Natl Acad Sci U S A*. 2010; 107: 10044-9.

81. Renner LD, Weibel DB. MinD and MinE interact with anionic phospholipids and regulate division plane formation in *Escherichia coli*. *J Biol Chem*. 2012; 287: 38835-44.

82. Rajendram M, Zhang L, Reynolds BJ, Auer GK, Tuson HH, Ngo KV, et al. Anionic phospholipids stabilize RecA filament bundles in *Escherichia coli*. *Mol Cell*. 2015; 60: 374-84.

83. Paradies G, Paradies V, De Benedictis V, Ruggiero FM, Petrosillo G. Functional role of cardiolipin in mitochondrial bioenergetics. *Biochim Biophys Acta*. 2014; 1837: 408-17.

84. Strahl H, Hamoen LW. Membrane potential is important for bacterial cell division. *Proc Natl Acad Sci U S A*. 2010; 107: 12281-6.

85. Alberge F, Espinosa L, Seduk F, Sylvi L, Toci R, Walburger A, et al. Dynamic subcellular localization of a respiratory complex controls bacterial respiration. *Elife*. 2015; 4: e05357.

86. Garcia-del Portillo F, Calvo E, D'Orazio V, Pucciarelli MG. Association of ActA to peptidoglycan revealed by cell wall proteomics of intracellular *Listeria monocytogenes*. *J Biol Chem*. 2011; 286: 34675-89.

87. Kocks C, Gouin E, Tabouret M, Berche P, Ohayon H, Cossart P. *L. monocytogenes*-induced actin assembly requires the *actA* gene product, a surface protein. *Cell*. 1992; 68: 521-31.

88. Kocks C, Hellio R, Gounon P, Ohayon H, Cossart P. Polarized distribution of *Listeria monocytogenes* surface protein ActA at the site of directional actin assembly. *J Cell Sci*. 1993; 105: 699-710.

89. Smith GA, Portnoy DA, Theriot JA. Asymmetric distribution of the *Listeria monocytogenes* ActA protein is required and sufficient to direct actin-based motility. *Mol Microbiol*. 1995; 17: 945-51.

90. Fleurie A, Lesterlin C, Manuse S, Zhao C, Cluzel C, Lavergne JP, et al. MapZ marks the division sites and positions FtsZ rings in *Streptococcus pneumoniae*. *Nature*. 2014; 516: 259-62.

91. Higgins ML, Shockman GD. Model for cell wall growth of *Streptococcus faecalis*. *J Bacteriol*. 1970; 101: 643-8.

92. Pinho MG, Kjos M, Veening JW. How to get (a)round: Mechanisms controlling growth and division of coccoid bacteria. *Nat Rev Microbiol*. 2013; 11: 601-14.

93. Yeh YC, Comolli LR, Downing KH, Shapiro L, McAdams HH. The *Caulobacter* Tol-Pal complex is essential for outer membrane integrity and the positioning of a polar localization factor. *J Bacteriol*. 2010; 192: 4847-58.

94. Goldberg MB, Theriot JA. *Shigella flexneri* surface protein IcsA is sufficient to direct actin-based motility. *Proc Natl Acad Sci U S A*. 1995; 92: 6572-6.

95. Steinhauer J, Agha R, Pham T, Varga AW, Goldberg MB. The unipolar *Shigella* surface protein IcsA is targeted directly to the bacterial old pole: IcsP cleavage of IcsA occurs over the entire bacterial surface. *Mol Microbiol*. 1999; 32: 367-77.

96. Robbins JR, Monack D, McCallum SJ, Vegas A, Pham E, Goldberg MB, et al. The making of a gradient: IcsA (VirG) polarity in *Shigella flexneri*. *Mol Microbiol*. 2001; 41: 861-72.

97. Charles M, Perez M, Kobil JH, Goldberg MB. Polar targeting of *Shigella* virulence factor IcsA in Enterobacteriacae and *Vibrio*. *Proc Natl Acad Sci U S A*. 2001; 98: 9871-6.

98. Rassam P, Copeland NA, Birkholz O, Toth C, Chavent M, Duncan AL, et al. Supramolecular assemblies underpin turnover of outer membrane proteins in bacteria. *Nature*. 2015; 523: 333-6.

99. Bergmiller T, Andersson AMC, Tomasek K, Balleza E, Kiviet DJ, Hauschild R, et al. Biased partitioning of the multidrug efflux pump AcrAB-TolC underlies long-lived phenotypic heterogeneity. *Science*. 2017; 356: 311-5.

100. Nikaido H. Multidrug efflux pumps of gram-negative bacteria. *J Bacteriol*. 1996; 178: 5853-9.

101. Glass JI, Lefkowitz EJ, Glass JS, Heiner CR, Chen EY, Cassell GH. The complete sequence of the mucosal pathogen *Ureaplasma urealyticum*. *Nature*. 2000; 407: 757-62.

102. Lluch-Senar M, Querol E, Pinol J. Cell division in a minimal bacterium in the absence of *ftsZ*. *Mol Microbiol*. 2010; 78: 278-89.

103. Fu G, Huang T, Buss J, Coltharp C, Hensel Z, Xiao J. In vivo structure of the *E. coli* FtsZ-ring revealed by photoactivated localization microscopy (PALM). *PLoS One*. 2010; 5: e12682.

104. Li Z, Trimble MJ, Brun YV, Jensen GJ. The structure of FtsZ filaments in vivo suggests a force-generating role in cell division. *EMBO J*. 2007; 26: 4694-708.

105. Szwedziak P, Wang Q, Bharat TA, Tsim M, Lowe J. Architecture of the ring formed by the tubulin homologue FtsZ in bacterial cell division. *Elife*. 2014; 3: e04601.

106. Lutkenhaus J, Pichoff S, Du S. Bacterial cytokinesis: From Z ring to divisome. *Cytoskeleton* (*Hoboken*). 2012; 69: 778-90.

107. Egan AJ, Vollmer W. The physiology of bacterial cell division. *Ann N Y Acad Sci*. 2013; 1277: 8-28.

108. Typas A, Banzhaf M, Gross CA, Vollmer W. From the regulation of peptidoglycan synthesis to bacterial growth and morphology. *Nat Rev Microbiol*. 2011; 10: 123-36.

109. Haeusser DP, Margolin W. Splitsville: Structural and functional insights into the dynamic bacterial Z ring. *Nat Rev Microbiol*. 2016; 14: 305-19.

110. Dai K, Lutkenhaus J. *ftsZ* is an essential cell division gene in *Escherichia coli*. *J Bacteriol*. 1991; 173: 3500-6.

111. Pinho MG, Errington J. Dispersed mode of *Staphylococcus aureus* cell wall synthesis in the absence of the division machinery. *Mol Microbiol*. 2003; 50: 871-81.

112. Den Blaauwen T, Buddelmeijer N, Aarsman ME, Hameete CM, Nanninga N. Timing of FtsZ assembly in *Escherichia coli*. *J Bacteriol*. 1999; 181: 5167-75.

113. Regamey A, Harry EJ, Wake RG. Mid-cell Z ring assembly in the absence of entry into the elongation phase of the round of replication in bacteria: Co-ordinating chromosome replication with cell division. *Mol Microbiol*. 2000; 38: 423-34.

114. Quardokus EM, Brun YV. DNA replication initiation is required for mid-cell positioning of FtsZ rings in *Caulobacter crescentus*. *Mol Microbiol*. 2002; 45: 605-16.

115. Wang JD, Levin PA. Metabolism, cell growth and the bacterial cell cycle. *Nat Rev Microbiol*. 2009; 7: 822-7.

116. Vicente M, Rico AI, Martinez-Arteaga R, Mingorance J. Septum enlightenment: Assembly of bacterial division proteins. *J Bacteriol*. 2006; 188: 19-27.

117. Sun Q, Margolin W. FtsZ dynamics during the division cycle of live *Escherichia coli* cells. *J Bacteriol*. 1998; 180: 2050-6.

118. Bailey MW, Bisicchia P, Warren BT, Sherratt DJ, Mannik J. Evidence for divisome localization mechanisms independent of the Min system and SlmA in *Escherichia coli*. *PLoS Genet*. 2014; 10: e1004504.

119. Kain J, He GG, Losick R. Polar localization and compartmentalization of ClpP proteases during growth and sporulation in *Bacillus subtilis*. *J Bacteriol*. 2008; 190: 6749-57.

120. Kirstein J, Strahl H, Moliere N, Hamoen LW, Turgay K. Localization of general and regulatory proteolysis in *Bacillus subtilis* cells. *Mol Microbiol*. 2008; 70: 682-94.

121. Leonardy S, Miertzschke M, Bulyha I, Sperling E, Wittinghofer A, Sogaard-Andersen L. Regulation of dynamic polarity switching in bacteria by a Ras-like G-protein and its cognate GAP. *EMBO J*. 2010; 29: 2276-89.

122. Zhang Y, Franco M, Ducret A, Mignot T. A bacterial Ras-like small GTP-binding protein and its cognate GAP establish a dynamic spatial polarity axis to control directed motility. *PLoS Biol*. 2010; 8: e1000430.

123. Indio V, Martelli PL, Savojardo C, Fariselli P, Casadio R. The prediction of organelle-targeting peptides in eukaryotic proteins with Grammatical-Restrained Hidden Conditional Random Fields. *Bioinformatics*. 2013; 29: 981-8.

124. Donnes P, Hoglund A. Predicting protein subcellular localization: Past, present, and future. *Geno Prot Bioinfo*. 2004; 2: 209-15.

125. Gardy JL, Brinkman FS. Methods for predicting bacterial protein subcellular localization. *Nat Rev Microbiol*. 2006; 4: 741-51.

126. Walsh CT. Validated targets and major antibiotic classes. In *Antibiotics: Actions, origins, resistance*. Wash CT, Ed. ASM Press: Washington, DC. 2003; pp 11-88.

127. Fischbach MA, Walsh CT. Antibiotics for emerging pathogens. *Science*. 2009; 325: 1089-93.

128. Hurley KA, Santos TM, Nepomuceno GM, Huynh V, Shaw JT, Weibel DB. Targeting the bacterial division protein FtsZ. *J Med Chem*. 2016; 59: 6975-98.

129. Santos TMA, Lammers MG, Zhou M, Sparks IL, Rajendran M, Fang D, De Jesus CLY, Carneiro GFR, Cui Q, Weibel DB. Small molecule chelators reveal that iron starvation inhibits late stages of bacterial cytokinesis. (*Submitted*)

130. Margolin W. FtsZ and the division of prokaryotic cells and organelles. *Nat Rev Mol Cell Biol*. 2005; 6: 862-71.

131. Marston AL, Thomaides HB, Edwards DH, Sharpe ME, Errington J. Polar localization of the MinD protein of *Bacillus subtilis* and its role in selection of the mid-cell division site. *Genes Dev*. 1998; 12: 3419-30.

132. Kiekebusch D, Michie KA, Essen LO, Lowe J, Thanbichler M. Localized dimerization and nucleoid binding drive gradient formation by the bacterial cell division inhibitor MipZ. *Mol Cell*. 2012; 46: 245-59.

133. Jensen SO, Thompson LS, Harry EJ. Cell division in *Bacillus subtilis*: FtsZ and FtsA association is Z-ring independent, and FtsA is required for efficient midcell Z-Ring assembly. *J Bacteriol*. 2005; 187: 6536-44.

134. Loose M, Mitchison TJ. The bacterial cell division proteins FtsA and FtsZ self-organize into dynamic cytoskeletal patterns. *Nat Cell Biol*. 2014; 16: 38-46.

135. Willemse J, Borst JW, de Waal E, Bisseling T, van Wezel GP. Positive control of cell division: FtsZ is recruited by SsgB during sporulation of *Streptomyces*. *Genes Dev*. 2011; 25: 89-99.

136. Treuner-Lange A, Aguiluz K, van der Does C, Gomez-Santos N, Harms A, Schumacher D, et al. PomZ, a ParA-like protein, regulates Z-ring formation and cell division in *Myxococcus xanthus*. *Mol Microbiol*. 2013; 87: 235-53.

137. Hamoen LW, Meile JC, de Jong W, Noirot P, Errington J. SepF, a novel FtsZ-interacting protein required for a late step in cell division. *Mol Microbiol*. 2006; 59: 989-99.

138. Duman R, Ishikawa S, Celik I, Strahl H, Ogasawara N, Troc P, et al. Structural and genetic analyses reveal the protein SepF as a new membrane anchor for the Z ring. *Proc Natl Acad Sci U S A*. 2013; 110: E4601-10.

139. Gueiros-Filho FJ, Losick R. A widely conserved bacterial cell division protein that promotes assembly of the tubulin-like protein FtsZ. *Genes Dev*. 2002; 16: 2544-56.

140. Ebersbach G, Galli E, Moller-Jensen J, Lowe J, Gerdes K. Novel coiled-coil cell division factor ZapB stimulates Z ring assembly and cell division. *Mol Microbiol*. 2008; 68: 720-35.

141. Durand-Heredia JM, Yu HH, De Carlo S, Lesser CF, Janakiraman A. Identification and characterization of ZapC, a stabilizer of the FtsZ ring in *Escherichia coli*. *J Bacteriol*. 2011; 193: 1405-13.

142. Durand-Heredia J, Rivkin E, Fan G, Morales J, Janakiraman A. Identification of ZapD as a cell division factor that promotes the assembly of FtsZ in *Escherichia coli*. *J Bacteriol*. 2012; 194: 3189-98.

143. Hale CA, de Boer PA. Direct binding of FtsZ to ZipA, an essential component of the septal ring structure that mediates cell division in *E. coli*. *Cell*. 1997; 88: 175-85.

144. Pichoff S, Lutkenhaus J. Unique and overlapping roles for ZipA and FtsA in septal ring assembly in *Escherichia coli*. *EMBO J*. 2002; 21: 685-93.

145. Camberg JL, Hoskins JR, Wickner S. ClpXP protease degrades the cytoskeletal protein, FtsZ, and modulates FtsZ polymer dynamics. *Proc Natl Acad Sci U S A*. 2009; 106: 10614-9.

146. Weart RB, Nakano S, Lane BE, Zuber P, Levin PA. The ClpX chaperone modulates assembly of the tubulin-like protein FtsZ. *Mol Microbiol*. 2005; 57: 238-49.

147. Haeusser DP, Lee AH, Weart RB, Levin PA. ClpX inhibits FtsZ assembly in a manner that does not require its ATP hydrolysis-dependent chaperone activity. *J Bacteriol*. 2009; 191: 1986-91.

148. Del Sol R, Mullins JG, Grantcharova N, Flardh K, Dyson P. Influence of CrgA on assembly of the cell division protein FtsZ during development of *Streptomyces coelicolor*. *J Bacteriol*. 2006; 188: 1540-50.

149. Levin PA, Kurtser IG, Grossman AD. Identification and characterization of a negative regulator of FtsZ ring formation in *Bacillus subtilis*. *Proc Natl Acad Sci U S A*. 1999; 96: 9642-7.

150. Beaufay F, Coppine J, Mayard A, Laloux G, De Bolle X, Hallez R. A NAD-dependent glutamate dehydrogenase coordinates metabolism with cell division in *Caulobacter crescentus*. *EMBO J*. 2015; 34: 1786-800.

151. Radhakrishnan SK, Pritchard S, Viollier PH. Coupling prokaryotic cell fate and division control with a bifunctional and oscillating oxidoreductase homolog. *Dev Cell*. 2010; 18: 90-101.

152. Hill NS, Buske PJ, Shi Y, Levin PA. A moonlighting enzyme links *Escherichia coli* cell size with central metabolism. *PLoS Genet*. 2013; 9: e1003663.

153. Bisson-Filho AW, Discola KF, Castellen P, Blasios V, Martins A, Sforca ML, et al. FtsZ filament capping by MciZ, a developmental regulator of bacterial division. *Proc Natl Acad Sci U S A*. 2015; 112: E2130-8.

154. Shen B, Lutkenhaus J. Examination of the interaction between FtsZ and MinCN in *E. coli* suggests how MinC disrupts Z rings. *Mol Microbiol*. 2010; 75: 1285-98.

155. Mukherjee A, Cao C, Lutkenhaus J. Inhibition of FtsZ polymerization by SulA, an inhibitor of septation in *Escherichia coli*. *Proc Natl Acad Sci U S A*. 1998; 95: 2885-90.

156. Chen Y, Milam SL, Erickson HP. SulA inhibits assembly of FtsZ by a simple sequestration mechanism. *Biochemistry*. 2012; 51: 3100-9.

157. Weart RB, Lee AH, Chien AC, Haeusser DP, Hill NS, Levin PA. A metabolic sensor governing cell size in bacteria. *Cell*. 2007; 130: 335-47.

158. Kawai Y, Moriya S, Ogasawara N. Identification of a protein, YneA, responsible for cell division suppression during the SOS response in *Bacillus subtilis*. *Mol Microbiol*. 2003; 47: 1113-22.

159. Adams DW, Errington J. Bacterial cell division: Assembly, maintenance and disassembly of the Z ring. *Nat Rev Microbiol*. 2009; 7: 642-53.

CHAPTER 2

Polar localization of *Escherichia coli* chemoreceptors requires an intact Tol-Pal complex

Adapted from:

Santos TMA, Lin T.Y., Rajendran M, Anderson SM, Weibel DB. Polar localization of *Escherichia coli* chemoreceptors requires an intact Tol-Pal complex. *Mol Microbiol.* 2014; 92: 985-1004.

TMAS designed and conducted experiments, analyzed data, and wrote the paper. TYL, MR, and SMA conducted experiments, and analyzed data. DBW designed experiments, analyzed data, and wrote the paper.

ABSTRACT

Subcellular biomolecular localization is critical for the metabolic and structural properties of the cell. The functional implications of the spatiotemporal distribution of protein complexes during the bacterial cell cycle have long been acknowledged; however, the molecular mechanisms for generating and maintaining their dynamic localization in bacteria are not completely understood. In this chapter, we demonstrate that the trans-envelope Tol-Pal complex, a widely-conserved component of the cell envelope of Gram-negative bacteria, is required to maintain the polar positioning of chemoreceptor clusters in *Escherichia coli*. Localization of the chemoreceptors was independent of phospholipid composition of the membrane and the curvature of the cell wall. Instead, our data indicate that chemoreceptors interact with components of the Tol-Pal complex and that this interaction is required to polarly localize chemoreceptor clusters. We found that disruption of the Tol-Pal complex perturbs the polar localization of chemoreceptors, alters cell motility, and affects chemotaxis. We propose that the *E. coli* Tol-Pal complex restricts mobility of the chemoreceptor clusters at the cell poles and may be involved in regulatory mechanisms that coordinate cell division and segregation of the chemosensory machinery.

INTRODUCTION

Asymmetric localization is a hallmark of many different bacterial proteins, including components of cell division, virulence, adhesion, development, chemotaxis, and motility [1-4]. Genomic and proteomic approaches for identifying subcellular protein localization have expanded our understanding of asymmetric patterns of localization in bacteria [5-8] and revealed several classes of proteins that localize to the cell poles in rod-shaped bacteria. The canonical example of polarly localized proteins is the methyl-accepting chemotaxis proteins (MCPs, herein referred to as chemoreceptors) [1, 9]. This family of transmembrane chemoreceptors is required for chemotaxis and is primarily positioned at the cell poles where it forms inter-communicating clusters that are ~200-400 nm in diameter [9-15]. The asymmetric distribution of chemoreceptors in cell membranes is evolutionarily conserved in Bacteria and Archaea [16], and recent cryotomographic studies demonstrate that the basic honeycomb lattice architecture of the arrays is conserved among chemotactic bacteria [13, 15, 17, 18]. Despite a deep understanding of the central role of this machinery in controlling cell behavior and facilitating adaptation and survival [19-22], the mechanisms underlying its localization and the relationship between its position and function are not completely understood.

The bacterial cell poles have distinct physical features that may be involved in controlling protein positioning [23-25]. Polar localization of the chemoreceptor clusters in *Escherichia coli* depends partially on the histidine kinase CheA and the adaptor protein CheW [1, 9, 26]. CheA and CheW form a ternary complex with chemoreceptors and participate in chemotactic signal transduction. Imaging studies have revealed that chemoreceptors are inserted randomly into the lateral cytoplasmic membrane along the

helically distributed Sec translocation machinery complexes and migrate to preexisting clusters [27]. In this model, it is unclear whether chemoreceptors are transported actively within the cytoplasmic membrane to the cell poles or diffuse passively and are trapped at the poles. Another model that has been hypothesized involves a stochastic nucleation mechanism in which cluster assembly and positioning at the cell poles depends on chemoreceptor concentration and on the distance of receptors from large chemoreceptor clusters [14, 28, 29].

The cell envelope of *E. coli* and other Gram-negative bacteria consists of the inner membrane (IM), a ~2-4 nm-thick layer of peptidoglycan [30] positioned beyond the IM, and the outer membrane (OM). Genetic and biochemical analyses have revealed protein complexes that bridge the three layers of the cell envelope. The functions of these complexes include: performing active transport of biomolecules through the cell envelope [31-33], maintaining cell envelope integrity [34-37], and mediating the final steps of cell division [38, 39]. The Tol-Pal complex (Figures 1A and 1B) is a widely conserved component of the cell envelope of Gram-negative bacteria [40] and its physiological roles include: maintaining cell wall integrity by mediating the physical connection between the OM and the peptidoglycan [35]; expressing lipopolysaccharide surface antigens and virulence factors [41]; promoting proper functioning of certain transport systems in the cytoplasmic membrane [42]; facilitating phage infection and translocation of group A colicins [43-45]; and reducing cell sensitivity to detergents [46]. In many bacteria, *tol* and *pal* mutants produce chains of cells that bleb in low-osmolarity or high-ionic-strength liquids, suggesting that the complex is part of the cell division machinery and plays a role in completing cell division under conditions of membrane stress [35, 38].

In *E. coli*, this trans-envelope complex consists of two sub-complexes (Figures 1A and 1B). One complex is located in the IM and consists of TolA, TolQ, and TolR, which interact through their transmembrane segments with a respective stoichiometry of 4-6:2:1 [47-49]. TolQ spans the IM three times whereas both TolR and TolA are anchored to the IM through a single membrane-spanning region located near their amino terminus [47, 48, 50-52]. A second complex is associated with the OM and consists of TolB—a predominantly soluble periplasmic protein—and the peptidoglycan-associated lipoprotein Pal, which is anchored to the OM [34, 53-55]. The assembly of these two sub-complexes bridges the three layers of the cell envelope through multiple interactions, including the association of the C-terminal periplasmic domain of TolA with Pal and TolB [34, 49, 56, 57]. Cross-linking studies and the isolation and characterization of suppressive mutations suggest interactions between individual components of the Tol-Pal complex and other components of the cell envelope. Pal is an abundant lipoprotein thought to interact with the peptidoglycan through a conserved α-helical motif [55, 58]. TolB interacts with the Braun's lipoprotein (Lpp) and the porin OmpA [34, 59, 60]. Additionally, both TolA and TolB form high molecular weight complexes with the trimeric porins OmpF, OmpC, PhoE, and LamB [61, 62]. The numerous interactions of the Tol and Pal components with other proteins suggest that the complex may be involved in a range of other physiological and regulatory cellular processes.

In this chapter, we demonstrate that the intact Tol-Pal complex is required for the polar localization of chemoreceptor clusters in *E. coli*, cell motility, and chemotaxis. We tested whether the components of the Tol-Pal complex interact with chemoreceptors to maintain the subcellular localization of polar clusters. We found that disruption of the trans-envelope Tol-Pal complex perturbs polar localization of chemoreceptor clusters

without affecting the localization of other membrane-associated polar proteins. Consistent with this interaction, the absence of the Tol-Pal complex affected both swimming and swarming cell motility. Importantly, mislocalization of chemoreceptor clusters upon deletion of the Tol-Pal complex affects chemotaxis by increasing the tumbling frequency of the cells. These results add a surprising new dimension to the subcellular organization of bacteria.

EXPERIMENTAL PROCEDURES

Bacterial strains and growth conditions

E. coli cells were grown aerobically in lysogeny broth (LB) (1% [w/v] tryptone, 0.5% [w/v] yeast extract, and 1% [w/v] NaCl) or in LB medium containing 1.5% (w/v) agar (LB agar) at 37°C, unless otherwise indicated. We added ampicillin (50 μg/mL), carbenicillin (50 μg/mL), chloramphenicol (25 μg/mL), and kanamycin (30 μg/mL) to the medium or agar as needed. Chemicals and culture media reagents were obtained from BD Biosciences (San Jose, CA), Fisher Scientific (Itasca, IL) or Sigma-Aldrich (St. Louis, MO). *E. coli* strains and plasmids used in this work are listed in Table S1.

Genetic methods

Standard recombinant DNA procedures and manufacturer protocols were used for genomic and plasmid DNA purification, restriction endonuclease digestion, DNA amplification, gene cloning, transformation, and mutagenesis. Genomic DNA from *E. coli* strains was isolated with the MasterPure DNA Purification Kit (Epicentre, Madison, WI). Oligonucleotide primers were obtained from IDT (Coralville, IA) and restriction

enzymes were from Promega (Madison, WI) or New England Biolabs (Ipswich, MA). We used platinum PfuUltra II Fusion HS DNA polymerase (Agilent Technologies, Santa Clara, CA) to produce DNA for cloning and mutagenesis, and GoTaq DNA polymerase (Promega) for general analytical PCR. Control reactions were always tested side-by-side. Plasmid constructs were purified using a QIAprep Miniprep Kit (Qiagen, Valencia, CA) and verified by PCR and DNA sequencing. We used electroporation or chemical methods to transform *E. coli* strains with plasmids. Chromosomal deletions, genetic integration, and removal of antibiotic resistance cassette FRT-*kan*-FRT were performed using λ-red method recombination [63]. P1 phage transduction was used, whenever possible, to transfer the FRT-*kan*-FRT cassette between *E. coli* strains. We verified chromosomal deletions and integrations by testing for the presence of antibiotic markers and by PCR analysis and DNA sequencing. In addition, we verified the successful deletion of *tol* and *pal* mutants by determining the susceptibility of these mutants to 0.5% SDS. All primers used in this study are listed in Table S2.

Fluorescence microscopy, imaging and data analysis

E. coli cells harboring plasmid pPA803 (encoding a functional YFP-CheR fusion) [64] or plasmid pPA801 (encoding a functional YFP-CheW fusion) [65] were grown overnight in LB broth, diluted (1:100) in 5 mL of fresh LB broth and incubated at 37°C with agitation (200 r.p.m.) until an absorbance of 0.6 (λ = 600 nm) was reached. We induced expression of YFP-CheR by adding 100 μM isopropyl β-D-1-thiogalactopyranoside (IPTG) and incubating the culture for 1 h at 37°C with agitation (200 r.p.m.). We induced expression of YFP-CheW by adding 0.04% (w/v) L-arabinose and incubating the culture for 1 h at 37°C with agitation (200 r.p.m.). *E. coli* cells

harboring a functional chromosomal TnaA-GFP fusion [8] were grown overnight in tryptone broth (TB) (1% [w/v] tryptone and 0.5% [w/v] NaCl), diluted (1:100) in 5 mL of fresh TB and incubated at 37°C with agitation (200 r.p.m.) until an absorbance of 0.6 (λ = 600 nm) was reached. *E. coli* cells harboring plasmid pMAC382 (encoding an IcsA-GFP fusion) [66] were grown overnight in M9 minimal medium (1× M9 salts [17 mM NaCl, 9 mM NH_4Cl, 22 mM KH_2PO_4, 48 mM $Na_2HPO_4 \cdot 7H_2O$], 0.1 mM $CaCl_2$, 2 mM $MgSO_4$, 0.4% [w/v] glucose) containing 0.2% [v/v] glycerol, diluted (1:100) in 5 mL of fresh M9 minimal medium and incubated at 37°C with agitation (200 r.p.m.) until an absorbance of 0.6 (λ = 600 nm) was reached. We induced expression of IcsA-GFP by adding 0.2% (w/v) L-arabinose and incubating the culture in the dark for 1 h at 25°C with agitation (200 r.p.m.).

We added an aliquot (4 μL) of the induced culture on 2% (w/v) agarose pads prepared in 1× PBS buffer (137 mM NaCl, 2.7 mM KCl, 10 mM Na_2HPO_4, 1.76 mM KH_2PO_4) [pH 7.4]), covered the samples with a glass coverslip and imaged the cells at 25°C on an inverted Nikon Eclipse TE2000 epifluorescence microscope equipped with an Andor iXon ^{EM}+ DU-897 electron-multiplying charge-coupled-device (EMCCD) camera (Andor Technology, South Windsor, CT). Images were acquired using a 100× objective (Nikon Plan Apo 100×/1.40 oil Ph3 DM) and the Metamorph software program (Version 7.5.6.0) (MDS Analytical Technologies, Downingtown, PA). Data was collected on the EMCCD using an exposure time of 33 msec; for fluorescent images, we used an electron-multiplying (EM) gain of 100.

To analyze the localization of proteins in *E. coli* cells, we created fluorescence intensity profiles of cells using the MATLAB (MathWorks, Natick, MA)-based program,

MicrobeTracker [67]. We only analyzed pre-divisional cells and verified the position of proteins by manual inspection. To display the images, we overlaid phase contrast and the corresponding fluorescence images and false-colored them using Adobe Photoshop CS5 (Adobe Systems Incorporated, San Jose, CA); no further adjustments or other image processing was performed.

Motility assay

Analysis and quantification of the swimming and swarming motility phenotypes were performed as described previously [68], with minor modifications. We measured the diameter of swimming migrating colonies in 0.25% (w/v) agar gel infused with nutrient broth (1.0% [w/v] peptone, 0.5% [w/v] NaCl, and 0.3% [w/v] beef extract), herein referred to as swimming motility agar. We measured the area of swarming migrating colonies in 0.45% (w/v) Eiken agar infused with nutrient broth (1.0% [w/v] peptone, 0.5% [w/v] NaCl, 0.3% [w/v] beef extract) and 0.5% (w/v) glucose, herein referred to as swarming motility agar. Briefly, we poured 50 mL of warm motility agar into 150 × 15 mm Petri dishes, allowed the agar to solidify at 25°C for 50 min, and removed excess liquid from the agar surface by storing the plates in a laminar flow hood for 20 min with the covers of the dishes ajar. We inoculated the surface of motility agar with 4 μL of a fresh *E. coli* cell suspension, containing approximately 10^5 colony forming units (c.f.u.)/mL, diluted in 1× PBS buffer (pH 7.4) and incubated the plates at 30°C in a static incubator. We measured the diameter of the swimming colonies after 14.5 h and the area of the swarming colonies after 16 h. For complementation experiments, we used the same procedure described above with a minor modification:

swimming or swarming motility agars were supplemented with the appropriate antibiotic and 1 mM or 0.1 mM IPTG.

Immunofluorescence microscopy of *E. coli* flagella

We performed flagella immunostaining in *E. coli* MG1655 and *E. coli* MG1655 Δ*tol-pal* cells as described previously [69], with minor modifications. We harvested 500 μL of overnight cultures at 2,500 *g* for 5 min at 25°C and gently resuspended the cells in the same volume of 1× PBS buffer (pH 7.4). We diluted (1:50) the cell suspension and added two aliquots of 15 μL to each glass slide chamber. The remaining procedure was performed according to that described in Tuson et al. (2013) [69]. Both the primary antibody (anti-FliC) and the secondary antibody (Alexa Fluor 488-conjugated goat anti-rabbit IgG) (Invitrogen, Grand Island, NY) were diluted 1:100 in blocking buffer. Cells were imaged at 25°C using an inverted Nikon Eclipse Ti microscope equipped with a Photometrics CoolSNAP HQ2 charge-coupled-device (CCD) camera (Photometrics, Tucson, AZ). Images were acquired using a 100× objective (Nikon Plan Apo 100×/1.40 oil Ph3 DM) and the Nikon Instruments Software (NIS)-Elements Advanced Research (AR) microscope imaging software program (Version 4.000.07) (Nikon Inc., Melville, NY). Data was collected on the CCD camera using an exposure time of 50 msec; for fluorescent images, we used an exposure time of 50 msec.

Cell velocity measurements

We measured the velocity of individual *E. coli* MG1655 and *E. coli* MG1655 Δ*tol-pal* cells (in μm/sec) using a particle-tracking algorithm, as described previously [68,

69], with minor modifications. Briefly, cell cultures were grown overnight at 37°C in TB. Saturated overnight cultures were diluted 1:100 into 10 mL of fresh TB and grown in 250-mL Erlenmeyer flasks at 37°C with agitation (200 r.p.m.). We harvested cells in the mid-log phase (absorbance of 0.8, $\lambda = 600$ nm), centrifuged an aliquot (1 mL) of the cell suspension for 5 min at 2,000 *g* at 25°C, and gently resuspended the cells in the same volume of motility buffer (10 mM KPO_4, 67 mM NaCl, 0.1 mM EDTA [pH 7.0]) [70], containing 100 mM glucose, and 0.001% (w/v) Brij-35. A 20-μL aliquot of the suspension diluted 1:1,000 in motility buffer containing 100 mM glucose, and 0.001% (w/v) Brij-35 was placed inside a ring of Apiezon M grease on pre-cleaned glass slides and sealed with a glass cover slip. Cells were imaged at 25°C using a Nikon Eclipse 80i phase contrast upright microscope equipped with an Andor LucaS EMCCD camera (Andor Technology). Images were acquired using a 40× objective (Nikon Plan Fluor ELWD 40×/0.60 Ph2 DM). Motility videos consisting of 300 frames were collected with a 33 msec exposure time (30 frames/sec). Microscopy data was analyzed using MATLAB (MathWorks) by identifying the center of mass of each bacterium in successive frames and grouping those points together to create a cell trajectory, from which we determined the mean cell velocity. We only used tracks that had more than 30 frames (i.e., more than 1 sec), minimal total length of 10 μm, and minimal displacement of 5 μm. Cells that moved in a constant tumbling or wobbling manner or stuck to the coverslip were manually discarded from the analysis.

We visually determined the reversals in swimming direction. Three individual experiments were performed and in each experiment at least 30 cells were analyzed. Cells were tracked for as long as possible, the number of reversals was counted, and the

reversal frequency was calculated as the number of reversals per second per cell. For each experiment, we calculated the average reversal frequency.

Chemotaxis assay

We qualitatively measured the chemotactic response of *E. coli* MG1655 and *E. coli* MG1655 Δ*tol-pal* using a modified plug-in-pond assay (microplug assay, μPlug) as described previously [71], with minor modifications. Briefly, *E. coli* containing the enhanced green fluorescent protein (EGFP)-encoding plasmid P_{tet}-egfp were grown overnight at 37°C in LB containing ampicillin (50 μg/mL). Saturated overnight cultures were diluted (1:100) in 10 mL of fresh LB containing ampicillin (50 μg/mL) in 125-mL Erlenmeyer flasks, and incubated at 37°C with agitation (200 r.p.m.). When the cultures reached an absorbance of 0.8 (λ = 600 nm), we induced expression of the fluorescent protein by adding 500 nM anhydrotetracycline for 1 h. We harvested an aliquot of the cell suspension (1 mL), centrifuged for 5 min at 2,000 *g* at 25°C, gently washed, and resuspended the cells in the same volume of motility buffer containing 0.001% (w/v) Brij-35. We examined cells by phase contrast microscopy to ensure robust motility and normal run-tumble swimming behavior. Cells were loaded into the microfluidic chamber containing the μPlug [0.5% (w/v) agarose dissolved in motility buffer containing 0.001% (w/v) Brij-35] infused with 1 mM L-aspartate or with motility buffer (negative control). Cells were imaged at 25°C for 1 h with a time-lapse of approximately 1 min using an inverted Nikon Eclipse Ti microscope equipped with a Photometrics CoolSNAP HQ2 CCD camera (Photometrics). Images were acquired using a 4× objective (Nikon Plan Apo 4×/0.2) and the NIS-Elements AR microscope imaging

software program (Version 4.000.07) (Nikon Inc). Data was collected on the CCD camera using an exposure time of 50 msec; for fluorescent images, we used an exposure time of 50 msec. We used IGOR Pro (Version 6.6A2) (WaveMetrics, Lake Oswego, OR) to analyze the images and calculate the total fluorescence intensity profiles.

Coimmunoprecipitation (Co-IP)

E. coli MG1655 and *E. coli* MG1655 Δ*tolA* cells were grown overnight in LB broth, diluted (1:100) in 500 mL of fresh LB broth, and incubated at 37°C with agitation (200 r.p.m.) for 5 h. For experiments in which we used *E. coli* MG1655 cells harboring the plasmid(s) encoding the tagged versions of the proteins of interest, *E. coli* MG1655 Δ*tolA* and *E. coli* MG1655 Δ*pal* cells were grown overnight in LB broth containing ampicillin (50 μg/mL) or chloramphenicol (25 μg/mL), diluted (1:100) in 500 mL of fresh LB broth, and incubated at 37°C with agitation (200 r.p.m.) until reaching an absorbance of 0.6 (λ = 600 nm). We induced expression of the HA-tagged TolA and the FLAG-tagged Pal by adding 0.04% (w/v) L-arabinose and 1 mM IPTG, respectively, for 3 h. We harvested the cells by centrifuging the cultures for 20 min at 5,000 *g* at 4°C, washed the pellets in 30 mL of co-IP buffer (20 mM HEPES [pH 7.5], 100 mM NaCl, and 20% [v/v] glycerol) by centrifuging for 10 min at 12,000 *g* at 4°C, and resuspended the cell pellets in 30 mL of co-IP buffer containing 0.05% (v/v) Triton X-100. We treated the cell suspension with formaldehyde to a final concentration of 1% for 30 min at room temperature on a rotatory platform, and quenched the mixture with 125 mM of glycine. We added 20 mg of lysozyme and 1 mM phenylmethylsulfonyl fluoride (PMSF) to the mixture, incubated for 30 min at 4°C on a rotatory platform, and lysed the cells by one passage through a

French pressure cell press (American Instrument Company, Inc., Silver Springs, MD) at 1,000 lb/in^2. We incubated the suspension for 30 min at 4°C on a rotatory platform and removed the insoluble material by centrifuging the cell lysate for 30 min at 12,000 *g* at 4°C. We collected 10 mL of the supernatant and incubated with anti-TolA (1:2,000), anti-Trg (1:5,000), anti-FLAG (1:2,000) (Thermo Scientific, Rockford, IL), or anti-HA (1:2,000) (Thermo Scientific) at 4°C for 18 hours. Subsequently, we added agarose beads conjugated with Protein A/G (Thermo Scientific) sufficient for binding 2.5 mg of IgG and incubated the mixture for 18 h at 4°C on a rotating platform. We harvested the beads by centrifugation for 3 min at 2,000 *g* at 25°C, washed them three times with 3 mL of co-IP buffer, and three times with 3 mL of wash buffer (50 mM Tris-HCl [pH 7.4] and 150 mM NaCl). After the last wash, we removed the supernatant, resuspended the beads in 100 μL of 1× Laemmli sample buffer (62.5 mM Tris-HCl [pH 6.8], 25% [v/v] glycerol, 2% SDS [w/v], 0.01% [w/v] bromophenol blue) containing 5% (v/v) β-mercaptethanol, and eluted the bound proteins by incubating the mixture for 15 min at 100°C. We centrifuged the samples at 12,000 *g* for 3 min to pellet the agarose beads and collected the supernatant to perform the immunoblot experiments.

SDS-PAGE and immunoblot analysis

All protein samples were separated on a 12.5% SDS-PAGE gel at 150 V for 60 min in protein electrophoresis buffer (25 mM Tris-HCl, 192 mM glycine, 0.1% SDS, pH 8.3). Following electrophoresis, we transferred proteins to an Amersham Hybond ECL nitrocellulose membrane (GE Healthcare, Pittsburgh, PA) for 2 h at 400 mV in transfer buffer (25 mM Tris-HCl, 192 mM glycine, 20% methanol). The nitrocellulose membrane was rinsed three times with deionized water and blocked overnight at 4°C overnight in

5% non-fat dry milk in TBST buffer (20 mM Tris-HCl, 137 mM NaCl, 1% [v/v] Tween-20) [pH 7.6]. The membrane was washed three times for 10 min in TBST buffer. Primary antibody was diluted in TBST and the membrane was incubated in this solution for 1 h. Subsequently, we washed the membrane three times for 10 min in TBST. Rabbit anti-mouse or goat anti-rabbit IgG secondary antibody conjugated to horseradish peroxidase (HRP) (Thermo Scientific) was diluted in TBST, and the membrane was incubated in this solution for 1 h. The membrane was washed three times for 10 min in TBST and developed using Pierce ECL Western Blotting Substrate (Thermo Scientific). Antibody dilutions were as follows: anti-Trg at 1:2,000; anti-Pal at 1:2,000; anti-TolA at 1:2,000; anti-FLAG monoclonal antibody (Thermo Scientific) at 1:2,000, anti-HA monoclonal antibody (Thermo Scientific) at 1:2,000, anti-6×His monoclonal antibody (Thermo Scientific) at 1:2,000, HRP-conjugated goat anti-rabbit IgG (Thermo Scientific) at 1:5,000, HRP-conjugated rabbit anti-mouse IgG (Thermo Scientific) at 1:5,000; anti-GFP monoclonal antibody (Thermo Scientific) at 1:2,000.

Fabrication of agarose microchannels

Analysis of chemoreceptor localization in filamented *E. coli* MG1655 cells confined in angled microchannels was performed as described previously [72]. Briefly, we used soft lithography to fabricate a polydimethylsiloxane (PDMS) stamp containing patterns of six repetitive microchannel structures that had a length of ~30 μm, a height of 1.3 μm, a width of 2.5 μm, and a central angle of 30°, 45°, 60°, 90°, 120°, or 180°. We used the stamp to emboss a layer of LB containing 3% (w/v) agarose [73, 74], 1 mM IPTG, cephalexin (25 μg/mL), and ampicillin (50 μg/mL).

E. coli MG1655 cells harboring the plasmid pPA803 were grown overnight in LB broth, diluted (1:100) in 5 mL of fresh LB broth and incubated at 37°C with agitation (200 r.p.m.) until an absorbance of 0.4 (λ = 600 nm) was reached. We induced expression of the fluorescent fusion protein by adding 100 μM IPTG and incubating the culture at 37°C with agitation (200 r.p.m.) until an absorbance of 0.6 (λ = 600 nm) was reached. We induced the filamentation of cells in the suspension by adding cephalexin (25 μg/mL) and incubating the culture for 5 min at 37°C with agitation (200 r.p.m.).

Following induction with IPTG and treatment with cephalexin, we added 5 μL of the cell suspension to the top surface of the LB agarose imprinted with the microchannels, covered the agar with glass cover slip, and incubated the preparation for 1.5 h at 37°C on a static incubator. *E. coli* cells growing inside the channels filamented and became curved at the bent region of the microchannel, adopting a new region of cell wall curvature corresponding to 1, 0.54, 0.47, 0.29, 0.145 or 0 μm^{-1}. We imaged the cells using a Nikon Eclipse 80i phase contrast upright microscope equipped with an Andor LucaS EMCCD camera (Andor Technology). Images were acquired using a 100× objective (Nikon Plan Apo 100 λ/1.45 oil Ph3 DM) and the Metamorph software program (Version 7.5.6.0) (MDS Analytical Technologies). Data was collected with the EMCCD using an exposure time of 33 msec; for fluorescent images, we used EM gain of 100.

Statistical analysis

All statistical tests used in our analysis were two-sided and P values < 0.05 were considered significant. Statistical analyses were performed using the computing

environment R (Version 3.0.1) (R Development Core Team, 2005). Refer to the figure legends for details about specific analysis performed for each experiment.

RESULTS

Chemoreceptors localize to the cell poles in *E. coli* mutants lacking the anionic phospholipid cardiolipin

An emerging hypothesis is that the accumulation of anionic phospholipids at the cell poles stabilizes mechanical strain that arises due to membrane curvature, influences the local physicochemical properties of phospholipid bilayers, and positions and regulates classes of membrane-associated proteins [75-78]. For example, diphosphatidylglycerol (also referred to as cardiolipin [CL]) has been reported to accumulate at the bacterial cell poles [77, 79, 80] and interact with and regulate several membrane-associated proteins in mitochondria [81] and bacteria [76, 82]. Due to the spatial proximity of CL and the chemoreceptors at the poles of *E. coli* cells, we tested whether this phospholipid was responsible for the position of the chemoreceptors.

To visualize chemoreceptors in vivo we used plasmid pPA803, a derivative of pBR322 that codes for the expression of yellow fluorescent protein (YFP) fused to the N-terminal region of CheR (YFP-CheR) controlled by a lactose-inducible promoter [64]. CheR is a methyltransferase that targets a specific C-terminal pentapeptide on the major chemoreceptors Tar and Tsr [83, 84]. Importantly, YFP-CheR is functional, co-localizes with chemoreceptors, does not localize in the absence of chemoreceptors, and has been used to determine the position of chemoreceptors in vivo [64, 83-85] (Figures S1A-S1C). We used the functional YFP-CheR as a proxy for chemoreceptor localization to prevent

the influence of a fluorescent tag fused to the chemoreceptors on their clustering and localization. YFP-CheR formed predominantly polar foci in cells of wild-type *E. coli* strain MG1655 (Figures 2A and 2B). We detected 62 ± 0.01% (mean ± standard error of the mean [s.e.m.]) of the YFP-CheR clusters positioned approximately within the first and/or fourth quarters of the cell (which we defined as cell poles) after 1 h of overexpression at 37°C. Approximately 38% of the chemoreceptor clusters were distributed along the lateral length of the cell between the polar regions and particularly concentrated at the mid-cell (Figure 2B). Only 1% ± 0.03% of the cells displayed diffused YFP-CheR signal, indicating that cluster formation was not being affected in the overexpression system (Figure S2). Importantly, the number of polar clusters did not change significantly after 18 h of overexpression at 25°C (68 ± 0.03%) (Figures 2A, S3A, and S3B).

To test whether CL at the cell poles was responsible for the polar localization of YFP-CheR, we used a CL null strain (*E. coli* MG1655 BKT12) in which the three enzymes (ClsA, ClsB, and ClsC) responsible for CL biosynthesis were deleted [86]. YFP-CheR displayed the same pattern of localization in *E. coli* strain MG1655 BKT12 as in the wild-type parent strain MG1655, suggesting that the decrease in CL content had no effect on chemoreceptor localization (Figures 2A and 2C). As observed for the wild-type *E. coli* MG1655, the number of polar clusters in the CL null strain did not change significantly after 18 h of overexpression at 25°C (Figures S3B and S3C). We observed, however, that patterns of YFP-CheR localization were altered in other *E. coli* strains in which phospholipid compositions were perturbed. For example, we found that *E. coli* UE54 expressing YFP-CheR displayed patterns of diffuse fluorescence and lacked defined YFP puncta (Figures 2A, 2C, and S2). *E. coli* UE54 is a *pgsA* null strain that has decreased

levels of the anionic phospholipids CL and phosphatidylglycerol (PG) [87, 88]. We also noticed that YFP-CheR was mislocalized in all the individual mutant strains that served as the genetic background for construction of *E. coli* UE54 (i.e., *E. coli* strains UE49, UE51, and UE53) (Figures 2A and 2C). A quantitative analysis of YFP-CheR fluorescence demonstrated that the distribution of fluorescence along the length of cells in all these mutants was different from cells of wild-type *E. coli* strain MG1655. The only common genetic alteration in all these *E. coli* UE strains in which YFP-CheR are mislocalized or unclustered is a mutation in the major outer membrane lipoprotein Lpp.

The major outer membrane lipoprotein Lpp and the Tol-Pal complex are determinants for polar localization of chemoreceptor clusters in *E. coli*

We investigated the role of the major outer membrane lipoprotein Lpp in positioning the chemoreceptors at the poles of *E. coli* cells. Lpp interacts both covalently and non-covalently with the peptidoglycan [89-91] and contributes to the structural and functional integrity of the cell envelope [92, 93]. To test whether Lpp was involved in the polar localization of YFP-CheR, we expressed YFP-CheR in the Lpp null strain *E. coli* MG1665 Δ*lpp* and observed the same pattern of localization as in the *E. coli* strains UE49, UE51, and UE53: that is, an increased number of YFP-CheR foci positioned along the cylindrical region of cells compared to at the poles (Figures 2A and 2C). Similar results were observed in the Lpp null mutant *E. coli* JW1667 from the Keio collection [94] (Figures S4A and S4B). This result suggests that Lpp is connected to the polar positioning of chemoreceptor clusters.

In *E. coli*, Lpp forms homotrimers that interact with components of the Tol-Pal complex and with the outer membrane protein A (OmpA) [59]. The *E. coli* Tol-Pal

complex is encoded by a cluster of seven genes organized into two transcription units [95, 96] and consists of five proteins that form two sub-complexes (Figures 1A and 1B). To assess whether the Tol-Pal proteins play a role in chemoreceptor localization, we determined the position of YFP-CheR in single-gene knockouts of *tolA*, *tolB*, *tolQ*, *tolR*, and *pal* derived from the wild-type MG1655 and in an *E. coli* MG1655 mutant lacking all the Tol and Pal proteins (we refer to this strain as Δ*tol-pal*) (Figures 2D, S5A-S5D). All knockout mutants displayed characteristically mislocalized puncta, which was similar to our observation for the *E. coli* UE strains: fluorescent puncta positioned primarily along the cylindrical body of the cells (Figures 2A and 2C). As observed for *E. coli* MG1655 cells, the number of polar clusters and distribution of fluorescence along the length of cells observed in most mutants did not change significantly after 18 h of overexpression at 25°C (Figures 2A, S3B, and S3C). Immunoblots of cell lysate showed that the YFP-CheR fusion protein was stable in UE54 and in all the *tol* and *pal* single-gene knockouts (Figure S6). Thus, diffused fluorescence signal inside the cells is not the result of proteolysis or degradation of the YFP-CheR fusion protein liberating the fluorescent protein. With the exception of *E. coli* UE54, all mutants displayed insignificant or absent diffused YFP-CheR fluorescence (Figure S2), indicating that the mutations did not affect clustering of chemoreceptors. In addition, we verified that the Δ*tol-pal* mutant still produces chemoreceptors at levels comparable to wild-type cells (Figure S7). Thus, mislocalization of YFP-CheR was not due to absence of chemoreceptors in the Δ*tol-pal* mutant. To confirm that the localization of the chemosensory machinery was perturbed in the Δ*tol-pal* mutant, we used the additional functional reporter YFP-CheW as a proxy for chemoreceptor localization. CheW is the

adaptor protein that physically couples CheA to the chemoreceptor to regulate phosphotransfer to CheY and CheB [15, 18, 20]. As observed for YFP-CheR localization, YFP-CheW formed predominantly polar foci in cells of wild-type *E. coli* strain MG1655 and characteristically mislocalized puncta in the Δ*tol-pal* mutant (Figures S8A and S8B). This observation provides additional evidence that polar localization of the *E. coli* chemosensory machinery is significantly affected in mutants lacking proteins of the Tol-Pal complex.

There are two additional genes in the *tol-pal* operon (Figure 1B): *ybgC* encodes a putative cytosolic protein and *ybgF* encodes a periplasmic protein [95, 96]. The function of YbgC has not yet been established. YbgF, recently renamed CpoB, localizes to the division site and coordinates peptidoglycan biosynthesis with OM invagination during cell division [97]. In contrast to our results with the other proteins encoded in the *tol-pal* operon, YFP-CheR remained polarly localized in *ybgC* and *ybgF* null mutants derived from *E. coli* strain BW25113 [94] (Figure S9). These results suggest that localization of YFP-CheR is exclusively dependent on the *tol* and *pal* genes within the *tol-pal* operon. As an additional control, we evaluated the localization of YFP-CheR in *tol* and *pal* single-gene knockout mutants from the Keio collection and in single-gene knockout mutants lacking other IM and OM components involved in transport, stress survival, or cell wall synthesis and remodeling, and found that YFP-CheR was only mislocalized in *tol* and *pal* mutants (Figure S9).

Interestingly, the *tol-pal* deletion (Δ*tol-pal*) had a large effect on the localization of YFP-CheR but did not affect the cellular localization of other proteins that are known to be enriched at the *E. coli* cell poles, including the *E. coli* IM-associated tryptophanase TnaA [8] and the heterologous OM protein IcsA from *Shigella* [66, 98] (Figures 2E and

2F). This observation suggests that the interaction between Tol-Pal proteins and the chemoreceptors may be unique and essential for the polar localization of the chemosensory machinery, but not for other biomolecular complexes.

Deletion of Tol-Pal components causes motility and chemotaxis defects in *E. coli*

We tested whether the changes in chemoreceptor localization that accompany the absence of Tol and Pal proteins affect cell motility and chemotaxis. We assessed the motility of wild-type *E. coli* MG1655 and the single-gene *tol* and *pal* null mutants in motility agar. All the single-gene mutants displayed a significant ($P < 0.05$) decrease in swimming motility compared to wild-type *E. coli* cells (Figures 3A and S10A). Plasmid-based complementation of each of the *tol* or *pal* deletion mutants reverted the swimming motility defects, with the exception of *tolB* (Figures 3A and S10B). As expected, cells of *E. coli* MG1655 Δ*tol-pal* also showed motility defects in swim plate assays compared to wild-type *E. coli* MG1655 cells (Figure 3B); overexpression of individual *tol* and *pal* genes was not sufficient to revert the motility phenotype in the Δ*tol-pal* mutant (Figures S10C and S10D). In all cases that we analyzed, the overexpression of *tolB* completely impaired cell growth (Figures S10B and S10C), suggesting that its accumulation may be cytotoxic. We bypassed its toxicity by decreasing the concentration of inducer and successfully reverted the motility defect of the *tolB* knockout strain (Figures S11A and S11B).

Similarly, all single-gene *tol* and *pal* null mutants and the Δ*tol-pal* mutant displayed impaired swarming motility compared to wild-type *E. coli* MG1655 cells (Figures 3C and S12A). Plasmid-based complementation of each of the *tol* or *pal* deletion mutants only reverted the swarming motility defects of mutants lacking *tolQ* and *tolR*

(Figures S12B and S12C). As observed in the swimming motility assay, overexpression of *tolB* impaired cell growth completely (Figures S12B and S12C). Importantly, the growth parameters of wild-type *E. coli* MG1655 and all the mutants were identical in liquid media (Figure S13), suggesting that the differences observed both in the swimming and swarming motility assays were not caused by growth defects associated with the deletion of the *tol* and *pal* genes. To determine whether the reduction in swimming motility was related to a decrease in flagella density, we immunolabeled flagella of wild-type *E. coli* MG1655 and Δ*tol-pal* mutant cells. We did not detect an apparent difference in flagella density between both cell strains that could explain the dramatic reduction in the size of the motility colonies observed for the mutant *E. coli* MG1655 Δ*tol-pal* (Figure 3D). It is possible that the deletion of the *tol* and *pal* genes change the size, position, spacing, stability, structure or function of flagella (Figure S14); however, we were unable to measure changes in these parameters using optical microscopy.

To further explore the role of the *tol* and *pal* genes in cell motility and verify whether the observed impairment of motility in the Δ*tol-pal* mutant was due to a decrease in cell velocity, we measured single cell velocities of wild-type *E. coli* MG1655 and *E. coli* MG1655 Δ*tol-pal* cells using particle-tracking algorithms. We found evidence of a difference in swimming velocity between these *E. coli* strains ($P = 0.039$, Figure 3E); however, it is unlikely that the difference accounts for the large defects in motility that we observed in the swimming and swarming motility assays (Figures 3B and 3C). Further analysis of cell trajectories from the tracking experiments indicated that deleting the Tol-Pal complex may alter the trajectory of cells during runs (Figure 3F). To

determine whether deletion of the *tol* and *pal* genes alters the motion of motile *E. coli* cells, we tracked cells suspended in motility buffer to determine the frequency at which cells tumble. We found that the mean (± s.e.m.) tumbling frequency of *E. coli* MG1655 Δ*tol-pal* cells (0.75 ± 0.09 tumbles/sec, $n = 95$) is significantly ($P < 0.05$) higher than the mean tumbling frequency observed for the wild-type strain (0.54 ± 0.05 tumbles/sec, $n = 102$) (Figures 3G and S15). This result indicates that the Δ*tol-pal* mutant displays biased clockwise flagella rotation.

To distinguish between differences in behavior due to motility and chemotaxis, we investigated the effect of the *tol* and *pal* genes on *E. coli* chemotaxis using a modified plug-in-pond assay (the μPlug assay) [71] and qualitatively measured the chemotactic response of *E. coli* MG1655 and *E. coli* MG1655 Δ*tol-pal* expressing enhanced green fluorescent protein (EGFP) (Figure 4). Both strains displayed a random distribution of cellular responses in the presence of plugs that lacked chemoattractant (Figures 4F and 4L). However, when cells were exposed to a plug containing L-aspartate, both wild-type *E. coli* MG1655 and *E. coli* MG1655 Δ*tol-pal* exhibited a strong response toward the attractant, which led to the accumulation of bacteria at the agarose plug-liquid interface (Figures 4A-4E and 4G-4K). Time-dependent quantification of the fluorescence intensity demonstrated that the community-wide chemotactic behavior of both strains was comparable, with the Δ*tol-pal* mutant showing an apparent delay in the response. The deletion of *tol* and *pal* genes alters the location of chemoreceptors—in the case of Δ*tol-pal*, causing diffuse localization of clusters and occasionally an absence of defined foci—yet the mislocalization of these sensors did not impair chemotaxis completely. Thus, our observations of changes in the diameter of colonies of *E. coli tol* and *pal* mutants

growing in swim plates—compared to the wild-type parent strain—is likely due to the bias in cell motion that accompanies these mutations.

Components of the Tol-Pal complex interact with chemoreceptors in *E. coli*

The IM protein TolA and the OM lipoprotein Pal are required for polar localization of the polar marker TipN in *Caulobacter crescentus* [39]. We reasoned that the intact Tol-Pal complex or its individual components may either polarly localize chemoreceptor arrays or nucleate their assembly at the cell poles. To test the hypothesis that chemoreceptors interact directly or indirectly with components of the Tol-Pal complex, we performed co-immunoprecipitation (co-IP) experiments to verify potential associations between chemoreceptors and TolA or Pal.

Initially, we used TolA and Pal null *E. coli* strains transformed, respectively, with a plasmid containing an N-terminal HA-tagged version of the *tolA* gene and a C-terminal FLAG-tagged version of the *pal* gene. Overexpression of the modified proteins restored cell viability in agar containing SDS (Figures S16A and S16B), indicating that the tags did not extensively affect the formation and function of the native complex. However, we did not detect a band indicating an association between the chemoreceptors and the tagged versions of TolA and Pal in the immunoblot of the immunoprecipitated samples (Figure S16C). We reasoned that the epitope tags or the levels of the overexpressed proteins that we tested could prevent interactions with the receptors. Consequently, we used wild-type cells lacking overexpression systems to verify potential interactions.

We performed co-IP experiments with wild-type *E. coli* MG1655 cells; as a negative control, we used the same approach in the mutant lacking the IM protein TolA

(*E. coli* MG1655 Δ*tolA*). Cells treated with the membrane permeable cross-linking agent formaldehyde were lysed and suspensions were immunoprecipitated with anti-TolA-coupled beads. Analysis of the purified products by western blot showed a band corresponding to the expected size for chemoreceptors (Figure 5), suggesting that TolA and chemoreceptors may interact directly or indirectly in vivo. To confirm our results, we performed a reverse co-IP with whole-cell lysate and immunoprecipitated the samples with anti-Trg-coupled beads. Similarly, analysis of the purified products showed a band corresponding to the expected size for TolA (Figure 5). As a positive control, in the cell lysate immunoprecipitated with anti-Trg-coupled beads we observed a band corresponding to CheA and CheW, which are known to interact directly with chemoreceptors and form a ternary complex that mediates transduction of the chemotactic signal in *E. coli* [1, 9, 13, 15, 20, 26]. In conjunction with our localization data, this observation supports the role of the Tol-Pal complex in polar localization of chemoreceptor clusters in *E. coli*.

DISCUSSION

Role of lipid composition in positioning of chemoreceptor clusters

A growing number of proteins and complexes have been found to localize to the division plane and the poles in rod-shaped bacteria, making these regions of the cell attractive targets for studying spatial and temporal biomolecule organization. The cell poles exhibit several unique physical features and bacteria may exploit several of them to position proteins at these subcellular regions. Several mechanisms have been formulated to account for the positioning of proteins at the bacterial cell poles,

including localization of anionic phospholipid 'domains' due to curvature-induced membrane strain, and their role as landmarks for recruitment of proteins to these regions of the cell [77, 78, 99, 100]. Consistent with this model, polar localization of the *E. coli* osmosensory transporter (ProP) and the mechanosensitive channel (MscS) correlated with the proportion and polar localization of CL [75, 76, 101]. We sought to test whether polar localization of chemoreceptor clusters was directly correlated with the presence and localization of CL. We observed that a CL null *E. coli* strain (*E. coli* MG1755 BKT12), in which the three known CL synthases are absent and no CL is detected [86], displayed the same pattern of localization observed in the wild-type parent strain MG1655. Our results indicate that CL content in the membrane does not alter chemoreceptor localization (Figures 2A and 2C).

Deletion of *pgsA* inhibits the last committed step in the synthesis of the two major anionic phospholipids—PG and CL—in *E. coli*. Anionic phospholipids are involved in essential cellular processes, including DnaA reactivation [102], regulation of division plane formation [78], and SecA-dependent protein translocation across the IM [82, 103-105]; however, they are not essential for cell viability [87, 88, 106]. We observed diffuse localization of YFP-CheR in the *pgsA* null mutant *E. coli* UE54 and the absence of defined fluorescent puncta. The diffuse fluorescence pattern is most likely due to the reduced concentration or complete absence of chemoreceptor clusters (Figure S7). Flagella immunostaining demonstrated an absence of flagella in *E. coli* UE54 (Figure S17A) and an impairment in swimming motility was confirmed in a swimming motility assay (Figures S17B and S17C). In contrast to the UE54 mutant, the Lpp mutant strains UE49, UE51, UE53, and the CL knockout MG1655 BKT12 were motile (Figures S17B and S17C). The mutant *E. coli* UE54 is originally derived from a *pgsA* mutant isolated during

the course of the construction of a strain in which anionic phospholipids content is controlled by an inducer added exogenously [87, 88]. Growth arrest in the *E. coli pgsA* null mutant is alleviated by the lack of the major outer membrane lipoprotein Lpp [87]. Two additional mutations, namely disruption of *rcsF* (to suppress thermosensitivity of the *lpp/pgsA* double-mutant) and deletion of *araC* (gene encoding the transcriptional regulator of the *ara* operon) were introduced into *E. coli* strain UE54. As the absence of *rcsF* did not perturb the polar localization of YFP-CheR in *E. coli* cells (Figure S9), it is likely that both the absence of chemoreceptors and flagellar filaments in *E. coli* UE54 is a consequence of alterations in the levels of anionic phospholipids caused by the deletion of the *pgsA* gene. Previous studies have shown the connection between flagella biosynthesis and PG levels in *E. coli* [107, 108]. As *E. coli* MG1655 BKT12 cells lack CL and do not display these chemoreceptor or flagella phenotypes, we hypothesize that these defects arise from the absence of PG. Our data indicate that CL clearly does not influence polar localization of the chemoreceptors.

Role of cell wall curvature in positioning of chemoreceptor clusters

Another model for the concentration of chemoreceptors at the polar region of cells is that chemoreceptor clusters may have a shape that is sufficient to sense negatively curved regions of the membrane, such as the cell poles. Biophysical models predict that protein complexes destined for the cell poles using this mechanism need to assemble into structures that have a length scale that is sufficient to sense membrane curvature [100, 109, 110]. Direct sensing of cell curvature by protein complexes has been reported for SpoVM and the self-assembling protein DivIVA in *Bacillus subtilis* [110-112]. To test whether chemoreceptor clusters localize to the *E. coli* cell poles by sensing

membrane curvature, we used microengineering approaches to artificially manipulate the bacterial cell curvature. We confined filamented cells into microchannels designed to physically impose curvature in the cylindrical region of the cell body mimicking the geometry of the bacterial poles [72] and studied the localization of YFP-CheR in cells with engineered curvature. The curvature imposed by the microchannels had no apparent influence on the localization or distribution of YFP-CheR (Figure S18); however, we are unable to achieve a cell wall curvature that matches the cell poles. This result suggests that the geometry of the cell wall—and the subsequent strain-induced organization of phospholipids within the cell membrane—is likely not the primary or the exclusive cue controlling the subcellular positioning of chemoreceptor clusters. However, recent studies have shown that chemoreceptor clusters of *B. subtilis* [113] and *E. coli* [114] are highly sensitive to membrane curvature and exploit regions of negative curvature to establish polar localization.

Role of auxiliary protein complexes in positioning of chemoreceptor clusters

Another hypothesized mechanism for localizing chemoreceptors at the cell poles and the septum is by diffusion through the membrane followed by direct or indirect association with proteins or protein complexes that localize to the poles. The "diffusion-and-capture" mechanism has been hypothesized for recruitment of several polarly localized proteins [115-118]. In association with the polar transmembrane protein HubP, the ATPase ParC polarly localizes *Vibrio cholerae* chemoreceptors and downstream signaling proteins by actively recruiting the proteins to the cell poles before cytokinesis, ensuring that newborn cells have a cluster from the old-pole after cell division [117, 118]. Recently, the function of the Tol-Pal complex in positioning a polar protein was

reported in *C. crescentus* [39]. The interaction of individual components of the Tol-Pal complex with the transmembrane protein TipN suggests that the complex may function as a molecular anchor to recruit proteins to the cell poles. Our observation that the disruption of the *E. coli* Tol-Pal complex affected polar chemoreceptor localization—and not clustering (Figures 2A, 2C and S2)—prompted us to investigate the connection between the complex and the polar positioning of chemoreceptor clusters. We found evidence of an interaction between the IM transmembrane protein TolA and the chemoreceptors (Figure 5). It is possible that the chemoreceptors interact with other IM components of the Tol-Pal components. Alternatively, cell envelope defects created by inactivation of the Tol-Pal complex may disrupt the interaction between chemoreceptor clusters and unknown positioning factors. Forward genetic screens may be useful for identifying these factors. We observed polar localization of the polar proteins TnaA and IcsA in cells containing Tol-Pal defects (Figures 2E and 2F), which suggests that membrane integrity mediated by the Tol-Pal complex may be particularly required for maintaining polar localization of chemoreceptor clusters or a subset of polar proteins.

Cell motility and chemotaxis defects in Tol-Pal mutants

The impairment of cell motility in cells lacking a Tol-Pal complex has been reported previously in *Pseudomonas putida* [42]. Similarly, we observed that the disruption of the Tol-Pal complex significantly affects both *E. coli* swimming and swarming motility (Figures 3A-3C, S10A-S10D, S11A, S11B and S12A-S12C). Single-cell tracking revealed that the Δ*tol-pal* mutant has enhanced clockwise-biased flagellar rotation (Figures 3F and 3G), which may reflect a defect in the phosphorelay cascade or in the sensory adaptation system. Interestingly, although the mutants that display

mislocalization of chemoreceptors caused by disruption of the Tol-Pal complex show motility and chemotaxis defects, they are still able to sense chemical gradient (Figures 4G-4L). Clustering of the ternary complexes—chemoreceptors, CheA, and CheW—is thought to play an essential role in chemotaxis signaling, and chemoeffector amplification and adaptation [10, 11, 21, 119, 120]. However, the role of chemoreceptor polarity on cell physiology and behavior is not completely understood. We tested a range of concentrations of chemoattractant to verify whether the sensitivity of the system was affected in Δ*tol-pal* mutants in which the chemoreceptor clusters were mislocalized. We did not observe dramatic changes in cell response over time (data not shown); however, it is possible that the lowest concentration of L-aspartate that we tested in the μPlug assay masks potential differences in sensitivity between the wild-type and Δ*tol-pal* mutant cells. The chemotactic response may be optimized for polarly localized machinery because accumulation at the poles favors the assembly of larger chemoreceptor lattices [9, 14, 121] that may have maximum sensitivity.

Positioning of chemoreceptors clusters mediated by the Tol-Pal complex

We envision a mechanism for the Tol-Pal-mediated polar localization and accumulation of *E. coli* chemoreceptor clusters as depicted in Figure 6. As newly synthesized chemoreceptors are inserted into the cytoplasmic membrane, the individual receptors freely migrate within the IM phospholipid bilayer to join existing clusters or nucleate new ones (Figure 6A). The stochastic nucleation model of clustering and positioning suggests that the distribution of receptors is distance-dependent and large clusters form in regions of the cell that are furthest from large existing clusters [14, 28, 121]. Therefore, in a cell with large clusters at both poles, new clusters will

preferentially form at the mid-cell, which is the location furthest from both poles (Figure 6B). The *E. coli* Tol-Pal complex, in coordination with other structural proteins such as Lpp, may restrict the diffusion of polar and mid-cell chemoreceptor clusters. The distance-dependent chemoreceptor nucleation mechanism results in a periodic distribution of clusters along the cell body that is coincident with future division sites [28, 29, 121]. We propose a mechanism in which the Tol-Pal complex imposes a physical barrier that favors the accumulation of the clusters at the poles and division site (Figures 6C and 6D). Previous studies have suggested that unknown periodic structures positioned at the future cell division sites may assist in the segregation of the receptors [121]. A mechanism that coordinates the position of the chemosensory proteins and cell division assures that each daughter cell inherits an intact chemosensory system.

The positioning of the lateral chemoreceptor clusters in *E. coli* is independent of the MinCDE division plane positioning system [121]. In support of the role of the Tol-Pal complex in the polar positioning of chemoreceptors, Tol and Pal proteins have been reported to localize dynamically during the *E. coli* cell cycle and form a subcomplex of the division apparatus in Gram-negative bacteria [38]. The Tol-Pal complex is held together by transient interactions near the septal ring during early stages of cell wall constriction and coordinates with the divisome to mediate the invagination of the OM during cytokinesis [38]. Similarly, components of the *C. crescentus* Tol-Pal complex localize to the division plane in early predivisional cells and remain predominantly at the new pole of swarmer and stalked progeny upon completion of division [39]. The role of the Tol-Pal complex in chemoreceptor positioning may not be a general mechanism in Gram-negative bacteria. However, a conceptually similar mechanism coordinating cell division, chromosome partitioning, and segregation of the chemotaxis

machinery has been recently reported. In some polar-flagellated bacteria such as *Vibrio*, chemoreceptor cluster positioning relies on the proteins HubP and ParC, which have a cell cycle-dependent localization pattern and actively recruit chemosensory proteins to the cell poles [117, 118]. In contrast, the positioning of membrane chemoreceptor clusters in *Rhodobacter sphaeroides* is not correlated with future division sites, and neither FtsZ or MreB affect localization of the receptors [122]. Thus, it is apparent that different organisms may use diverse mechanisms to orchestrate the positioning and segregation of the chemosensory machinery and cell division. It also possible that multiples mechanisms operate in combination to influence the subcellular localization of chemoreceptors. A recent study has shown that nucleoid occlusion is also important for promoting polar localization of chemoreceptor clusters in *E. coli* [123].

CONCLUSIONS

In summary, our results demonstrate that the intact *E. coli* Tol-Pal complex is required for polar localization of chemoreceptors clusters. Polar accumulation of receptor arrays occurs independently of the lipid composition of the cytoplasmic membrane and may not be exclusively dictated by the geometry of the cell poles. Mutations that prevent the trans-envelope connections of the Tol-Pal complex and cause mislocalization of chemoreceptors affect cell motility and chemotaxis. Cumulatively, our data suggest that the *E. coli* Tol-Pal complex interacts with chemoreceptors and restricts the diffusion of receptor arrays. This mechanism may establish and maintain the polar localization of chemoreceptors at specific regions of the

cell and may be component of a regulatory mechanism that coordinates cell division and segregation of the chemosensory machinery.

ACKNOWLEDGEMENTS

We acknowledge materials from Howard Berg (anti-FliC antibody), Marcia Goldberg (plasmid pMAC382); Gerald Hazelbauer (anti-Trg antibody), Roland Lloubès (anti-TolA antibody), Sandy Parkinson (plasmid pPA803, anti-CheA, and anti-CheW antibodies), Chris Raetz (*E. coli* strain MG1655 BKT12), Victor Sourjik (plasmid pVS102), and Kevin Young (*E. coli* strain GL40). We also thank the following scientists for their input: Matthew Copeland, Ye-Jin Eun, Piercen Oliver, Lars Renner, Hannah Tuson, and Ned Wingreen. This research was supported by the National Institutes of Health (1DP2OD008735-01, D.B.W.) and the National Science Foundation (MCB-1120832 and DMR-1121288, D.B.W.).

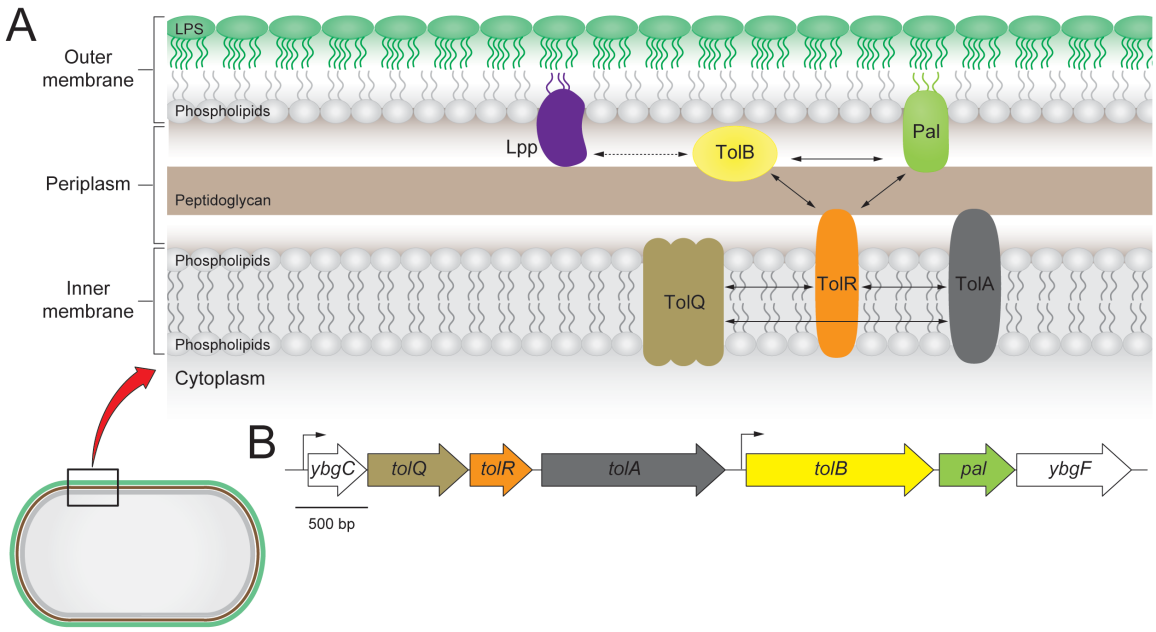

Figure 1. The organization of the *E. coli* Tol-Pal complex.

(A) Cartoon depicting the predicted organization of the Tol-Pal complex in the *E. coli* cell envelope. TolQ, TolR, and TolA are integral inner membrane (IM) proteins that interact through their transmembrane segments [48, 124, 125]. TolB is a soluble periplasmic protein and Pal is anchored to the outer membrane (OM) [34, 53, 59] (See text for details). The major OM lipoprotein Lpp is not part of the Tol-Pal complex; however, it is able to interact with TolB (indicated by a dashed arrow) [59]. Arrows indicate the interaction of the proteins in the cell envelope. LPS, lipopolysaccharide.

(B) Schematic diagram of the gene organization of the *E. coli tol-pal* gene cluster. The cluster is organized in two operons (*ybgC-ybgF* and *tolB-ybgF*). The *ybgC* gene encodes a cytoplasmic protein whereas the *ybgF* gene encodes a periplasmic protein. Inactivation of YbgC and YbgF induces no obvious alteration in phenotype. Black arrows indicate the direction of transcription and position of promoters [95, 96].

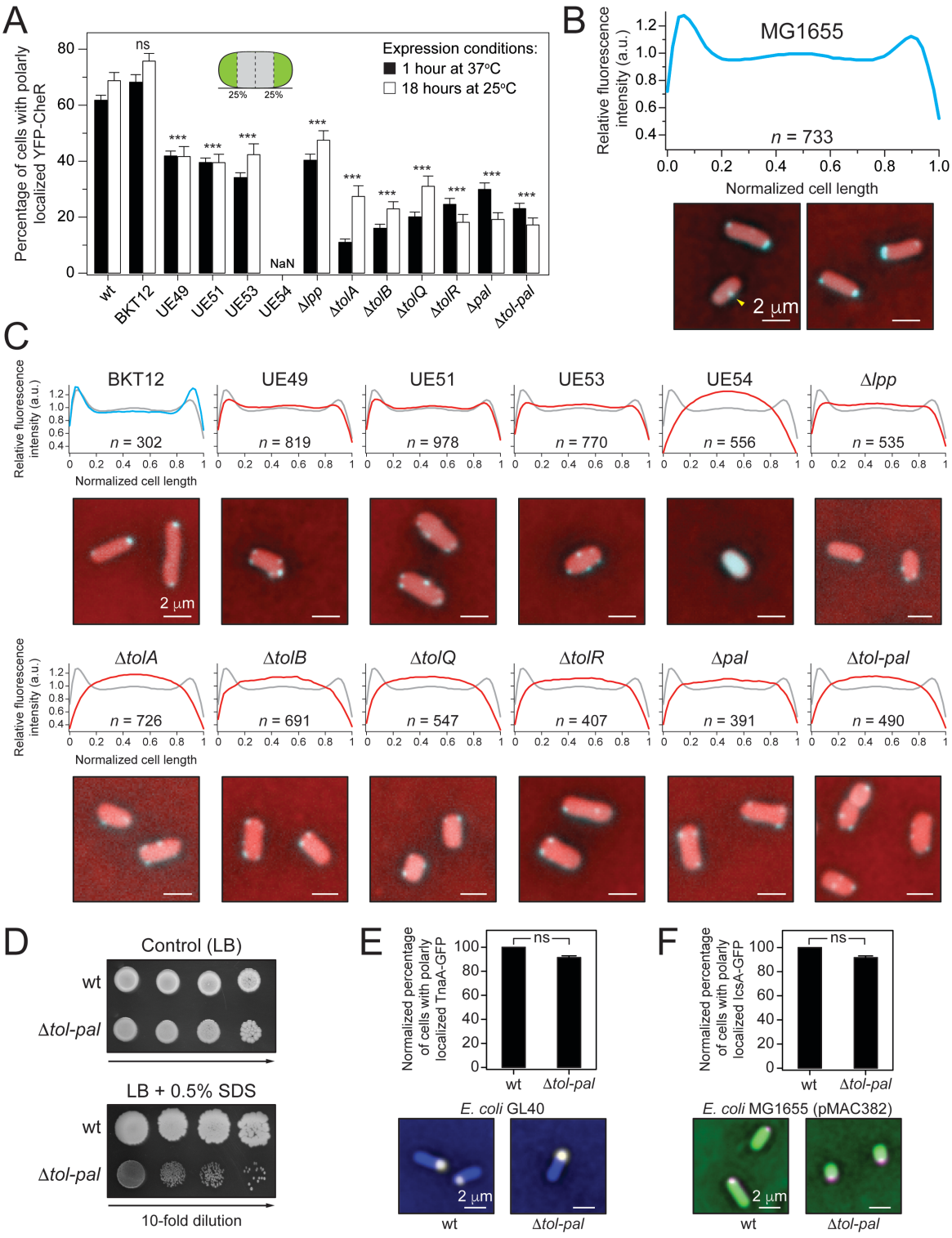

Figure 2. The Tol-Pal complex is a determinant for polar localization of chemoreceptor clusters in *E. coli* cells.

(A) Percentage of wild-type (wt) *E. coli* MG1655 cells and various mutants with polarly (unipolar or bipolar) localized YFP-CheR imaged after 1 h at 37°C (black bars) and after 18 h at 25°C (white bars). *Inset*: Cartoon depicting the poles as the outmost quartiles of cells (colored in green). Here and elsewhere, cells were determined to display a "wild-type phenotype" if all the clusters were located within the first and/or fourth quartiles of the cell. Otherwise, cells were labeled as displaying "non-wild-type phenotype". NaN, no polar clusters were detected.

(B) Fluorescence intensity profile of the subcellular distribution of YFP-CheR in wild-type *E. coli* MG1655 cells (n = 733) imaged after 1 h at 37°C. (a.u., arbitrary units). *Panel below the graph*: Representative fluorescence microscopy images depicting the localization pattern of YFP-CheR in wild-type *E. coli* MG1655 cells. Microscopy images are representative of at least three independent experiments. The yellow arrowhead indicates the YFP-CheR foci at mid-cell. Scale bars = 2 μm.

(C) Fluorescence intensity profile of the subcellular distribution of YFP-CheR in *E. coli* MG1655 mutants imaged after 1 h at 37°C. (a.u., arbitrary units). We superimposed the fluorescence profile of the wild-type cells (gray line) on top of the profile of the mutants (blue or red line). *Panel below each graph*: Representative fluorescence microscopy images depicting the localization pattern of YFP-CheR in the mutants. Images are representative of at least three independent experiments. Scale bars = 2 μm.

(D) Growth assay of serial dilutions (left to right) of wild-type (wt) *E. coli* MG1655 and *E. coli* MG1655 Δ*tol-pal*. Aliquots of 10-fold serial dilutions (5 μL, 10^1-10^4 c.f.u./mL) from

overnight cultures were spotted on control agar (LB) and agar containing 0.5% SDS. The plates were incubated at 37°C for 24 h and then at 25°C for additional 24 h.

(E) Percentage of wild-type (wt) *E. coli* MG1655 (n = 464) and *E. coli* MG1655 Δ*tol-pal* (n = 386) cells with polarly localized TnaA-GFP. *Panel below the graph*: Representative images obtained in at least three independent experiments.

(E) Percentage of wild-type (wt) *E. coli* MG1655 (n = 601) and in *E. coli* MG1655 Δ*tol-pal* (n = 406) cells with polarly localized IcsA-GFP. *Panel below the graph*: Representative images obtained in at least three independent experiments.

To assess differences between the localization patterns in the various *E. coli* strains (panels A, E, and F), we performed chi-squared tests. Error bars indicate the standard error of the mean. ns, non-significant; ***, $P < 0.001$ compared to the wild-type phenotype. Scale bars = 2 μm.

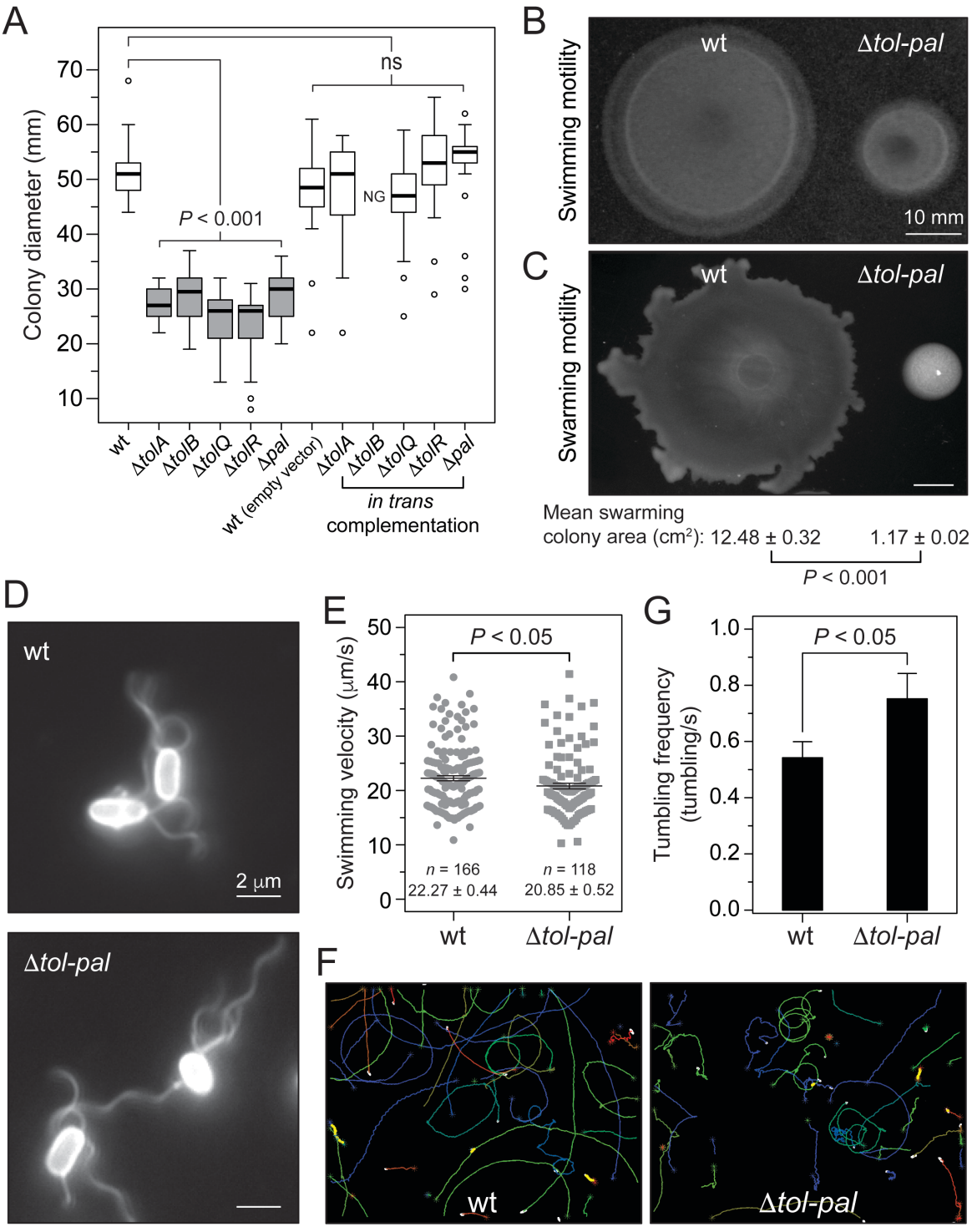

Figure 3. Deletion of the Tol-Pal complex affects motility in *E. coli* cells.

(A) Box-and-whisker plots depicting the size of the migrating colonies measured for wild-type (wt) *E. coli* MG1655 cells and various mutants. The extent of the box encompasses the interquartile range (IQR) of the diameter (in mm) and the black line within each box represents the median. The upper whisker extends to the maximum data value, or 1.5 of the IQR, whichever is the smaller. The lower whisker extends to the maximum data value, or 1.5 of the IQR, whichever is the larger. Outliers are represented as open black circles. For complementation experiments, carbenicillin (50 μg/mL) and 1 mM IPTG were added to the motility agar. To test for differences between motility phenotype in the various *E. coli* strains, we performed two-way ANOVA followed by Tukey's multiple-comparison post-hoc test. ns, non-significant; NG, no growth. Box-and-whisker plots colored in gray represent migrating colonies that were significantly smaller than the wild-type colony. Analyses represent the combination of at least three independent experiments.

(B) Representative image of swimming colonies of wild-type (wt) *E. coli* MG1655 and *E. coli* MG1655 Δ*tol-pal* after 14.5 h of incubation at 30°C on swimming motility agar. Scale bar = 10 mm.

(C) Representative image of swarming colonies of wild-type (wt) *E. coli* MG1655 and *E. coli* MG1655 Δ*tol-pal* after 16 h on swarming motility agar at 30°C. The area of individual swarming colonies ($n = 20$) was measured using ImageJ and the mean swarming colony areas were compared using an unpaired two-sample Student's t-test. The mean swarming colony area for *E. coli* MG1655 and *E. coli* MG1655 Δ*tol-pal*, the

standard error of the mean, and the correspondent *P* value are indicated below the representative image. Scale bar = 10 mm.

(D) Representative immunofluorescence images of wild-type (wt) *E. coli* MG1655 and *E. coli* MG1655 Δ*tol-pal* cells labeled with a polyclonal anti-FliC primary antibody and an Alexa Fluor 488-conjugated secondary antibody. Scale bars = 2 μm.

(E) Plot depicting velocity of individual cells (n = 166 for wild-type (wt) *E. coli* MG1655 and n = 118 for *E. coli* MG16655 Δ*tol-pal*). Error bars indicate the standard error of the mean. The mean velocity and standard error for each population are indicated below each plot. To compare the mean velocity of the two populations, we performed an unpaired two-sample Student's t-test. Analyses represent the combination of at least three independent experiments.

(F) Representative image of cell trajectories of wild-type (wt) *E. coli* MG1655 and *E. coli* MG1655 Δ*tol-pal* cells. The images consist of an overlay of three images from two independent experiments. Each colored line represents the trajectory of an individual cell.

(G) Average swimming reversal rate of wild-type *E. coli* MG1655 and *E. coli* MG1655 Δ*tol-pal*. We compared the reversal frequency using an independent sample randomization (permutation) test (10,000 simulations of differences of mean).

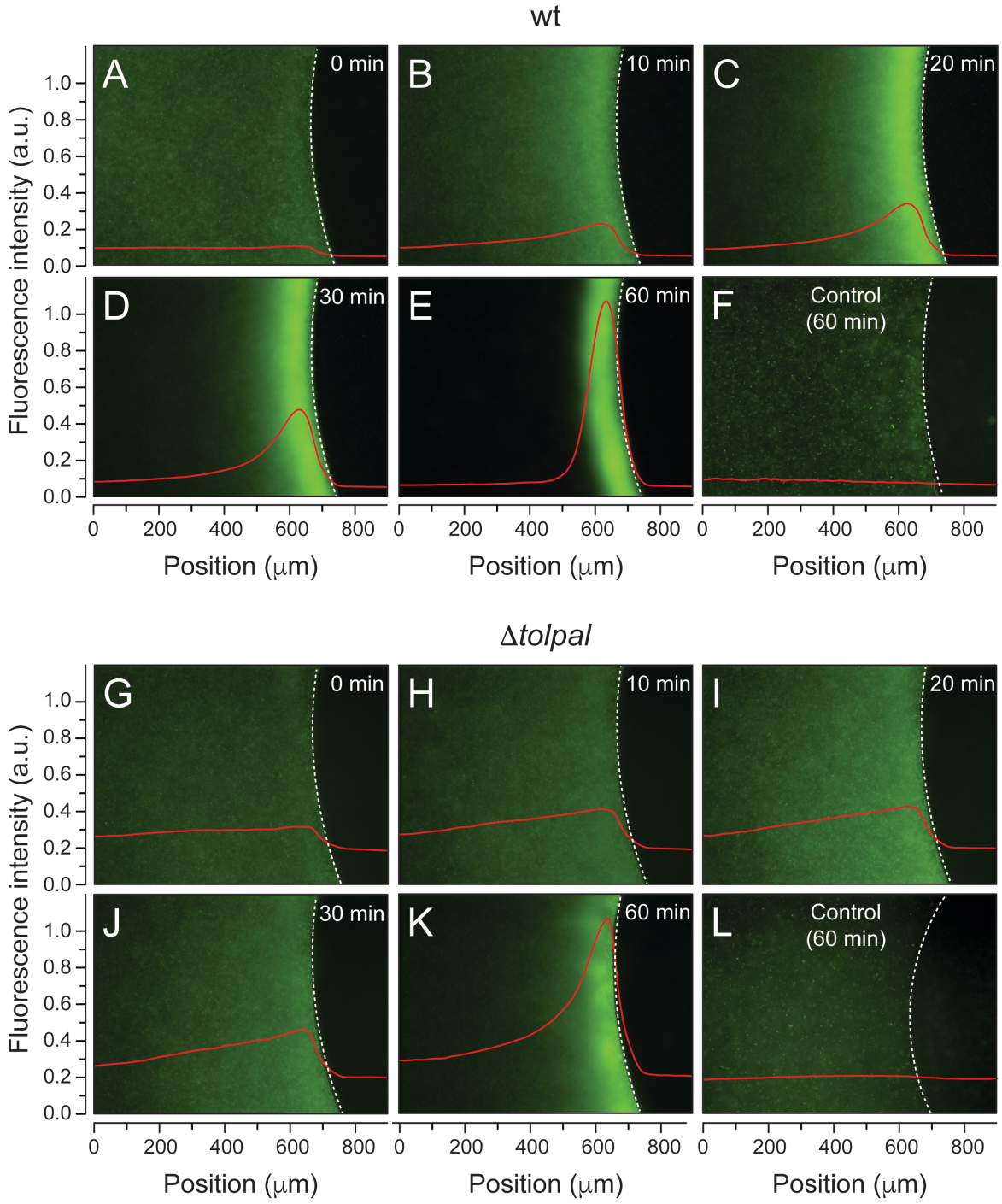

Figure 4. Deletion of the Tol-Pal complex affects chemotaxis in *E. coli* cells.

Chemotatic response of *E. coli* cells to L-aspartate using the μPlug assay. Spatial distribution of EGFP-labeled wild-type (wt) *E. coli* MG1655 (A-E; F, control) and *E. coli* MG1655 Δ*tol-pal* cells (G-K; L, control) in the presence of 1 mM of L-aspartate. Panels A-E and G-K show a series of representative images obtained from the same time-lapse experiment for each strain. Fluorescence intensity profiles demonstrating the chemotatic response of cells to the μPlug (represented by red lines; a.u., arbitrary units) are overlaid on each image. A dashed white line delineates the agarose plug-liquid interface. A moving average was used to smooth the data trend in the series of images. Controls show the distribution of EGFP-labeled cells in the absence of L-aspartate. Images were false-colored using ImageJ.

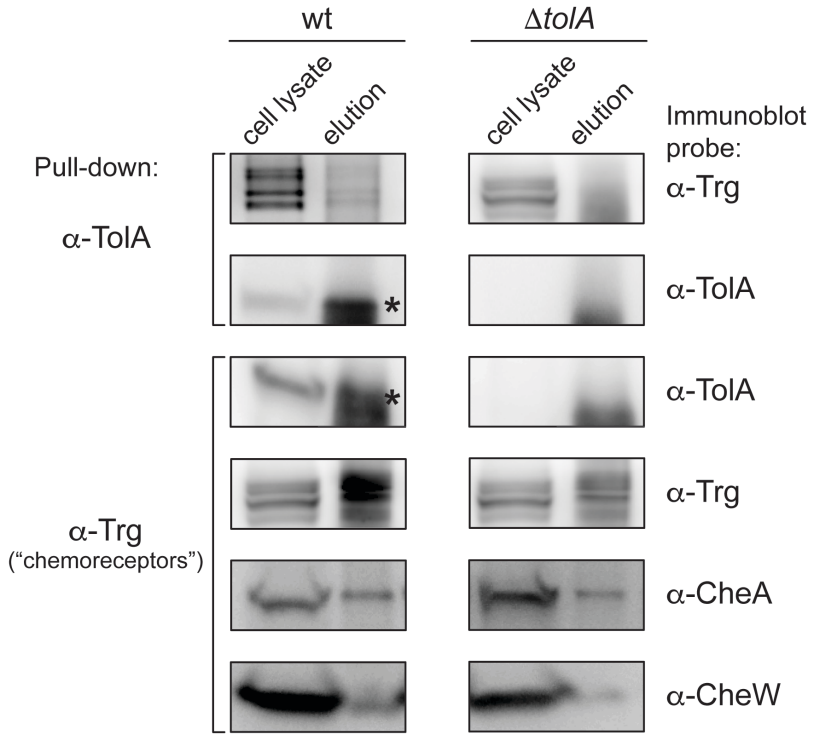

Figure 5. The inner membrane protein TolA interacts with chemoreceptors.

In vivo co-immunoprecipitation (Co-IP) of TolA in wild-type (wt) *E. coli* MG1655 and in the mutant *E. coli* MG1655 Δ*tolA*. Western blots of whole-cell lysate and elution fraction of samples immunoprecipitated with anti-TolA (α-TolA) (indicated on the left) were probed with anti-Trg (α-Trg) and with α-TolA (indicated on the right). The reverse co-IP was performed with whole-cell lysate samples immunoprecipitated with α-Trg (indicated on the left) and probed with α-TolA. As a control, western blots of whole-cell lysate and elution fraction of samples immunoprecipitated with α-Trg were separately probed with anti-CheA (α-CheA), anti-CheW (α-CheW), and α-Trg. The α-Trg is an antiserum raised to highly purified *E. coli* Trg, however it also recognizes the other *E. coli* chemoreceptors (Tar, Tsr, and Tap) [126]. Because cross-reactivity of α-TolA with unknown components of the co-IP eluate generated another signal close to the band of interest (TolA), asterisks were added to facilitate visualization of TolA.

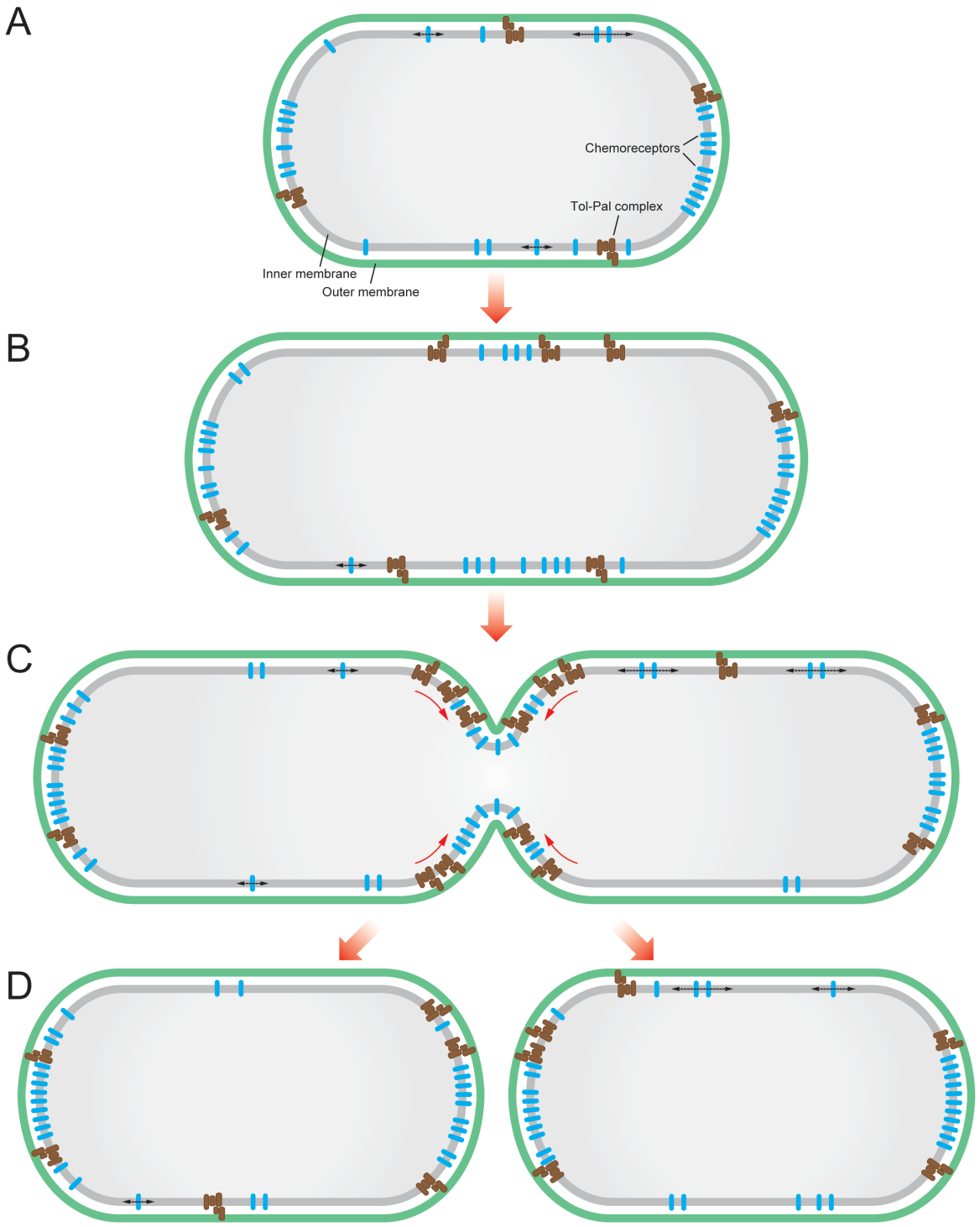

Figure 6. Proposed model for Tol-Pal-mediated polar localization of chemoreceptor clusters in *E. coli*.

(A) As newly synthesized chemoreceptors are inserted into the cytoplasmic membrane, the individual receptors migrate freely (dashed black arrows) within the IM and join existing clusters or nucleate new ones. (B) Receptor distribution is distance-dependent and clusters accumulate in regions that are furthest from existing clusters [14, 28, 29, 121]. (C and D) The Tol-Pal complex localizes to the division plane in early pre-divisional cells (red arrows) to facilitate constriction of the outer membrane during cell division [38]. The trans-envelope complex may restrict the mobility of polar and mid-cell chemoreceptor clusters by creating a physical barrier that favors their accumulation at these cellular locations. Refer to the text for an additional explanation and discussion.

SUPPLEMENTARY INFORMATION

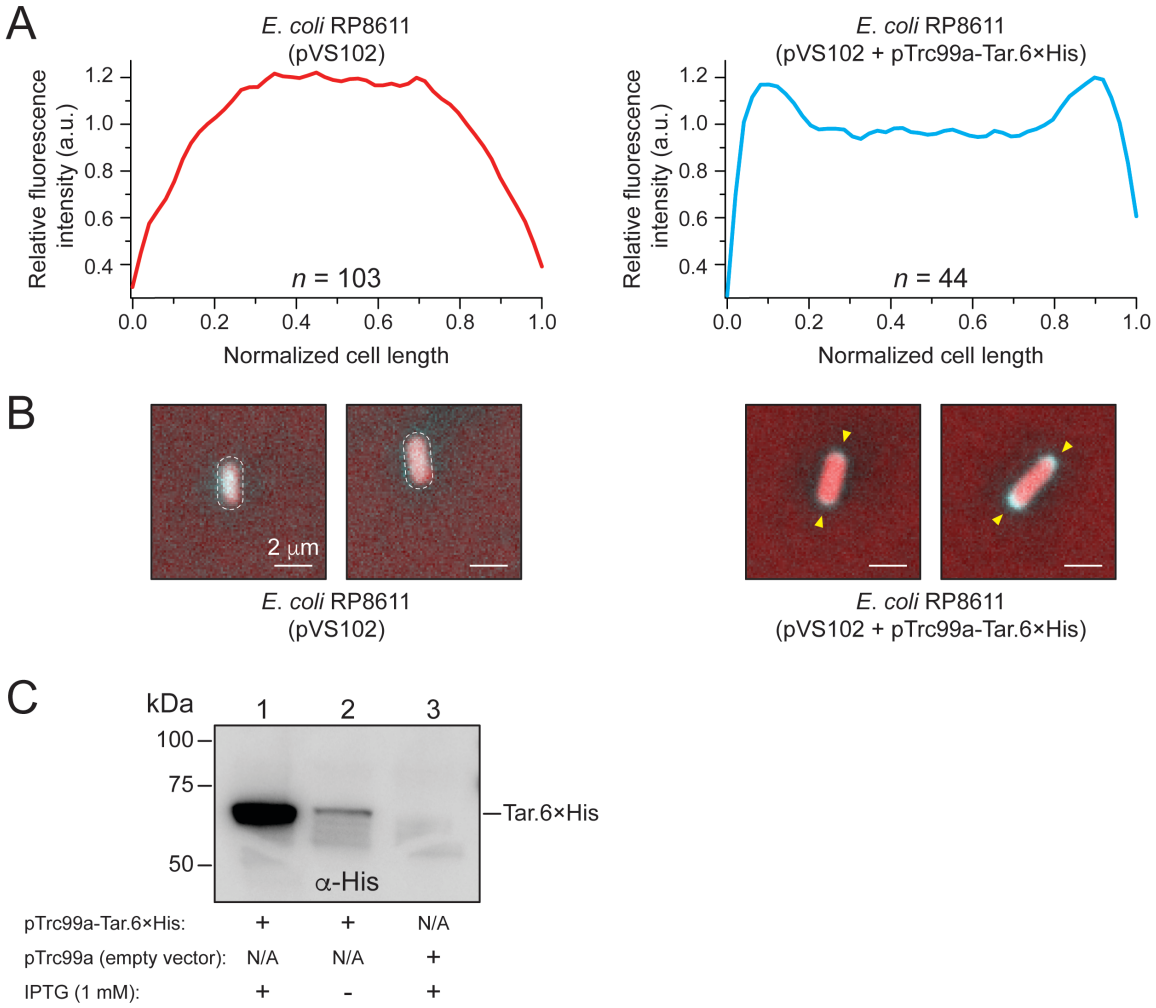

Figure S1. The methyltransferase CheR does not localize to the cell poles in the absence of chemoreceptors.

(A) Fluorescence intensity profile of the subcellular distribution of YFP-CheR in *E. coli* RP8611 expressing YFP-CheR (n = 103; red line) and in *E. coli* RP8611 co-expressing YFP-CheR and Tar.6×His (n = 44; blue line). Cells were imaged after 1 h at 37°C. (a.u., arbitrary units).

(B) Representative fluorescence microscopy images depicting the localization pattern of YFP-CheR in *E. coli* RP8611 and in *E. coli* RP8611 overexpressing Tar.6×His. Note the accumulation of YFP-CheR at the cell poles (yellow arrowheads) when the chemoreceptor Tar is co-overexpressed in *E. coli* RP8611 cells. White dashed lines indicate the perimeter of the cell. *E. coli* RP8611 is a well-characterized mutant strain that does not express the chemoreceptors Tar, Tsr, Trg, and Tap [127], but is otherwise wild-type for chemotaxis genes. The plasmid pVS102 encodes a functional YFP-CheR fusion controlled by an arabinose-inducible promoter [85]. Scale bars = 2 μm.

(C) Immunoblot confirming in-trans expression of Tar.6×His in *E. coli* MG1655. Immunoblot was probed with anti-6×His (α-His) antibody. *E. coli* cells harboring the plasmid pTrc99a-Tar.6×His (encoding a tagged version of the chemoreceptor Tar) were grown overnight in LB broth, diluted (1:100) in 5 mL of fresh LB broth and incubated at 37°C with agitation (200 r.p.m.) until an absorbance of 0.6 (λ = 600 nm) was reached. We induced expression of the 6×His-tagged Tar protein by adding 1 mM IPTG and incubating the cultures for 1 h at 37°C with agitation (200 r.p.m.). Calibrated cell suspensions containing the same number of cells (approximately 10^7 c.f.u./mL) were washed in 1× PBS buffer, heated to 100°C for 15 min and loaded into a 12% SDS-PAGE gel. Electrophoresis and immunoblot analysis were performed as described in the

Experimental Procedures section. Non-induced cells (lane 2) and cells containing the empty vector (lane 3) were used as a control. Note the leaky expression of His-tagged Tar in non-induced cells (lane 2).

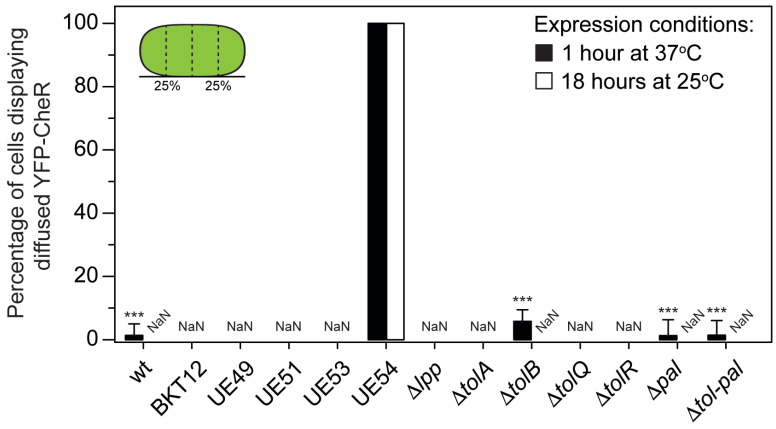

Figure S2. Subcellular localization of chemoreceptors in wild-type *E. coli* MG1655 and various mutant strains.

Percentage of wild-type (wt) *E. coli* MG1655 cells and various mutants displaying diffuse YFP-CheR after 1 h at 37°C (black bars) and after 18 h at 25°C (white bars). *Inset*: Cartoon depicting the poles as the outmost quartiles of cells. To assess differences between the localization patterns in the various *E. coli* strains, we performed chi-squared tests. Error bars indicate the standard error of the mean. ***, $P < 0.001$ compared to *E. coli* UE54. NaN, absence of diffuse signal.

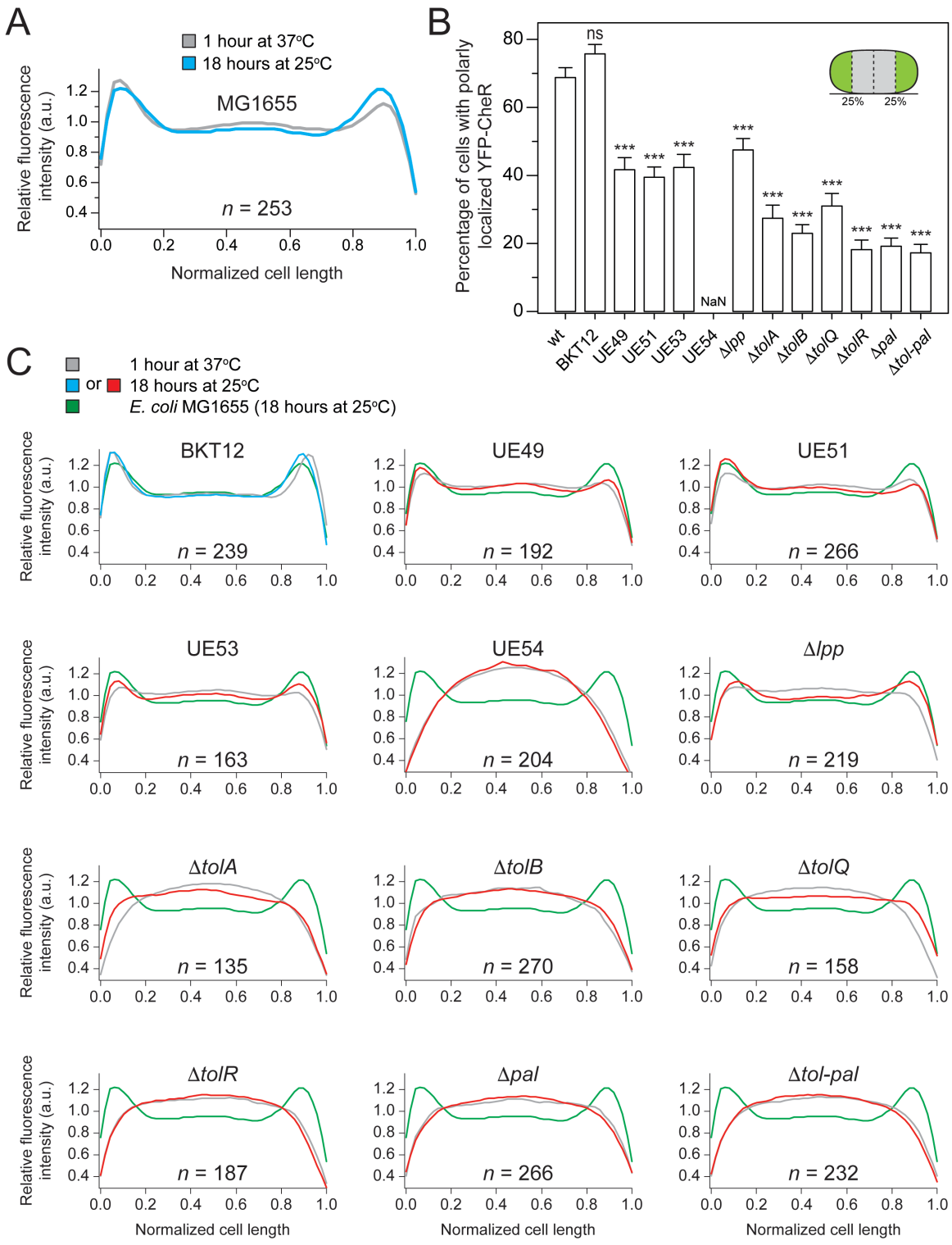

Figure S3. Subcellular localization of chemoreceptors in wild-type *E. coli* MG1655 and various mutant strains.

(A) Fluorescence intensity profile of the subcellular distribution of YFP-CheR in wild-type *E. coli* MG1655 cells imaged after 1 h at 37°C ($n = 733$; gray line) and after 18 h at 25°C ($n = 253$; blue line). (a.u., arbitrary units).

(B) Percent of wild-type (wt) *E. coli* MG1655 cells and various mutants with polarly (unipolar or bipolar) localized YFP-CheR imaged after 18 h at 25°C. *Inset*: Cartoon depicting the poles as the outmost quartiles of cells (colored in green). To assess differences between the localization patterns in the various *E. coli* strains, we performed chi-squared tests. Error bars indicate the standard error of the mean. ns, non-significant; ***, $P < 0.001$ compared to the wild-type phenotype. NaN, no polar clusters were detected.

(C) Fluorescence intensity profile of the subcellular distribution of YFP-CheR in mutants of *E. coli* MG1655 imaged after 18 h at 25°C (continuous blue or red line). (a.u., arbitrary units). For each graph, we superimposed the YFP-CheR fluorescence profile of the wild-type cells (dashed green lines) imaged after 18 h at 25°C (shown in a continuous blue line panel A) and the YFP-CheR fluorescence profile of the respective mutant imaged after 1 h at 37°C (continuous gray line). Continuous blue lines indicate the YFP-CheR fluorescence profile in mutants that display a percentage of polar foci comparable to the wild-type cells (non-significant difference, as shown in panel B). Continuous red lines indicate the YFP-CheR fluorescence profile in mutant cells that display a percentage of polar foci statistically different ($P < 0.05$) from wild-type cells (as shown in panel B).

All analyses were performed with data obtained in at least three independent experiments.

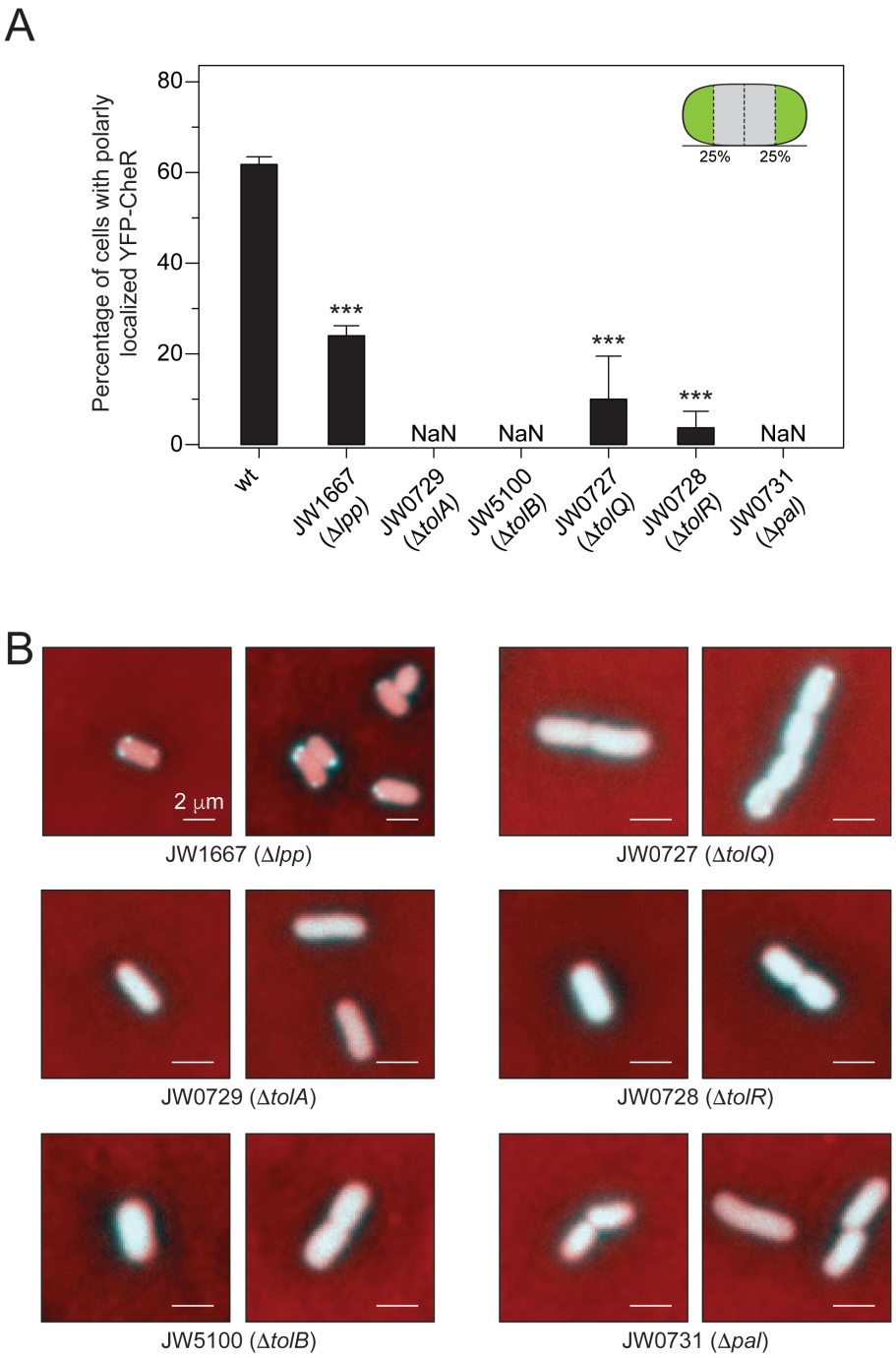

Figure S4. Subcellular localization of chemoreceptors in wild-type *E. coli* MG1655 and in various mutant strains from the Keio collection.

(A) Percent of wild-type (wt) *E. coli* MG1655 cells and various mutants from the Keio collection with polarly (unipolar or bipolar) localized YFP-CheR imaged after 1 h at 37°C. *Inset*: Cartoon depicting the poles as the outmost quartiles of cells (colored in green). To assess differences between the localization patterns in the various *E. coli* strains, we performed chi-squared tests. Error bars indicate the standard error of the mean. ns, non-significant; ***, $P < 0.001$ compared to the wild-type phenotype. NaN, no polar clusters were detected.

(B) Representative fluorescence microscopy images depicting the localization pattern of YFP-CheR in *lpp*, and single-deletion *tol* and *pal* mutants. Images are representative of cells observed in at least three independent experiments. Scale bars= 2 μm.

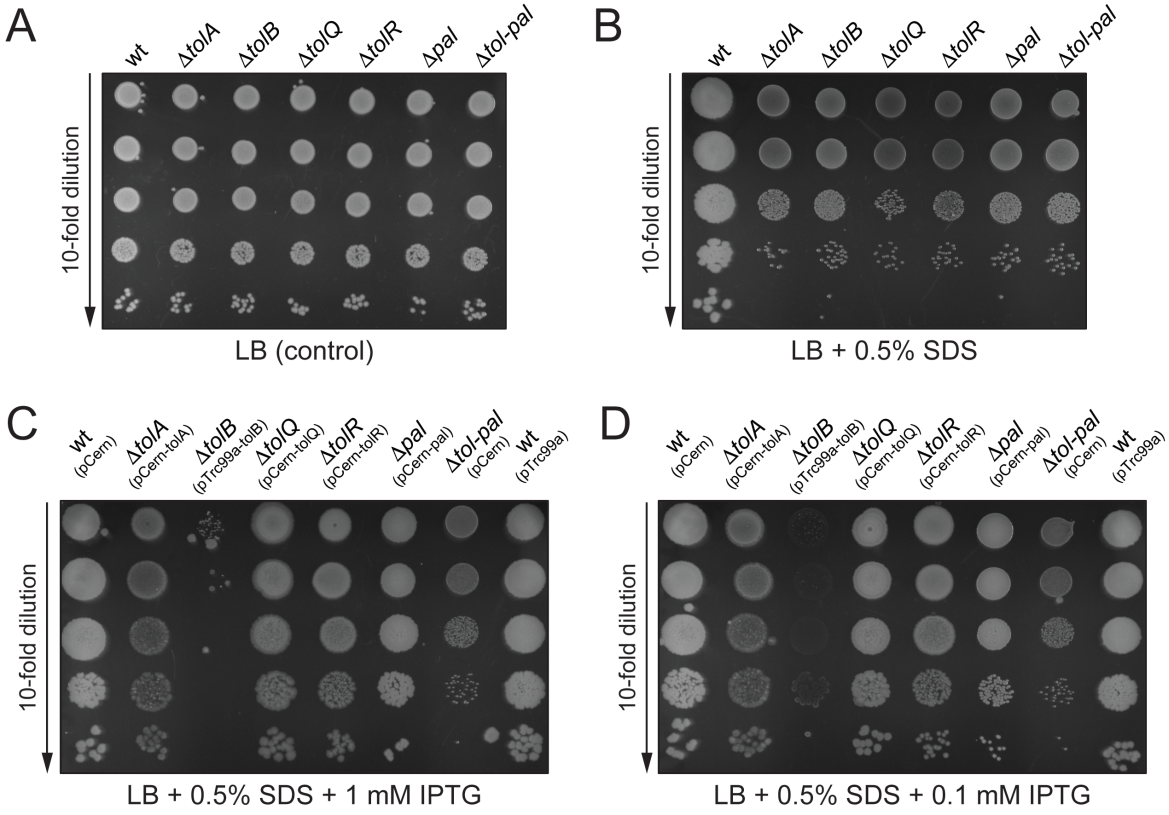

Figure S5. Growth assay of cultures containing wild-type *E. coli* MG1655 and various mutant strains.

(A) Growth of wild-type (wt) *E. coli* MG1655, single-gene knockouts of *tolA*, *tolB*, *tolQ*, *tolR*, and *pal* derived from wild-type MG1655, and an *E. coli* MG1655 mutant lacking all the Tol and Pal proteins (Δ*tol-pal*) on LB agar.

(B) Growth of wild-type (wt) *E. coli* MG1655, single-gene knockouts of *tolA*, *tolB*, *tolQ*, *tolR*, and *pal*, and Δ*tol-pal* on LB agar containing 0.5% SDS.

(C) Suppression of hypersensitivity to 0.5% SDS in single-gene knockouts of *tolA*, *tolB*, *tolQ*, *tolR*, and *pal* transformed with plasmids encoding the gene able to complement the correspondent chromosomal deletion. Cells were spotted on LB agar containing 0.5% SDS, carbenicillin (50 μg/mL), and 1 mM IPTG. wt, wild-type *E. coli* MG1655.

(D) Suppression of hypersensitivity to 0.5% SDS in single-gene knockouts of *tolA*, *tolB*, *tolQ*, *tolR*, and *pal* transformed with plasmids encoding the gene able to complement the correspondent chromosomal deletion. Cells were spotted on LB agar containing 0.5% SDS, carbenicillin (50 μg/mL), and 0.1 mM IPTG. The concentration of IPTG was reduced because high levels of TolB expression appeared to be toxic to cells and inhibited growth. wt, wild-type *E. coli* MG1655.

Aliquots of 10-fold serial dilutions (5 μL of dilutions 10^{-1}-10^{-5}; top to bottom) from normalized cultures initially calibrated to an absorbance of 1.0 (λ = 600 nm) and containing approximately 10^8 c.f.u./mL were spotted on the agar. The plates were incubated at 37°C for 24 h and then at 25°C for additional 72 h. Because Tol-Pal mutants

are hypersensitive to detergents [43, 45], we performed this assay to confirm the deletion of the *tol* and *pal* genes.

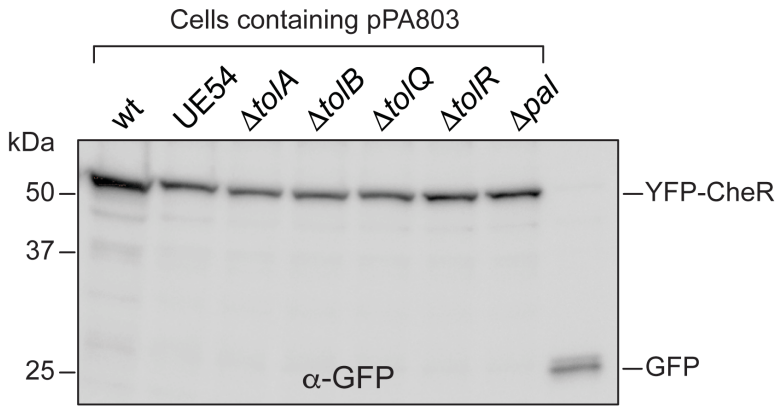

Figure S6. The YFP-CheR fusion protein encoded in the plasmid pPA803 is stable in *E. coli* UE54 and in the *tol* and *pal* single-gene knockouts.

Expression of YFP-CheR was performed as described in the Experimental Procedures section. Calibrated cell suspensions of each strain, containing the same number of cells (approximately 10^7 c.f.u./mL), were washed in 1× PBS buffer, heated to 100°C for 15 min. ~10 μL of cell lysate was loaded into a 12% SDS-PAGE gel. Electrophoresis and immunoblot analysis were performed as described in Experimental Procedures section. Cell lysate of *E. coli* MG1655 expressing EGFP from the plasmid P_{tet}-egfp was used as a control. wt, wild-type *E. coli* MG1655.

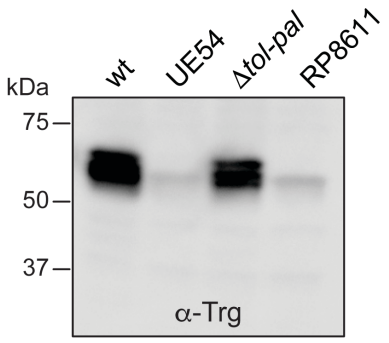

Figure S7. Deletion of the Tol-Pal complex does not prevent synthesis of chemoreceptors in *E. coli*.

E. coli UE54 displays a dramatic reduction in the levels of expressed chemoreceptors. Calibrated cell suspensions of each strain containing the same number of cells (approximately 10^7 c.f.u./mL) were washed in 1× PBS buffer, heated to 100°C for 15 min. ~10 μL of cell lysate was loaded into a 12% SDS-PAGE gel. Electrophoresis and immunoblot analysis were performed as described in the Experimental Procedures section. wt, wild-type *E. coli* MG1655. The anti-Trg (α-Trg) is an antiserum raised to highly purified *E. coli* Trg, but it also recognizes the other *E. coli* chemoreceptors (Tar, Tsr, and Tap) and related proteins in other bacteria [126]. *E. coli* RP8611, a well-characterized mutant strain that does not express the chemoreceptors Tar, Tsr, Trg, and Tap [127], was used as a negative control.

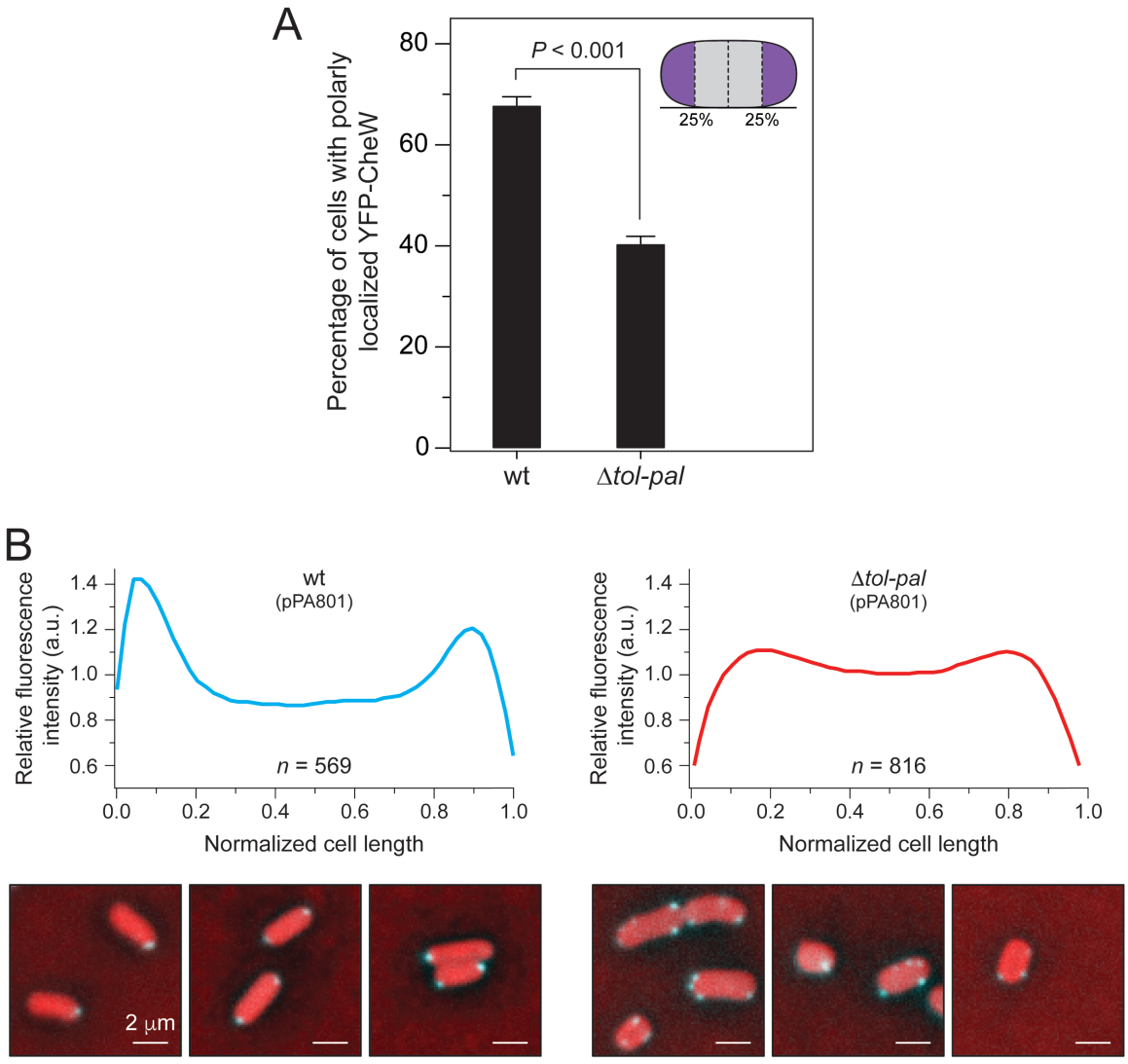

Figure S8. Subcellular localization of chemoreceptors in wild-type *E. coli* MG1655 and in *E. coli* MG1655 Δ*tol-pal*.

(A) Percent of wild-type (wt) *E. coli* MG1655 and MG1655 Δ*tol-pal* cells with polarly (unipolar or bipolar) localized YFP-CheW imaged after 1 h at 37°C. *Inset*: Cartoon depicting the poles as the outmost quartiles of cells (colored in purple). To assess differences between the localization patterns in the various *E. coli* strains, we performed chi-squared tests. Error bars indicate the standard error of the mean.

(B) Fluorescence intensity profile of the subcellular distribution of YFP-CheW in wild-type (wt) *E. coli* MG1655 ($n = 569$; blue line) and in *E. coli* MG1655 Δ*tol-pal* ($n = 816$; red line). Cells were imaged after 1 h at 37°C. (a.u., arbitrary units). Scale bars = 2 μm. The plasmid pPA801 encodes a yellow fluorescent protein (YFP) fused to the N-terminal region of CheW (YFP-CheW) controlled by an arabinose-inducible promoter [65].

All analyses were performed with data obtained in at least two independent experiments.

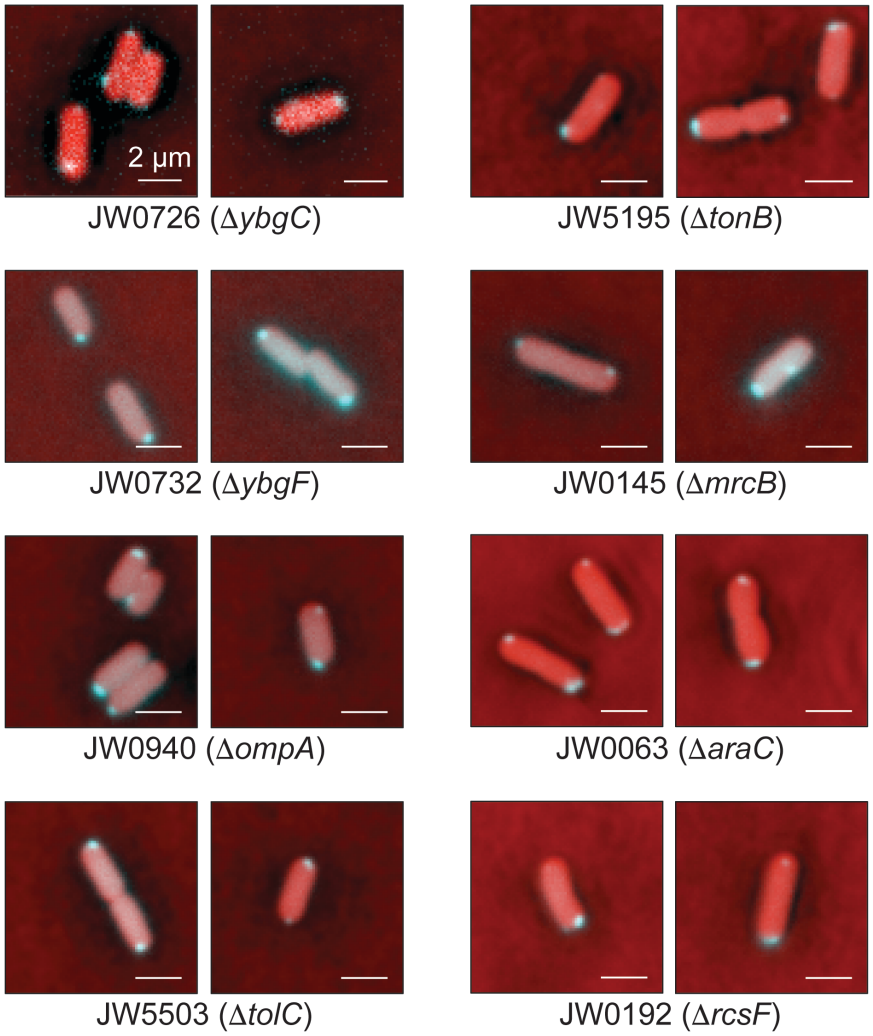

Figure S9. Subcellular localization of chemoreceptors in *E. coli* mutant strains from the Keio collection.

Representative fluorescence microscopy images depicting the localization pattern of YFP-CheR in single-deletion *E. coli* mutants lacking genes that encode proteins important for transport, stress survival, or cell wall synthesis and remodeling. Images are representative of cells observed in at least three independent experiments. Scale bars = 2 μm.

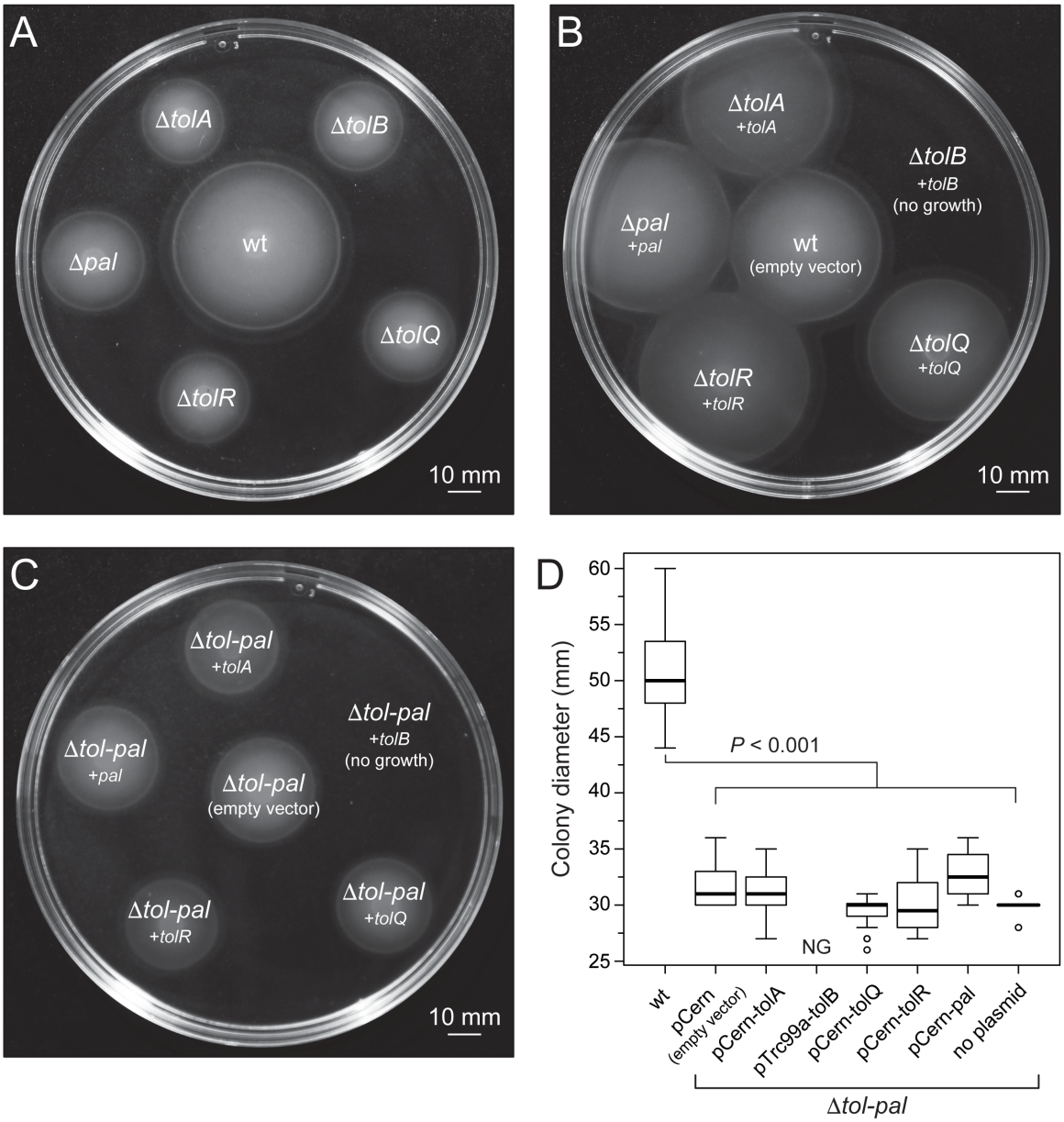

Figure S10. Swimming motility assay of wild-type *E. coli* MG1655 and mutants lacking components of the Tol-Pal complex.

(A) Representative image of colonies of wild-type (wt) *E. coli* MG1655 and single-gene knockout mutants after 14.5 h of incubation at 30°C on swimming motility agar. The deleted gene is indicated for each colony. Scale bar = 10 mm.

(B) Representative image of complementation experiments that reverted the swimming defect of *E. coli* MG1655 single-gene knockout mutants. Single-gene *E. coli* knockout mutants were transformed with a plasmid encoding the deleted gene—as indicated for each colony—able to complement the corresponding chromosomal mutation. The colonies were grown for 14.5 h at 30°C on swimming motility agar containing carbenicillin (50 μg/mL) and 1 mM IPTG. wt, wild-type *E. coli* MG1655. Scale bar = 10 mm.

(C) Representative image of the complementation experiments confirming the requirement of the intact Tol-Pal complex for reversion of motility defects. *E. coli* MG1655 Δ*tol-pal* was transformed with a plasmid encoding the individual *tol* and *pal* genes indicated for each colony. The colonies were grown for 14.5 h at 30°C on swimming motility agar containing carbenicillin (50 μg/mL) and 1 mM IPTG. Scale bar = 10 mm.

(D) Box-and-whisker plots depicting the size of the migrating colonies ($n = 20$) measured for wild-type (wt) *E. coli* MG1655 and MG1655 Δ*tol-pal* strains complemented with a plasmid encoding the individual *tol* and *pal* genes. The extent of the box encompasses the interquartile range (IQR) of the diameter (in mm) and the black line

within each box represents the median. The upper whisker extends to the maximum data value, or 1.5 of the IQR, whichever is the smaller. The lower whisker extends to the maximum data value, or 1.5 of the IQR, whichever is the larger. Outliers are represented as open black circles. Statistical analysis was performed using two-way ANOVA followed by Tukey's multiple-comparison post-hoc test. The bar indicating the statistical significance represents the *P* value obtained from the comparison between the mean colony diameter of the wild-type (wt) *E. coli* MG1655 and the various mutants overexpressing the individual *tol* and *pal* proteins. NG, no growth. Plots represent the combination of at least two independent experiments.

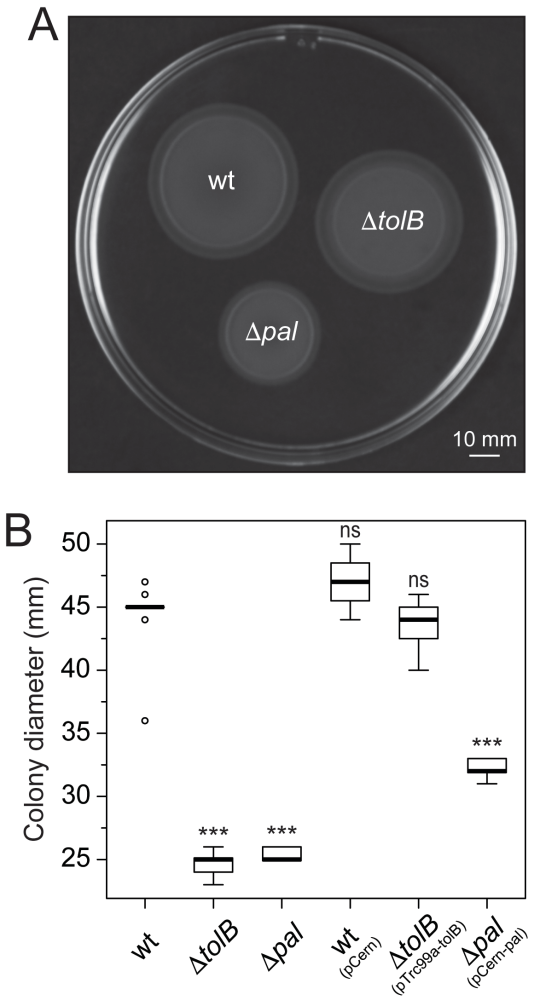

Figure S11. Swimming motility assay of wild-type *E. coli* MG1655 and mutants lacking components of the Tol-Pal complex.

(A) Representative image of the complementation experiments that reverted the swimming defect of *E. coli* MG1655 Δ*tolB*. Single-gene *E. coli* knockout mutants were transformed with a plasmid (pTrc99a-TolB or pCern-Pal) encoding the deleted gene—as indicated for each colony—able to complement the corresponding chromosomal mutation. The colonies were grown for 14.5 h at 30°C on motility agar containing carbenicillin (50 μg/mL) and 0.1 mM IPTG. High levels of TolB expression appeared to be toxic to cells and inhibited cell growth. Note that the concentration of IPTG used in this assay (0.1 mM) was not sufficient to revert the motility defect in the *E. coli* MG1655 Δ*pal*. wt, wild-type *E. coli* MG1655. Scale bar = 10 mm.

(B) Box-and-whisker plots depicting the size of the migrating colonies ($n = 11$) measured for wild-type (wt) *E. coli* MG1655, *E. coli* MG1655 Δ*tolB*, and *E. coli* MG1655 Δ*pal* strains complemented with a plasmid encoding *tolB* or *pal*. The extent of the box encompasses the interquartile range (IQR) of the diameter (in mm) and the black line within each box represents the median. The upper whisker extends to the maximum data value, or 1.5 of the IQR, whichever is the smaller. The lower whisker extends to the maximum data value, or 1.5 of the IQR, whichever is the larger. Outliers are represented as open black circles. Statistical analysis was performed using two-way ANOVA followed by Tukey's multiple-comparison post-hoc test. ns, non-significant; ***, $P < 0.001$ compared to the wild-type phenotype.

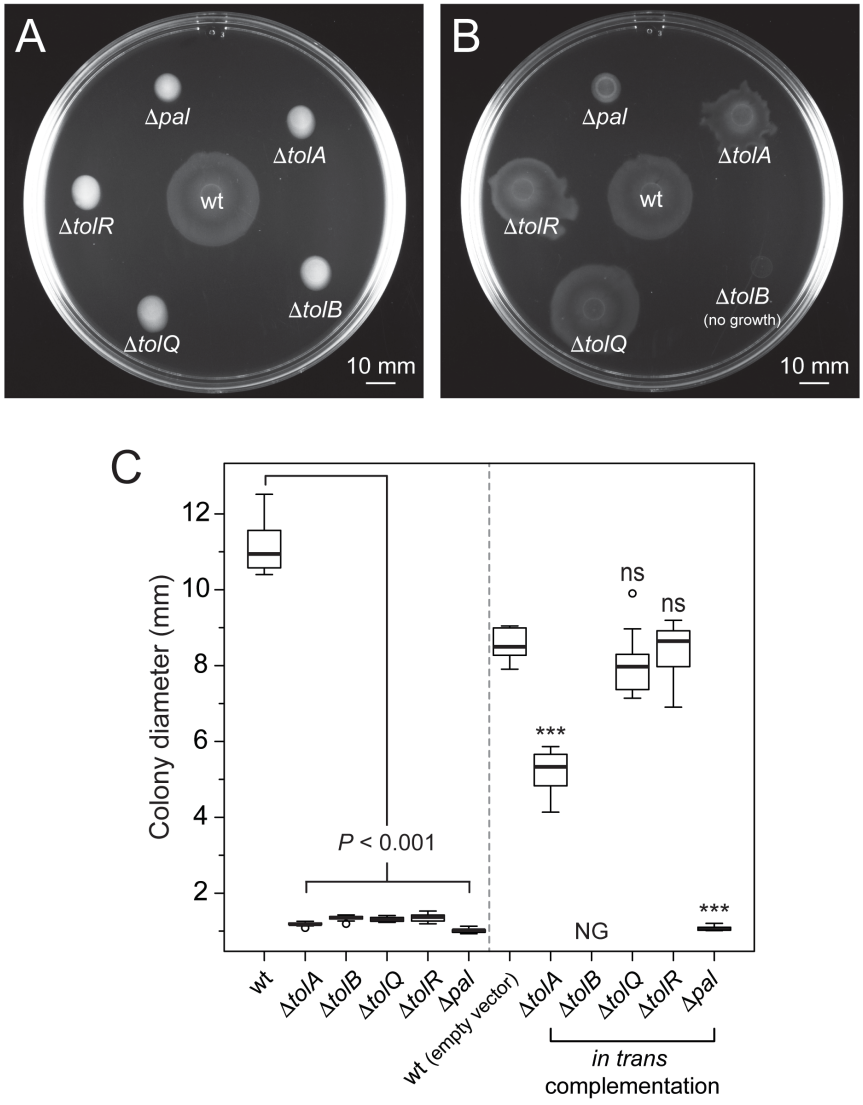

Figure S12. Swarming motility assay of wild-type *E. coli* MG1655 and mutants lacking components of the Tol-Pal complex.

(A) Representative image of colonies of wild-type (wt) *E. coli* MG1655 and single-gene knockout mutants after 16 h of incubation at 30°C on swarming motility agar. The deleted gene is indicated for each colony. Scale bar = 10 mm.

(B) Representative image of complementation experiments that partially reverted the swarming defect of wild-type (wt) *E. coli* MG1655 single-gene knockout mutants. Single-gene knockout mutants were transformed with a plasmid encoding the deleted gene—as indicated for each colony—able to complement the corresponding chromosomal mutation. The colonies were grown for 30 h at 30°C on swarming motility agar containing carbenicillin (50 μg/mL) and 1 mM IPTG. Scale bar = 10 mm.

(C) Box-and-whisker plots depicting the size of the migrating colonies ($n = 10$) measured for wild-type (wt) *E. coli* MG1655 and *tol* and *pal* single-gene knockout mutants non-complemented (left section of the plot) or complemented (right section of the plot) with a plasmid encoding the individual *tol* and *pal* genes. The extent of the box encompasses the interquartile range (IQR) of the diameter (in mm) and the black line within each box represents the median. The upper whisker extends to the maximum data value, or 1.5 of the IQR, whichever is the smaller. The lower whisker extends to the maximum data value, or 1.5 of the IQR, whichever is the larger. Outliers are represented as open black circles. Statistical analysis was performed using two-way ANOVA followed by Tukey's multiple-comparison post-hoc test. Plots represent the combination of at least two independent experiments. NG, no growth. ns, non-significant; ***, $P < 0.001$ compared to the wild-type phenotype (on the left section of the

plot) or compared to wild-type cells containing the empty vector (on the right section of the plot that indicates the complementation experiment).

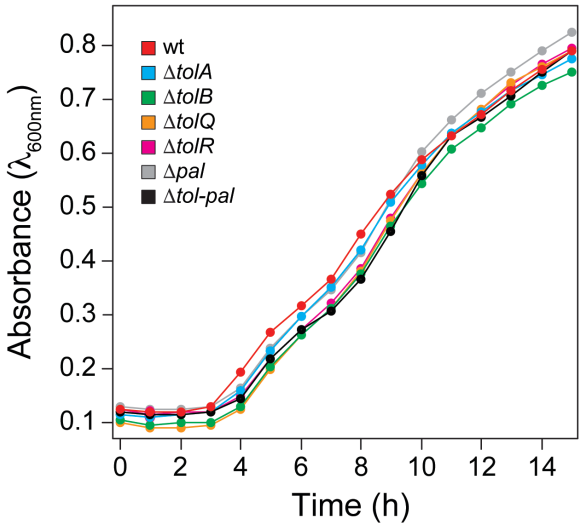

Figure S13. Growth curve of wild-type *E. coli* MG1655 and various mutants lacking components of the Tol-Pal complex.

The data points shown are the average from two independent experiments. Error bars were omitted for clarity. Cultures were grown in LB broth for 8 h at 37°C with agitation (200 r.p.m.) until an absorbance of 1.0 (λ = 600 nm) was reached. A 1-mL aliquot was harvested by centrifugation, washed once with 1× PBS (pH 7.4), and resuspended in 1× PBS (pH 7.4). An aliquot of ~1×10^5 c.f.u. was inoculated in 200 μL of fresh LB, the suspension was incubated at 37°C in a Tecan Infinite M1000 microplate reader (Tecan, Männedorf, Switzerland), and measurements were taken every hour for 15 h. wt, wild-type *E. coli* MG1655.

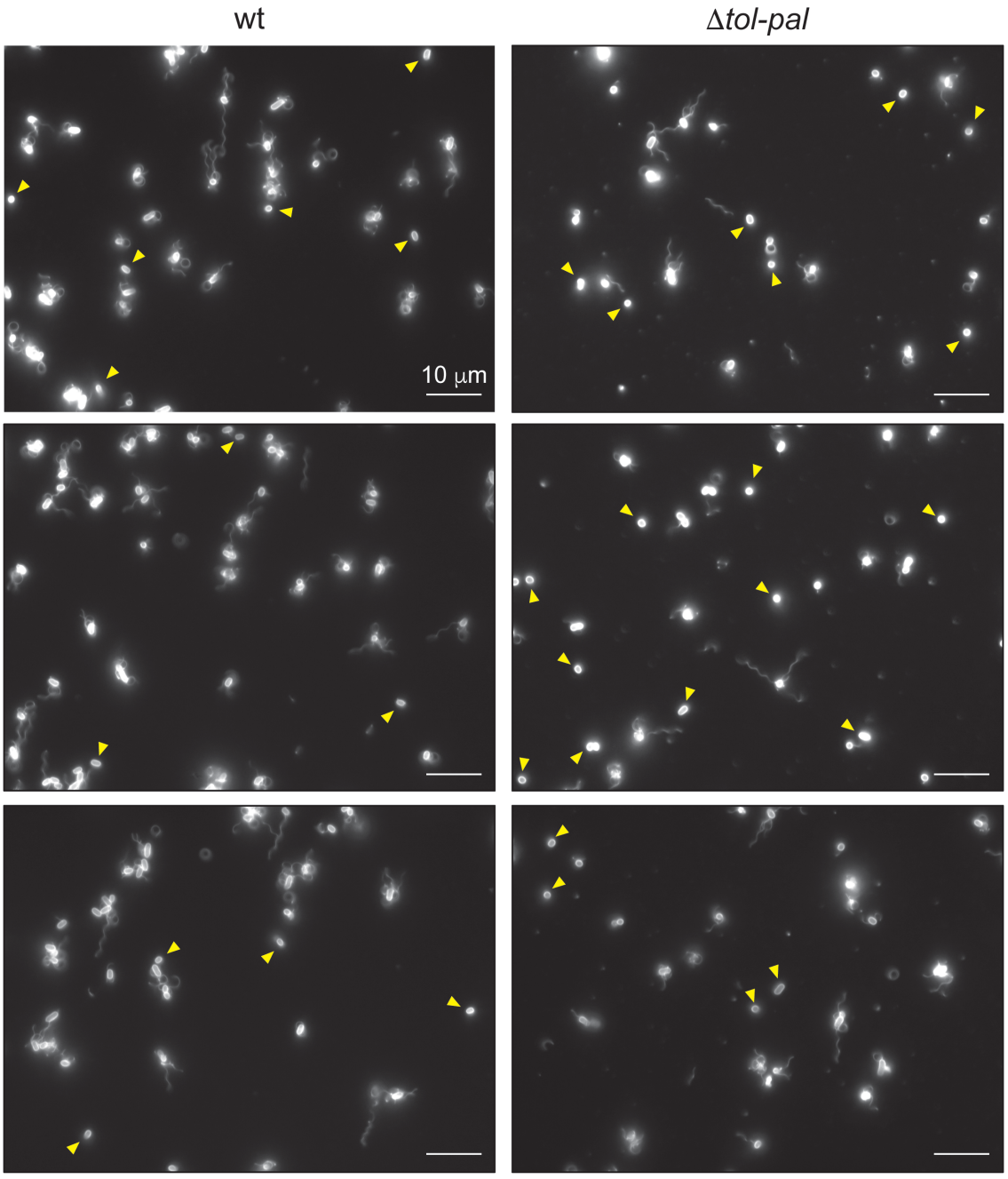

Figure S14. Flagella immunostaining of wild-type *E. coli* MG1655 and *E. coli* MG1655 Δ*tol-pal* cells.

Representative immunofluorescence images of wild-type (wt) *E. coli* MG1655 and *E. coli* MG1655 Δ*tol-pal* cells labeled with a polyclonal anti-FliC primary antibody and an Alexa Fluor 488-conjugated secondary antibody. The yellow arrowheads indicate cells lacking flagella. Scale bars = 10 μm.

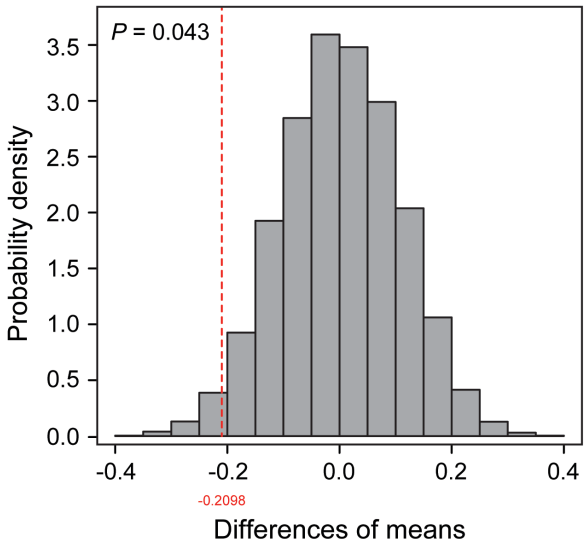

Figure S15. Histogram of the randomization distribution based on randomizing labels *E. coli* MG1655 and *E. coli* MG1655 Δ*tol-pal* for the reversal frequency experiment.

The vertical red line indicates the observed difference. We performed 10,000 simulations of differences of means using the R software (Version 3.0.1, R Development Core Team, 2005) to calculate the approximated *P* value (indicated on the top left side of the histogram).

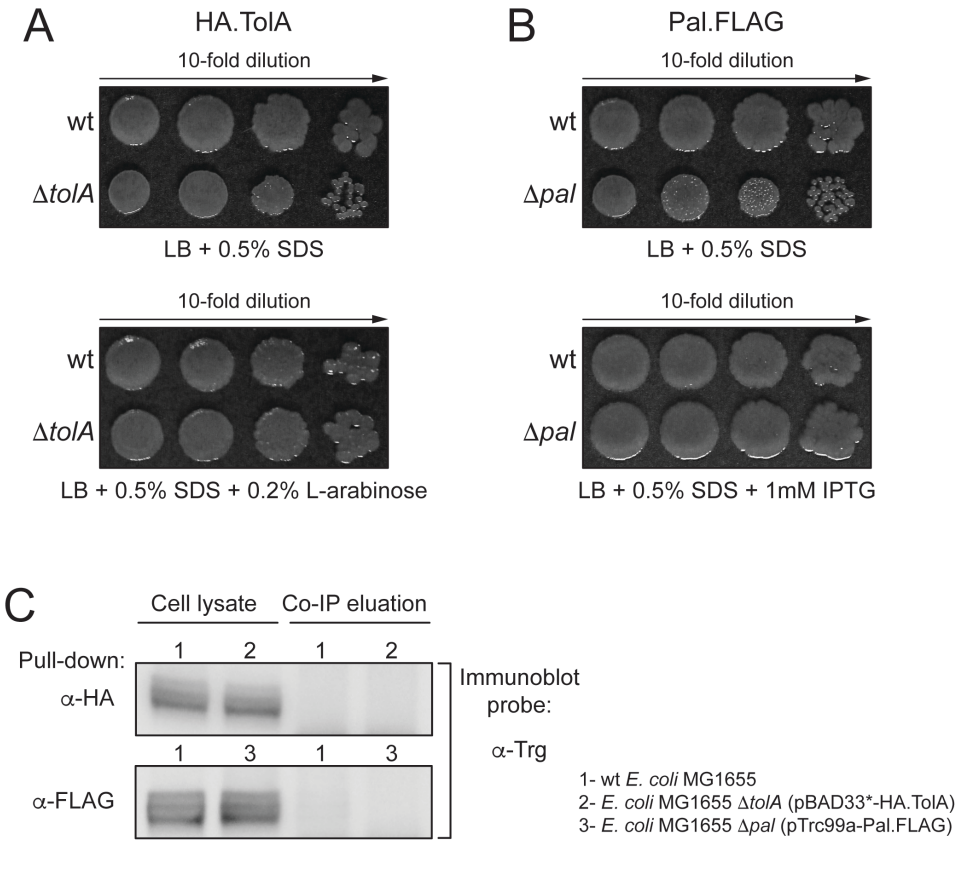

Figure S16. The Tol-Pal complex does not interact with HA-TolA or FLAG-Pal.

(A) Growth assay (serial dilutions; left to right) of wild-type (wt) *E. coli* MG1655 and *E. coli* MG1655 Δ*tolA*. Both the wild-type and the mutant strains contain a plasmid that encodes a functional HA-tagged TolA under the control of an arabinose-inducible promoter. Overexpression of HA-TolA suppresses the hypersensitive to detergent (0.5% SDS) in the mutant.

(B) Growth assay (serial dilutions; left to right) of wild-type (wt) *E. coli* MG1655 and the mutant strain *E. coli* MG1655 Δ*pal*. Both the wild-type and the mutant strains contain a plasmid that encodes a functional FLAG-tagged Pal under the control of a lactose-inducible promoter. Overexpression of FLAG-Pal suppresses the hypersensitive to detergent (0.5% SDS) in the mutant.

In panels A and B, aliquots of 10-fold serial dilutions (5 μL of dilutions 10^{-1}-10^{-5}; top to bottom) from normalized cultures initially calibrated to an absorbance of 1.0 (λ = 600 nm) and containing approximately 10^8 c.f.u./mL were spotted on control LB agar and in LB agar containing 0.5% SDS. The plates were incubated at 37°C for 24 h and then at 25°C for additional 72 h.

(C) In vivo co-immunoprecipitation of HA-TolA or FLAG-Pal with chemoreceptors in wild-type (wt) *E. coli* MG1655 and in the mutants *E. coli* MG1655 Δ*tolA* and *E. coli* MG1655 Δ*pal*. Western blots of whole-cell lysate and elution fraction of samples immunoprecipitated with anti-HA (α-HA) or anti-FLAG (α-FLAG) (indicated on the left) were probed with anti-Trg (α-Trg). The α-Trg is an antiserum raised to highly

purified *E. coli* Trg, but it also recognizes the other *E. coli* chemoreceptors (Tar, Tsr, and Tap) and related proteins in other bacteria [126].

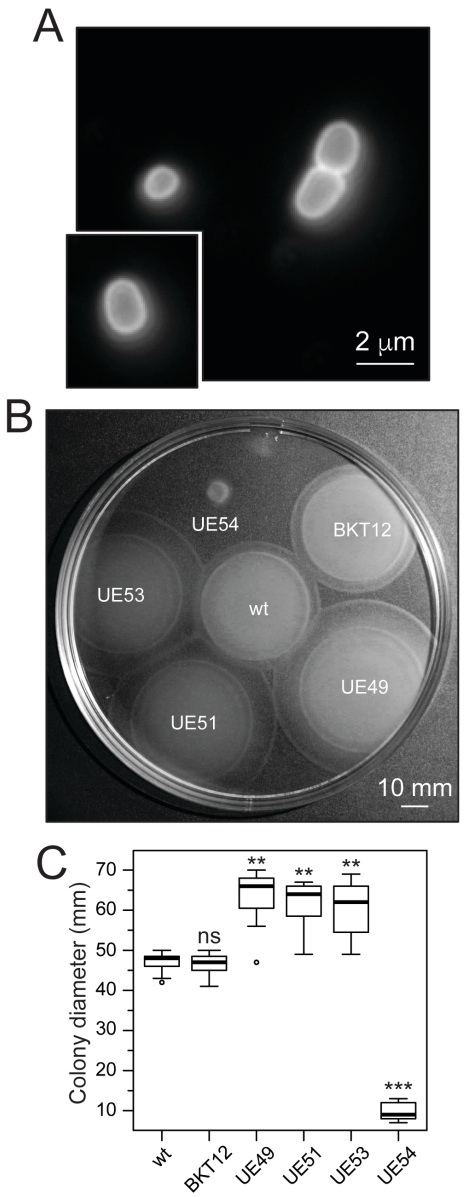

Figure S17. Swimming motility assay of wild-type *E. coli* MG1655 and various mutants.

(A) Representative immunofluorescence images of *E. coli* UE54 cells labeled with a polyclonal anti-FliC primary antibody and an Alexa Fluor 488-conjugated secondary antibody. Scale bar = 2 μm.

(B) Representative image of swimming colonies of wild-type (wt) *E. coli* MG1655, *E. coli* MG1655 BKT12 and various *E. coli* UE strains after 14.5 h of incubation at 30°C on swimming motility agar. Scale bar = 10 mm.

(C) Box-and-whisker plots depicting the size of the migrating colonies ($n = 20$) measured for wild-type (wt) *E. coli* MG1655, *E. coli* MG1655 BKT12, and various *E. coli* UE strains. The extent of the box encompasses the interquartile range (IQR) of the diameter (in mm) and the black line within each box represents the median. The upper whisker extends to the maximum data value, or 1.5 of the IQR, whichever is the smaller. The lower whisker extends to the maximum data value, or 1.5 of the IQR, whichever is the larger. Outliers are represented as open black circles. Statistical analysis was performed using two-way ANOVA followed by Tukey's multiple-comparison post-hoc test. ns, non-significant; **, $P < 0.01$; ***, $P < 0.001$ compared to the wild-type phenotype. Plots represent the combination of at least two independent experiments.

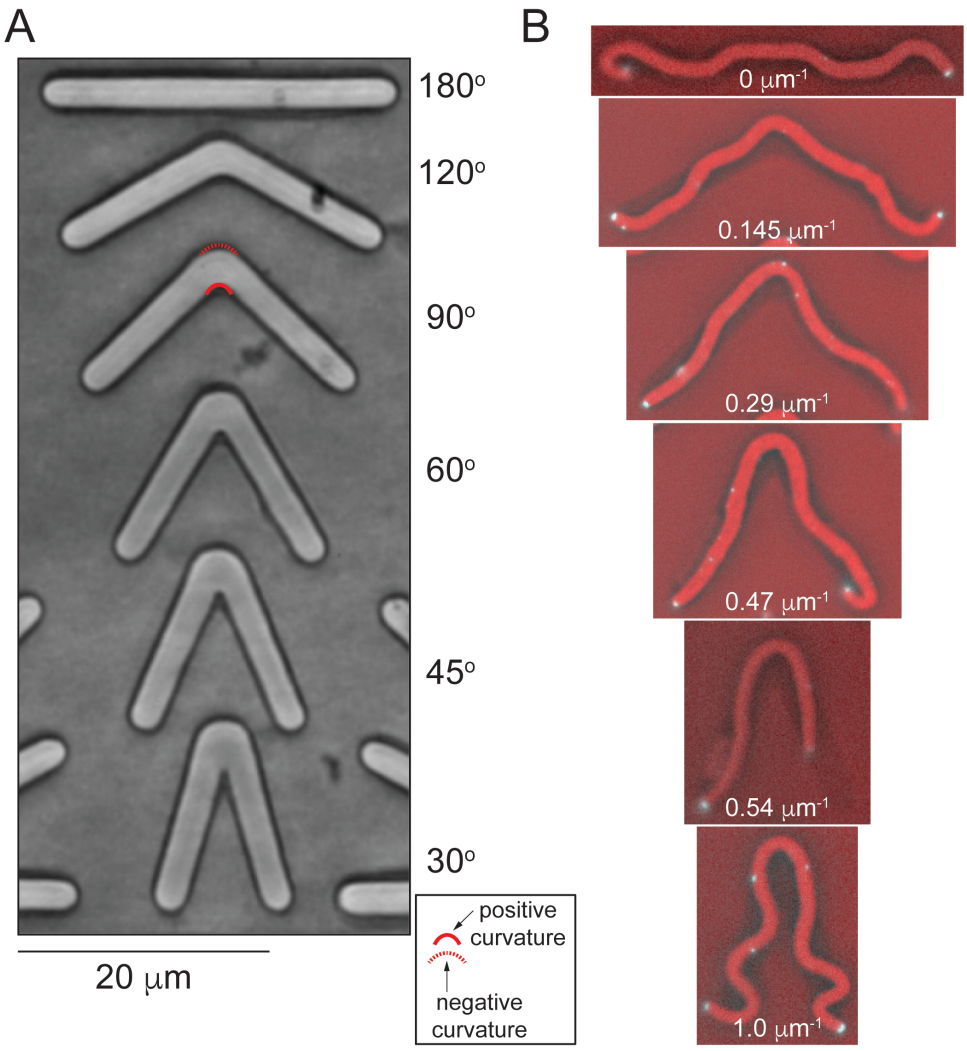

Figure S18. Subcellular localization of chemoreceptor clusters in filamented wild-type *E. coli* MG1655 with artificially manipulated cell wall curvature.

(A) Bight field image of the microchannel arrays consisting of six repetitive structures embossed in LB infused with 3% (w/w) agarose. The central angle correspondent to each microchannel is shown on the right. *Inset*: An image depicting the positive and negative regions of curvature imposed on the cell wall by the angled microchannels (an example is shown in the microchannel with a central angle of 90°). Scale bar = 20 μm.

(B) Representative fluorescence microscopy image depicting the localization pattern of YFP-CheR in filamented wild-type *E. coli* MG1655 cells that display a new region of cell wall curvature. Microscopy images are representative of three independent experiments.

Table S1. *E. coli* strains and plasmids used in this study.

Designation	Genotype or description	Source or reference
***E. coli* strains**		
DH5α	F$^-$ Δ*(argF-lac)169* ϕ80d*lacZ*(M15) Δ*phoA8 glnV44*(AS) λ^- *deoR481 rfbC1*? *gyrA96*(NalR) *recA1 endA1 thiE1 hsdR17*	CGSC #12384 [a]
BW25113	F$^-$ Δ(*araD-araB*)567 Δ*lacZ4787 (::rrnB)* λ^- *rph-1* Δ(*rhaD-rhaB*)568 *hsdR514*	CGSC #7636
JW0063	BW25113, Δ*araC771*::*kan*, Km^R	Keio collection [94]
JW0145	BW25113, Δ*mrcB765*::*kan*, Km^R	[94]
JW0192	BW25113, Δ*rcsF721*::*kan*, Km^R	[94]
JW0726	BW25113, Δ*ybgC785*::*kan*, Km^R	[94]
JW0727	BW25113, Δ*tolQ786*::*kan*, Km^R	[94]
JW0728	BW25113, Δ*tolR787*::*kan*, Km^R	[94]
JW0729	BW25113, Δ*tolA788*::*kan*, Km^R	[94]
JW0731	BW25113, Δ*pal-790*::*kan*, Km^R	[94]
JW0732	BW25113, Δ*ybgF720*::*kan*, Km^R	[94]
JW0940	BW25113, Δ*ompA772*::*kan*, Km^R	[94]
JW1667	BW25113, Δ*lpp-752*::*kan*, Km^R	[94]
JW5100	BW25113, Δ*tolB789*::*kan*, Km^R	[94]
JW5195	BW25113, Δ*tonB760*::*kan*, Km^R	[94]
JW5503	BW25113, Δ*tolC732*::*kan*, Km^R	[94]
MG1655	F$^-$ λ^- *rph-1*	CGSC #6300
MG1655 BKT12	MG1655, Δ*clsA*, Δ*clsB*, Δ*clsC*::*kan*, Km^R	Gift from Christian Raetz

MG1655 Δ*lpp*	MG1655, Δ*lpp-752*::*kan* [b], Km^R	This study
MG1655 Δ*tolA*	MG1655, Δ*tolA788*::*kan* [b], Km^R	This study
MG1655 Δ*tolB*	MG1655, Δ*tolB760*::*kan* [b], Km^R	This study
MG1655 Δ*tolQ*	MG1655, Δ*tolQ786*::*kan* [b], Km^R	This study
MG1655 Δ*tolR*	MG1655, Δ*tolR787*::*kan* [b], Km^R	This study
MG1655 Δ*pal*	MG1655, Δ*pal-790*::*kan* [b], Km^R	This study
MG1655 Δ*tol-pal*	MG1655, Δ*tolQ786* Δ*tolR787* Δ*tolA788* Δ*tolB760* Δ*pal-790*::*kan* [b], Km^R	This study
UE49	MG1655, *lpp-2*	Gift from Hiroshi Hara and Kouji Matsumoto
UE51	MG1655, *lpp-2*, Δ*ara174*	Gift from Hiroshi Hara and Kouji Matsumoto
UE53	MG1655, *lpp-2*, Δ*ara174*, *rcsF*::mini-Tn10, Cm^R	Gift from Hiroshi Hara and Kouji Matsumoto
UE54	MG1655, *lpp-2*, Δ*ara174*, *rcsF*::mini-Tn10, Δ*pgsA*::*kan*, Cm^R and Km^R	[88]
GL40	MG1655, *tnaA-GFP*::*frt*	[8]
GL40 Δ*tol-pal*	MG1655, *tnaA-GFP*::*frt*, Δ*tolQ786* Δ*tolR787* Δ*tolA788* Δ*tolB760* Δ*pal-790*::*kan* [b], Km^R	This study
RP8611	RP437, Δ*tsr-7028*, Δ*(tar-tap)5201*, Δ*trg-100*	[127]
Plasmids [c]		
pBAD33*	Cm^R, P_{ara} promoter, pBAD33 containing *araC*-C280* mutation [d]	[128]
pBAD33*-HA.tolA	Encodes an N-terminal, HA-tagged TolA regulated by an arabinose-inducible promoter	This study
pCern	Crb^K, P_{tac} promoter, a derivative of pBR322	Laboratory collection

pCern-tolA	Encodes TolA regulated by a lactose-inducible promoter	This study
pCern-tolQ	Encodes TolQ regulated by a lactose-inducible promoter	This study
pCern-tolR	Encodes TolR regulated by a lactose-inducible promoter	This study
pCern-pal	Encodes Pal regulated by a lactose-inducible promoter	This study
pCP20	Amp^R, Cm^R, temperature-conditional replicon expressing a thermal-induced Flp recombinase	[129]
P_{tet}-egfp	Amp^R, P_{tet} promoter, encodes EGFP regulated by a tetracycline-inducible promoter	[130]
pKD4	Amp^R, Km^R, FRT-*kan*-FRT cassette	[63]
pKD46	Amp^R, P_{ara} promoter, γ β *exo* (red recombinase), temperature-conditional replicon	[63]
pMC382	Amp^K, P_{ara} promoter, a derivative of pBAD24. Encodes an IcsA-GFP regulated by an arabinose-inducible promoter	[66]
pPA801	Cm^K, P_{ara} promoter, a derivative of pACYC184. Encodes YFP-CheW regulated by an arabinose-inducible promoter	[65]
pPA803	Amp^K, P_{tac} promoter, a derivative of pBR322. Encodes YFP-CheR regulated by a lactose-inducible promoter	[64]
pTrc99a	Amp^K, P_{trc} promoter, a derivative of pBR322	Amersham Pharmacia
pTrc99a-tolB	Encodes TolB regulated by a lactose-inducible promoter	This study

pTrc99a-pal.FLAG	Encodes a C-terminal FLAG-tagged Pal under regulation of a lactose-inducible promoter	This study
pTrc99a-tar.6×His	Encodes a C-terminus 6×His-tagged Tar under regulation of a lactose-inducible promoter	This study
pVS102	Cm^R, P_{ara} promoter, a derivative of pACYC184. Encodes YFP-CheR regulated by an arabinose-inducible promoter	[85]

[a] CGSC, Coli Genetic Stock Center, Yale University, New Haven, Connecticut.

[b] Allele numbers as indicated in the CGSC.

[c] Plasmids expressing genes in an operon are described using the convention "backbone-gene".

[d] The *araC*-C280* mutation enables more efficiently compatible co-induction of IPTG-inducible and arabinose-inducible promoter systems [128].

Abbreviation: Amp, ampicillin; Cm, chloramphenicol; Crb, carbenicillin; Km, kanamycin; R, resistance; frt, indicates the presence of the scar sequence "GAAGTTCCTATTCTCTAGAAAGTATAGGAACTTC" left after removal of the FRT-*kan*-FRT cassette.

Table S2. Primers used in this study.

Primer [a]	**Sequence (5′-3′)** [b]	**Reference**
k1	CAGTCATAGCCGAATAGCCT	[63]
k2	CGGTGCCCTGAATGAACTGC	[63]
kt	CGGCCACAGTCGATGAATCC	[63]
pyk-F	GGTACTGAGCAAAGGCGTTG	This study
ynhG-R	GTACATCGACCACTATCGGC	This study
ybgC-F	GAATGAAGCAGAGGTTCTGG	This study
tolR-R	GCGGATTATCGTTACTGCTC	This study
tolQ-F	GACTGCAATTGGTCTGTTTG	This study
tolA-R	CTTGCGCTGTTCATCAGAAC	This study
tolR-F	CGGTTGGTTTAATGACGCAG	This study
tolB-R	CAAATGCTACTCGTAATGCC	This study
tolA-F	GCCAGGCAGTATATGAAGTG	This study
pal-R	GCCCTTTCAGCACTTTGTTC	This study
tolB-F	CTACAGATGGGCGTTTCAAAG	This study
ybgF-R	GGCTGTGAGCATTAGAAATACG	This study
tolA-F-EcoRI	CCG**GAATTC*ATG***GTGTCAAAGGCAACCGAA	This study
tolA-R-BamHI	CGC**GGATCC***TTA*CGGTTTGAAGTCCAA	This study
tolB-F-EcoRI	CCG**GAATTC**AGGAGGA**CCCTCGAG*ATG***AAGCAGGCATTACGA	This study
tolB-R-XbaI	CTAG**TCTAGA***TCA*CAGATACGGCGACCA	This study
tolQ-F-EcoRI	CCG**GAATTC*ATG***GTGACTGACATGAATATC	This study
tolQ-R-BamHI	CGC**GGATCC***TTA*CCCCTTGTTGCTCTC	This study
tolR-F-EcoRI	CCG**GAATTC*ATG***GCCAGAGCGCGTGGA	This study
tolR-R-BamHI	CGC**GGATCC***TTA*GATAGGCTGCGTCAT	This study
pal-F-EcoRI	CCG**GAATTC*ATG***CAACTGAACAAAGTG	This study
pal-R-BamHI	CGC**GGATCC***TTA*GTAAACCAGTACCGC	This study

tolQdel-F	AAAATGAAGCCTCGTGCGCTTCCCAAGTCTATTGTCGCGGAGT TTAAGCAgtgtaggctggagctgcttc	This study
tolQdel-R	ATTTCGGACTTGAGATCGCGACGACCTCGTCCACGCGCTCTGG CCATGGCcatatgaatatcctccttag	This study
tolpaldel-F	TGAAGCCTCGTGCGCTTCCCAAGTCTATTGTCGCGGAGTTTAAG CAGTGAgtgtaggctggagctgcttc	This study
tolpaldel-F	AACGACAGACTCAATAGTTGATGTCTGAAGTTACTGCTCATGC AATTCTCcatatgaatatcctccttag	This study
palFLAG-F	CCG**GAATTC**AGGAAGGTGCCTT***ATG***CAACTGAACAAAGTGC	This study
palFLAG-R	CGC**GGATCC***TTA***CTTGTCGTCATCGTCTTTGTAGTC*acc*GTAAA CCAGTACCGC	This study
tar6×His-F	CCG**GAATTC**AGGAAGGTGCCTT***ATG***ATTAACCGTATCCGC	This study
tar6×His-R	CGC**GGATCC***TCA***ATGGTGATGGTGATGATG***acc*AAATGTTTCC CAGTTTGGATC	This study
HAtolA-F	CTAG**GAGCTC**AGGAAGGTGCCTT***ATG*TACCCATACGACGTCC CAGACTACGCT*ggt*GTGTCAAAGGCAACCGAA	This study
HAtolA-R	ACGC**GTCGAC***TTA*CGGTTTGAAGTCCAA	This study
pBAD33*-F	GTCACACTTTGCTATGCCATA	[128]
pBAD33*-R	CTGCGTTCTGATTTAATCTGT	[128]
pCern-F	AGGCTTTACACTTTATGC	This study
pCern-R	TGGTGCAGATGAACTTC	This study
pTrc99a-F	AGCGGATAACAATTTCACACAGG	This study
pTrc99a-R	GATTTAATCTGTATCAGG	This study

[a] Oligonucleotide primers were from Integrated DNA Technology, IDT (Coralville, IA). Primer names correspond to the gene that the primer amplifies, the forward (F) primer or the reverse (R) primer of that gene, and the restriction site incorporated into the primer sequence for cloning.

[b] The restriction sites used for cloning are in bold. Ribosomal binding sites (RBS) are underlined. Start codons are italicized in bold and underlined. Stop codons are italicized. Affinity tags are in bold and underlined. The priming sites of the plasmid pKD4, used as template during amplification of the FRT-*kan*-FRT cassette for gene displacement, are in lower case. A three-base linker sequence (bold lower case) was inserted between the affinity tag and the template-specific sequence to diminish any effect that the composite primer might have on the efficiency of the amplification.

REFERENCES

1. Alley MR, Maddock JR, Shapiro L. Polar localization of a bacterial chemoreceptor. *Genes Dev*. 1992; 6: 825-36.
2. Steinhauer J, Agha R, Pham T, Varga AW, Goldberg MB. The unipolar *Shigella* surface protein IcsA is targeted directly to the bacterial old pole: IcsP cleavage of IcsA occurs over the entire bacterial surface. *Mol Microbiol*. 1999; 32: 367-77.
3. Marston AL, Errington J. Dynamic movement of the ParA-like Soj protein of *B. subtilis* and its dual role in nucleoid organization and developmental regulation. *Mol Cell*. 1999; 4: 673-82.
4. Lam H, Schofield WB, Jacobs-Wagner C. A landmark protein essential for establishing and perpetuating the polarity of a bacterial cell. *Cell*. 2006; 124: 1011-23.
5. Lai EM, Nair U, Phadke ND, Maddock JR. Proteomic screening and identification of differentially distributed membrane proteins in *Escherichia coli*. *Mol Microbiol*. 2004; 52: 1029-44.
6. Kitagawa M, Ara T, Arifuzzaman M, Ioka-Nakamichi T, Inamoto E, Toyonaga H, et al. Complete set of ORF clones of *Escherichia coli* ASKA library (a complete set of *E. coli* K-12 ORF archive): Unique resources for biological research. *DNA Res*. 2005; 12: 291-9.
7. Werner JN, Chen EY, Guberman JM, Zippilli AR, Irgon JJ, Gitai Z. Quantitative genome-scale analysis of protein localization in an asymmetric bacterium. *Proc Natl Acad Sci U S A*. 2009; 106: 7858-63.
8. Li G, Young KD. Isolation and identification of new inner membrane-associated proteins that localize to cell poles in *Escherichia coli*. *Mol Microbiol*. 2012; 84: 276-95.
9. Maddock JR, Shapiro L. Polar location of the chemoreceptor complex in the *Escherichia coli* cell. *Science*. 1993; 259: 1717-23.
10. Bray D, Levin MD, Morton-Firth CJ. Receptor clustering as a cellular mechanism to control sensitivity. *Nature*. 1998; 393: 85-8.
11. Gestwicki JE, Kiessling LL. Inter-receptor communication through arrays of bacterial chemoreceptors. *Nature*. 2002; 415: 81-4.
12. Zhang P, Khursigara CM, Hartnell LM, Subramaniam S. Direct visualization of *Escherichia coli* chemotaxis receptor arrays using cryo-electron microscopy. *Proc Natl Acad Sci U S A*. 2007; 104: 3777-81.
13. Briegel A, Ding HJ, Li Z, Werner J, Gitai Z, Dias DP, et al. Location and architecture of the *Caulobacter crescentus* chemoreceptor array. *Mol Microbiol*. 2008; 69: 30-41.

14. Greenfield D, McEvoy AL, Shroff H, Crooks GE, Wingreen NS, Betzig E, et al. Self-organization of the *Escherichia coli* chemotaxis network imaged with super-resolution light microscopy. *PLoS Biol*. 2009; 7: e1000137.

15. Liu J, Hu B, Morado DR, Jani S, Manson MD, Margolin W. Molecular architecture of chemoreceptor arrays revealed by cryoelectron tomography of *Escherichia coli* minicells. *Proc Natl Acad Sci U S A*. 2012; 109: E1481-8.

16. Gestwicki JE, Lamanna AC, Harshey RM, McCarter LL, Kiessling LL, Adler J. Evolutionary conservation of methyl-accepting chemotaxis protein location in Bacteria and Archaea. *J Bacteriol*. 2000; 182: 6499-502.

17. Briegel A, Ortega DR, Tocheva EI, Wuichet K, Li Z, Chen S, et al. Universal architecture of bacterial chemoreceptor arrays. *Proc Natl Acad Sci U S A*. 2009; 106: 17181-6.

18. Briegel A, Li X, Bilwes AM, Hughes KT, Jensen GJ, Crane BR. Bacterial chemoreceptor arrays are hexagonally packed trimers of receptor dimers networked by rings of kinase and coupling proteins. *Proc Natl Acad Sci U S A*. 2012; 109: 3766-71.

19. Wadhams GH, Armitage JP. Making sense of it all: Bacterial chemotaxis. *Nat Rev Mol Cell Biol*. 2004; 5: 1024-37.

20. Hazelbauer GL, Falke JJ, Parkinson JS. Bacterial chemoreceptors: High-performance signaling in networked arrays. *Trends Biochem Sci*. 2008; 33: 9-19.

21. Sourjik V, Armitage JP. Spatial organization in bacterial chemotaxis. *EMBO J*. 2010; 29: 2724-33.

22. Porter SL, Wadhams GH, Armitage JP. Signal processing in complex chemotaxis pathways. *Nat Rev Microbiol*. 2011; 9: 153-65.

23. Lybarger SR, Maddock JR. Polarity in action: Asymmetric protein localization in bacteria. *J Bacteriol*. 2001; 183: 3261-7.

24. Shapiro L, McAdams HH, Losick R. Generating and exploiting polarity in bacteria. *Science*. 2002; 298: 1942-6.

25. Rudner DZ, Losick R. Protein subcellular localization in bacteria. *Cold Spring Harb Perspect Biol*. 2010; 2: a000307.

26. Skidmore JM, Ellefson DD, McNamara BP, Couto MM, Wolfe AJ, Maddock JR. Polar clustering of the chemoreceptor complex in *Escherichia coli* occurs in the absence of complete CheA function. *J Bacteriol*. 2000; 182: 967-73.

27. Shiomi D, Yoshimoto M, Homma M, Kawagishi I. Helical distribution of the bacterial chemoreceptor via colocalization with the Sec protein translocation machinery. *Mol Microbiol*. 2006; 60: 894-906.

28. Thiem S, Sourjik V. Stochastic assembly of chemoreceptor clusters in *Escherichia coli*. *Mol Microbiol*. 2008; 68: 1228-36.

29. Wang H, Wingreen NS, Mukhopadhyay R. Self-organized periodicity of protein clusters in growing bacteria. *Phys Rev Lett*. 2008; 101: 218101.

30. Gan L, Chen S, Jensen GJ. Molecular organization of Gram-negative peptidoglycan. *Proc Natl Acad Sci U S A*. 2008; 105: 18953-7.

31. Skareso JT, Ahmern BMM, Seachordll CL, Darveau RP, Postle K. Energy transduction between membranes. *J Biol Chem*. 1993; 268: 16302-8.

32. Braun V. Energy-coupled transport and signal transduction through the gram-negative outer membrane via TonB-ExbB-ExbD-dependent receptor proteins. *FEMS Microbiol Rev*. 1995; 16: 295-307.

33. Okuda S, Freinkman E, Kahne D. Cytoplasmic ATP hydrolysis powers transport of lipopolysaccharide across the periplasm in *E. coli*. *Science*. 2012; 338: 1214-7.

34. Bouveret E, Derouiche R, Rigal A, Lloubes R, Lazdunski C, Benedetti H. Peptidoglycan-associated lipoprotein-TolB interaction. A possible key to explaining the formation of contact sites between the inner and outer membranes of *Escherichia coli*. *J Biol Chem*. 1995; 270: 11071-7.

35. Bernadac A, Gavioli M, Lazzaroni JC, Raina S, Lloubes R. *Escherichia coli tol-pal* mutants form outer membrane vesicles. *J Bacteriol*. 1998; 180: 4872-8.

36. Lazzaroni JC, Germon P, Ray M-Cl, Vianney A. The Tol proteins of *Escherichia coli* and their involvement in the uptake of biomolecules and outer membrane stability. *FEMS Microbiology Letters*. 1999; 177: 191-7.

37. Lloubes R, Cascales E, Walburger A, Bouveret E, Lazdunski C, Bernadac A, et al. The Tol-Pal proteins of the *Escherichia coli* cell envelope: An energized system required for outer membrane integrity?. *Res Microbiol*. 2001; 152: 523-9.

38. Gerding MA, Ogata Y, Pecora ND, Niki H, de Boer PA. The trans-envelope Tol-Pal complex is part of the cell division machinery and required for proper outer-membrane invagination during cell constriction in *E. coli*. *Mol Microbiol*. 2007; 63: 1008-25.

39. Yeh YC, Comolli LR, Downing KH, Shapiro L, McAdams HH. The *Caulobacter* Tol-Pal complex is essential for outer membrane integrity and the positioning of a polar localization factor. *J Bacteriol*. 2010; 192: 4847-58.

40. Sturgis JN. Organisation and evolution of the *tol-pal* gene cluster. *J Mol Microbiol Biotechnol*. 2001; 3: 113-22.

41. Gaspar JA, Thomas JA, Marolda CL, Valvano MA. Surface expression of O-specific lipopolysaccharide in *Escherichia coli* requires the function of the TolA protein. *Mol Microbiol*. 2000; 38: 262-75.

42. Llamas MA, Rodriguez-Herva JJ, Hancock RE, Bitter W, Tommassen J, Ramos JL. Role of *Pseudomonas putida tol-oprL* gene products in uptake of solutes through the cytoplasmic membrane. *J Bacteriol*. 2003; 185: 4707-16.

43. Davies JK, Reeves P. Genetics of resistance to colicins in *Escherichia coli* K-12: Cross-resistance among colicins of group A. *J Bacteriol*. 1975; 123: 102-17.

44. Click EM, Webster RE. Filamentous phage infection: Required interactions with the TolA protein. *J Bacteriol*. 1997; 179: 6464-71.

45. Lazzaroni JC, Dubuisson JF, Vianney A. The Tol proteins of *Escherichia coli* and their involvement in the translocation of group A colicins. *Biochimie*. 2002; 84: 391-7.

46. Lahiri A, Ananthalakshmi TK, Nagarajan AG, Ray S, Chakravortty D. TolA mediates the differential detergent resistance pattern between the *Salmonella enterica* subsp. *enterica* serovars Typhi and Typhimurium. *Microbiology*. 2011; 157: 1402-15.

47. Vianney A, Lewin TM, Beyer WF, Jr., Lazzaroni JC, Portalier R, Webster RE. Membrane topology and mutational analysis of the TolQ protein of *Escherichia coli* required for the uptake of macromolecules and cell envelope integrity. *J Bacteriol*. 1994; 176: 822-9.

48. Derouiche R, Benedetti H, Lazzaroni JC, Lazdunski C, Lloubes R. Protein complex within *Escherichia coli* inner membrane. TolA N-terminal domain interacts with TolQ and TolR proteins. *J Biol Chem*. 1995; 270: 11078-84.

49. Cascales E, Lloubes R, Sturgis JN. The TolQ-TolR proteins energize TolA and share homologies with the flagellar motor proteins MotA-MotB. *Mol Microbiol*. 2001; 42: 795-807.

50. Levengood SK, Beyer WF, Jr., Webster RE. TolA: A membrane protein involved in colicin uptake contains an extended helical region. *Proc Natl Acad Sci U S A*. 1991; 88: 5939-43.

51. Kampfenkel K, Braun V. Membrane topologies of the TolQ and TolR proteins of *Escherichia coli*: Inactivation of TolQ by a missense mutation in the proposed first transmembrane segment. *J Bacteriol*. 1993; 175: 4485-91.

52. Muller MM, Vianney A, Lazzaroni JC, Webster RE, Portalier R. Membrane topology of the *Escherichia coli* TolR protein required for cell envelope integrity. *J Bacteriol*. 1993; 175: 6059-61.

53. Lazzaroni JC, Portalier R. The *excC* gene of *Escherichia coli* K-12 required for cell envelope integrity encodes the peptidoglycan-associated lipoprotein (PAL). *Mol Microbiol*. 1992; 6: 735-42.

54. Isnard M, Rigal A, Lazzaroni JC, Lazdunski C, Lloubes R. Maturation and localization of the TolB protein required for colicin import. *J Bacteriol*. 1994; 176: 6392-6.

55. Bouveret E, Benedetti H, Rigal A, Loret E, Lazdunski C. In vitro characterization of peptidoglycan-associated lipoprotein (PAL)-peptidoglycan and PAL-TolB interactions. *J Bacteriol*. 1999; 181: 6306-11.

56. Walburger A, Lazdunski C, Corda Y. The Tol/Pal system function requires an interaction between the C-terminal domain of TolA and the N-terminal domain of TolB. *Mol Microbiol*. 2002; 44: 695-708.

57. Dubuisson JF, Vianney A, Lazzaroni JC. Mutational analysis of the TolA C-terminal domain of *Escherichia coli* and genetic evidence for an interaction between TolA and TolB. *J Bacteriol*. 2002; 184: 4620-5.

58. Koebnik R. Proposal for a peptidoglycan-associating alpha-helical motif in the C-terminal regions of some bacterial cell-surface proteins. *Mol Microbiol*. 1995; 16: 1269-70.

59. Clavel T, Germon P, Vianney A, Portalier R, Lazzaroni JC. TolB protein of *Escherichia coli* K-12 interacts with the outer membrane peptidoglycan-associated proteins Pal, Lpp and OmpA. *Mol Microbiol*. 1998; 29: 359-67.

60. Ray MC, Germon P, Vianney A, Portalier R, Lazzaroni JC. Identification by genetic suppression of *Escherichia coli* TolB residues important for TolB-Pal interaction. *J Bacteriol*. 2000; 182: 821-4.

61. Derouiche R, Gavioli M, Benedetti H, Prilipov A, Lazdunski C, Lloubes R. TolA central domain interacts with *Escherichia coli* porins. *EMBO J*. 1996; 15: 6408-15.

62. Rigal A, Bouveret E, Lloubes R, Lazdunski C, Benedetti H. The TolB protein interacts with the porins of *Escherichia coli*. *J Bacteriol*. 1997; 179: 7274-9.

63. Datsenko KA, Wanner BL. One-step inactivation of chromosomal genes in *Escherichia coli* K-12 using PCR products. *Proc Natl Acad Sci U S A*. 2000; 97: 6640-5.

64. Zhou Q, Ames P, Parkinson JS. Biphasic control logic of HAMP domain signalling in the *Escherichia coli* serine chemoreceptor. *Mol Microbiol*. 2011; 80: 596-611.

65. Mowery P, Ostler JB, Parkinson JS. Different signaling roles of two conserved residues in the cytoplasmic hairpin tip of Tsr, the *Escherichia coli* serine chemoreceptor. *J Bacteriol*. 2008; 190: 8065-74.

66. Charles M, Perez M, Kobil JH, Goldberg MB. Polar targeting of *Shigella* virulence factor IcsA in Enterobacteriacae and *Vibrio*. *Proc Natl Acad Sci U S A*. 2001; 98: 9871-6.

67. Sliusarenko O, Heinritz J, Emonet T, Jacobs-Wagner C. High-throughput, subpixel precision analysis of bacterial morphogenesis and intracellular spatio-temporal dynamics. *Mol Microbiol*. 2011; 80: 612-27.

68. Copeland MF, Flickinger ST, Tuson HH, Weibel DB. Studying the dynamics of flagella in multicellular communities of *Escherichia coli* by using biarsenical dyes. *Appl Environ Microbiol*. 2010; 76: 1241-50.

69. Tuson HH, Copeland MF, Carey S, Sacotte R, Weibel DB. Flagellum density regulates *Proteus mirabilis* swarmer cell motility in viscous environments. *J Bacteriol*. 2013; 195: 368-77.

70. Turner L, Ryu WS, Berg HC. Real-time imaging of fluorescent flagellar filaments. *J Bacteriol*. 2000; 182: 2793-801.

71. Englert DL, Jayaraman A, Manson MD. Microfluidic techniques for the analysis of bacterial chemotaxis. *Methods Mol Biol*. 2009; 571: 1-23.

72. Renner LD, Eswaramoorthy P, Ramamurthi KS, Weibel DB. Studying biomolecule localization by engineering bacterial cell wall curvature. *PLoS One*. 2013; 8: e84143.

73. Takeuchi S, DiLuzio WR, Weibel DB, Whitesides GM. Controlling the shape of filamentous cells of *Escherichia coli*. *Nano Lett*. 2005; 5: 1819-23.

74. Weibel DB, Diluzio WR, Whitesides GM. Microfabrication meets microbiology. *Nat Rev Microbiol*. 2007; 5: 209-18.

75. Romantsov T, Helbig S, Culham DE, Gill C, Stalker L, Wood JM. Cardiolipin promotes polar localization of osmosensory transporter ProP in *Escherichia coli*. *Mol Microbiol*. 2007; 64: 1455-65.

76. Romantsov T, Stalker L, Culham DE, Wood JM. Cardiolipin controls the osmotic stress response and the subcellular location of transporter ProP in *Escherichia coli*. *J Biol Chem*. 2008; 283: 12314-23.

77. Renner LD, Weibel DB. Cardiolipin microdomains localize to negatively curved regions of *Escherichia coli* membranes. *Proc Natl Acad Sci U S A*. 2011; 108: 6264-9.

78. Renner LD, Weibel DB. MinD and MinE interact with anionic phospholipids and regulate division plane formation in *Escherichia coli*. *J Biol Chem*. 2012; 287: 38835-44.

79. Mileykovskaya E, Dowhan W. Visualization of phospholipid domains in *Escherichia coli* by using the cardiolipin-specific fluorescent dye 10-N-nonyl acridine orange. *J Bacteriol*. 2000; 182: 1172-5.

80. Koppelman CM, Den Blaauwen T, Duursma MC, Heeren RM, Nanninga N. *Escherichia coli* minicell membranes are enriched in cardiolipin. *J Bacteriol*. 2001; 183: 6144-7.

81. Paradies G, Paradies V, De Benedictis V, Ruggiero FM, Petrosillo G. Functional role of cardiolipin in mitochondrial bioenergetics. *Biochim Biophys Acta*. 2014; 1837: 408-17.

82. Gold VA, Robson A, Bao H, Romantsov T, Duong F, Collinson I. The action of cardiolipin on the bacterial translocon. *Proc Natl Acad Sci U S A*. 2010; 107: 10044-9.

83. Wu J, Li J, Li G, Long DG, Weis RM. The receptor binding site for the methyltransferase of bacterial chemotaxis is distinct from the sites of methylation. *Biochemistry*. 1996; 35: 4984-93.

84. Shiomi D, Zhulin IB, Homma M, Kawagishi I. Dual recognition of the bacterial chemoreceptor by chemotaxis-specific domains of the CheR methyltransferase. *J Biol Chem*. 2002; 277: 42325-33.

85. Kentner D, Thiem S, Hildenbeutel M, Sourjik V. Determinants of chemoreceptor cluster formation in *Escherichia coli*. *Mol Microbiol*. 2006; 61: 407-17.

86. Tan BK, Bogdanov M, Zhao J, Dowhan W, Raetz CR, Guan Z. Discovery of a cardiolipin synthase utilizing phosphatidylethanolamine and phosphatidylglycerol as substrates. *Proc Natl Acad Sci U S A*. 2012; 109: 16504-9.

87. Kikuchi S, Shibuya I, Matsumoto K. Viability of an *Escherichia coli pgsA* null mutant lacking detectable phosphatidylglycerol and cardiolipin. *J Bacteriol*. 2000; 182: 371-6.

88. Shiba Y, Yokoyama Y, Aono Y, Kiuchi T, Kusaka J, Matsumoto K, et al. Activation of the Rcs signal transduction system is responsible for the thermosensitive growth defect of an *Escherichia coli* mutant lacking phosphatidylglycerol and cardiolipin. *J Bacteriol*. 2004; 186: 6526-35.

89. Inouye M, Shaw J, Shen C. The assembly of a structural lipoprotein in the envelope of *Escherichia coli*. *J Biol Chem*. 1972; 247: 8154-9.

90. Braun V. Covalent lipoprotein from the outer membrane of *Escherichia coli*. *Biochim Biophys Acta*. 1975; 415: 335-77.

91. Cowles CE, Li Y, Semmelhack MF, Cristea IM, Silhavy TJ. The free and bound forms of Lpp occupy distinct subcellular locations in *Escherichia coli*. *Mol Microbiol*. 2011; 79: 1168-81.

92. Choi DS, Yamada H, Mizuno T, Mizushima S. Trimeric structure and localization of the major lipoprotein in the cell surface of *Escherichia coli*. *J Biol Chem*. 1986; 261: 8953-7.

93. Shu W, Liu J, Ji H, Lu M. Core structure of the outer membrane lipoprotein from *Escherichia coli* at 1.9 A resolution. *J Mol Biol*. 2000; 299: 1101-12.

94. Baba T, Ara T, Hasegawa M, Takai Y, Okumura Y, Baba M, et al. Construction of *Escherichia coli* K-12 in-frame, single-gene knockout mutants: The Keio collection. *Mol Syst Biol*. 2006; 2: 2006 0008.

95. Vianney A, Muller MM, Clavel T, Lazzaroni JC, Portalier R, Webster RE. Characterization of the tol-pal region of *Escherichia coli* K-12: Translational control of *tolR* expression by TolQ and identification of a new open reading frame downstream of *pal* encoding a periplasmic protein. *J Bacteriol*. 1996; 178: 4031-8.

96. Muller MM, Webster RE. Characterization of the *tol-pal* and *cyd* region of *Escherichia coli* K-12: Transcript analysis and identification of two new proteins encoded by the *cyd* operon. *J Bacteriol*. 1997; 179: 2077-80.

97. Gray AN, Egan AJ, Van't Veer IL, Verheul J, Colavin A, Koumoutsi A, et al. Coordination of peptidoglycan synthesis and outer membrane constriction during *Escherichia coli* cell division. *Elife*. 2015; 4: e07118.

98. Goldberg MB, Barzu O, Parsot C, Sansonetti PJ. Unipolar localization and ATPase activity of IcsA, a *Shigella flexneri* protein involved in intracellular movement. *J Bacteriol.* 1993; 175: 2189-96.

99. Mileykovskaya E, Fishov I, Fu X, Corbin BD, Margolin W, Dowhan W. Effects of phospholipid composition on MinD-membrane interactions in vitro and in vivo. *J Biol Chem*. 2003; 278: 22193-8.

100. Huang KC, Ramamurthi KS. Macromolecules that prefer their membranes curvy. *Mol Microbiol*. 2010; 76: 822-32.

101. Romantsov T, Battle AR, Hendel JL, Martinac B, Wood JM. Protein localization in *Escherichia coli* cells: Comparison of the cytoplasmic membrane proteins ProP, LacY, ProW, AqpZ, MscS, and MscL. *J Bacteriol*. 2010; 192: 912-24.

102. Kitchen JL, Li Z, Crooke E. Electrostatic interactions during acidic phospholipid reactivation of DnaA protein, the *Escherichia coli* initiator of chromosomal replication. *Biochemistry*. 1999; 38: 6213-21.

103. de Vrije T, de Swart RL, Dowhan W, Tommassen J, de Kruijff B. Phosphatidylglycerol is involved in protein translocation across *Escherichia coli* inner membranes. *Nature*. 1988; 334: 173-5.

104. Hendrick JP, Wickner W. SecA protein needs both acidic phospholipids and SecY/E protein for functional high-affinity binding to the *Escherichia coli* plasma membrane. *J Biol Chem*. 1991; 266: 24596-600.

105. Lill R, Dowhan W, Wickner W. The ATPase activity of SecA is regulated by acidic phospholipids, SecY, and the leader and mature domains of precursor proteins. *Cell*. 1990; 60: 271-80.

106. Matsumoto K. Dispensable nature of phosphatidylglycerol in *Escherichia coli*: Dual roles of anionic phospholipids. *Mol Microbiol*. 2001; 39: 1427-33.

107. Tomura A, Ishikawa T, Sagara Y, Miki T, Sekimizu K. Requirement of phosphatidylglycerol for flagellation of *Escherichia coli*. *FEBS Letters*. 1993; 329: 287-90.

108. Mizushima T, Koyanagi R, Suzuki E, Tomura A, Kutsukake K, Miki T, et al. Control by phosphatidylglycerol of expression of the *flhD* gene in *Escherichia coli*. *Biochim Biophys Acta*. 1995; 1245: 397-401.

109. Huang KC, Mukhopadhyay R, Wingreen NS. A curvature-mediated mechanism for localization of lipids to bacterial poles. *PLoS Comput Biol*. 2006; 2: e151.

110. Lenarcic R, Halbedel S, Visser L, Shaw M, Wu LJ, Errington J, et al. Localisation of DivIVA by targeting to negatively curved membranes. *EMBO J*. 2009; 28: 2272-82.

111. Ramamurthi KS, Losick R. Negative membrane curvature as a cue for subcellular localization of a bacterial protein. *Proc Natl Acad Sci U S A*. 2009; 106: 13541-5.

112. Ramamurthi KS, Lecuyer S, Stone HA, Losick R. Geometric cue for protein localization in a bacterium. *Science*. 2009; 323: 1354-7.

113. Strahl H, Ronneau S, Gonzalez BS, Klutsch D, Schaffner-Barbero C, Hamoen LW. Transmembrane protein sorting driven by membrane curvature. *Nat Commun*. 2015; 6: 8728.

114. Draper W, Liphardt J. Origins of chemoreceptor curvature sorting in *Escherichia coli*. *Nat Commun*. 2017; 8: 14838.

115. Bowman GR, Comolli LR, Zhu J, Eckart M, Koenig M, Downing KH, et al. A polymeric protein anchors the chromosomal origin/ParB complex at a bacterial cell pole. *Cell*. 2008; 134: 945-55.

116. Ebersbach G, Briegel A, Jensen GJ, Jacobs-Wagner C. A self-associating protein critical for chromosome attachment, division, and polar organization in *Caulobacter*. *Cell*. 2008; 134: 956-68.

117. Ringgaard S, Schirner K, Davis BM, Waldor MK. A family of ParA-like ATPases promotes cell pole maturation by facilitating polar localization of chemotaxis proteins. *Genes Dev*. 2011; 25: 1544-55.

118. Yamaichi Y, Bruckner R, Ringgaard S, Moll A, Cameron DE, Briegel A, et al. A multidomain hub anchors the chromosome segregation and chemotactic machinery to the bacterial pole. *Genes Dev*. 2012; 26: 2348-60.

119. Shimizu TS, Le Novere N, Levin MD, Beavil AJ, Sutton BJ, Bray D. Molecular model of a lattice of signalling proteins involved in bacterial chemotaxis. *Nat Cell Biol*. 2000; 2: 792-6.

120. Sourjik V, Berg HC. Receptor sensitivity in bacterial chemotaxis. *Proc Natl Acad Sci U S A*. 2002; 99: 123-7.

121. Thiem S, Kentner D, Sourjik V. Positioning of chemosensory clusters in *E. coli* and its relation to cell division. *EMBO J*. 2007; 26: 1615-23.

122. Chiu S-W, Roberts MAJ, Leake MC, Armitage JP. Positioning of chemosensory proteins and FtsZ through the *Rhodobacter sphaeroides* cell cycle. *Mol Microbiol*. 2013; 90: 322-37.

123. Neeli-Venkata R, Startceva S, Annila T, Ribeiro AS. Polar localization of the serine chemoreceptor of *Escherichia coli* is nucleoid exclusion-dependent. *Biophys J*. 2016; 111: 2512-22.

124. Lazzaroni JC, Vianney A, Popot JL, Benedetti H, Samatey F, Lazdunski C, et al. Transmembrane alpha-helix interactions are required for the functional assembly of the *Escherichia coli* Tol complex. *J Mol Biol*. 1995; 246: 1-7.

125. Germon P, Clavel T, Vianney A, Portalier R, Lazzaroni JC. Mutational analysis of the *Escherichia coli* K-12 TolA N-terminal region and characterization of its TolQ-interacting domain by genetic suppression. *J Bacteriol*. 1998; 180: 6433-9.

126. Morgan DG, Baumgartner JW, Hazelbauer GL. Proteins antigenically related to methyl-accepting chemotaxis proteins of *Escherichia coli* detected in a wide range of bacterial species. *J Bacteriol*. 1993; 175: 133-40.

127. Liu JD, Parkinson JS. Role of CheW protein in coupling membrane receptors to the intracellular signaling system of bacterial chemotaxis. *Proc Natl Acad Sci U S A*. 1989; 86: 8703-7.

128. Lee SK, Chou HH, Pfleger BF, Newman JD, Yoshikuni Y, Keasling JD. Directed evolution of AraC for improved compatibility of arabinose- and lactose-inducible promoters. *Appl Environ Microbiol*. 2007; 73: 5711-5.

129. Cherepanov PP, Wackernagel W. Gene disruption in *Escherichia coli*: TcR and KmR cassettes with the option of Flp-catalyzed excision of the antibiotic-resistance determinant. *Gene*. 1995; 158: 9-14.

130. Eun YJ, Utada AS, Copeland MF, Takeuchi S, Weibel DB. Encapsulating bacteria in agarose microparticles using microfluidics for high-throughput cell analysis and isolation. *ACS Chem Biol*. 2011; 6: 260-6.

CHAPTER 3

Small molecule chelators reveal that iron starvation inhibits late stages of bacterial cytokinesis

Adapted from:

Santos TMA, Lammers MG, Zhou M, Sparks IL, Rajendran M, Fang D, De Jesus CLY, Carneiro GFR, Cui Q, Weibel, D.B. (*Article submitted*).

TMAS designed and conducted experiments, analyzed data, and wrote the paper. MGL and MZ designed and conducted experiments, and analyzed data. ILS, MR, DF, CLYDJ, and GFRC conducted experiments and analyzed data. QC analyzed data. DBW designed experiments, analyzed data, and wrote the paper.

ABSTRACT

Bacterial cell division requires identification of the division site, assembly of the division machinery, and constriction of the cell envelope. These processes are regulated in response to several cellular and environmental signals. In this chapter, we use small molecule iron chelators to characterize the surprising connections between bacterial iron homeostasis and cell division. We demonstrate that iron starvation downregulates the transcription of genes encoding proteins involved in cell division, reduces protein biosynthesis, and prevents correct positioning of the division machinery at the division site. These combined events arrest the constriction of the mother and daughter cells during late stages of cytokinesis in a manner distinct from known mechanisms of inhibiting cell division. Overexpression of genes encoding late stage cell division proteins or iron transporters partially suppresses the biological activity of iron chelators and restores growth and division. We propose a model demonstrating the effect of iron availability on the regulatory mechanisms coordinating division in response to the nutritional state of the cell.

INTRODUCTION

In bacteria, with few exceptions, cell division initiates with the polymerization of the essential cell division protein FtsZ into a ring-like structure that locates at the division site and recruits other proteins to form a multiprotein complex called the "divisome" [1, 2]. Several mechanisms regulate the spatiotemporal assembly and function of the divisome in bacteria [3-6]; however, the molecular details underlying the coordination of these cell-cycle events are not completely understood. In addition to the systems controlling division in response to the developmental state of the cell, bacteria have evolved specific regulators that interact with components of the divisome and regulate division in response to external signals, such as nutrient availability [7-9], light (circadian rhythms) [10], and DNA damage [11-13]. The majority of these mechanisms involve protein-protein interactions [7, 9, 12-14] and target FtsZ or other components of the division machinery [12, 13].

Metal ions such as iron, zinc, and manganese, are essential in biological catalysis [15] and their absence alters bacterial cell physiology. Iron, for example, is a cofactor of many enzymes important for central metabolism, DNA biosynthesis, nitrogen fixation, photosynthesis, and respiration [16]. A single bacterial cell needs ~10^5-10^6 ferric ions to meet intracellular iron requirements [17]; thus, iron-poor environments pose a major challenge to survival. To thrive in these conditions, bacteria have developed sophisticated mechanisms to harvest extracellular iron, including using small molecule siderophores [18]. The classic ferric uptake regulator (Fur) and Fur-like proteins control the transcription of a large set of genes in response to iron availability [16, 19]. The role of iron in bacterial transcriptional regulation is complex and recent genome-wide

studies show that this regulatory network is still evolving [20, 21].

Iron homeostasis plays a central role in bacterial growth and survival [19-21]. Just as different cell stresses (e.g., nutrient starvation and DNA damage) have been shown to inhibit cell division until conditions become favorable, it is plausible that iron starvation may lead to a similar phenotype. However, there is currently no evidence connecting these two processes. In this chapter, we investigate the consequences of iron starvation on bacterial cell division using small molecule chelators. We demonstrate that divin [22], a synthetic small molecule identified in a high-throughput screen for inhibitors of bacterial division, is a potent intracellular chelator of iron that arrests late stages of cytokinesis by blocking the physical constriction in dividing cells. Iron starvation induced by chemically unrelated families of iron chelators recapitulates the division defects triggered by divin. We demonstrate that iron chelators downregulate the transcription of genes encoding proteins involved in cell division (predominantly, those that are late-stage), reduce protein biosynthesis, and affect the spatiotemporal localization of the division machinery. The combination of these cellular events arrests late stages of bacterial cell division, suggests that iron regulation and cell division are intertwined, and indicates that bacterial cytokinesis may include checkpoints akin to eukaryotic cell division.

EXPERIMENTAL PROCEDURES

Bacterial strains and growth conditions

Unless stated otherwise, *Escherichia coli* strains were routinely grown aerobically in M8 minimal medium (1× M8 salts [8.5 mM NaCl, 22 mM KH_2PO_4, and 48 mM

$Na_2HPO_4 \cdot 7H_2O$], supplemented with 2 mM $MgSO_4$, 0.4% [w/v] glucose, and 0.5% [w/v] casamino acids) or in M8 minimal medium containing 1.5% (w/v) agar at 37°C. *Caulobacter crescentus* strains were routinely grown aerobically in peptone-yeast extract (PYE) broth (0.2% [w/v] peptone, 0.1% [w/v] yeast extract, 0.8 mM $MgSO_4$, and 0.5 mM $CaCl_2$) or in PYE broth containing 1.5% (w/v) agar at 30°C. *Bacillus subtilis* 168 was routinely grown aerobically in Belitsky minimal medium (BMM) (8 mM $MgSO_4$, 27 mM KCl, 7 mM sodium citrate, 50 mM Tris-HCl (pH 7.5), 2 mM $CaCl_2$, 0.6 mM KH_2PO_4, 15 mM $(NH_4)_2SO_4$, 10 μM $MnSO_4$, 1 μM $FeSO_4$, 0.5% [w/v] glucose, 250 μM thymine, and 0.025% [w/v] of each of the 20 standard L-amino acids) at 37°C. *Streptococcus pyogenes* ATCC 12344 was routinely grown aerobically in brain-heart infusion (BHI) broth (BD Difco, Sparks, MD) at 37°C. We added ampicillin (50 μg/mL), chloramphenicol (25 μg/mL), kanamycin (30 μg/mL for *E. coli*; 5 μg/mL for *C. crescentus*), spectinomycin (25 μg/mL), or streptomycin (2.5 μg/mL) to the liquid growth medium or agar as needed. For some experiments, culture medium was treated with the transition-metal-chelating resin Chelex 100 (BioRad, Hercules, CA). Briefly, culture medium containing 5% (w/v) of Chelex 100 was incubated in a rotating platform for 1 h, centrifuged for 10 min at 1,000 *g* at 25°C, and filtered through a 0.20 μm filter. Bacterial strains and plasmids used in this study are listed in Table S1.

Chemicals

Reagents for culture medium were from Fisher Scientific (Itasca, IL) and Sigma-Aldrich (St. Louis, MO). All metals used in the experiments were from Sigma-Aldrich or Alfa Aesar (Reston, VA) and used without further purification (purity was >97%).

Chemicals tested in this study were: 1,10-phenanthroline (Sigma-Aldrich), 1b (5-ethyl-5'-phenyl-3'H-spiro[indoline-3,2'-[1,3,4]thiadiazol]-2-one [23]) (Sigma-Aldrich), 11c (N'-[(E)-(2-hydroxynaphthalen-1-yl)methylidene]-3-(5-chloro-2-methyl-1H-benzimidazol-1-yl)propanehydrazide [24]), 2,2'-bipyridine (bipy, Sigma-Aldrich), actinonin (Adipogen, San Diego, CA), deferasirox (Selleck Chemicals LLC, Houston, TX), deferiprone (Sigma-Aldrich), deferoxamine mesylate salt (Calbiochem, La Jolla, CA), divin (N'-[(E)-(2-hydroxynaphthalen-1-yl)methylidene]-3-(2-methyl- 1H-benzimidazol-1-yl)propanehydrazide [22, 24]), D-penicillamine (Alfa Aesar), DTPA (diethylenetriaminepentaacetic acid) (Sigma-Aldrich), EDTA (ethylenediaminetetraacetic acid) (Acros Organics, Morris Plains, NJ), NIH (2-hydroxyl-naphthylaldehyde benzoyl hydrazone) (Sigma-Aldrich), pyrogallol (Sigma-Aldrich), and TPEN (N,N,N',N'-tetrakis(2-pyridylmethyl)ethylenediamine) (Sigma-Aldrich). Stock solutions of these chemicals were prepared in DMSO or water.

Genetic methods

Standard procedures were used for genomic and plasmid DNA purification, restriction endonuclease digestion, DNA amplification, gene cloning, transformation, and mutagenesis. Genomic DNA from *E. coli* strains was isolated with the MasterPure™ DNA Purification Kit (Epicentre, Madison, WI) according to the manufacturer's instructions. Oligonucleotide primers were obtained from IDT (Coralville, IA) and restriction enzymes were from Promega (Madison, WI) or New England Biolabs (Ipswich, MA). We used Q5 High-Fidelity DNA Polymerase (New England Biolabs) to produce DNA for cloning, and GoTaq DNA polymerase (Promega) for general analytical PCR. Control reactions were tested side-by-side. Gene cloning

was performed using the In-Fusion HD Cloning Plus kit (Clontech Laboratories, Inc., Mountain View, CA). Plasmid constructs were purified using a QIAprep Miniprep Kit (Qiagen, Valencia, CA) and verified by PCR and DNA sequencing. We used electroporation or chemical methods to transform *E. coli* strains with plasmids. P1 phage transduction was used to transfer selectable genetic markers between *E. coli* strains. When necessary, we removed the cassette FRT-*kan*-FRT using plasmid pCP20 [25]. We verified chromosomal deletions and integrations by testing for the presence of antibiotic markers, PCR analysis, and DNA sequencing. All primers used in this study are listed in Table S2.

Metal ion screen

Cultures of *E. coli* BW25113 Δ*tolC* were grown overnight in M8 minimal medium for 12 h at 37°C with agitation (200 r.p.m.), diluted (1:100) in fresh medium, incubated at 37°C with agitation (200 r.p.m.), and calibrated to an absorbance of 1.0 (λ = 600 nm). Cultures of *C. crescentus* CB15N were grown in PYE broth for 24 h at 30°C with agitation (200 r.p.m.) and calibrated to an absorbance of 1.0 (λ = 600 nm). Calibrated cultures were diluted (1:10,000) in fresh media and used as inoculum in the metal screen. To identify metals that antagonize the inhibitory properties of divin, we inoculated a suspension of *E. coli* cells in 200 μL of M8 minimal medium containing 25 μM (2× MIC) divin and various concentrations of metals. We measured the initial absorbance (λ = 600 nm) of the *E. coli* cell suspensions at 25°C in a Tecan Infinite M1000 microplate reader (Tecan, Männedorf, Switzerland). The 96-well plate was incubated at 37°C with agitation (200 r.p.m.) and the final absorbance (λ = 600 nm) was measured after 16 h.

Control experiments to verify culture viability and the inhibitory effects of divin were performed in parallel. We calculated bacterial growth in each condition as a percentage relative to the growth of cells in medium containing the tested metal (100 μM, higher concentration tested) without divin. To study the antagonistic relationship between the metals of interest and divin, we inoculated a suspension of *E. coli* or *C. crescentus* cells in 200 μL of M8 minimal medium or PYE broth, respectively, containing various concentrations of divin and the following metals: $CoCl_2 \cdot 6H_2O$, $CuSO_4 \cdot 5H_2O$, $FeSO_4 \cdot 7H_2O$, or $FeCl_3 \cdot 6H_2O$. We measured the initial absorbance (λ = 600 nm) of the cell suspensions at 25°C, incubated the 96-well plate with agitation (200 r.p.m.), and measured the final absorbance (λ = 600 nm) after 16 h (at 37°C for *E. coli*) or 24 h (at 30°C for *C. crescentus*). We performed control experiments to verify culture viability and metal toxicity.

Growth curves

Cultures of *E. coli* BW25113 Δ*tolC* were grown overnight in M8 minimal medium for 12 h at 37°C with agitation (200 r.p.m.), diluted (1:100) in fresh medium, incubated at 37°C with agitation (200 r.p.m.), and calibrated to an absorbance of 1.0 (λ = 600 nm). Calibrated cultures were diluted (1:10,000) in fresh media and used as inoculum in the growth curve experiments. To study the time-dependent antagonistic effect of metals on divin-treated cells, we monitored bacterial growth of *E. coli* cells in M8 minimal medium containing 25 μM (2× MIC) of divin and various concentrations of $CoCl_2 \cdot 6H_2O$, $CuSO_4 \cdot 5H_2O$, $FeSO_4 \cdot 7H_2O$, or $FeCl_3 \cdot 6H_2O$. We monitored two different growth conditions. In the first condition, metals were added simultaneously with divin, cells

were incubated at 37°C in a microplate reader, and the absorbance (λ = 600 nm) was measured every 10 min for 16 h. In the second condition, divin was added to the culture, cells were incubated at 37°C in a microplate reader, and the absorbance (λ = 600 nm) was measured every 10 min for 16 h. Following the 16 h incubation time, we added metals to the culture, incubated cells at 37°C in a microplate reader, and measured the absorbance (λ = 600 nm) every 10 min for an additional 12 h. We performed similar experiments with the known iron chelator 2,2′-bipyridine (bipy).

Minimum inhibitory concentration (MIC) assays

We used the broth microdilution method according to the Clinical and Laboratory Standards Institute (CLSI) standard protocol. Briefly, *E. coli* strains, *C. crescentus* CB15N, and *B. subtilis* 168 were grown overnight for 12 h in M8 minimal medium, PYE broth, and BBM, respectively, at the appropriate temperature with agitation (200 r.p.m.), diluted (1:100) in fresh medium, and grown to mid-exponential phase. *S. pyogenes* ATCC 12344 was grown overnight for 16-18 h at 37°C in BHI broth in a static incubator. The cultures were calibrated to a final concentration of ~10^5 colony-forming unit (c.f.u.)/mL and 100-μL aliquots of the adjusted cultures were transferred to a 96-well plate. We transferred additional 100-μL aliquots of the adjusted culture to the top wells, added the drug to be tested and performed 2-fold serial dilutions. We incubated the plates for 16-18 h at 37°C with agitation (200 r.p.m.) for *E. coli* and *B. subtilis* 168, 24 h at 30°C with agitation (200 r.p.m.) for *C. crescentus*, and 16-18 h at 37°C for *S. pyogenes*. The MIC was defined as the lowest concentration of antimicrobial agent that produced no visible growth. We performed the assay in triplicates with, at least,

two biological replicates for each compound and strain combination. Control experiments to verify culture viability and sterility were performed in parallel. To study the synergistic effect of iron-depleted medium and divin, we also measured the MIC of divin against *E. coli* in Chelex-treated M8 minimal medium. After growing the cell culture to mid-exponential phase, we harvested the cells, discarded the supernatant, and resuspended the pellet in an equal volume of Chelex-treated M8 minimal medium prior to transferring to a 96-well plate.

Microscopy and image analysis.

To visualize the phenotypic alterations in bacterial cells treated with inhibitory concentrations of the tested compounds, cultures of *E. coli* BW25113 Δ*tolC* or *C. crescentus* CB15N were grown overnight in M8 minimal medium or PYE broth, respectively, for 12 h at 37°C with agitation (200 r.p.m.), diluted (1:100) in fresh M8 minimal medium, and incubated at 37°C with agitation (200 r.p.m.) to an absorbance of 0.1 (λ = 600 nm). *S. pyogenes* cultures were grown overnight for 12 h at 37°C in BHI broth, and calibrated to an absorbance of 0.1 (λ = 600 nm). We treated the cultures with DMSO or the test compounds, incubated the cultures at adequate conditions for different amount of time, and imaged the cells as described below.

To study the spatiotemporal localization of cell division proteins, we used *C. crescentus* strains containing functional, fluorescently labeled versions of cell division proteins. Cells were grown overnight in PYE broth, diluted (1:10) in fresh PYE broth, and incubated at 30°C with agitation (200 r.p.m.) to an absorbance of 0.1 (λ = 600 nm). We treated 2 mL aliquots of the culture with DMSO, 2× MIC of divin (25 μM), or bipy

(400 μM), and incubated the cells for 6 or 16 h at 30°C with agitation (200 r.p.m.).

To image cells, we added 4-μL aliquots of the culture on 2% (w/v) agarose pads prepared in 1× PBS buffer (137 mM NaCl, 2.7 mM KCl, 10 mM Na_2HPO_4, 1.76 mM KH_2PO_4, pH 7.4), for *E. coli* and *S. pyogenes*, or 1× M2 salts (6.1 mM Na_2HPO_4, 3.9 mM KH_2PO_4, 9.3 mM NH_4Cl, pH 7.0) for *C. crescentus* and imaged the cells at 25°C on an inverted Nikon Eclipse Ti microscope equipped with a Photometrics CoolSNAP HQ2 charge-coupled-device (CCD) camera (Photometrics, Tucson, AZ). Images were acquired using a 100× objective (Nikon Plan Apo 100×/1.40 oil Ph3 DM) and the Nikon Instruments Software (NIS)-Elements Advanced Research (AR) microscope imaging software program (Version 4.000.07) (Nikon Inc., Melville, NY). Data was collected on the CCD camera using an exposure time of 50 msec; for fluorescent images, we used an exposure time of 50 msec or 2 sec. In some cases, to visualize data, we overlaid phase contrast images and the corresponding fluorescence images and false-colored them using ImageJ (version 1.48); no further adjustments or other image processing was performed. To quantify cell length and study the localization of the labeled proteins, we created cell length profiles and fluorescence intensity profiles of cells using Oufti [26]. We verified automated cell detection by manual inspection.

Peptidoglycan labeling with fluorescent D-amino acids

C. crescentus CB15N cells were grown overnight in PYE broth, diluted (1:100) in 5 mL of fresh PYE broth, and incubated at 30°C with agitation (200 r.p.m.) to an absorbance of 0.1 (λ = 600 nm). We treated 1 mL aliquots of the cell culture with DMSO, 2× MIC (25 μM) of divin, or 2× MIC (400 μM) of bipy and incubated the cells for 6 or 16

h at 30°C with agitation (200 r.p.m.). Following the incubation time, we added 0.5 mM HADA (a fluorescent hydroxycoumarin derivative of D-alanine) [27] to the cultures and incubated the cells at 30°C with agitation (200 r.p.m.) for 10 min. To remove excess, unincorporated HADA, we washed the cells three times with 1 mL of 1× M2 salts at 25°C and resuspended the pellet in 1 mL of 1× M2 salts. We imaged the cells as described above and used Oufti [26] to measure the spatial localization of HADA incorporation.

Flow cytometry

Cultures of *E. coli* BW25113 Δ*tolC* were grown overnight in M8 minimal medium for 12 h at 37°C with agitation (200 r.p.m.), diluted (1:100) in fresh M8 minimal medium, and incubated at 37°C with agitation (200 r.p.m.) to an absorbance of 0.1 (λ = 600 nm). Cultures of *C. crescentus* CB15N were grown in PYE broth for 24 h at 30°C with agitation (200 r.p.m.), diluted (1:100) in fresh PYE medium, and incubated at 37°C with agitation (200 r.p.m.) to an absorbance of 0.1 (λ = 600 nm). An aliquot of 6 mL of each calibrated culture was treated with DMSO, deionized water, or 2× MIC of test compound. We incubated the cultures for 16 h at 37°C or 30°C with agitation (200 r.p.m.), harvested the cells by centrifugation for 5 min at 10,000 *g* at 25°C, and resuspended the pellet in 4 mL of 1× PBS. We labeled an aliquot of 1 mL of the cell suspension with FM4-64 (Thermo Fisher Scientific, Rockford, IL), PicoGreen (Thermo Fisher Scientific), or both dyes. We incubated the cell suspensions at 25°C in the dark for 30 min, harvested the cells by centrifugation for 5 min at 10,000 *g* at 25°C, discarded the supernatant, and resuspended the cell pellets in 1 mL of 1× PBS. Cells were kept on ice in the dark.

Cells in suspension were automatically imaged in flow using the ImageStream MkII Imaging Flow Cytometer (Amnis/EMD Millipore, Darmstat, Germany). We acquired images simultaneously in four channels corresponding to bright field (transmitted light), dark field (side scatter), the two channels of fluorescence [corresponding to FM4-64 (λ_{ex} = 515 nm, λ_{em} = 640 nm) and Picogreen (λ_{ex} = 480 nm, λ_{em} = 530 nm] using a 60× objective (Olympus, UPlanApo, 0.9 numeric aperture, 0.3 × 0.3 μm pixel size, 40 × 170 μm field of view, 600 cell/sec imaging rate). We ran single color controls for FM4-64 and Picogreen to correct for spectral overlap across channels. A compensation matrix was derived using the single-color controls acquired under the same experimental conditions as the treatments. We used IDEAS (EMD Millipore/Merck, Darmstadt, Germany) to analyze the cell size distribution and defined the gates based on the bright field and fluorescent images of each event. For our analysis, we used a gating strategy that favored events containing single cell.

Construction and monitoring of iron-responsive biosensors

We constructed transcriptional fusions of green fluorescent protein (GFP) to two Fur-regulated promoters of *E. coli* in the low-copy-number plasmid pUA66. The vector pUA66 used for construction of these iron-responsive biosensors contains the promoter-less reporter gene *gfp* mutant 2 derivative (*gfpmut2*), which encodes a variant of the green fluorescent protein GFP. Briefly, we amplified the promoter region containing the Fur-binding site (Fur box) of the genes *fepA* and *yncE* from *E. coli* MG1655 and cloned the fragments upstream of the *gfpmut2* gene. We transformed *E. coli* BW25113 Δ*tolC* and *E. coli* BW25113 Δ*tolC* Δ*fur* with the plasmids pUA66 (empty vector), pUA66-

P_{fepA}::*gfpmut2*, or pUA66-P_{yncE}::*gfpmut2*. To monitor the iron-starvation response in *E. coli* BW25113 Δ*tolC* and *E. coli* BW25113 Δ*tolC* Δ*fur*, cultures were grown overnight in M8 minimal medium for 12 h at 37°C with agitation (200 r.p.m.), diluted (1:100) in fresh M8 minimal medium, and incubated at 37°C with agitation (200 r.p.m.) to an absorbance of 0.4-0.5 (λ = 600 nm). Calibrated cultures were diluted (1:10,000) (~10^5 c.f.u./mL) in fresh M8 minimal medium and 200 μL of the cell suspension was treated with DMSO, 0.5× MIC (6.25 μM) of divin, 0.5× MIC (100 μM) of bipy, or 100 μM $FeSO_4$. We performed the experiment in a 96-well plate at 37°C. We measured the absorbance (λ = 600 nm) and the GFP fluorescence intensity (λ_{ex} = 475 nm, λ_{em} = 509 nm) of the cell suspensions every 20 min for 20 h in a Tecan Infinite M200Pro microplate reader (Tecan). Control experiments to verify culture viability and metal toxicity were performed in parallel. We analyzed the iron-starvation response in each treatment as a ratio of the GFP fluorescence intensity to the absorbance when the cells cultures reached an absorbance of 0.18 (λ = 600 nm).

Molecular modeling and binding affinity determinations

We computed the binding affinity of a hydrated metal ion to metal chelators (two copies of divin or three copies of bipy) using the approach used in previous studies [28, 29]. The structures of the relevant molecules were optimized using density functional theory [B3LYP [30, 31]] with the LANL2DZ effective core potential/basis set [32] for the metal and 6-31G(d) [33] on the other atoms. Energetics was further improved with single point calculations with the larger 6-311++G(2d,2p) [34] basis set on the main group elements. Enthalpic and entropic contributions were estimated with

vibrational frequency calculations and the rigid-rotor-harmonic-oscillator approximations under the condition of 300 K and 1 atm. Solvation free energies were calculated with the SMD solvation model [35]. All calculations are performed using Gaussian 09 (Gaussian 09, Revision E.01).

Precursor incorporation studies

Cultures of *E. coli* BW25113 Δ*tolC* and *B. subtilis* 168 were grown overnight in M8 minimal medium or BMM, respectively, for 16-20 h at 37°C with agitation (200 r.p.m.), diluted (1:10) in fresh medium, and incubated at 37°C with agitation (200 r.p.m.) to an absorbance of 0.1 (λ = 600 nm). An aliquot of 1 mL of cell suspension was labeled with 0.5 μCi [6-^{3}H]glucosamine D-hydrochloride (American Radiolabeled Chemicals, St. Louis, MO), [methyl-^{3}H]thymidine (Moravek Biochemicals, Brea, CA, USA), [5,6-^{3}H]uridine (Moravek Biochemicals), or [4,5-^{3}H]L-leucine (Moravek Biochemicals). After 1 min, we treated the labeled cultures with DMSO, 0.5× or 2× MIC of divin or bipy. Vancomycin (2× MIC, 400/0.39 μM for *E. coli*/*B. subtilis*), ciprofloxacin (2× MIC, 0.05/1.56 μM), rifampicin (16× MIC, 100 μM, for *E. coli* and 2× MIC, 1.56 μM, for *B. subtilis*), and chloramphenicol (2× MIC, 6.25/25 μM) served as reference antibiotics for inhibition of peptidoglycan, DNA, RNA, or protein biosynthesis, respectively. After 1h following treatment with DMSO, divin, or bipy, we transferred 0.2 mL of sample to microcentrifuge tubes containing 0.4 mL of cold 10% trichloroacetic acid (TCA), mixed thoroughly and placed the tubes at 4°C for 12 h. We washed the precipitated material with 0.2 mL of a solution of 5% TCA containing 1.5 M NaCl, followed by washing with 0.2 mL of 5% TCA. After the second wash, we solubilized the samples with 0.2 mL of a

solution of 0.1% SDS containing 0.1 M NaOH and vortexed. All centrifugation steps were performed at 10,000 *g* for 10 min at 25°C. The solubilized samples were transferred into scintillation vials and thoroughly mixed with 3 mL of Ultima-Flo AP scintillation cocktail (PerkinElmer, Waltham, MA, USA). Radioactivity was measured in counts/min using a Tri-Carb 2100TR liquid scintillation analyzer (Packard/PerkinElmer) and the results were expressed as percentage incorporation compared to the DMSO control.

Measurement of ATP levels

Cultures of *E. coli* BW25113 Δ*tolC* were grown overnight in M8 minimal medium for 12 h at 37°C with agitation (200 r.p.m.), diluted (1:100) in fresh M8 minimal medium, incubated at 37°C with agitation (200 r.p.m.), and calibrated to an absorbance of 0.1 (λ = 600 nm). An aliquot (200 μL) of the calibrated culture was treated with DMSO, 0.5× or 2× MIC of divin, bipy, or carbonyl cyanide *m*-chlorophenyl hydrazone (CCCP) and incubated for 1 h at 37°C with agitation (200 r.p.m.). Following incubation, we measured the absorbance (λ = 600 nm) of the cultures, added 100 μL of BacTiter-Glo (Promega) reagent to 100 μL of culture, incubated the mixture for 5 min at 25°C in a rotating platform, and measure luminescence using a Tecan Infinite M1000 microplate reader (Tecan). The relative luminescence was expressed as percentage compared to the DMSO control.

Target-multicopy suppression screen

We selected 79 genes encoding proteins involved in cell division, envelope biogenesis, and iron metabolism from a library of the *E. coli* K-12 derivative (*E. coli*

AG1) strains harboring a complete set of operational reading frames cloned in the multicopy plasmid vector pCA24N [25]. We grew cultures overnight in a 96-well plate in M8 minimal medium supplemented with chloramphenicol (20 μg/mL) for 12 h at 37°C with agitation (200 r.p.m.), diluted (1:10) in fresh M8 minimal medium supplemented with chloramphenicol (20 μg/mL), and incubated at 37°C with agitation (200 r.p.m.) to an approximate absorbance of 0.2 (λ = 600 nm). The cultures were treated with 100 μM IPTG and grown for 3 h at 37°C with agitation (200 r.p.m.). Following induction, we diluted the cultures (1:10) in 200 μL of fresh M8 minimal medium supplemented with chloramphenicol (20 μg/mL), 100 μM IPTG, 100 μM phenylalanine-arginine beta-naphthylamide (PAβN, an efflux pump inhibitor), and different concentrations of DMSO or divin. We measured the initial absorbance (λ = 600 nm) of the *E. coli* cell suspensions, incubated at 37°C with agitation (200 r.p.m.), and measured the absorbance (λ = 600 nm) after 24 and 48 h following treatment. We reported bacterial growth in each condition as a ratio relative to growth of the correspondent overexpression strain growing in the absence of divin.

Gene expression analysis

Cultures of *E. coli* BW25113 Δ*tolC* were grown overnight in M8 minimal medium for 12 h at 37°C with agitation (200 r.p.m.), diluted (1:20) in fresh M8 minimal medium, incubated for 2 h at 37°C with agitation (200 r.p.m.), and calibrated to an absorbance of 0.2-0.25 (λ = 600 nm). An aliquot (8 mL) of calibrated cultures was treated with 100 μM $FeSO_4$, 2× MIC (25 μM) of divin, or 2× MIC (400 μM) bipy and grown for 1 h at 37°C

with agitation (200 r.p.m.). We extracted RNA from four biological replicates for each treatment using TRI-Reagent (Zymo Research, Irvine, CA, USA) and Direct-zol (Zymo Research). Briefly, we harvested the cells, resuspended the pellets in 750 μL of TRI-Reagent (Zymo Research), incubated the samples for 5 min at 25ºC, added 200 μL of chloroform, and mixed the sample for 15 sec. Following 3 min of incubation at 25ºC, we centrifuged the sample for 15 min at 12,000 *g* at 4ºC, collected the upper aqueous phase, and proceeded to RNA purification using Direct-zol (Zymo Research). We measured the RNA concentration using a Nanodrop spectrophotometer and verified the RNA integrity by electrophoresis. We treated the samples with HL-dsDNase (ArcticZymes, Plymouth Meeting, USA) and performed analytical PCR with the samples to confirm the absence of DNA contamination in the RNA preparations. We only used RNA preparations that did not generate PCR fragments. ~1,500 ng of RNA was reverse-transcribed using the High Capacity RNA-to-cDNA Kit (Applied Biosystems/Thermo Fisher Scientific) and treated with RNase H (New England Biolabs), according to manufacturer's instructions. For qRT-PCR, we monitored amplification and measured the amount of amplification products for each sample in triplicate for each biological replicate in a reaction mixture of 10 μL [1× PowerUp SYBR Green Master Mix (Applied Biosystems/Thermo Fisher Scientific), 5 pmol of forward primer, 5 pmol of reverse primer, and ~10 ng of cDNA] using the Applied Biosystems (ABI) 7500 Real-Time PCR system (Applied Biosystems/Thermo Fisher Scientific). Real-time PCR was performed with an initial incubation of 2 min at 50°C, 2 min at 95°C, followed by 40 cycles of 15 sec at 95°C, and 1min at 60°C. Relative quantification of gene expression was calculated

using the comparative C_T method ($2^{-\Delta\Delta C_T}$ method) and we used expression of the reference gene *idnT* [36] as an endogenous control for normalization.

Statistical analysis

All statistical tests used in our analysis were two-sided and P values < 0.05 were considered significant. Statistical analyses were performed using the computing environment R (Version 3.2.0) (R Development Core Team, 2005). Refer to the figure legends for details about specific analysis performed for each experiment.

RESULTS

Divin arrests cytokinesis during late stages of bacterial cell division

We previously demonstrated that divin arrests late stages of bacterial cell division to create a unique phenotype not previously observed [22]. However, the mechanism of action of this small molecule was not characterized in detail. *E. coli* cells treated with divin (2× minimum inhibitory concentration [MIC], 25 μM) display a distinct morphological defect characterized by cytokinesis arrest after initial constriction at the division site (Figures 1A and 1B). Although the phenotype is apparent after 1-2 h, we chose to characterize it at later time points when it was more evident within a large population of cells. To quantify the effect of divin on cell division of different bacteria, we used imaging flow cytometry and microscopy. Analysis of *E. coli* cells treated with divin revealed two distinct populations of cells compared to the DMSO control (Figure 1C). ~43% of the bacterial cells have an aspect ratio and area similar to those of cells treated with DMSO (Figure 1C, *region I*). >35% of the cells have an average length (*L*) of

3.5 ± 0.7 μm (mean ± standard deviation) (Figure 1C, *region II and inset histogram*). To avoid artifacts from cell debris or aggregates, we used a more stringent gating strategy and manually inspected the data to favor single cells. A probability density histogram of the cell population treated with divin had a bimodal distribution (Figure 1D). The average cell length of the population treated with divin ($L = 2.9 \pm 0.8$ μm, $n = 3{,}553$ cells analyzed) is significantly higher ($P < 0.001$) than the average length of the DMSO-treated cells ($L = 2.0 \pm 0.6$ μm, $n = 4{,}216$). Importantly, cells treated with divin do not filament, which is a phenotype that commonly accompanies inhibition of cell division; e.g., antibiotics that inhibit cell division by blocking DNA replication (e.g., ciprofloxacin or nalidixic acid) or peptidoglycan biosynthesis (e.g., cephalexin) [37].

To confirm that divin-dependent cytokinetic arrest occurs in other bacterial species, we treated *C. crescentus* with divin (2× MIC = 25 μM) and performed time-course imaging (Figure 1E). The average length of cells after 12 h of treatment with DMSO was 2.4 ± 0.6 μm ($n = 961$) and the size range was 1.5-5.6 μm. Less than 3.5% of the total cells at each time point analyzed were ≥4 μm in length, which corresponds to the mean length of *C. crescentus* cells at division [38]. However, *C. crescentus* treated with divin became slightly elongated ~4 h following treatment ($L = 3.5 \pm 0.9$ μm, $n = 457$, $P < 0.001$ compared to the DMSO control) and 31% displayed arrested cell division. We continued to study cells at longer growth times to see what would happen to their morphology. After 6 h, >60% of the cells were two-cells long (i.e., ≥4 μm) and displayed the typical division arrest observed in *E. coli* cells treated with divin. The average length of cells 12 h following treatment was 5.1 ± 1.4 μm ($n = 624$) with a size range of 1.7-9.2 μm, confirming that cells treated with divin continue to grow slowly but do not

filament, as happens with most methods of blocking cell division. Similarly, flow cytometric analysis of *C. crescentus* cells treated with divin revealed morphological changes in the cell population when compared to DMSO-treated cells (Figure S1A). Divin is also active against Gram-positive bacteria, as cultures of *S. pyogenes* treated with DMSO contained long, bead-like chains of cocci with a homogeneous cell morphology, yet treatment with divin (2× MIC = 3.12 μM) resulted in short chains of cells with heterogeneous morphology and size (Figures S2A and S2B).

Insight into the mode of action of divin came from chemical structure searching, structure-activity relationship (SAR) studies, and whole genome sequencing of spontaneous mutants. A number of cell-permeable anti-cancer agents contain an arylhydrazone moiety that is reported to chelate iron [39-41]. Our previous SAR studies of divin demonstrated that the 2-hydroxynaphthalenyl hydrazide portion of the molecule is essential for its biological activity (Figure 1A) [24]. Whole genome sequencing of *C. crescentus* spontaneous mutants resistant to 1× MIC of divin revealed mutations mapping to the gene encoding the putative TonB-dependent hemin receptor (CC_2194), which is an outer membrane protein involved in iron uptake [42].

These observations led us to hypothesize that the bacteriostactic activity of divin and its role in inhibiting cytokinesis arises from its function as an iron chelator. This hypothesis leads to several testable predictions; the following sections test these predictions, describe data supporting the hypothesis, and include a model explaining how divin and other iron chelators arrest bacterial cytokinesis.

Iron, cobalt, and copper antagonize the biological activity of divin.

To verify the antagonistic effect of metal ions on the biological activity of divin,

we compared the growth of *E. coli* cells in medium containing divin and various concentrations of metals. Divin completely inhibited bacterial growth in all conditions tested, except when cobalt (100 μM), copper (100 μM), or iron (10 μM and 100 μM) was supplemented in the medium (Figure 2A). Cells treated with a mixture of divin and 100 μM of $CoCl_2$, $FeCl_3$, or $FeSO_4$ grew similarly to cells treated with DMSO. Addition of 100 μM of $CuSO_4$ partially antagonized the biological activity of divin, as the final absorbance of the culture reached ~40% of the absorbance measured for cells treated with DMSO.

We further measured the antagonist effect of $CoCl_2$, $CuSO_4$, $FeCl_3$, and $FeSO_4$ on divin by assessing the growth of *E. coli* cells in medium containing various concentrations of divin (Figure 2A, *inset heat map*). In the absence of metal ions, cell growth inhibition required >12.5 μM divin. An increase in the concentration of metals was necessary to rescue growth of cells in increasing concentrations of divin. A concentration of iron of 50 μM and higher was sufficient to support bacterial growth in the presence of 100 μM divin (8× MIC). We found similar results for cultures of *C. crescentus* (Figure S1B).

We confirmed the antagonistic effect of these specific metals in growth curve assays. As expected, only $CoCl_2$, $CuSO_4$, $FeCl_3$, and $FeSO_4$ antagonized the inhibitory activity of divin and enabled *E. coli* cells to grow in medium containing divin when the metal ions were added immediately following drug treatment (Figure S3A). Similarly, bacterial growth and division were rescued when cobalt, copper, or iron was added to the culture after cells had been treated with divin for 16 h (Figures S3B and S3C). These results suggest that divin chelates cobalt, copper, and iron ions preferentially.

Divin binds Fe^{3+} and triggers the iron starvation response in *E. coli*.

We used molecular modeling to predict the structure and binding affinities of different metal-divin complexes. Our model reveals two divin molecules complexed to Fe^{3+} through an octahedral geometry arising from three coordination sites on each ligand (Figure 2B). The coordination sites map to the 2-hydroxynaphthalenyl hydrazide region of divin, which is in agreement with our previous SAR studies [24]. The predicted binding affinity of divin for Fe^{3+} (ΔG = -35.7 kcal/mol) is preferred over binding to Fe^{2+} (-3.8 kcal/mol), Co^{2+} (-5.9 kcal/mol; octahedral coordination sphere), and Cu^{2+} (-9.5 kcal/mol; square planar configuration). As a point of comparison, we modeled the complexes of these metals bound to the known iron chelator bipy, which predicted three bipy molecules complexed to Fe^{2+}, Fe^{3+}, Co^{2+}, or Cu^{2+} in a conserved octahedral coordination sphere (Figure 2B). The models reveal that divin is more selective for binding to Fe^{3+} than to other metal ions (compared to bipy), making it a potentially more useful probe for studying iron starvation in bacteria.

The ferric uptake regulator (Fur) binds Fe^{2+} and controls iron homeostasis in *E. coli* and many other Gram-negative bacteria [16]. In *E. coli*, Fur regulates the iron-dependent expression of more than 90 genes [16, 19-21]. The classical view of Fur regulation in *E. coli* involves the binding of Fur-Fe^{2+} (holo-Fur) to the promoter region of Fur-regulated genes as a repressor. Iron-depleted conditions release repression by Fur and trigger the expression of genes involved in iron uptake. For example, the outer membrane ferric enterobactin receptor FepA is involved in the active transport of iron bound to enterobactin from the extracellular space into the periplasm and is transcriptionally repressed by Fur-Fe^{2+}.

To determine whether bacterial cells treated with divin display the phenotypic

hallmarks of the iron starvation response, we constructed iron-responsive biosensors using GFP-promoter fusions and measured time-dependent GFP levels after treatment with divin. *E. coli* cells harboring a plasmid in which the promoter region of the gene *fepA* regulates the expression of GFP (pUA66-P_{fepA}-*gfpmut2*) showed an increase (~105% increase compared to the DMSO control) in GFP expression when treated with divin (Figures 2C and 2D). Similarly, we observed an ~72% increase in GFP expression following treatment with the intracellular iron chelator bipy. Addition of 100 μM $FeSO_4$ caused an ~54% reduction in GFP expression compared to the control. The repression observed for cells harboring pUA66-P_{fepA}-*gfpmut2* and grown in medium supplemented with $FeSO_4$ was lost in *E. coli* Δ*fur* cells (Figures 2C and 2D), demonstrating that this system is Fur-regulated. We observed similar results for cultures harboring a plasmid (pUA66-P_{yncE}-*gfpmut2*) in which the promoter region of the Fur-regulated gene *yncE* controls GFP expression. (Figures S4A and S4B).

Other iron chelators arrest bacterial cell division similarly to divin.

We expected that cells treated with inhibitory concentrations of iron chelators that are structurally unrelated to divin would also arrest cell division. We tested this prediction by measuring the growth and morphological changes of *E. coli* cells in medium containing 2× MIC (400 μM) of bipy. *E. coli* cells treated with bipy displayed an identical phenotypic alteration observed in cells treated with divin (Figure 1). The average cell length of the bipy-treated *E. coli* cell population was significantly higher ($L = 2.7 \pm 0.8$ μm, $n = 2{,}777$, $P < 0.001$) than the average cell length of the DMSO treatment (Figure 1D). Bipy also causes cytokinetic arrest in *C. crescentus* cells ~4-6 h after drug

treatment. The average length of cells 12 h following treatment with bipy was 4.9 ± 1.4 μm (n = 747, $P < 0.001$ compared to DMSO control). After 6 h, ~66% of the cells were doublets (i.e., ≥4 μm) and displayed cytokinetic arrest (Figure 1E). Flow cytometric analysis of *C. crescentus* cells treated with bipy for 16 h showed a change in the aspect ratio and area of the cell population when compared to DMSO-treated cells (Figure S1A). Although bipy has been widely used as a metal chelator in bacterial studies [19-21], we were unable to find reports of its effect on cell morphology and division. Only $CoCl_2$, $CuSO_4$, $FeCl_3$, or $FeSO_4$ antagonized the bacteriostactic effect of bipy and enabled *E. coli* to grow (Figure S3D).

To verify whether the division defects we observed in cells treated with divin or bipy were also evident in cells dosed with other iron chelators, we determined the MIC of several well-characterized or putative chelators against *E. coli* cells (Figure S5A), treated cells with 2× MIC of compound, and analyzed the cell morphology. In general, the compounds we tested recapitulated the division defect observed for cells treated with divin or bipy (Figures S5B, S6A, and S6B), suggesting that iron chelators block bacterial cell division in a similar manner. The antagonistic effect of metals was not observed for other common antibiotics that target protein or peptidoglycan biosynthesis (Figure S7).

We reasoned that cells growing in iron-depleted medium—in the absence of small molecule chelators—would also display growth impairment and arrested cell division. To test this hypothesis, we grew *E. coli* in medium treated with Chelex, which is a chelating resin that binds transition metal ions—including copper, cobalt, and iron—with different affinities. *E. coli* grown in Chelex-treated medium reaches ~60% of the cell density of a culture grown in regular medium. Only the addition of $FeCl_3$ or

$FeSO_4$ restored growth completely in Chelex-treated medium (Figure S8A). These results demonstrate that iron depletion with Chelex is sufficient to partially inhibit growth in the absence of small molecule chelators.

To confirm that iron depletion by Chelex inhibits growth by the same mechanism as divin and other metal chelators, we imaged *E. coli* cells grown in Chelex-treated medium (Figures S8B and S8C). Compared to cells growing in untreated medium, cells growing in Chelex-treated medium were significantly longer and many cells displayed the characteristic arrest in cytokinesis observed when they are treated with chelators (Figure S8C); addition of 100 μM iron restored cell morphology and size. These results support the hypothesis that the biological activity of divin and its role in arresting cell division arise from disrupting iron homeostasis by chelating iron.

Iron deprivation affects general biosynthesis of macromolecules

Bacteria contain many iron-containing proteins that biosynthesize essential macromolecule precursors, including deoxyribonucleotides for DNA biosynthesis and isoprenoids involved in the biosynthesis of cell wall carbohydrate polymers (e.g., peptidoglycan and teichoic acids). To investigate the consequences iron starvation on the biosynthesis of macromolecules and establish a connection to arrested cell division, we measured the incorporation of radioactive precursors of peptidoglycan, DNA, RNA, and protein in *E. coli* following treatment with DMSO, divin, or bipy. Both divin and bipy blocked incorporation of all families of precursors within 1 h after treatment (Figure 3A), confirming the quick and pleiotropic effect of iron starvation on major biosynthetic processes. A large decrease (~90%) in incorporation of radiolabeled L-leucine following treatment with divin suggests that protein biosynthesis is extensively

inhibited. Divin reduced peptidoglycan and RNA biosynthesis by ~40%, and DNA biosynthesis by ~15%; we also observed reduction of these processes using sub-MIC concentrations of divin (Figures S9A and S9B). Similarly, treatment with bipy reduced incorporation of all four families of precursors (Figure S9B). To confirm a similar response in Gram-positive bacteria, we studied the biosynthesis of macromolecules in *B. subtilis* and found an ~35-50% reduction in precursor incorporation for all four processes following treatment with divin (Figure S9B).

We measured the ATP levels of *E. coli* cells to determine their metabolic activity and found a difference in ATP levels following 1 h of treatment with divin ($P = 0.04$) or bipy ($P = 0.03$) (Figure 3B); the small change observed (an ~5% reduction in the ATP levels in cells treated with either chelator) is unlikely to account for the division defect or the decrease in the incorporation of the 4 precursors that we observed. As a point of comparison, treatment of *E. coli* cells with carbonyl cyanide *m*-chlorophenyl hydrazone (CCCP)—a compound that disrupts transmembrane potential and reduces oxidative phosphorylation—caused an ~43% reduction in cellular ATP levels.

Iron deprivation inhibits divisome assembly and reduces peptidoglycan synthesis at the division site

The assembly of the bacterial divisome occurs in a sequential series of defined steps that requires multiple essential cytoplasmic, membrane, and periplasmic proteins [43, 44]. We hypothesized that the inhibition of cell division by divin may arise from the mislocalization of the divisome or several of its key components. To study the effects of iron starvation on divisome assembly, we observed the spatiotemporal localization of the division machinery in *C. crescentus* cells treated with DMSO, divin, or bipy for 6 h.

Although we observe division inhibition as early as 1 h after treatment with compound, we used 6 h for this experiment as it corresponds to the approximate time required to observe division arrest in > 60% of the cell population (Figure 1E). We used functional, fluorescently labeled versions of cell division proteins as a proxy for divisome localization, and a selection of proteins (ZapA, FzlA, FtsE, MurG, FtsN, FtsK, FtsI, FtsW) that are recruited to the incipient division site at different stages in the process [44]. Fluorescent fusions were located at the original loci on the chromosome under regulation of their native promoter.

Cells treated with DMSO displayed the characteristic localization pattern observed in other studies [44] in which fluorescent foci accumulated at the incipient division site prior to cell septation (Figures 4 and S10). With one exception (FtsE), cell division protein localization was significantly perturbed in cells treated with divin or bipy; in some cases (e.g., FzlA, MurG, and FtsW) the fluorescent signal became diffuse over time. After treating cells with the iron chelators, ZapA, FtsN, FtsK, and FtsI were enriched at the division site; however, there was a significant reduction in the fluorescent signal (Figure 4). These results demonstrate that iron chelators affect the assembly and localization of the divisome, providing an explanation for arrested cytokinesis.

We also analyzed the synthesis and remodeling of septal peptidoglycan following treatment with divin and bipy to determine whether it was inhibited and therefore the responsible factor for arresting cytokinesis. We studied synthesis of nascent peptidoglycan by in vivo pulse labeling using HADA (7-hydroxycoumarin-3-carboxylic acid-3-amino-D-alanine) [27]. *C. crescentus* cells treated with DMSO for 6 or 16 h displayed intense synthesis/remodeling of peptidoglycan at mid-cell in dividing

cells (Figure 5). HADA-labeling of peptidoglycan at the division site was reduced in cells treated with divin or bipy for 6 h and became diffuse after 16 h (Figure 5). The results indicate that peptidoglycan assembly is inhibited at the site of cell division.

Iron deprivation downregulates the expression of cell division proteins

We performed a small target-multicopy suppression screen to identify potential molecular targets of divin and understand the downstream consequences of iron deprivation on cell division. In this approach, the copy number of a protein target is increased, exceeds the toxicity of a compound, and suppresses growth inhibition. We selected 79 genes from a library of *E. coli* clones harboring a complete set of operational reading frames on a multicopy plasmid vector [25]; 24 of the selected genes encode proteins involved in cell division, cell-cycle regulation, or envelope biogenesis, and the remaining 55 genes encode proteins involved in iron metabolism (e.g., transcription factors and iron transporters) or iron-containing proteins. Overexpression of some genes from each group partially suppressed the biological activity of divin and enabled cell growth and division (Figure 6A). For example, overexpression of genes encoding "late" cell division proteins (e.g., FtsK, FtsQ, FtsL, FtsW) partially antagonized the inhibitory effect of divin. Of the genes involved in iron metabolism, overexpression of *fecA* (gene encoding the outer membrane component of the ferric dicitrate uptake system), *fecC* (gene encoding a permease component of the ferric dicitrate uptake system) and *fhuA* (gene encoding the outer membrane protein receptor for the ferric hydroxamate uptake system) supported bacterial growth and division.

Some iron chelators of the pyridoxal isonicotinoyl hydrazone class downregulate the expression of proteins that control cell-cycle progression in eukaryotes [41]. Because

the antagonistic effect of divin can be partially suppressed by individual overexpression of genes encoding some of the proteins involved in cell division, we hypothesized that divin could similarly affect expression of a set of bacterial genes encoding proteins necessary for cell division. We used quantitative reverse transcription PCR (qRT-PCR) to assess changes in transcription of *ftsZ*, *ftsQ*, and *ftsW* in *E. coli* cells grown under iron-replete and iron-depleted conditions. We observed small, but significant ($P < 0.05$), decrease in transcription of *ftsZ* (~2.5-fold), *ftsQ* (~2-fold decrease) and *ftsW* (~2-fold decrease) in cells treated with divin or bipy compared to cells grown in iron-replete conditions (Figure 6B). For further comparison, we measured the transcription of the iron-deprivation-induced genes *entC* and *fepA* [16, 45]. Both genes were highly transcribed (~20-fold increase) in cells treated with divin or bipy, suggesting that the decrease in RNA levels observed for the genes encoding cell division proteins is not the consequence of a general impact on transcription by sequestration of iron.

DISCUSSION

Bacterial cells adapt to environmental changes rapidly and have evolved multiple mechanisms to regulate cell division in response to environmental cues [46]. Using the small molecule iron chelator divin—and other structurally unrelated chelators—we demonstrate that perturbations in iron homeostasis directly affect the cell division regulatory network. Interesting, the outcome does not arise through a scenario in which one might anticipate cell metabolism grinding to a halt in the absence of iron; the result is much more nuanced and interesting. We found that depletion of iron arrests a very late stage in bacterial cell division by affecting the structure and

localization of a functional divisome.

Divin is selective for Co^{2+}, Cu^{2+}, Fe^{2+}/Fe^{3+} over abundant cellular alkali (Na^{+} and K^{+}), alkaline earth (Mg^{2+} and Ca^{2+}), and other biologically relevant metals (Mn^{2+}, Ni^{2+}, and Zn^{2+}). This observation corroborates previous findings that anticancer drugs containing an arylhydrazine moiety have a high affinity for Fe^{3+} in addition to a range of other metals [47]. Unable to solve a crystal structure of the divin-Fe^{3+} complex, we used molecular modeling to predict a 2:1 divin/iron (Fe^{2+} or Fe^{3+}) complex. In addition to chelating extracellular Fe^{3+}, evidence from other studies with salicylaldehyde isonicotinoyl hydrazone (SIH) supports internalization of divin into cells and chelation of intracellular iron [48]. Our experimental data show that divin depletes the bacterial iron pool and triggers the iron starvation response.

Iron homeostasis in bacteria is maintained through a balance of iron acquisition, storage, and incorporation into proteins as cofactors. These iron-containing proteins participate in a variety of metabolic and developmental processes [15, 16]. The transcription factor Fur regulates iron-dependent expression of numerous genes to maintain a precise concentration of the cytoplasmic levels of iron and prevent iron-induced toxicity. A recent reconstruction of the Fur regulatory network in *E. coli* shows that Fur may coordinate cellular processes beyond its canonical role in iron metabolism [20]. We envision a model in which divin and other iron chelators (e.g., bipy) deplete the intracellular iron pool, downregulate genes encoding proteins involved in cell division, block biosynthesis of the corresponding proteins, prevent assembly/localization of the complete divisome, and inhibit late stages of cell division (Figure 8). Our model posits a direct effect of iron starvation on the division machinery as opposed to indirect cellular effects propagated through general metabolic constraints

and energy depletion. As divisome assembly is a quasi-step-wise process and is dependent on the concentration and position of proteins, in principle, a reduction in the concentration of a single family of division proteins is sufficient to alter the position of other proteins or the divisome.

The direct effect of iron depletion on key regulators of the eukaryotic cell cycle involves multiple molecular targets, including ribonucleotide reductase, cyclins, and cyclin-dependent kinases (cdks) [41, 49]. Iron depletion in eukaryotic cells caused by chemically diverse iron chelators—including a compound containing an arylhydrazine (referred to as 311)—decreases the protein level of cyclins and cdks [41, 50, 51]. Treating eukaryotic cells with a complex consisting of compound 311 bound to iron prevented the negative effect of this small molecule on cyclin expression, supporting the connection between iron availability and expression of cell-cycle regulators [41]. Divin and bipy downregulate the transcription of cell division genes, while upregulating the transcription of genes involved in iron acquisition (Figure 7B), and reduce protein biosynthesis by ~90% in *E. coli* (Figure 3A), suggesting an analogous effect—to eukaryotes—of iron chelators on bacterial gene expression. Importantly, *E. coli* cells treated with protein biosynthesis inhibitors (e.g., chloramphenicol, tetracycline, kanamycin) [37] do not display the characteristic division defect observed in cells treated with iron chelators, suggesting that division arrest promoted by iron chelators does not arise from a general collapse in protein biosynthesis. Instead, our results support the presence of an iron-dependent checkpoint on bacterial division.

Cellular stress has an important role in regulating the bacterial cell cycle by influencing the assembly and activity of the divisome [46, 52]. Some types of metabolic stress, such as carbon starvation and prolonged cultivation in stationary phase have

been linked to a decrease in the level of FtsZ and consequent cell filamentation in *C. crescentus* [53, 54]. Similarly, controlled inactivation of the master cell-cycle regulator CtrA in *C. crescentus* during NaCl and ethanol stress conditions results in downregulation of the cell division genes *ftsA*, *ftsQ*, and *ftsW*, blocks cell division and causes cell filamentation [52]. We did not observe filamentation in cells treated with divin or bipy for < 12-16 h (Figures 1D and 1E), suggesting that the decrease in expression of cell division genes may be insufficient to trigger molecular events that activate filamentation or may avoid filamentation by design, in which division is inhibited and cell growth is reduced. Recent transcriptional network analysis in cyanobacteria indicates that the late cell division protein *ftsW* is downregulated under iron starvation conditions [55].

E. coli or *C. crescentus* cells incubated in medium supplemented with iron grow in the presence of concentrations of divin or bipy that would be inhibitory otherwise (Figures 2A, S1B, S3A, and S3B). We performed time-lapse experiments to explore how an increase in iron availability following long-term exposure to divin or bipy affects division in arrested cells. Surprisingly, we found a subpopulation of cells that is unable to resume growth and divide even after 2 h of recovery in iron-replete conditions (Figure S11). Interestingly, a subpopulation of cells starts dividing at a new site in the cell quartile and never complete constriction at the primary, arrested division site at mid-cell. These results suggest that the cellular damage caused by long-term iron deprivation may alter the division machinery and prevent its reactivation.

The antibacterial potential of small molecule iron chelators has been long acknowledged [56-58]; however, clinical applications of metal chelators are limited to the treatment of diseases that require removing metals from the body (e.g., iron

overload and heavy metal toxicity) [59]. We have previously demonstrated the antibacterial activity of divin and its chemical analogs against various clinical strains of pathogenic bacteria, including *Acinetobacter baumannii*, *Enterobacter aerogenes*, *Salmonella enterica* subsp. *enterica* serovar Typhimurium, *Shigella boydii*, and *Vibrio cholerae* [22, 24]. Iron is essential in a variety of biological processes in bacteria and, consequently, the activity of divin and other antimicrobial iron chelators arises from affecting multiple downstream targets. The ability of iron chelators to interfere with the activity of multiple cellular targets can reduce the frequency at which bacteria develop resistance; this point is supported by our challenge isolating divin-resistant strains of *E. coli* and *C. crescentus* through a variety of different approaches (e.g., through multiple passaging experiments). Recent studies have proposed the therapeutic use of metal chelators in combination with other drugs as an adjuvant to overcome antibiotic resistance [58, 60].

CONCLUSIONS

We demonstrate that divin and other structurally unrelated iron chelators perturb bacterial iron homeostasis and arrest late stages of cell division by preventing the formation of a functional divisome. The observation that cells that are able to engage in division become arrested at a specific point in the process (i.e., during late stages of cytokinesis) suggests the existence of iron-dependent cellular checkpoints in bacterial cell division. These studies provide insight into mechanisms by which iron homeostasis and cell division are coordinated in bacteria, and will guide future experiments testing whether disruption of iron homeostasis may be a viable target for development of new families of antibacterial agents.

ACKNOWLEDGEMENTS

We acknowledge materials from Erin Goley (*C. crescentus* EG120, EG123, EG383, EG384, EG645, EG648, EG652) and Martin Thanbichler (*C. crescentus* MT46). This research was supported by the National Institutes of Health (1DP2OD008735, D.B.W.; R01-GM106443, Q.C.), National Science Foundation (DMR-1121288, D.B.W.), and the Human Frontier Science Program (RGY0076/2013, D.B.W.). The flow cytometry instrumentation facility is supported by the University of Wisconsin Carbone Cancer Center Support (Grant P30 CA014520). T.M.A.S. thanks the Louis and Elsa Thomsen Wisconsin Distinguished Graduate Fellowship Award.

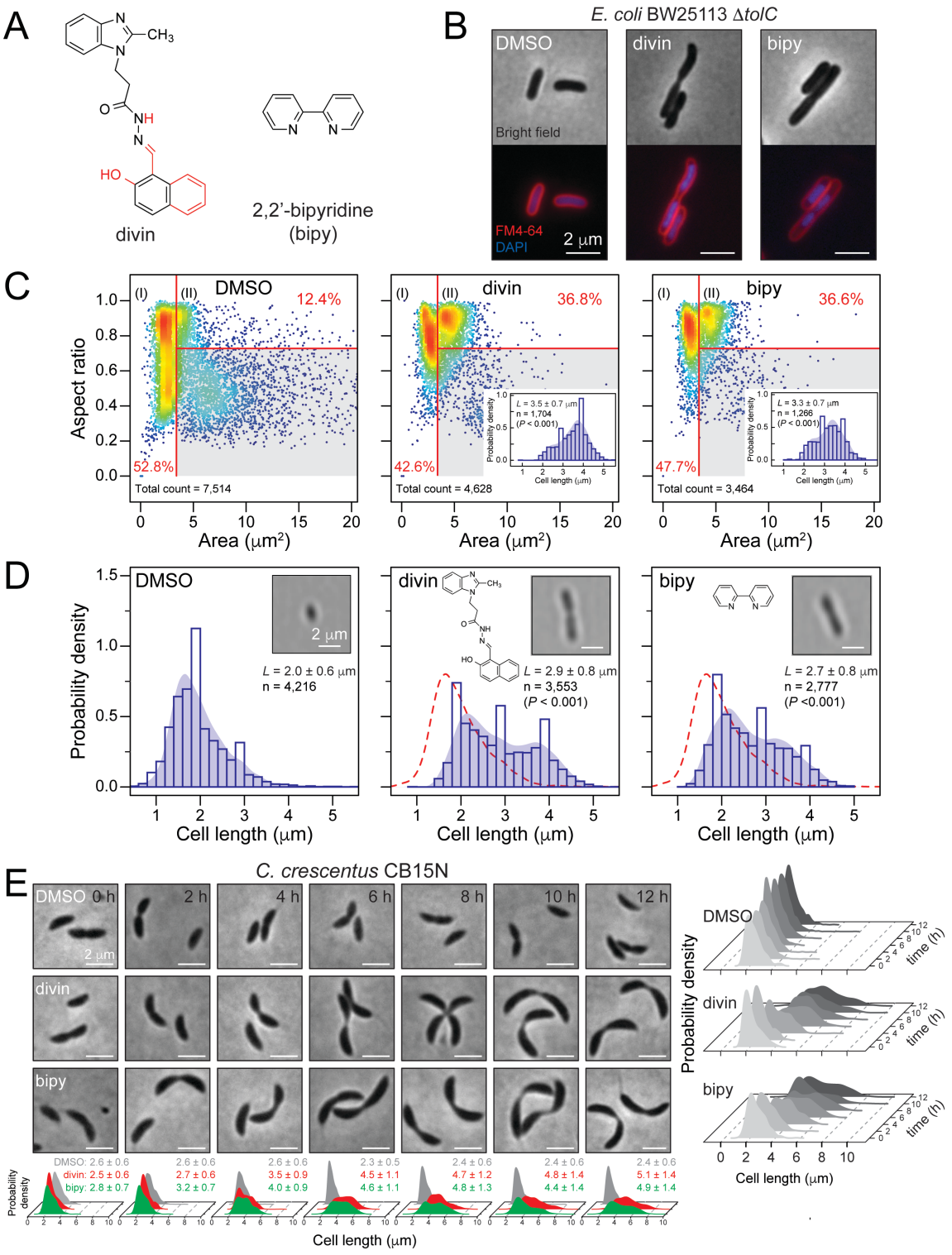

Figure 1. Divin and bipy inhibit late stages of bacterial cytokinesis.

(A) Chemical structure of divin and bipy. Regions highlighted in red are essential for the biological activity of divin [24].

(B) Representative bright field and fluorescence microscopy images of *E. coli* BW25113 Δ*tolC* treated with DMSO, 2× MIC of divin (25 μM) or bipy (400 μM) for 16h. The cell membrane was labeled with FM4-64 (false-colored in red) and the DNA was labeled with DAPI (false-colored in blue). Scale bars = 2 μm.

(C) Scatter plots displaying the area and aspect ratio of *E. coli* BW25113 Δ*tolC* treated with DMSO, 2× MIC of divin or bipy for 16 h. *Inset*: Probability density histograms of the cell length distribution of the population gated in region II.

(D) Probability density histograms of the cell length distribution of *E. coli* BW25113 Δ*tolC* treated with DMSO, 2× MIC of divin or bipy for 16 h. Red dashed line represents the kernel density estimation (KDE) of the cell length distribution of the DMSO-treated population. The images were automatically obtained in flow using the ImageStream MkII Imaging Flow Cytometer. Scale bars = 2 μm.

In panels C and D, shaded blue area overlaying the histogram corresponds to the KDE of cell length distribution. Average cell length (L) is given with standard deviations for a total of n cells. Statistical analysis was performed using a Kruskal-Wallis test followed by Dunn's post-hoc test.

(E) Time-course experiments showing the morphological changes and the KDE of cell length distribution of *C. crescentus* CB15N treated with DMSO, 2× MIC of divin (25 μM) or bipy (400 μM). Average cell length (*L*) is given with standard deviations for a total of *n* cells. Scale bars = 2 μm.

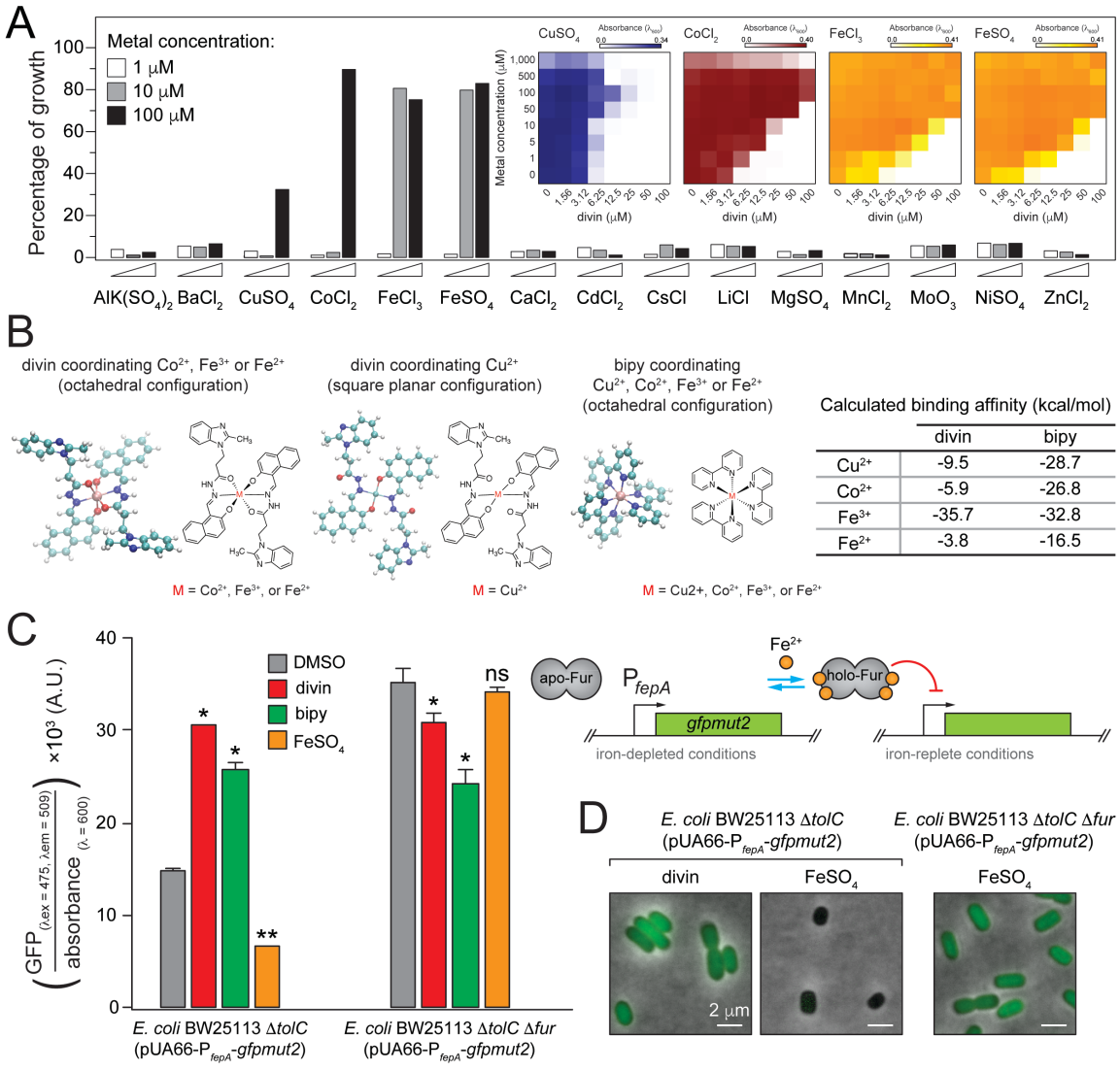

Figure 2. Divin binds iron with high affinity and triggers the iron-starvation response in bacteria.

(A) Growth of *E. coli* BW25113 Δ*tolC* in the presence of 2× MIC (25 μM) of divin and various metals. Bars show the percentage of growth compared to cells treated with DMSO and the highest concentration of the respective metal. *Inset*: Checkerboard growth assays of the effect of cobalt, copper, and iron in combination with divin on the growth of *E. coli* BW25113 Δ*tolC*. Dark colored squares to white squares represent full growth and complete growth inhibition, respectively. Analyses represent the combination of two independent experiments.

(B) Optimized structures and calculated binding affinity of divin and bipy complexed with copper, cobalt, or iron.

(C) Ratio of GFP fluorescence intensity and absorbance of *E. coli* BW25113 Δ*tolC* and *E. coli* BW25113 Δ*tolC* Δ*fur* harboring the plasmid pUA66-P_{fepA}-*gfpmut2* following culturing in M8 minimal medium supplemented with DMSO, divin (6.25 μM), bipy (100 μM), or $FeSO_4$ (100 μM). Analyses are the average of two independent experiments. Error bars indicate the standard deviation. *Inset*: A cartoon depicting the classical view of Fur regulation in *E. coli* (summarized in the text). We performed one-sample Student's t-tests to test the null hypothesis that the GFP fluorescence intensity mean is equal to 100 (the normalized signal for the DMSO control). ns, non-significant; *, $P < 0.05$; **, $P < 0.01$ compared to the DMSO control treatment.

(D) Representative microscopy images of *E. coli* BW25113 Δ*tolC* and *E. coli* BW25113 Δ*tolC* Δ*fur* harboring the plasmid pUA66-P_{fepA}-*gfpmut2* and treated with divin (6.25 μM)

or $FeSO_4$ (100 μM) for 20 h. Scale bars = 2 μm.

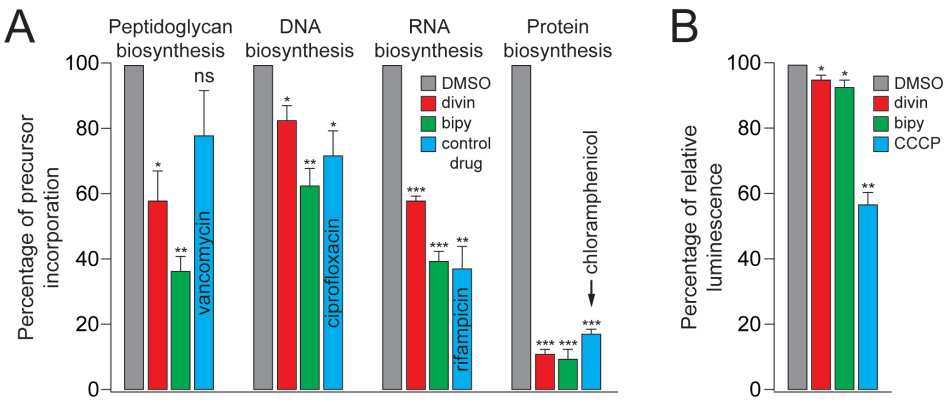

Figure 3. Iron deprivation affects biosynthesis of macromolecules and metabolic activity in bacteria.

(A) Incorporation of ^{3}H-glucosamine (peptidoglycan), ^{3}H-thymidine (DNA), ^{3}H-uridine (RNA), or ^{3}H-leucine (protein) in *E. coli* BW25113 Δ*tolC* treated with DMSO, 2× MIC of divin (25 μM), bipy (400 μM), or control drugs.

(B) Measurement of ATP level in *E. coli* BW25113 Δ*tolC* treated with 2× MIC of divin or bipy. Carbonyl cyanide *m*-chlorophenyl hydrazone CCCP (2× MIC, 25 μM) was used as a control drug.

In panels A and B, analyses are the average of three independent experiments. Error bars indicate the standard deviation. Results are expressed as percentage compared to the DMSO control. We performed one-sample Student's t-tests to test the null hypothesis that the tritium-labeled metabolic precursor incorporation or the ATP level mean is equal to 100. ns, non-significant; *, $P < 0.05$; **, $P < 0.01$; ***, $P < 0.001$ compared to the DMSO control.

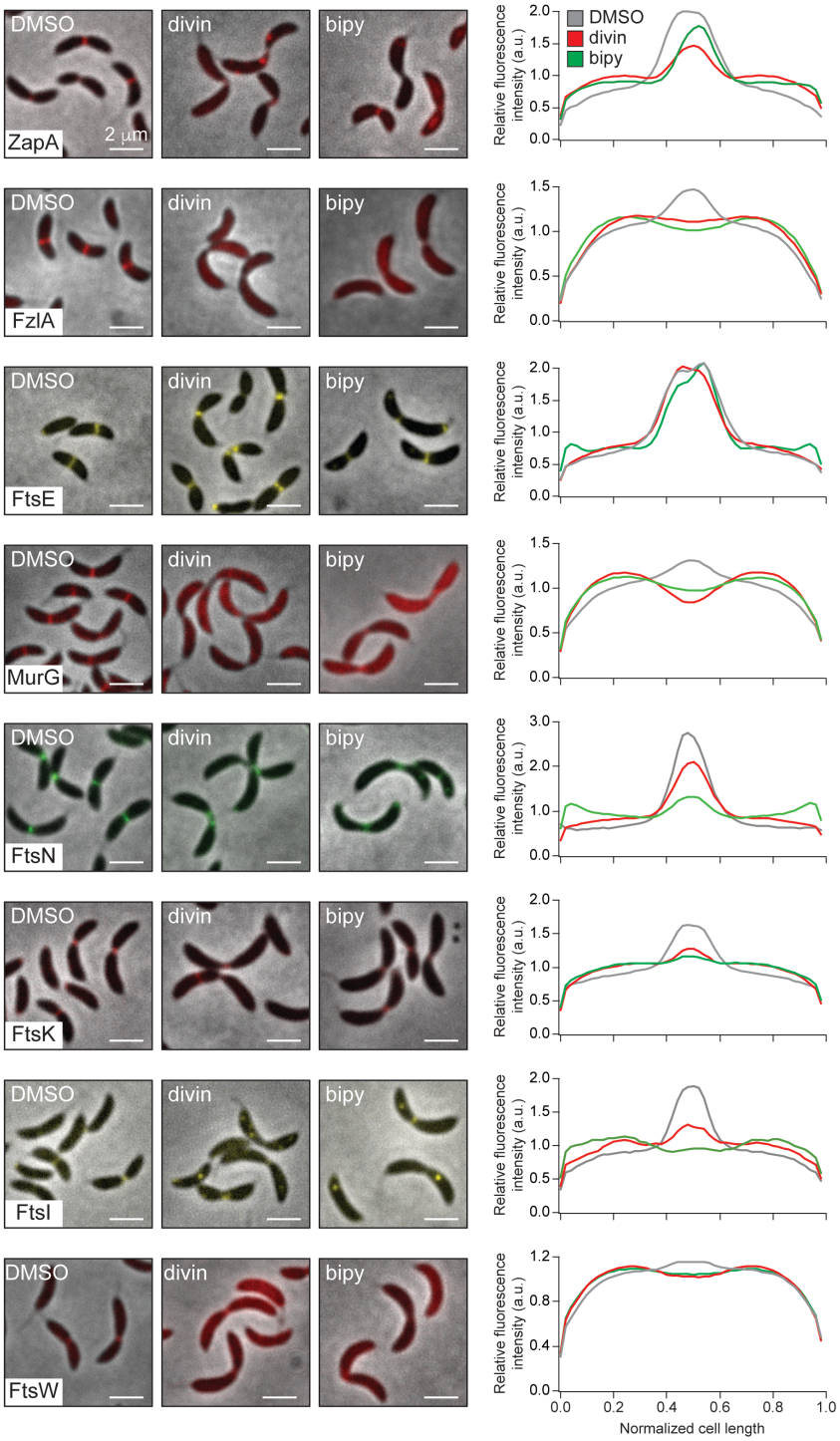

Figure 4. Iron deprivation affects localization of the bacterial divisome.

Representative fluorescence microscopy images depicting the localization pattern of various cell division proteins in *C. crescentus* CB15N grown for 6 h at 30ºC in PYE broth containing DMSO, 2× MIC of divin (25 μM) or bipy (400 μM). *Right panel*: Comparative fluorescence intensity profile of the subcellular distribution of cell division proteins for each treatment tested. a.u., arbitrary units. For this analysis, we only compared cells undergoing division. Analyses are the average of two independent experiments. Scale bars = 2 μm.

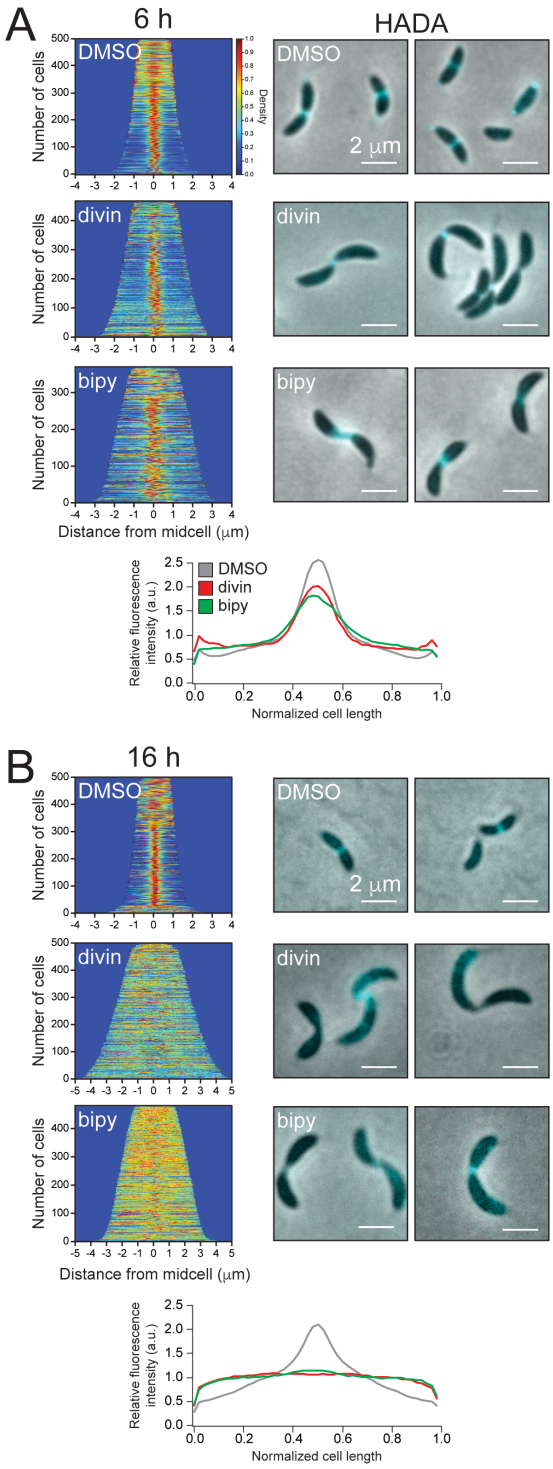

Figure 5. Iron deprivation reduces peptidoglycan incorporation in bacteria.

(A) *Left panel:* Demographs representing normalized signal profiles of HADA incorporation in *C. crescentus* CB15N arranged by increasing cell length. Cells were grown for 6 h at 30ºC in PYE broth containing DMSO, 2× MIC of divin (25 μM) or bipy (400 μM). *Right panel*: Representative fluorescence microscopy images depicting the localization pattern of HADA labeling. *Bottom panel*: Fluorescence intensity profile of the subcellular distribution of HADA. a.u., arbitrary units. For this analysis, we only compared cells undergoing division. Scale bars = 2 μm.

(B) Same as Figure 5A for *C. crescentus* CB15N grown for 16 h.

In panels A and B, analyses are the average of two independent experiments.

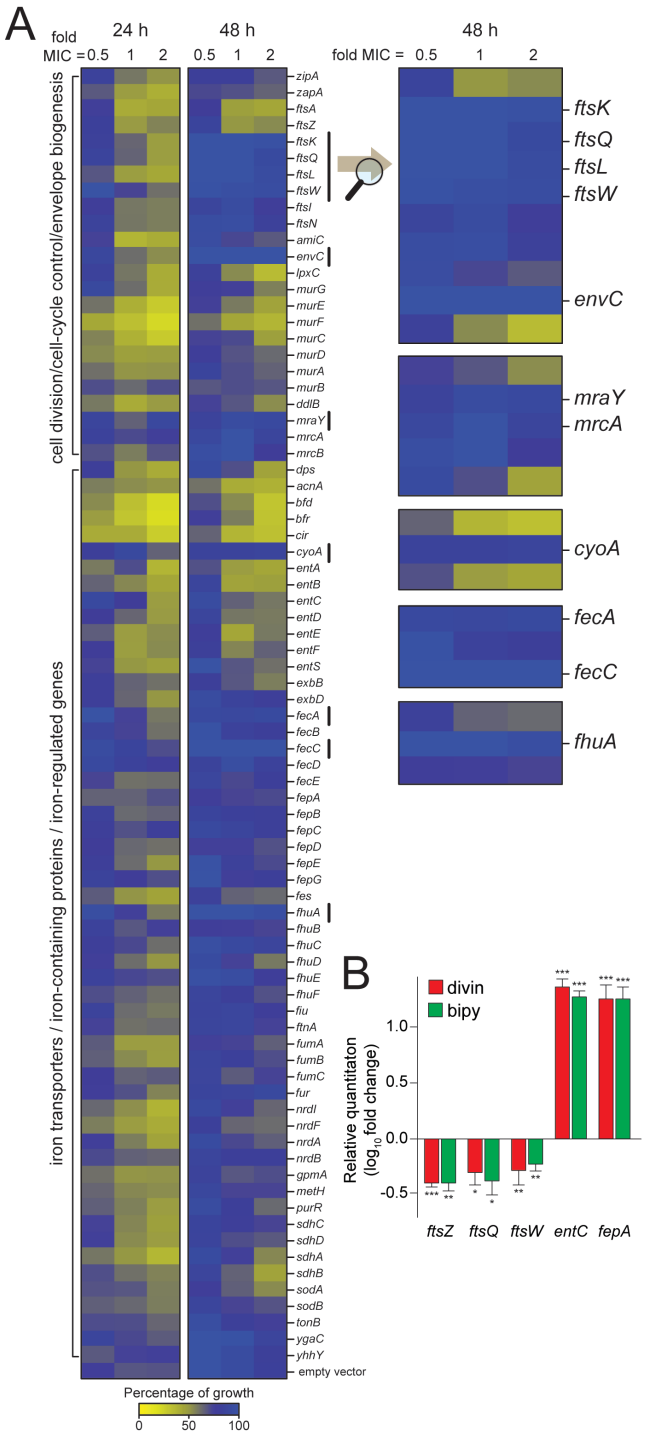

Figure 6. Iron deprivation downregulates the expression of cell division genes in bacteria.

(A) Heat map depicting *E. coli* growth in a target-multicopy suppressor screen. Growth was calculated as the percentage of the absorbance of the divin-treated culture compared to the same culture treated with DMSO. The measurements are the average of five independent experiments. *Right*: Enhanced view of growth after 48 h of strains overexpressing selected genes. Overexpression of these genes resulted in >10% increase in growth compared to the empty vector control.

(B) Relative gene expression in *E. coli* BW25113 Δ*tolC* treated with 2× MIC of divin (25 μM) or bipy (400 μM). Analyses are the average of four independent experiments. Error bars indicate the standard deviation. We performed one-sample Student's t-tests to test the null hypothesis that the $\log_{10}$-fold-change mean is equal to 0 (the normalized gene expression for cells treated with $FeSO_4$). *, $P < 0.05$; **, $P < 0.01$; ***, $P < 0.001$ compared to the cells treated with $FeSO_4$.

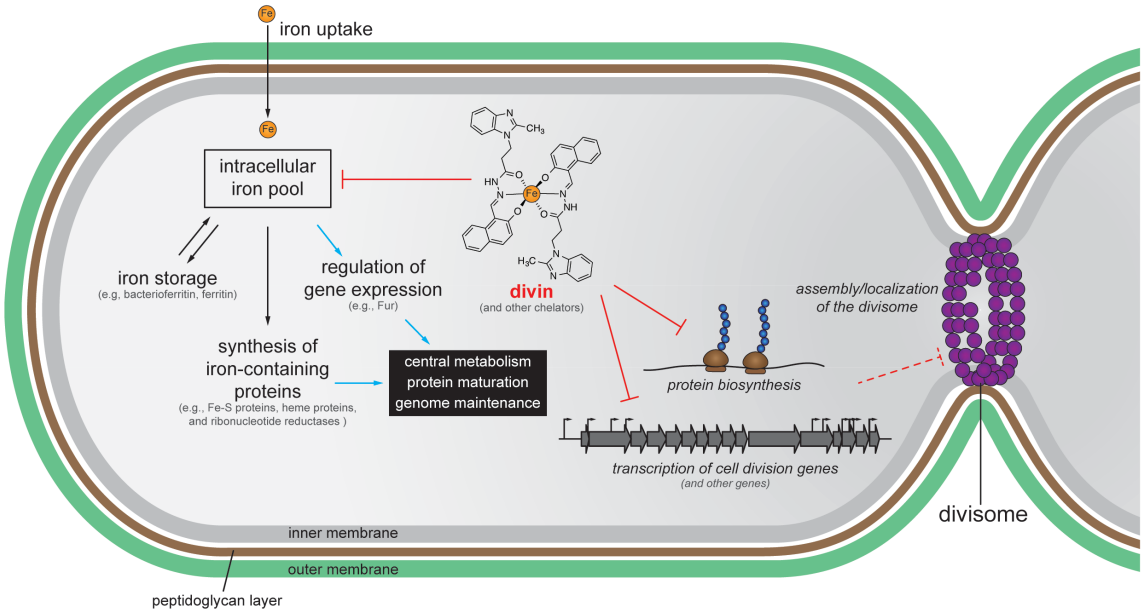

Figure 7. Iron deprivation inhibits bacterial cell division.

Iron homeostasis in bacteria results from a balance between iron acquisition, storage, and incorporation into proteins. Iron-containing proteins play a major role in a variety of metabolic and developmental processes. Transcription factors (e.g., Fur in *E. coli* and other Gram-negative bacteria) regulate gene expression to maintain precise control of the cytoplasmic levels of iron and prevent iron-induced toxicity. Divin and other iron chelators disrupts this intricate network by depleting the iron pool, interrupting biosynthesis of macromolecules and preventing assembly of a functional divisome during cell division.

SUPPLEMENTARY INFORMATION

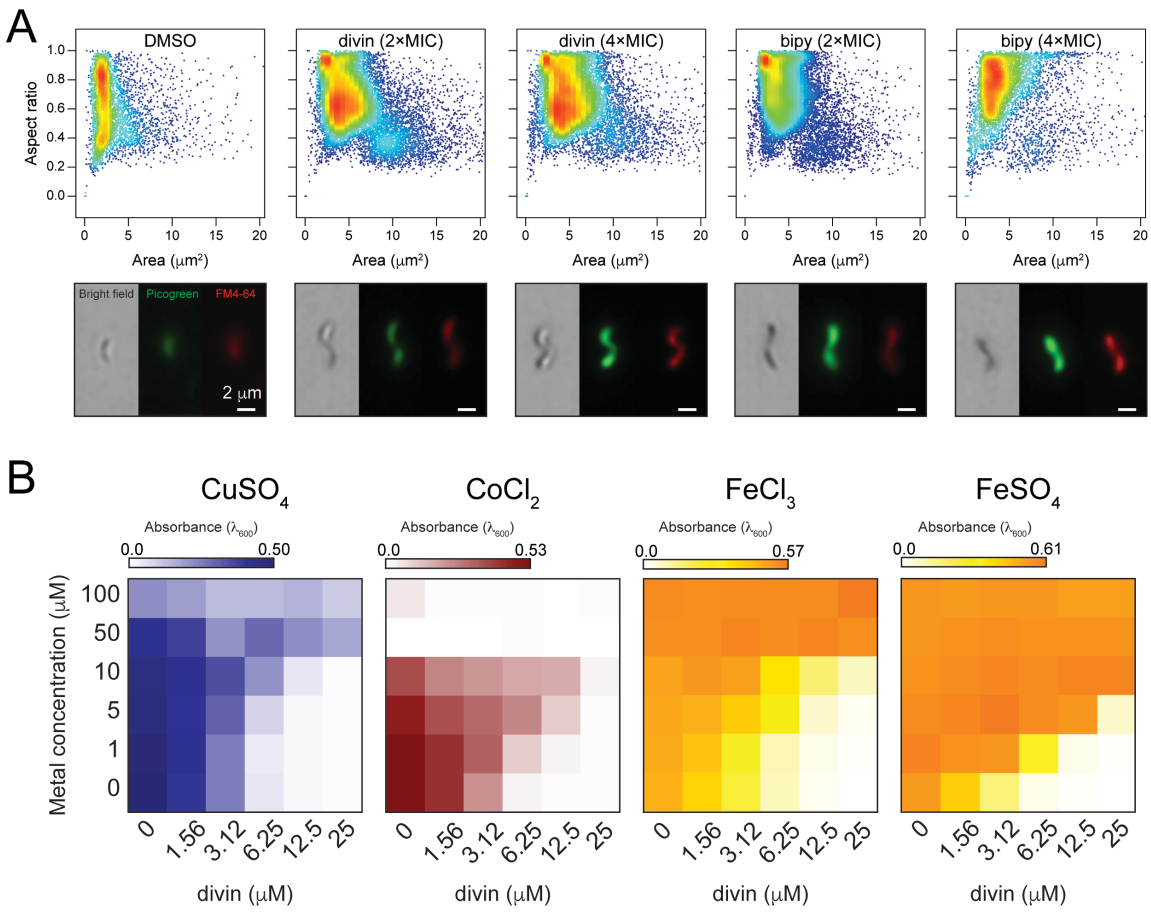

Figure S1. Divin and bipy inhibit cell division in *C. crescentus*.

(A) Scatter plots displaying the area and aspect ratio of *C. crescentus* CB15N cells grown for 16 h at 30°C in PYE broth containing DMSO, 2× MIC of divin (25 μM), 4× MIC of divin (50 μM), 2× MIC of bipy (400 μM), or 4× MIC of bipy (800 μM). Representative bright field and fluorescence microscopy images of cells from each treatment are displayed below each plot. The images were automatically obtained in flow using the ImageStream MkII Imaging Flow Cytometer. The cell membrane was labeled with FM4-64 (false-colored in red) and the DNA was labeled with Picogreen (false-colored in green). Scale bars = 2 μm.

(B) Checkerboard growth assays of the effect of cobalt, copper, and iron in combination with divin on the growth of *C. crescentus* CB15N cells. Dark colored squares to white squares represent full growth and complete growth inhibition, respectively. Analyses represent the combination of two independent experiments.

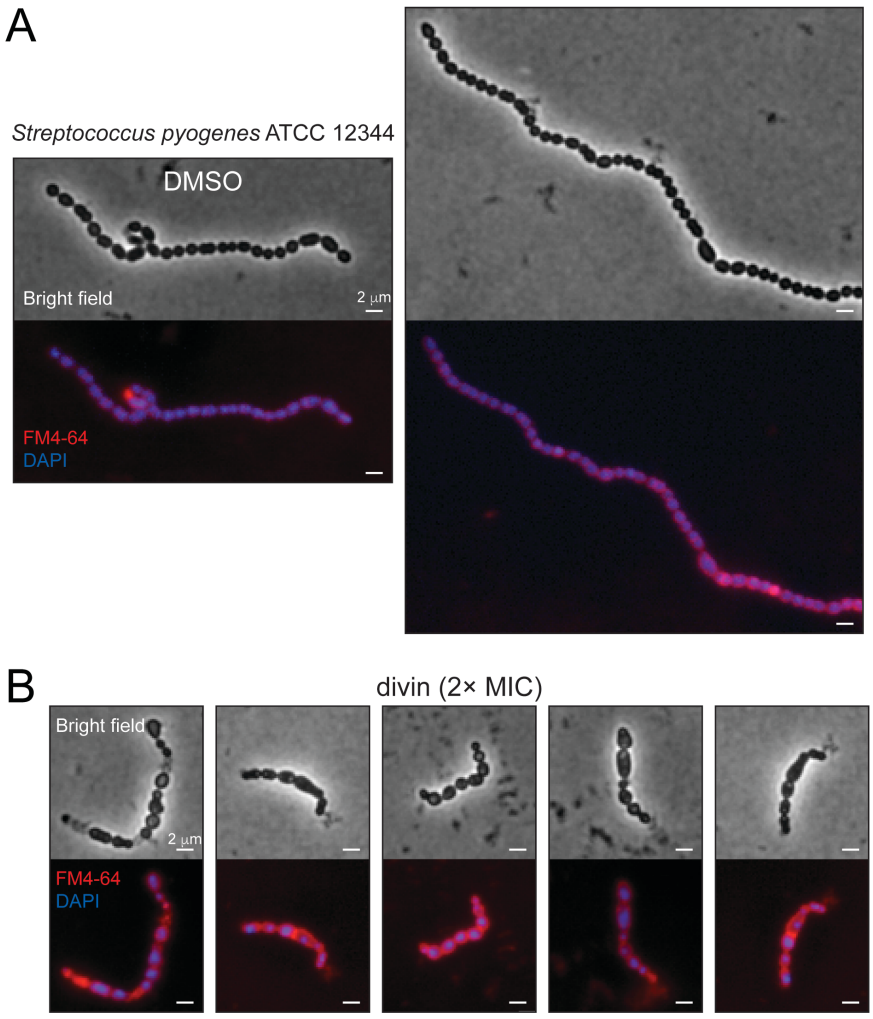

Figure S2. Divin inhibits cell division in *S. pyogenes*.

Representative bright field and fluorescence microscopy images of wild-type *S. pyogenes* ATCC 12344 cells grown for 16 h at 37°C in BHI broth containing (A) DMSO or (B) 2× MIC of divin (3.12 μM). The cell membrane was labeled with FM4-64 (false-colored in red) and the DNA was labeled with DAPI (false-colored in blue). Scale bars = 2 μm.

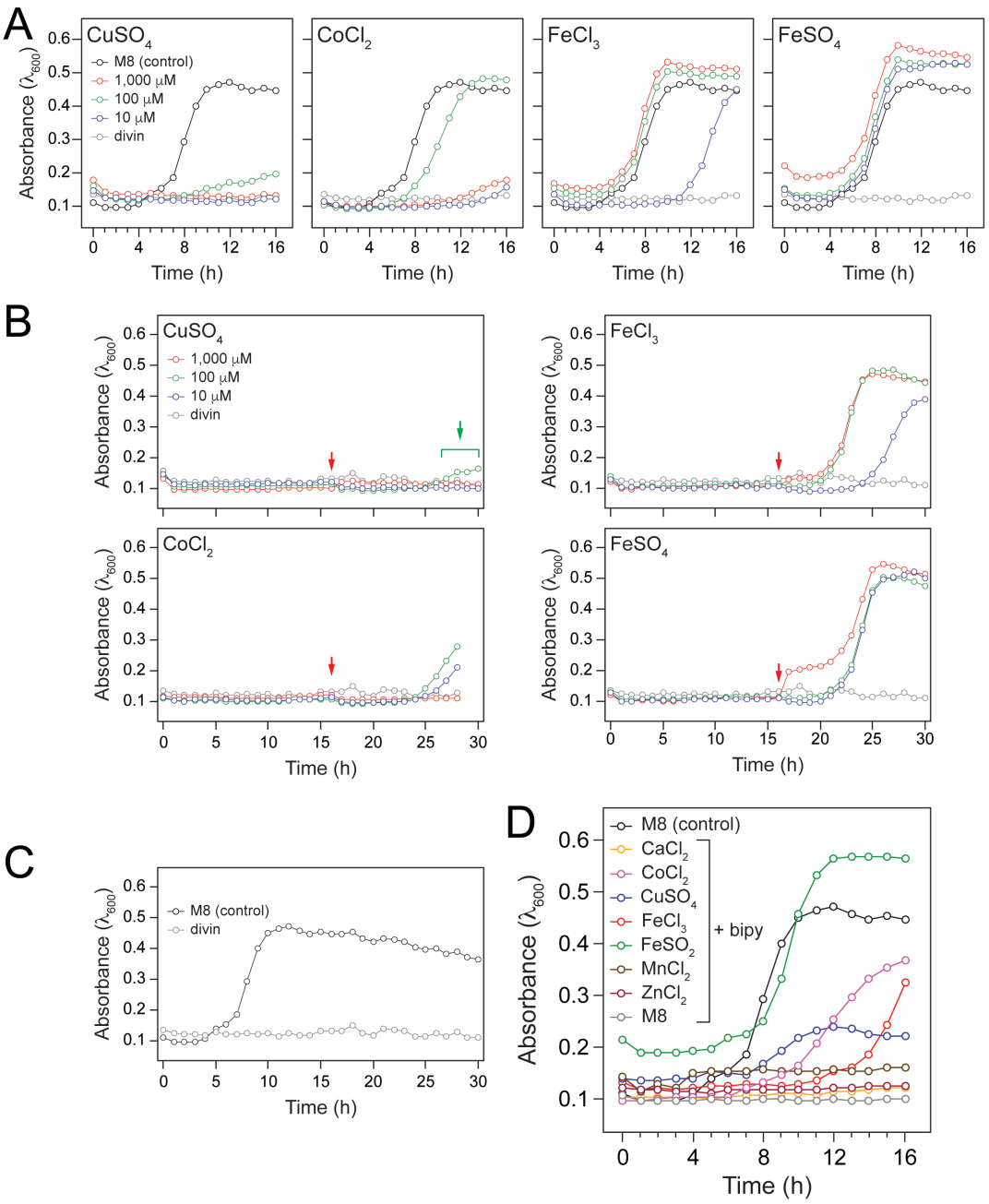

Figure S3. Iron, cobalt, and copper antagonize the biological activity of divin and bipy.

(A) Growth curves of *E. coli* BW25113 Δ*tolC* in the presence of 2× MIC of divin (25 μM) and various metals. Control curve (black) shows the growth curve of cells in M8 minimal medium in the presence of DMSO and divin curve (gray) shows the growth curve of cells in the presence of 2× MIC of divin without addition of metal.

(B) Growth curves of *E. coli* BW25113 Δ*tolC* in the presence of 2× MIC of divin and various metals. Different concentrations of each metal were added to the cultures at the time point indicated by the red arrow and additional measurements were taken every hour for about 14 h. Divin curve (gray) shows the growth curve of cells in the presence of 2× MIC of divin without addition of metal. Green arrow indicates growth of cells in the presence of 2× MIC of divin and 100 μM $CUSO_4$.

(C) Growth curve of *E. coli* BW25113 Δ*tolC* in M8 minimal medium (black) and in M8 minimal medium containing 2× MIC of divin (gray).

(D) Growth curves of *E. coli* BW25113 Δ*tolC* in the presence of 1× MIC of bipy (200 μM) and various metal (100 μM). M8 control curve (black) shows the growth curve of cells in the presence of DMSO and M8 curve (gray) shows the growth curve of cells in the presence of 1× MIC of bipy.

Growth curves are the average from two independent experiments. Error bars were omitted for clarity.

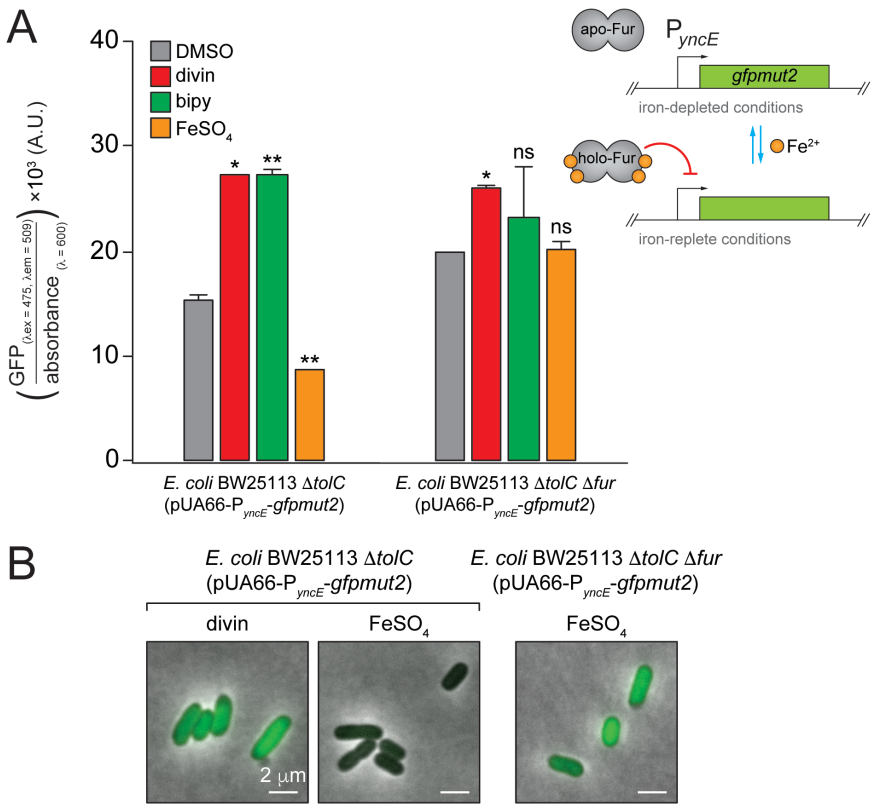

Figure S4. Divin triggers the iron-starvation response in *E. coli*.

(A) Ratio of GFP fluorescence intensity and absorbance of *E. coli* BW25113 Δ*tolC* and *E. coli* BW25113 Δ*tolC* Δ*fur* harboring the plasmid pUA66-P_{yncE}-*gfpmut2* following culturing in M8 minimal medium supplemented with DMSO, divin (6.25 μM), bipy (100 μM), or $FeSO_4$ (100 μM). Analyses are the average of two independent experiments. Error bars indicate the standard deviation. *Inset*: A cartoon depicting the classical view of Fur regulation in *E. coli* (summarized in the text). We performed one-sample Student's t-tests to test the null hypothesis that the GFP fluorescence intensity mean is equal to 100 (the normalized signal for the DMSO control). ns, non-significant; *, $P < 0.05$; **, $P < 0.01$ compared to the DMSO control treatment.

(B) Representative microscopy images of *E. coli* BW25113 Δ*tolC* and *E. coli* BW25113 Δ*tolC* Δ*fur* harboring the plasmid pUA66-P_{yncE}-*gfpmut2* and treated with divin (6.25 μM) or $FeSO_4$ (100 μM) for 20 h. Scale bars = 2 μm.

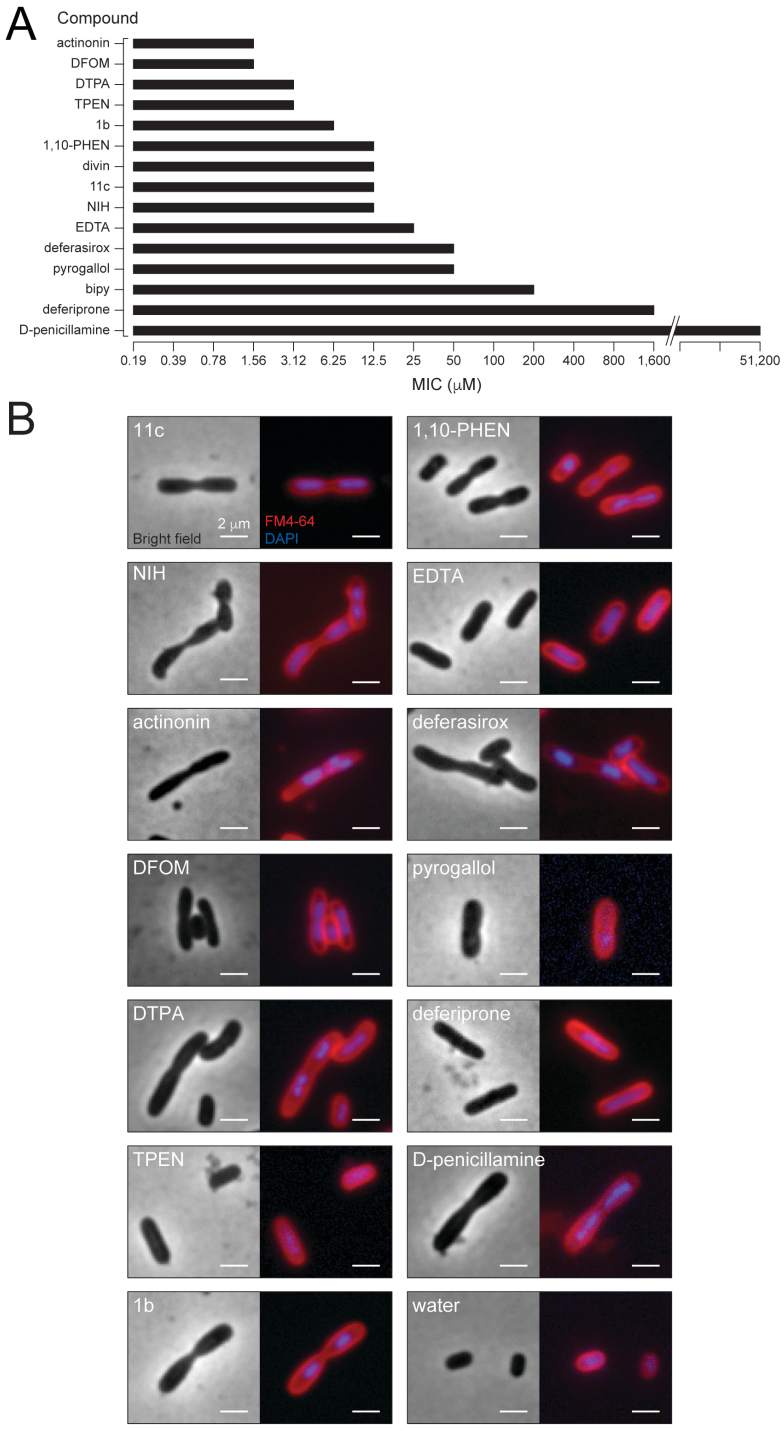

Figure S5. Iron chelators inhibit cell division in *E. coli* by arresting constriction at the division site.

(A) Minimum inhibitory concentration (in μM) of various known and putative iron chelators for *E. coli* BW25113 Δ*tolC*. Analyses are the average of two independent experiments.

(B) Representative bright field and fluorescence microscopy images of *E. coli* BW25113 Δ*tolC* grown for 16 h at 37°C in M8 minimal medium containing 2× MIC of various compounds. The cell membrane was labeled with FM4-64 (false-colored in red) and DNA was labeled with DAPI (false-colored in blue). Scale bars = 2 μm.

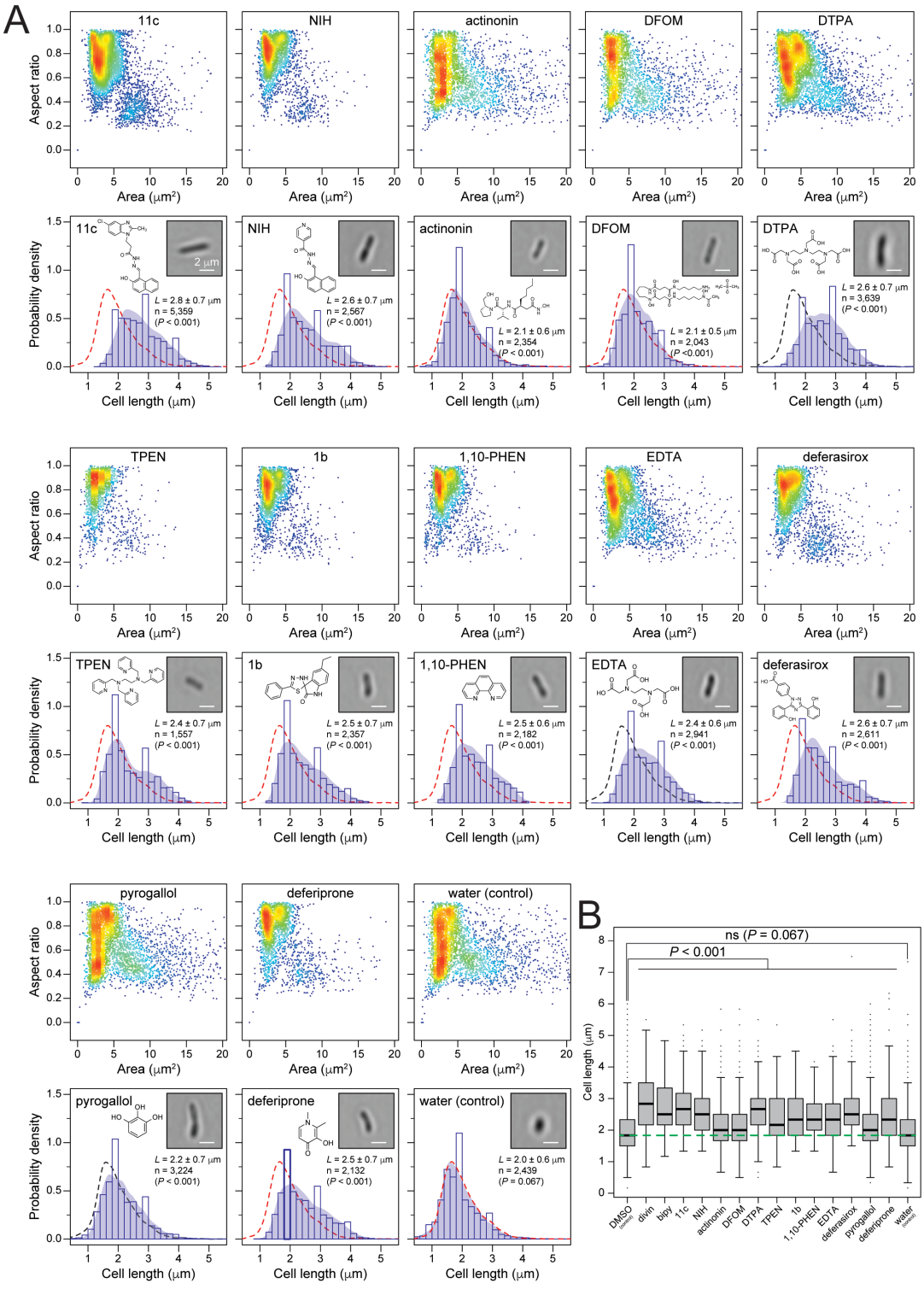

Figure S6. Iron chelators inhibit cell division in *E. coli* by arresting constriction at the division site.

(A) Scatter plots displaying the area and aspect ratio of *E. coli* BW25113 Δ*tolC* grown for 16 h at 37°C in M8 minimal medium containing 2× MIC of each compound or solvent indicated. Below each scatter plot, we show a probability density histogram of the cell length distribution of events containing single cells. Shaded blue area overlaying the histogram corresponds to the kernel density estimation (KDE) of cell length distribution for the correspondent treatment. Average cell length (*L*) is given with standard deviations for a total of *n* cells analyzed. Chemical structure of the compound treatment and representative bright field microscopy images of cells from each treatment are displayed in the top part of the histogram. The images were automatically obtained in flow using the ImageStream MkII Imaging Flow Cytometer. Scale bars = 2 μm. Red and black dashed line represents the KDE of the cell length distribution for the DMSO- and water-treated populations, respectively, and it was overlaid to facilitate comparison between the treatments and the control group. Statistical analysis was performed using a Kruskal-Wallis test followed by Dunn's post-hoc test.

(B) Box-and-whisker plots of the cell length of *E. coli* BW25113 Δ*tolC* grown for 16 h at 37°C in M8 minimal medium containing 2× MIC of each compound or solvent indicated. The extent of the box encompasses the interquartile range (IQR) of the cell length and the black line within each box represents the median. The upper whisker extends to the maximum data value, or 1.5 of the IQR, whichever is the smaller. The lower whisker extends to the maximum data value, or 1.5 of the IQR, whichever is the larger. Outliers are represented as the black dots that do not overlay on top of the box

plots. Green dashed line was drawn to facilitate comparison with the median cell length for the DMSO treatment. n.s., non-significant compared to the DMSO control.

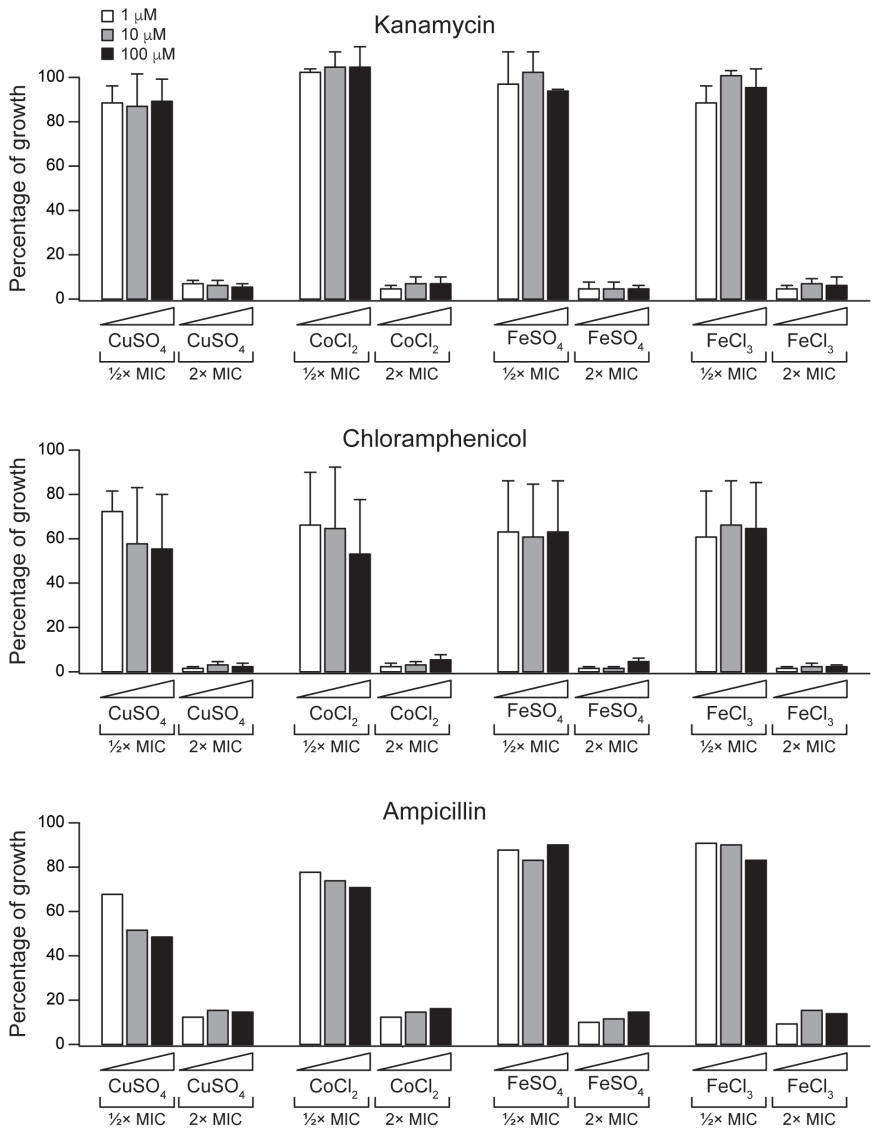

Figure S7. Cobalt, copper, and iron do not antagonize the biological activity of common antibiotics.

Growth of *E. coli* BW25113 Δ*tolC* in the presence of 0.5× MIC and 2× MIC of kanamycin, chloramphenicol, or ampicillin in M8 minimal medium supplemented with different concentrations of cobalt, copper, or iron. Bars show the percentage of growth compared to cells treated with DMSO and the highest concentration of the respective metal. Error bars indicate the standard error of the mean. Except for the treatment with ampicillin, analyses are the average of two independent experiments.

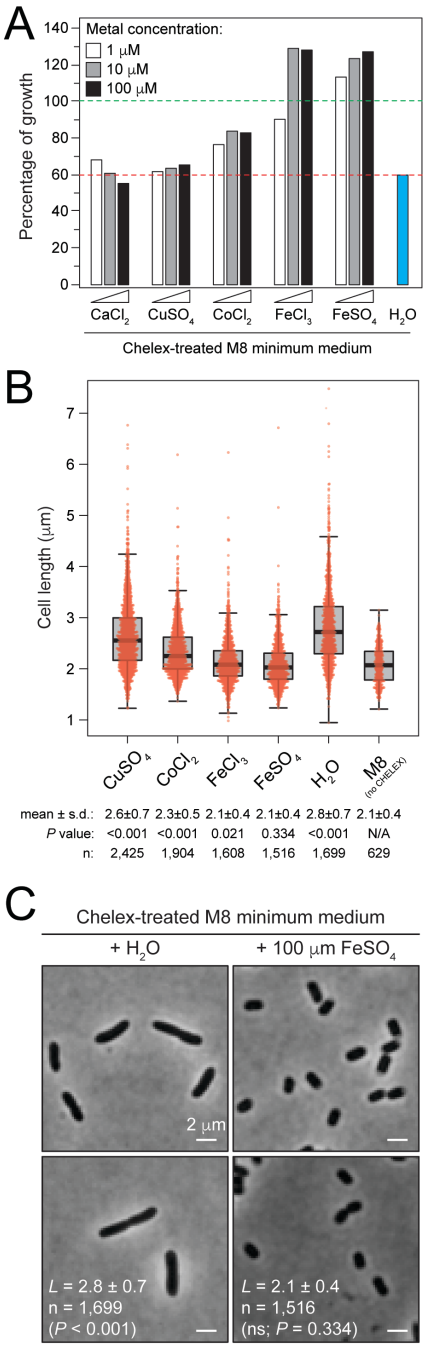

Figure S8. Iron depletion in the absence of a small molecule chelator arrests cell division in *E. coli*.

(A) Growth of *E. coli* BW25113 Δ*tolC* in the presence of various metals in Chelex-treated M8 minimal medium without addition of divin. Chelex is a chelating resin that binds transition metal—including copper, cobalt, and iron—with different affinities. Bars show the percentage of growth compared to cells grown in regular M8 minimal medium (green dashed line). Red dashed line was drawn to facilitate comparison with the water control.

(B) Box-and-whisker plots of the cell length of *E. coli* BW25113 Δ*tolC* grown for 16 h at 37°C in M8 minimal medium or Chelex-treated M8 minimal medium containing 100 μM or metal. The extent of the box encompasses the interquartile range (IQR) of the cell length and the black line within each box represents the median. The upper whisker extends to the maximum data value, or 1.5 of the IQR, whichever is the smaller. The lower whisker extends to the maximum data value, or 1.5 of the IQR, whichever is the larger. Overlaid on top of each plot is a bee swarm plot. Outliers are represented as the red dots that do not overlay on top of the box plots. N/A, not applicable.

(C) Representative images of *E. coli* BW25113 Δ*tolC* grown for 16 h at 37°C in Chelex-treated M8 minimal medium containing water or 100 μM $FeSO_4$. n.s., non-significant compared to the cells grown in regular M8 minimal medium. Scale bars = 2 μm.

In panels B and C, average cell length (*L*) is given with standard deviations for a total of *n* cells analyzed. Statistical analysis was performed using a Kruskal-Wallis test followed by Dunn's post-hoc test.

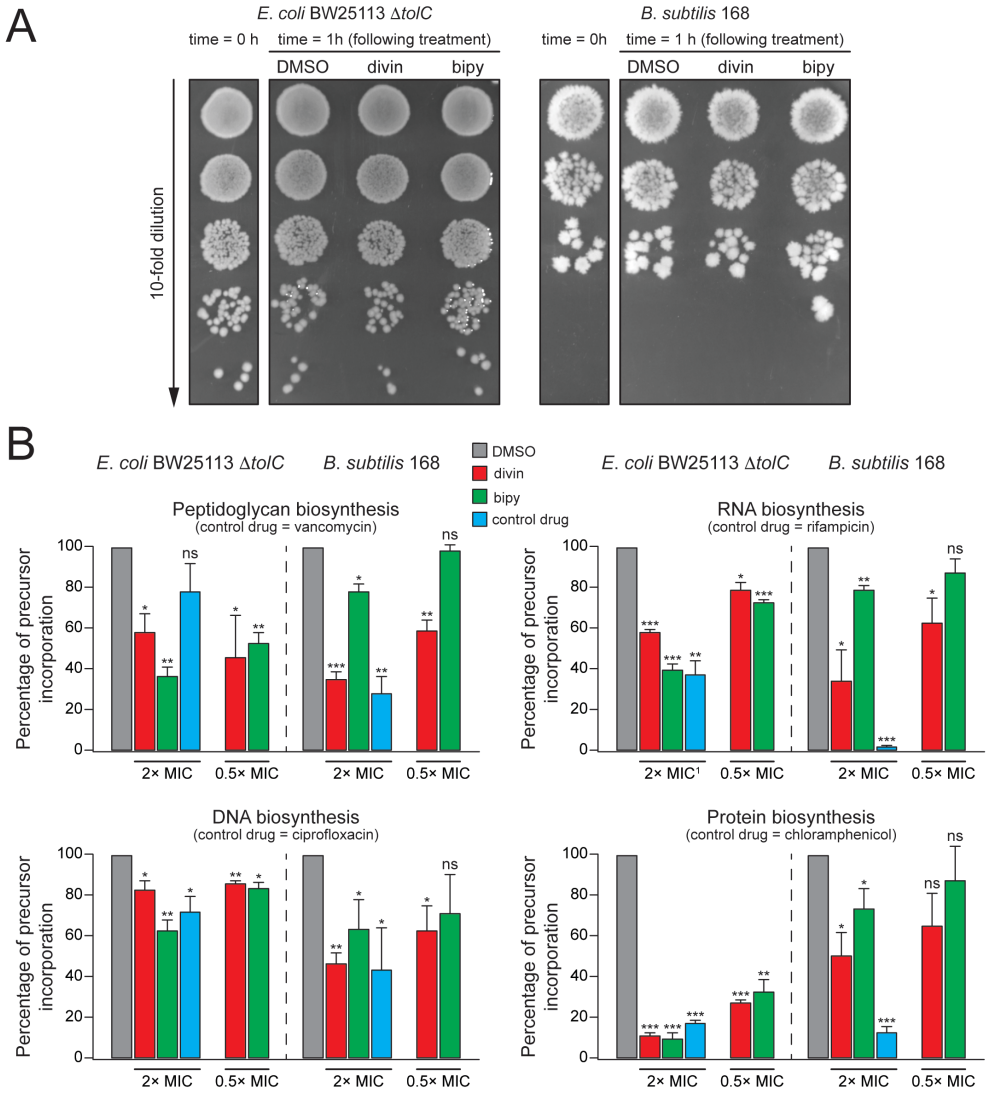

Figure S9. Iron deprivation affects biosynthesis of macromolecules in *E. coli* and *B. subtilis*.

(A) Growth assay of serial dilutions (top to bottom) of *E. coli* BW25113 Δ*tolC* and *B. subtilis* 168 cultures before and 1 h after treatment with DMSO, 2× MIC of divin (25 μM, *E. coli*; 100 μM, *B. subtilis*) or bipy (400 μM *E. coli*; 1,600 μM, *B. subtilis*). Aliquots (10 μL) of 10-fold serial dilutions from each culture were spotted on LB agar. The plates were incubated at 37°C for 24 h. *Note*: There is no substantial difference in growth following 1 h treatment with DMSO, 2× MIC of divin or bipy. However, there is a dramatic reduction in biosynthesis of macromolecules.

(B) Biosynthesis of macromolecules in *E. coli* BW25113 Δ*tolC* and *B. subtilis* 168 following treatment with divin or bipy. Incorporation of [6-^{3}H]glucosamine D-hydrochloride into peptidoglycan, [methyl-^{3}H]thymidine into DNA, [5,6-^{3}H]uridine into RNA, or [4,5-^{3}H]L-leucine into protein was determined in cells treated with DMSO, 2× MIC of divin or bipy. Vancomycin (2× MIC, 400/0.39 μM for *E. coli*/*B. subtilis*), ciprofloxacin (2× MIC, 0.05/1.56 μM), rifampicin ([1]16× MIC, 100 μM, for *E. coli* and 2× MIC, 1.56 μM, for *B. subtilis*), and chloramphenicol (2× MIC, 6.25/25 μM) were used as control drugs and served as reference antibiotics for inhibition of peptidoglycan, DNA, RNA, or protein biosynthesis, respectively. Analyses are the average of three independent experiments. Error bars indicate the standard deviation. Results are expressed as percentage of tritium-labeled metabolic precursor incorporation compared to the DMSO control (100% incorporation). We performed one-sample Student's t-tests to test the null hypothesis that the tritium-labeled metabolic precursor incorporation mean is equal to 100 (the normalized incorporation for the DMSO control). ns, non-

significant; *, $P < 0.05$; **, $P < 0.01$; ***, $P < 0.001$ compared to the DMSO control.

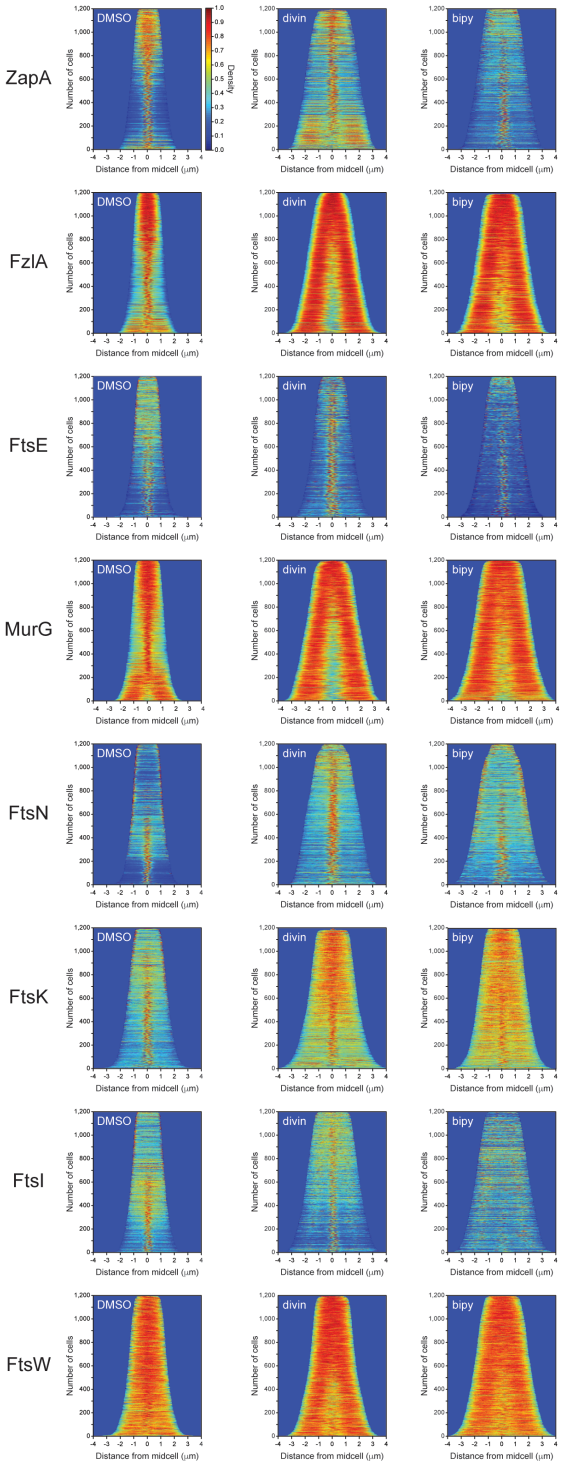

Figure S10. Iron deprivation affects localization of the bacterial divisome.

Demographs representing normalized signal profiles of cell division proteins in *C. crescentus* CB15N cells arranged by increasing cell length.

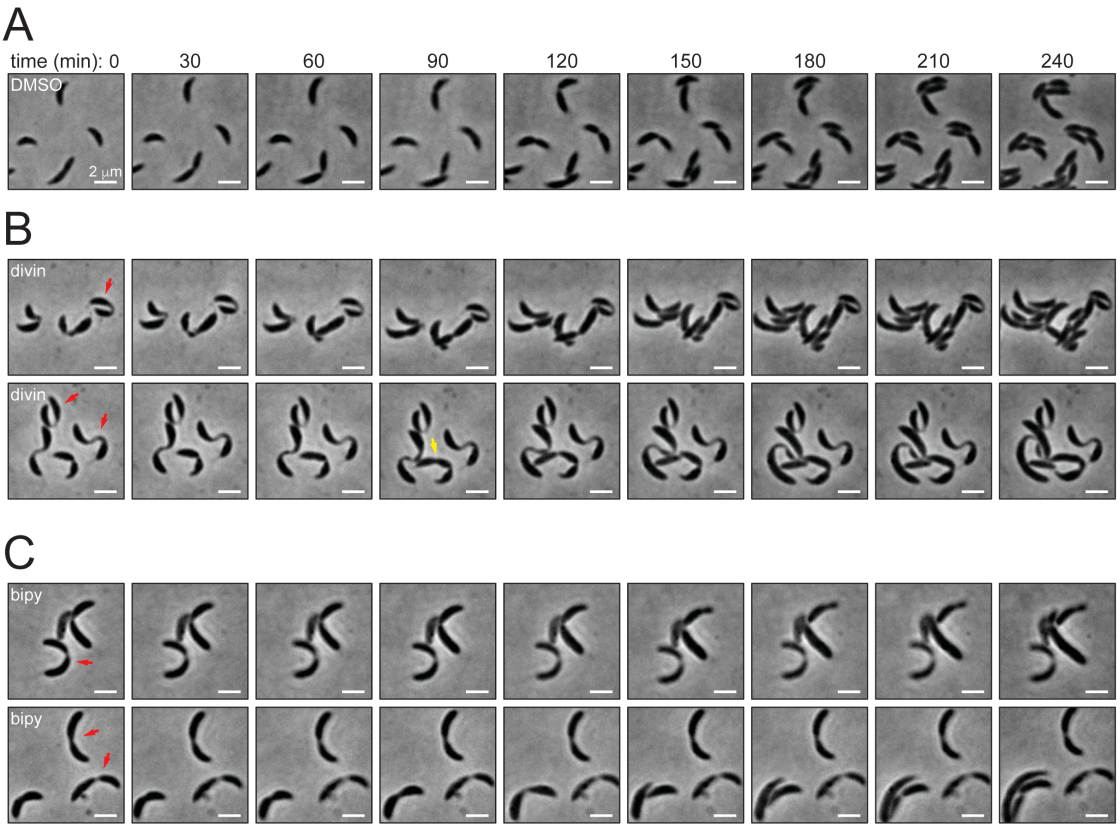

Figure S11. Long-term exposure to iron chelators causes permanent cell division arrest.

Bright field microscopy images from time-lapse experiments showing the morphological changes of *C. crescentus* CB15N cells grown for 4 h at 30°C in PYE agar pads. Prior to each time lapse, cells were grown for 16 h at 30°C in PYE broth containing (A) DMSO, (B) 2× MIC of divin (25 μM), or (C) 2× MIC of bipy (400 μM). Following this initial treatment, cells were harvested, washed and grown for additional 2 h in fresh PYE broth supplemented with 100 μM $FeSO_4$ to allow recovery. Red arrows indicate cells that fail to divide for the duration of the experiment (4 h). Yellow arrow indicates a cell that develops a second division site and completes division at this new site prior to completing division at the primary site. Scale bars = 2 μm.

Table S1. Bacterial strains and plasmids used in this study.

Designation	Genotype or description	Source or reference
Bacterial strain		
Bacillus subtilis 168	*sfp0 swrA trpC2*	Gift from Dan Kearns
Caulobacter crescentus CB15N (or NA1000)	Synchronizable derivative of the wild-type strain CB15	[61]
C. crescentus EG120	CB15N, *ftsI*::*venus–ftsI*	[44]
C. crescentus EG123	CB15N, *ftsW*::*mCherry–ftsW*	[44]
C. crescentus EG383	CB15N, *murG*::*murG–mCherry*, Gm^R	[44]
C. crescentus EG384	CB15N, *fzlA*::*mCherry–fzlA*	[44]
C. crescentus EG645	CB15N, *zapA*::*zapA–mCherry*, Gm^R	[44]
C. crescentus EG652	CB15N, *mipZ*::*mipZ–cerulean ftsE*::*venus–ftsE*	[44]
C. crescentus EG658	CB15N, *ftsK*::*ftsK–mCherry ftsI*::*venus–ftsI*, Gm^R	[44]
C. crescentus MT46	CB15N, *ftsN*::*egfp–ftsN*	[62]
Escherichia coli AG1	*recA1 endA1 gyrA96 thi-1 hsdR17* ($r\ K^-\ m\ K^+$) *supE44 relA1*	ASKA collection [25]
E. coli DH5α	F^- Δ*(argF-lac)169* ϕ80d*lacZ*(M15) Δ*phoA8 glnV44*(AS) λ^- *deoR481 rfbC1*? *gyrA96*(NalR) *recA1 endA1 thiE1 hsdR17*	CGSC #12384 [a]
E. coli BW25113 Δ*tolC* (*E. coli* JW5503)	BW25113, Δ*tolC732*::*kan*, Km^R	Keio collection [63]
E. coli BW25113 Δ*fur* (*E. coli* JW0669)	BW25113, Δ*fur-731*::*kan*, Km^R	[63]
E. coli BW25113 Δ*tolC*::frt	BW25113, Δ*tolC732*::frt We used plasmid pCP20 to remove the FRT-*kan*-FRT cassette from *E. coli* BW25113 Δ*tolC*.	This study

E. coli BW25113 Δ*tolC* Δ*fur*	BW25113, Δ*tolC732*::frt, Δ*fur-731*::*kan* [b], Km^R We used P1 transduction to transfer the FRT-*kan*-FRT cassette from *E. coli* BW25113 Δ*fur* to *E. coli* BW25113 Δ*tolC*.	This study
E. coli MG1655	$F^- \lambda^-$ *rph-1*	CGSC #6300
Streptococcus pyogenes	Origin unavailable	ATCC 12344 [c]
Plasmids		
pCP20	Amp^R, Cm^R, temperature-conditional replicon expressing a thermal-induced Flp recombinase	[64]
pUA66 (pUA66-*gfpmut2*)	Km^R, the plasmid (pSC101 ori) encodes a promoter-less fast-folding *gfpmut2* gene as a reporter gene with a strong ribosome binding site, low copy-number	[65]
pUA66-P_{fepA}-*gfpmut2*	Km^R, this plasmid encodes a fast-folding *gfpmut2* gene regulated by a P_{fepA} promoter	This study
pUA66-P_{yncE}-*gfpmut2*	Km^R, this plasmid encodes a fast-folding *gfpmut2* gene regulated by a P_{yncE} promoter	This study

[a] CGSC, Coli Genetic Stock Center, Yale University, New Haven, Connecticut.

[b] Allele numbers as indicated in the CGSC.

[c] ATCC, American Type Culture Collection, Manassas, VA.

Abbreviation: Amp, ampicillin; Cm, chloramphenicol; Gm, gentamycin; Km, kanamycin; Spec, spectinomycin; Str, streptomycin; R, resistance; frt, indicates the presence of the scar sequence "GAAGTTCCTATTCTCTAGAAAGTATAGGAACTTC" left after removal of the FRT-*kan*-FRT cassette.

Table S2. Primers used in this study.

Primer [a]	**Sequence (5′-3′)** [b]	**Reference**
Primers for cloning and analytical PCR		
k1	CAGTCATAGCCGAATAGCCT	[66]
k2	CGGTGCCCTGAATGAACTGC	[66]
kt	CGGCCACAGTCGATGAATCC	[66]
entC-F	GCGTTACCTCAAGAGTTGAC	This study
entC-R	GCATGTCGCGTCAGAATGTC	This study
fur-F	CAACATCAGCAGTTTGCC	This study
fur-R	AGACTCATGTCTACGCCG	This study
tolC-F	GTAGCGGCTTCTGCTAGAATCCGCAATAATTTTAC	This study
tolC-R	AGAAGGGGGAAGAATGCGGCAGATAAC	This study
fepA-F-XhoI	TCGTCTTCAC**CTCGAG**TTCGTCATTCAGACGCTGC	This study
fepA-R-BamHI	TAAATCTAGA**GGATCC**TGTTTTATTCCTGCATTTTTGCCACGAAT TGC	This study
yncE-F-XhoI	TCGTCTTCAC**CTCGAG**ACGGGGGAAAGGACAAG	This study
yncE-R-BamHI	TAAATCTAGA**GGATCC**GACGACTCCCTTTGATGAACCGATA	This study
pUA66-F	GCTTCCCAACCTTACCAGAGGG	This study
pUA66-R	CCACTGACAGAAAATTTGTGCCCA	This study
Primers for qRT-PCR		
entC-F	CAGGCGATGAAAGAGGTACTG	This study
entC-R	TCAAAGGGAGTTGCGAGATG	This study
fepA-F	CACCTGGTTCCGTAACGATTAT	This study
fepA-R	GCACGTTATCCCACTGATAGAG	This study
ftsQ-F	GGTAGACGCGGAAGGAAATAC	This study
ftsQ-R	GATAGCCCTGCAACACTTCA	This study
ftsW-F	GTAGTGGGTAGCTCGGTTAAAG	This study

ftsW-R	GCCTTTACGCACCAGATAGT	This study
ftsZ-F	CGAACGACAAACTGCTGAAAG	This study
ftsZ-R	CATCAAACCCGGACGAGTAAT	This study
idnT-F	CTGTTTAGCGAAGAGGAGATGC	This study
idnT-R	ACAAACGGCGGCGATAGC	This study

[a] Oligonucleotide primers were from Integrated DNA Technology, IDT (Coralville, IA). In general, primer names correspond to the gene that the primer amplifies, the forward (F) primer or the reverse (R) primer of that gene, and the restriction site incorporated into the primer sequence for cloning.

[b] The restriction sites used for cloning are in bold.

REFERENCES

1. Lutkenhaus J, Pichoff S, Du S. Bacterial cytokinesis: From Z ring to divisome. *Cytoskeleton* (Hoboken). 2012; 69: 778-90.
2. Haeusser DP, Margolin W. Splitsville: Structural and functional insights into the dynamic bacterial Z ring. *Nat Rev Microbiol*. 2016; 14: 305-19.
3. Raskin DM, de Boer PA. Rapid pole-to-pole oscillation of a protein required for directing division to the middle of *Escherichia coli*. *Proc Natl Acad Sci U S A*. 1999; 96: 4971-6.
4. Wu LJ, Errington J. Coordination of cell division and chromosome segregation by a nucleoid occlusion protein in *Bacillus subtilis*. *Cell*. 2004; 117: 915-25.
5. Thanbichler M, Shapiro L. MipZ, a spatial regulator coordinating chromosome segregation with cell division in *Caulobacter*. *Cell*. 2006; 126: 147-62.
6. Fleurie A, Lesterlin C, Manuse S, Zhao C, Cluzel C, Lavergne JP, et al. MapZ marks the division sites and positions FtsZ rings in *Streptococcus pneumoniae*. *Nature*. 2014; 516: 259-62.
7. Weart RB, Lee AH, Chien AC, Haeusser DP, Hill NS, Levin PA. A metabolic sensor governing cell size in bacteria. *Cell*. 2007; 130: 335-47.
8. Hill NS, Buske PJ, Shi Y, Levin PA. A moonlighting enzyme links *Escherichia coli* cell size with central metabolism. *PLoS Genet*. 2013; 9: e1003663.
9. Beaufay F, Coppine J, Mayard A, Laloux G, De Bolle X, Hallez R. A NAD-dependent glutamate dehydrogenase coordinates metabolism with cell division in *Caulobacter crescentus*. *EMBO J*. 2015; 34: 1786-800.
10. Dong G, Yang Q, Wang Q, Kim YI, Wood TL, Osteryoung KW, et al. Elevated ATPase activity of KaiC applies a circadian checkpoint on cell division in *Synechococcus elongatus*. *Cell*. 2010; 140: 529-39.
11. Mukherjee A, Cao C, Lutkenhaus J. Inhibition of FtsZ polymerization by SulA, an inhibitor of septation in *Escherichia coli*. *Proc Natl Acad Sci U S A*. 1998; 95: 2885-90.
12. Modell JW, Hopkins AC, Laub MT. A DNA damage checkpoint in *Caulobacter crescentus* inhibits cell division through a direct interaction with FtsW. *Genes Dev*. 2011; 25: 1328-43.
13. Modell JW, Kambara TK, Perchuk BS, Laub MT. A DNA damage-induced, SOS-independent checkpoint regulates cell division in *Caulobacter crescentus*. *PLoS Biol*. 2014; 12: e1001977.
14. Chen Y, Milam SL, Erickson HP. SulA inhibits assembly of FtsZ by a simple sequestration mechanism. *Biochemistry*. 2012; 51: 3100-9.
15. Andreini C, Bertini I, Cavallaro G, Holliday GL, Thornton JM. Metal ions in biological catalysis: From enzyme databases to general principles. *J Biol Inorg Chem*. 2008; 13: 1205-18.

16. Andrews SC, Robinson AK, Rodriguez-Quinones F. Bacterial iron homeostasis. *FEMS Microbiol Rev*. 2003; 27: 215-37.

17. Braun V, Killmann H. Bacterial solutions to the iron-supply problem. *Trends Biochem Sci*. 1999; 24: 104-9.

18. Caza M, Kronstad JW. Shared and distinct mechanisms of iron acquisition by bacterial and fungal pathogens of humans. *Front Cell Infect Microbiol*. 2013; 3: 80.

19. McHugh JP, Rodriguez-Quinones F, Abdul-Tehrani H, Svistunenko DA, Poole RK, Cooper CE, et al. Global iron-dependent gene regulation in *Escherichia coli*. A new mechanism for iron homeostasis. *J Biol Chem*. 2003; 278: 29478-86.

20. Seo SW, Kim D, Latif H, O'Brien EJ, Szubin R, Palsson BO. Deciphering Fur transcriptional regulatory network highlights its complex role beyond iron metabolism in *Escherichia coli*. *Nat Commun*. 2014; 5: 4910.

21. Beauchene NA, Myers KS, Chung D, Park DM, Weisnicht AM, Keles S, et al. Impact of anaerobiosis on expression of the iron-responsive Fur and RyhB regulons. *MBio*. 2015; 6: e01947-15.

22. Eun YJ, Zhou M, Kiekebusch D, Schlimpert S, Trivedi RR, Bakshi S, et al. Divin: A small molecule inhibitor of bacterial divisome assembly. *J Am Chem Soc*. 2013; 135: 9768-76.

23. Falconer SB, Wang W, Gehrke SS, Cuneo JD, Britten JF, Wright GD, et al. Metal-induced isomerization yields an intracellular chelator that disrupts bacterial iron homeostasis. *Chem Biol*. 2014; 21: 136-45.

24. Zhou M, Eun YJ, Guzei IA, Weibel DB. Structure-activity studies of divin: An inhibitor of bacterial cell division. *ACS Med Chem Lett*. 2013; 4: 880-5.

25. Kitagawa M, Ara T, Arifuzzaman M, Ioka-Nakamichi T, Inamoto E, Toyonaga H, et al. Complete set of ORF clones of *Escherichia coli* ASKA library (a complete set of *E. coli* K-12 ORF archive): Unique resources for biological research. *DNA Res*. 2005; 12: 291-9.

26. Paintdakhi A, Parry B, Campos M, Irnov I, Elf J, Surovtsev I, et al. Oufti: An integrated software package for high-accuracy, high-throughput quantitative microscopy analysis. *Mol Microbiol*. 2016; 99: 767-77.

27. Kuru E, Hughes HV, Brown PJ, Hall E, Tekkam S, Cava F, et al. In situ probing of newly synthesized peptidoglycan in live bacteria with fluorescent D-amino acids. *Angew Chem Int Ed Engl*. 2012; 51: 12519-23.

28. Bryantsev VS, Diallo MS, Goddard WA, 3rd. Calculation of solvation free energies of charged solutes using mixed cluster/continuum models. *J Phys Chem B*. 2008; 112: 9709-19.

29. Rao L, Cui Q, Xu X. Electronic properties and desolvation penalties of metal ions plus protein electrostatics dictate the metal binding affinity and selectivity in the copper efflux regulator. *J Am Chem Soc*. 2010; 132: 18092-102.

30. Lee C, Yang W, Parr RG. Development of the Colle-Salvetti correlation-energy formula into a functional of the electron density. *Phys Rev B*. 1988; 37: 785-9.

31. Becke AD. Density-functional thermochemistry. III. The role of exact exchange. *J Chem Phys*. 1993; 98: 5648-52.

32. Hay PJ, Wadt WR. Ab initio effective core potentials for molecular calculations. Potentials for the transition metal atoms Sc to Hg. *J Chem Phys*. 1985; 82: 270-83.

33. Francl MM, Pietro WJ, Hehre WJ, Binkley JS, Gordon MS, DeFrees DJ, et al. Self-consistent molecular orbital methods. XXIII. A polarization-type basis set for second-row elements. *J Chem Phys*. 1982; 77: 3654-65.

34. Krishnan R, Binkley JS, Seeger R, Pople JA. Self-consistent molecular orbital methods. XX. A basis set for correlated wave functions. *J Chem Phys*. 1980; 72: 650-4.

35. Marenich AV, Cramer CJ, Truhlar DG. Universal solvation model based on solute electron density and on a continuum model of the solvent defined by the bulk dielectric constant and atomic surface tensions. *J Phys Chem B*. 2009; 113: 6378-96.

36. Zhou K, Zhou L, Lim Q, Zou R, Stephanopoulos G, Too HP. Novel reference genes for quantifying transcriptional responses of *Escherichia coli* to protein overexpression by quantitative PCR. *BMC Mol Biol*. 2011; 12: 18.

37. Nonejuie P, Burkart M, Pogliano K, Pogliano J. Bacterial cytological profiling rapidly identifies the cellular pathways targeted by antibacterial molecules. *Proc Natl Acad Sci U S A*. 2013; 110: 16169-74.

38. Campos M, Surovtsev IV, Kato S, Paintdakhi A, Beltran B, Ebmeier SE, et al. A constant size extension drives bacterial cell size homeostasis. *Cell*. 2014; 159: 1433-46.

39. Richarson DR, Vitolo LMW, Hefter GT, May PM, Clare BW, Webb J. Iron chelators of the pyridoxal isonicotinoyl hydrazone class. Part I. Ionisation characteristics of the ligands and their relevance to biological properties. *Inorg Chim Acta*. 1990; 170: 165-70.

40. Richardson DR, Bernhardt PV. Crystal and molecular structure of 2-hydroxy-1-naphthaldehyde isonicotinoyl hydrazone (NIH) and its iron(III) complex: An iron chelator with anti-tumour activity. *J Biol Inorg Chem*. 1999; 4: 266-73.

41. Gao J. The potential of iron chelators of the pyridoxal isonicotinoyl hydrazone class as effective antiproliferative agents, IV: The mechanisms involved in inhibiting cell-cycle progression. *Blood*. 2001; 98: 842-50.

42. Balhesteros H, Shipelskiy Y, Long NJ, Majumdar A, Katz BB, Santos NM, et al. TonB-dependent heme/hemoglobin utilization by *Caulobacter crescentus* HutA. *J Bacteriol*. 2017; 199: e00723-16.

43. Aarsman ME, Piette A, Fraipont C, Vinkenvleugel TM, Nguyen-Disteche M, den Blaauwen T. Maturation of the *Escherichia coli* divisome occurs in two steps. *Mol Microbiol*. 2005; 55: 1631-45.

44. Goley ED, Yeh YC, Hong SH, Fero MJ, Abeliuk E, McAdams HH, et al. Assembly of the *Caulobacter* cell division machine. *Mol Microbiol*. 2011; 80: 1680-98.

45. Bleuel C, Grosse C, Taudte N, Scherer J, Wesenberg D, Krauss GJ, et al. TolC is involved in enterobactin efflux across the outer membrane of *Escherichia coli*. *J Bacteriol*. 2005; 187: 6701-7.

46. Jonas K. To divide or not to divide: Control of the bacterial cell cycle by environmental cues. *Curr Opin Microbiol*. 2014; 18: 54-60.

47. Richardson DR, Hefter GT, May PM, Webb J, Baker E. Iron chelators of the pyridoxal isonicotinoyl hydrazone class lII. Formation constants with calcium(II), magnesium(II) and zinc(II). *Biol Met*. 1989; 2: 161-7.

48. Epsztejn S, Kakhlon O, Glickstein H, Breuer W, Cabantchik I. Fluorescence analysis of the labile iron pool of mammalian cells. *Anal Biochem*. 1997; 248: 31-40.

49. Yu Y, Kovacevic Z, Richardson DR. Tuning cell cycle regulation with an iron key. *Cell Cycle*. 2007; 6: 1982-94.

50. Kulp KS, Green SL, Vulliet PR. Iron deprivation inhibits cyclin-dependent kinase activity and decreases cyclin D/CDK4 protein levels in asynchronous MDA-MB-453 human breast cancer cells. *Exp Cell Res*. 1996; 229: 60-8.

51. Chaston TB, Lovejoy DB, Watts RN, Richardson DR. Examination of the antiproliferative activity of iron chelators: multiple cellular targets and the different mechanism of action of triapine compared with desferrioxamine and the potent pyridoxal isonicotinoyl hydrazone analogue 311. *Clin Cancer Res*. 2003; 9: 402-14.

52. Heinrich K, Sobetzko P, Jonas K. A kinase-phosphatase switch transduces environmental information into a bacterial cell cycle circuit. *PLoS Genet*. 2016; 12: e1006522.

53. Wortinger MA, Quardokus EM, Brun YV. Morphological adaptation and inhibition of cell division during stationary phase in *Caulobacter crescentus*. *Mol Microbiol*. 1998; 29: 963-73.

54. Britos L, Abeliuk E, Taverner T, Lipton M, McAdams H, Shapiro L. Regulatory response to carbon starvation in *Caulobacter crescentus*. *PLoS One*. 2011; 6: e18179.

55. Wang J, Wu G, Chen L, Zhang W. Cross-species transcriptional network analysis reveals conservation and variation in response to metal stress in cyanobacteria. *BMC Genomics*. 2013; 14: 112.

56. Jones RL, Peterson CM, Grady RW, Kumbaraci T, Cerami A, Graziano JH. Effects of iron chelators and iron overload on *Salmonella* infection. *Nature*. 1977; 267: 63-5.

57. Thompson MG, Corey BW, Si Y, Craft DW, Zurawski DV. Antibacterial activities of iron chelators against common nosocomial pathogens. *Antimicrob Agents Chemother*. 2012; 56: 5419-21.

58. Tatano Y, Kanehiro Y, Sano C, Shimizu T, Tomioka H. ATP exhibits antimicrobial action by inhibiting bacterial utilization of ferric ions. *Sci Rep*. 2015; 5: 8610.

59. Hatcher HC, Singh RN, Torti FM, Torti SV. Synthetic and natural iron chelators: Therapeutic potential and clinical use. *Future Med Chem*. 2009; 1: 1643-70.

60. Falconer SB, Reid-Yu SA, King AM, Gehrke SS, Wang W, Britten JF, et al. Zinc Chelation by a small-molecule adjuvant potentiates meropenem activity in vivo against NDM-1-producing *Klebsiella pneumoniae*. *ACS Infect Dis*. 2015; 1: 533-43.

61. Evinger M, Agabian N. Envelope-associated nucleoid from *Caulobacter crescentus* stalked and swarmer cells. *J Bacteriol*. 1977; 132: 294-301.

62. Moll A, Thanbichler M. FtsN-like proteins are conserved components of the cell division machinery in proteobacteria. *Mol Microbiol*. 2009; 72: 1037-53.

63. Baba T, Ara T, Hasegawa M, Takai Y, Okumura Y, Baba M, et al. Construction of *Escherichia coli* K-12 in-frame, single-gene knockout mutants: The Keio collection. *Mol Syst Biol*. 2006; 2: 2006 0008.

64. Cherepanov PP, Wackernagel W. Gene disruption in *Escherichia coli*: TcR and KmR cassettes with the option of Flp-catalyzed excision of the antibiotic-resistance determinant. *Gene*. 1995; 158: 9-14.

65. Zaslaver A, Bren A, Ronen M, Itzkovitz S, Kikoin I, Shavit S, et al. A comprehensive library of fluorescent transcriptional reporters for *Escherichia coli*. *Nat Methods*. 2006; 3: 623-8.

66. Datsenko KA, Wanner BL. One-step inactivation of chromosomal genes in *Escherichia coli* K-12 using PCR products. *Proc Natl Acad Sci U S A*. 2000; 97: 6640-5.

CHAPTER 4

Targeting quinolone- and aminocoumarin-resistant bacteria with new gyramide analogs that inhibit DNA gyrase

Adapted from:

Hurley KA[§], Santos TMA[§], Fensterwald MR, Rajendran M, Moore JT, Balmond EI, Blahnik BJ, Faulkner KC, Foss MH, Heinrich VA, Lammers MG, Moore LC, Reynolds GD, Shearn-Nance GP, Stearns BA, Yao ZW, Shaw JT, Weibel, DB. Targeting quinolone- and aminocoumarin-resistant bacteria with new gyramide analogs that inhibit DNA gyrase. *MedChemComm.* 2017; 8: 942-951. ([§]*Denotes equal contribution*).

T.M.A.S. and K.A.H. designed and conducted experiments, analyzed data, and wrote the paper. M.R.F. and M.R. designed and conducted experiments, and analyzed data. J.T.M., E.I.B., B.J.B., K.C.F., M.H.F., V.A.H., M.G.L., L.C.M., G.D.S.-N. conducted experiments. B.A.S. wrote the paper. J.T.S. and D.B.W. designed experiments, analyzed data, and wrote the paper.

ABSTRACT

Bacterial DNA gyrase is an essential type II topoisomerase that enables cells to overcome topological barriers encountered during replication, transcription, recombination, and repair. This enzyme is ubiquitous in bacteria and represents an important clinical target for antibacterial therapy. In this chapter, we report the characterization of three new gyramide analogs—from a library of 183 derivatives—that are potent inhibitors of DNA gyrase and are active against clinical strains of Gram-negative and Gram-positive bacteria. *Escherichia coli* strains resistant to the DNA gyrase inhibitors ciprofloxacin and novobiocin display little cross-resistance to these new gyramides. In vitro studies demonstrate that the new analogs are potent inhibitors of the DNA supercoiling activity of DNA gyrase (IC_{50}s of 47-170 nM) but do not alter the ATPase activity of the enzyme. Although mutations that confer bacterial cells resistant to these new gyramides map to the genes encoding the subunits of the DNA gyrase (*gyrA* and *gyrB* genes), overexpression of GyrA, GyrB, or GyrA and GyrB together does not suppress the inhibitory effect of the gyramides. These observations support the hypothesis that the gyramides inhibit DNA gyrase using a mechanism that is distinct from other known inhibitors.

INTRODUCTION

DNA gyrase is a validated antibiotic target that continues to capture attention in drug discovery [1]. DNA gyrase is a type II topoisomerase consisting of two subunits that combine into a heterotetrameric A2B2 holoenzyme complex and uses the energy from ATP hydrolysis to negatively supercoil double-stranded DNA preceding the replication fork. The GyrA subunit is involved in stabilizing the double-stranded DNA break, passing the second DNA strand through the break, and religating the DNA strands. The GyrB subunit contains the ATP binding site and is involved in ATP hydrolysis [2, 3].

Antibiotics that bind to different regions of DNA gyrase have been reported. Ciprofloxacin (Figure 1A) is a clinical fluoroquinolone antibiotic that binds DNA gyrase between the DNA nucleotides on either side of the double stranded DNA break, prevents DNA religation, and stabilizes double-stranded breaks in the DNA bound to the protein [4]. The formation of linear double stranded DNA triggers the SOS response and inhibits cell division until the DNA is repaired [5]. Novobiocin (Figure 1A) is an aminocoumarin that binds in the ATP pocket of the GyrB subunit and competitively inhibits its ATPase activity [6, 7]. In contrast to ciprofloxacin, novobiocin does not cause DNA damage or activate the SOS response [5]; however, it causes many species of cells to become filamentous [8], which is a hallmark of the SOS response. Both ciprofloxacin and novobiocin also inhibit topoisomerase IV [9-11]—the bacterial topoisomerase involved in decatenation of chromosomes during DNA replication. Ciprofloxacin also binds to the eukaryotic homologue topoisomerase II (topo II) causing associated side effects [12].

The gyramides are a family of synthetic, small molecules that inhibit the type II topoisomerase DNA gyrase [13, 14]; our current data supports these compounds binding to a new site of DNA gyrase [14] that differentiates them from the binding site for ciprofloxacin, novobiocin, and other families of DNA gyrase inhibitors [4, 15, 16]. Mapping amino acid mutations that convey gyramide resistance to *Escherichia coli* cells and comparing to related data for ciprofloxacin and novobiocin reveals that these positions are spatially distinct [14]. Gyramides are specific inhibitors of DNA gyrase and do not inhibit bacterial topoisomerase IV [17]. We hypothesize that DNA gyrase inhibition by the gyramides stalls replication fork progression, impairs chromosome segregation, and initiates the SOS response through a non-canonical pathway that ultimately blocks cell division [17]. A challenge with this family of compounds has been reducing drug efflux out of cells, which has limited in vivo experiments to-date and create a roadblock toward developing antimicrobial agents that are effective against wild-type cells. Using insight gleaned from an analysis of successful antibiotics proved largely ineffective in our design of gyramide analogs [18].

In this chapter, we describe a series of new gyramides with potent activity against DNA gyrase and that have an apparent reduction in efflux from different bacterial species. We tested the compounds for antibacterial activity against 9 strains of non-pathogenic (biosafety level 1, BSL 1) bacteria and 13 pathogenic isolates (BSL 2) to identify compounds with reduced drug efflux, improved inhibitory activity, and extended spectrum. We performed further characterization of three new gyramide analogs (gyramide D, gyramide E, and gyramide F) (Figures 1B and 1C) that fit these criteria, and demonstrate that these compounds have several exciting characteristics: 1) they are among the most potent inhibitors of the supercoiling activity of DNA gyrase

to-date; 2) they have MICs in the single μg/mL range against a range of wild-type, clinical Gram-negative and Gram-positive bacteria; 3) they have activity against *Escherichia coli* strains resistant to ciprofloxacin and novobiocin; and 4) their activity is not antagonized by the overexpression of DNA gyrase (akin to ciprofloxacin). Our data supports the hypothesis that the improvement of the antibacterial activity of these compounds arises from reducing efflux, suggests chemical modifications for reducing the efflux of other aryl-containing antibiotics, and moves these compounds one step further along their development as a new family of antibiotics.

EXPERIMENTAL PROCEDURES

Bacterial strains and growth conditions

Unless stated otherwise, *E. coli* strains were routinely grown aerobically in lysogeny broth (LB) (1% [w/v] tryptone, 0.5% [w/v] yeast extract, and 1% [w/v] NaCl) or in LB medium containing 1.5% (w/v) agar (LB agar) at 37°C. We added ampicillin (50 μg/mL), chloramphenicol (25 μg/mL), or kanamycin (30 μg/mL) to the broth or agar as needed. Chemicals for culture media and culture media reagents were obtained from BD Biosciences (San Jose, CA, USA), Fisher Scientific (Itasca, IL, USA) and Sigma-Aldrich (St. Louis, MO, USA). Ciprofloxacin and novobiocin were obtained from LKT Laboratories (St Paul, MN, USA) and Sigma-Aldrich (St. Louis, MO, USA), respectively. Stock solutions of gyramide D-F were prepared in dimethyl sulfoxide (DMSO), ciprofloxacin was prepared in 1:1 MeOH: 0.1 M HCl and novobiocin was prepared in sterile deionized water. Bacterial strains and plasmids used in this study are listed in Table S1.

Genetic Methods

We followed standard procedures for genomic and plasmid DNA purification, restriction endonuclease digestion, DNA amplification, gene cloning, and transformation. Genomic DNA from *E. coli* strains was isolated using the MasterPure DNA purification kit (Epicentre, Madison, WI, USA). Oligonucleotide primers were obtained from IDT (Coralville, IA, USA), restriction enzymes were obtained from Promega (Madison, WI, USA) or New England Biolabs (Ipswich, MA, USA). We used Q5 High-Fidelity DNA polymerase (New England Biolabs) to produce DNA for cloning and EconoTaq DNA polymerase (Lucigen Corporation, Middleton, WI) for general analytical PCR. PCR products and plasmid constructs were purified using DNA Clean and concentrator kit and Zyppy plasmid miniprep kit, respectively (Zymo Research Corporation, Irvine, CA). We used T4 DNA Ligase (New England Biolabs) or In-Fusion HD Cloning Kit (Clontech Laboratories Inc., Mountain View, CA) for routine cloning procedures and chemical methods to transform *E. coli* strains with plasmids. We verified all cloning and transformation procedures by testing for the presence of antibiotic markers and by PCR analysis followed by DNA sequencing. The primers used in this study are listed in Table S2.

Selection of spontaneous *E. coli* mutants resistant to ciprofloxacin

We grew 20 parallel cultures (2 mL, each) of *E. coli* JW5503 cells initially containing 10^4 colony forming units (c.f.u.)/mL. Following 7 h of incubation at 37°C incubation, we spread the whole cell suspension onto LB agar supplemented with 16 ng/mL (10× MIC) or 25 ng/mL (15× MIC) ciprofloxacin. For enumeration, we performed a 10-fold dilution series of the starter cultures in a solution of 0.1% (w/v)

peptone, spread an aliquot of 100 μL of each dilution onto non-selective LB agar and incubated them for 12-16 h at 37°C. The colonies for each dilution were counted and the starting c.f.u./mL was calculated. Plates were incubated at 37°C in a static incubator for 24-48 h before counting resistant colonies. After 24-48 h, we counted the colonies, isolated one resistant colony from each plate containing resistant mutants, and transferred the colonies to LB broth and LB broth containing ciprofloxacin to confirm that the observed resistance phenotype was a heritable trait. We further confirmed the mutation by sequencing the genes *gyrA* and *gyrB*. To calculate the mutation frequency, we determined the population size plated by enumerating the c.f.u. in triplicate from cultures grown in parallel with those plated on selective media.

Determination of the minimum inhibitory concentration (MIC)

To measure the minimum inhibitory concentration (MIC) of the compounds against *E. coli* strains, we used the broth microdilution method according to the Clinical and Laboratory Standards Institute (CLSI) standards, with some modifications. Briefly, *E. coli* cultures were grown overnight in LB for 12 h at 37°C with agitation (200 r.p.m.). We calibrated the cultures to a final concentration of ~10^5 c.f.u./mL and transferred 100 μL aliquots of the adjusted cultures to a 96-well plate. We transferred additional 100 μL aliquots of the adjusted culture to the top row of wells, added the drug to be tested, and performed 2-fold serial dilutions. Finally, we incubated the plates for 16-18 h at 37°C or 30°C and read the results. The MIC was defined as the lowest concentration of compound in which no visible growth was observed. We performed the assay in duplicate with at least two biological replicates. Control experiments to verify culture viability and sterility were performed in parallel. Additionally, we performed a

preliminary MIC screen of the gyramide analogs against BSL 1 and BSL 2 strains in Müeller-Hinton or Brain-Heart Infusion broth using the aforementioned protocol.

Determination of in vitro DNA supercoiling IC_{50} for *E. coli* DNA gyrase

We determined the IC_{50} for DNA gyrase supercoiling activity in the presence of DNA gyrase inhibitors as previously described [14]. Briefly, the reaction mixture contained 6 μL of 5× buffer [35 mM Tris-HCl (pH 7.5), 24 mM KCl, 4 mM $MgCl_2$, 2 mM dithiothreitol, 1.75 mM ATP, 5 mM spermidine, 0.1 mg/mL BSA, and 6.5% glycerol], 1 U (0.2 μl of 5,000 U/mL) of *E. coli* DNA gyrase (New England Biolabs), 2 μL of different concentrations of compound and 21.3 μL of deionized water to a final volume of 29.5 μL. We initiated the reactions by adding 0.5 μg (0.5 μL of 1,000 μg/mL) of pUC19 substrate (relaxed plasmid) and incubated the tubes for 30 min at 37°C. We immediately quenched the reactions by adding 5 μL of quenching buffer (6× blue/orange loading dye [Promega], 1% [w/v] SDS). We loaded 15 μL aliquots of the reactions into a 0.8% (w/v) agarose gel prepared with 1× Tris-borate-EDTA (TBE, 90 mM Tris-borate, 2 mM EDTA) and we separated the DNA mixtures by electrophoresis at a constant voltage (65 V) for 3 h. We stained the gel in a solution of ethidium bromide (0.5 μg/mL) for 1 h and distained it in deionized water for 30 min. We imaged the gel and performed band densitometry with ImageJ (version 1.48v) to quantitate the intensity of each supercoiled band on the gel for the different concentrations of inhibitor. We used GraphPad Prism (GraphPad Software Inc., La Jolla, CA, USA) to perform non-linear curve fitting of the data and determine the concentration of compound required to inhibit 50% of the production of the fully supercoiled DNA.

Determination of the in vitro ATPase IC_{50} for *E. coli* DNA gyrase

We used an *E. coli* DNA gyrase ATP hydrolysis kit (Profoldin, Hudson, MA, USA) to determine the IC_{50} values of DNA gyrase inhibitors. Briefly, the 30 μL reaction mixture contained 16 μL of water, 3 μL of 10× buffer (20 mM Tris-HCl [pH 8.0], 35 mM NH_4OAc, 4.6% glycerol, 1 mM DTT, 0.005% Brij35, 8 mM $MgCl_2$), 3 μL of 100 μg/mL of DNA, 3 μL of 10× DNA gyrase, and 2 μL of different concentrations of compounds. We initiated the reactions with 3 μL of 2 mM ATP. The reaction was incubated at 25°C for 60 min. We then added 45 μL of dye to stop the reaction and measured light absorbance (λ = 650 nm) using a Tecan Infinite M200 microplate reader (Tecan, Männedorf, Switzerland). To determine IC_{50} values, we plotted the absorbance at 650 nm versus log of the inhibitor concentrations. We used GraphPad Prism to perform non-linear curve fitting of the data and determine the concentration of compound required to inhibit 50% of the ATPase activity of *E. coli* DNA gyrase.

Target-multicopy suppression of DNA gyrase inhibitors

To study the effect of target overexpression on the biological activity of DNA gyrase inhibitors, we performed a target-multicopy suppression experiment. Briefly, *E. coli* JW5503 or *E. coli* JW5503 carrying plasmid pCA24N (empty vector) [19], pCA24N-gyrA, or pCA24N-gyrB were grown overnight in LB for 12 h at 37°C with agitation (200 r.p.m.), diluted (1:100) in fresh LB, and incubated at 37°C with agitation (200 r.p.m.) to an absorbance of ~0.3 (λ = 600 nm). We added isopropyl-β-D-1-thiogalactopyranoside (IPTG) to the final concentrations of 1 μM, 10 μM, or 100 μM, and incubated the cultures for 1.5 h at 37°C with agitation (200 r.p.m.). Following induction, the cultures were used

as inoculum in a modified MIC experiment. We diluted the cultures (1:10,000) in 200 μL of fresh LB supplemented with chloramphenicol (20 μg/mL), different concentrations (1 μM, 10 μM, or 100 μM) of IPTG, and different concentrations of DNA gyrase inhibitor or solvent control. We incubated the plates for 16 h at 37°C with agitation (200 r.p.m.). The MIC was defined as the lowest concentration of antimicrobial agent with no visible growth. We performed the assay in duplicate with, at least, two biological replicates. Control experiments to verify culture viability and sterility were performed in parallel.

Similarly, to test whether the DNA gyrase holoenzyme was necessary to suppress the biological activity of the inhibitors used, we cloned *gyrA* and *gyrB* into different compatible plasmids (pBAD33*-gyrA and pTrc99a-gyrB) that enabled simultaneous overexpression of GyrA and GyrB in cells. Briefly, *E. coli* JW5503 carrying plasmids pBAD33* and pTrc99a (empty vectors), pBAD33*-gyrA and pTrc99a, pBAD33* and pTrc99a-gyrB, or pBAD33*-gyrA and pTrc99a-gyrB were grown overnight in LB for 12 h at 37°C with agitation (200 r.p.m.), diluted (1:100) in fresh LB, and incubated at 37°C with agitation (200 r.p.m.) to an absorbance of ~0.3 (λ = 600 nm). We induced protein expression by adding 1 mM IPTG and 0.2% L-arabinose, and incubated the cultures for 1.5 h at 37°C with agitation (200 r.p.m.). Following induction, the cultures were used as inoculum in a modified MIC experiment. We diluted the cultures (1:10,000) in 200 μL of fresh LB supplemented with ampicillin (50 μg/mL), chloramphenicol (20 μg/mL), 1 mM IPTG, 0.2% L-arabinose, and different concentrations of DNA gyrase inhibitor or solvent control. We incubated the plates for 16 h at 37°C with agitation (200 r.p.m.). The MIC was defined as the lowest concentration of antimicrobial agent with no visible growth. We performed the assay in

duplicate with at least two biological replicates.

To confirm that the genes being overexpressed simultaneously were producing functional GyrA and GyrB, we performed additional experimental controls using *E. coli* mutant strains containing temperature sensitive GyrA or GyrB. Cultures of *E. coli* temperature-sensitive mutants transformed with compatible plasmids harboring *gyrA* or *gyrB* (or the empty vector) were grown overnight in LB broth supplemented with ampicillin (50 μg/mL) and chloramphenicol (25 μg/mL) for 12 h at 30°C with agitation (200 r.p.m.), diluted (1:100) in fresh LB supplemented with the same antibiotics, and incubated at 30°C with agitation (200 r.p.m.) for 2.5 h. We split the culture into two equal aliquots, added 1 mM IPTG and 0.2% L-arabinose to one aliquot to induce expression of the genes of interest, and incubated both cultures (induced and non-induced) for 3 h at 30°C with agitation (200 r.p.m.). Following the incubation time, we calibrated the cultures to an absorbance of 1.0 (λ = 600 nm) [c.f.u./mL = 6×10^8], diluted the cultures serially in 1× PBS buffer (137 mM NaCl, 2.7 mM KCl, 10 mM Na_2HPO4, 1.76 mM KH_2PO4) [pH 7.4], and spotted 5 μL of each dilution on LB agar supplemented with antibiotics and inducer (1 mM IPTG or 0.2% L-arabinose). The plates were incubated at 30°C or 42°C for 16 h.

RESULTS

Discovery and characterization of the antibacterial activity of gyramide D

We previously altered the substituents of the benzyl group in gyramide A—discovered in a high-throughput screen—to create analogs with limited success, including gyramide B and gyramide C [13]. In this paper, we introduce different

functional groups to the arylsulfonamide ring to change its size and polarity (Figure 1B). In lieu of a co-crystal structure to enable a rational optimization of the compounds, we expanded the initial set of compounds reported previously by exploring the diversity available within commercially available aldehydes and sulfonyl chlorides, while avoiding functionality on the two aromatic rings with known metabolic liabilities (e.g., nitro groups). We initially prepared 48 analogs and found that 47 had higher MICs than the parent compounds (gyramide A-C, Figure 1B) against *E. coli* strains. The remaining compound (gyramide D, Figure 1B)—containing a 3-cyano group on the arylsulfonamide ring—was remarkably potent and killed wild-type *E. coli* strains. Based on this compound, we performed a thorough and systematic variation of the two core appendages; i.e., the N-benzyl and N-arylsulfonyl substituents. Although we initially envisioned a matrix of four cores containing 50 appendages, the limited availability of different benzaldehydes, sulfonyl chlorides, and hetero-aromatic substrates created a hurdle. After scrutinizing available building blocks, we settled on an expanded set of cores: a set of three 3-amino-1-benzyl pyrrolidines treated with 31 sulfonyl chlorides and a set of three 3-sulfonamido pyrrolidines benzylated with 30 substituted benzaldehydes and heteroaromatic analogs (Figure S1); the combination of these two sets of intermediates yielded a library consisting of 183 analogs (Figure 1C). Each gyramide analog in the library was synthesized on >5 mg scale and purified to >95% purity by high-performance liquid chromatography. Screening of these 183 compounds as described below revealed two new gyramides (E and F) that we re-synthesized on preparative scale to perform additional experiments (Figure 1C).

We found that inclusion of a 3-cyano group in gyramide D significantly improved the MIC of the compounds against a wild-type laboratory strain of *E. coli* (16

μg/mL) compared to previously reported analogs gyramide A, gyramide B, and gyramide C (activity of >160 μg/mL against wild-type *E. coli*) [14]; gyramide D also displayed activity against an *E. coli* UPEC strain (16 μg/mL), *Edwardsiella tarda* (16 μg/mL), *Salmonella enterica* subsp. *enterica* serovar Typhimurium (S. *enterica* Typhimurium) (2 μg/mL), and *Shigella flexneri* (8 μg/mL) (Table 1).

Gyramide D-F are active against various strains of Gram-negative and Gram-positive bacteria

The antibacterial activity of gyramide D against *E. coli*, *E. tarda*, *S. enterica* Typhimurium, and *S. flexneri* encouraged us to explore additional changes to the substituents on the sulfonamide ring. We were interested in whether we could increase the activity against *E. coli*, identify derivatives that were potent and effective against other Gram-negative bacteria, and discover compounds with a preference for Gram-negative or Gram-positive bacteria. After introducing a series of electron-withdrawing groups into the 3-position of the aryl-sulfonamide ring (not shown), we noticed that a nitrile increased activity and inhibited growth of wild-type *E. coli* cells. Additional modifications eventually produced gyramide E and gyramide F, both of which have an MIC of 8 μg/mL against *E. coli* BW25113 (Figure 1C and Table 1).

Of the Gram-negative strains we tested, gyramide D-F were effective against *E. coli*, *E. tarda*, *S. enterica* Typhimurium, and *S. flexneri* with MICs in the range of 2-16 μg/mL (Table 1). Of the three gyramide analogs, gyramide E was the only compound that was effective against all Gram-positive strains tested (MIC values ranging from 4-16 μg/mL), including *Bacillus cereus*, *Bacillus subtilis*, *Enterococcus faecalis*, *Enterococcus*

faecium, *Staphylococcus aureus* subsp. *aureus*, *Staphylococcus epidermidis*, *Staphylococcus saprophyticus* subsp. *saprophyticus*, *Streptococcus agalactiae*, and *Streptococcus pyogenes*.

Analogs gyramide D-F reduce gyramide efflux in bacteria

Drug efflux systems and membrane permeability are two factors that affect the activity of antimicrobials against Gram-negative and Gram-positive bacteria [20]. To gauge the extent of drug efflux, we measured the MIC of gyramide D-F against an *E. coli* strain lacking the outer membrane component of the AcrAB-TolC efflux pump (TolC): strain JW5503 (derived from *E. coli* BW25113). We used the relative ratio of the MICs of compounds against *E. coli* BW25113 and *E. coli* JW5503 as an indicator of compound efflux, where $MIC_{BW25113}/MIC_{JW5503}$ is 1 in the absence of efflux, and high values indicate more efflux. As a point of reference, gyramide C (a previously reported analogue structurally related to gyramide D [14]) had the same MIC (0.1 μg/mL) as gyramide D against *E. coli* strain JW5503, yet its MIC against *E. coli* BW25113 was >160 μg/mL (a ratio of $MIC_{BW25113}/\ MIC_{JW5503} > 1600$, indicating significant efflux). We found ratios for gyramide D, gyramide E, and gyramide F of 160, 20, and 80, respectively, indicating that the AcrAB-TolC efflux pump complex reduces the potency of the gyramides (Table 1), albeit less so than for previous analogues. Modification of the gyramides to include a cyano group (gyramide D and gyramide F) or a trifluoromethyl group (gyramide E) at the 3-position of the benzenesulfonamide ring reduced efflux significantly; our data suggests that the trifluoromethyl modification has the largest reduction on efflux. To study the role of membrane permeability on the potency of gyramides in *E. coli*, we tested the MIC of gyramide D against a strain with increased membrane permeability, *E. coli* BAS849 [21]. This strain contains multiple mutations,

including changes in *lptD* that alters outer membrane permeability to small organic molecules; although this mutation does not change inner membrane structure per se, it increases the concentration of antibiotics presented at the inner membrane and thereby increases the permeability of lipophilic molecules across this barrier [21, 22]. We found that the MIC of gyramide D against *E. coli* BAS849 is 1 μg/mL and is 8-fold lower than the MIC against its parent strain *E. coli* MC4100 (8 μg/mL), indicating that poor membrane permeability also reduces the antibacterial activity of the gyramides.

E. coli strains resistant to ciprofloxacin and novobiocin are susceptible to gyramide D-F

We evaluated the cross-resistance of gyramide-resistant (Gyr^R) [14], ciprofloxacin-resistant (Cip^R), and novobiocin-resistant (Nov^R) strains of *E. coli* to ciprofloxacin, novobiocin, and gyramide D-F [23]. MIC values of gyramide D-F against the five Gyr^R strains derived from *E. coli* JW5503 were ~10-100-fold higher than against *E. coli* JW5503. Gyr^R strains remained susceptible to ciprofloxacin and novobiocin and the MIC values of these compounds were 1.6-3.2 μg/mL and 0.8 μg/mL, respectively, and thus similar to *E. coli* JW5503 (Table 2). MIC values of gyramide D-F against the Cip^R strains derived from *E. coli* JW5503 were 2-4-fold higher than against *E. coli* JW5503, and the MIC value of novobiocin against the Cip^R strains was 0.8 μg/mL for all the strains, including *E. coli* JW5503 (Table 2). These results demonstrate minor cross-resistance of Gyr^R and Cip^R *E. coli* strains to the gyramides.

Gyramide D-F are effective against Nov^R strains in the presence of 100 μM of the efflux pump inhibitor, phenylalanine arginine β-naphthylamide (PAβN) [23]. We used

PAβN because, unlike the Cip^R and Gyr^R strains, the Nov^R strains contain the TolC protein and therefore are capable of pumping the drug out of the cell [23, 24]. MIC values of gyramide D-F against Nov^R strains were 2-4-fold higher than the MIC values against *E. coli* HB101 (the background strain used to make the Nov^R strains). These results indicate the absence of cross-resistance between novobiocin and gyramide D-F in Nov^R strains. We detected some examples of cross-resistance to ciprofloxacin and novobiocin in Nov^R strains; ciprofloxacin had MIC values of 13 ng/mL and 26 ng/mL against the Nov^R strains CC5 and LE316, respectively, which is 8-fold and 16-fold higher than the MIC observed for the background strain *E. coli* HB101 (Table 2). The cross-resistance between ciprofloxacin and novobiocin in Nov^R strains contrasts with a previous report [25]. Based on the promising potent antibacterial activity of the gyramides and the lack of cross-resistance between gyramide D-F and the known DNA gyrase inhibitors ciprofloxacin and novobiocin, we characterized the activity of these analogs against *E. coli* DNA gyrase in vitro.

Gyramide D-F inhibit the supercoiling activity of DNA gyrase in vitro

We evaluated the effect of gyramide D-F on the DNA supercoiling activity of DNA gyrase as described previously [14]. We measured the 50% inhibitory concentration (IC_{50}) of compounds using *E. coli* DNA gyrase and relaxed pUC19 plasmid as a substrate. IC_{50} values of gyramide D, gyramide E, and gyramide F were 52 ± 9.2, 170 ± 48, and 47 ± 19 nM, respectively. The IC_{50} value of ciprofloxacin and novobiocin was 170 ± 63 nM and 144 ± 20 nM, respectively (Figures 2 and S2). Gyramide IC_{50}s are ~4-fold lower than the corresponding MICs, suggesting that efflux systems and membrane permeability are the primary barriers currently limiting the

activity of the gyramides.

We attempted to measure IC_{50} values of ATPase activity of the tested compounds; however, we were only reliably able to measure an IC_{50} for novobiocin (245 ± 42 nM). We measured the inhibition of ATPase activity of ciprofloxacin, and gyramide D-F up to a concentration of 100 μM and did not observe a decrease in ATPase activity, which is expected for ciprofloxacin [26]; gyramide D-F precipitated at a concentration >100 μM, which invalidates earlier measurements suggesting that these compounds are ATPase inhibitors [17].

Overexpression of GyrA and GyrB does not suppress the biological activity of gyramides

To obtain more insight into the potency of gyramide D and the region of DNA gyrase to which it binds, we performed a target-multicopy suppression experiment. In this experiment, we tested whether an abundance of DNA gyrase outcompetes the toxicity of an inhibitor and its suppression of cell growth. We used two *E. coli* JW5503 strains for these experiments, each containing a *gyrA* or *gyrB* operational reading frame on a multicopy plasmid vector [19]. Overexpression of GyrB—and not GyrA—was sufficient to suppress the inhibitory effect of novobiocin, as cultures of cells harboring pCA24N-gyrB grew at concentrations of novobiocin as high as 51 μg/mL, which corresponds to a >10-fold increase in the MIC observed for *E. coli* JW5503 (Table S3). The result we observed for novobiocin is consistent with the model for it binding to DNA gyrase and its inhibition of the ATP hydrolysis activity of the GyrB subunit [6, 7, 27]. Overexpression of GyrA or GyrB was not sufficient to suppress the susceptibility of cells to ciprofloxacin or gyramide D (Table S3). Although we are unsure of the DNA

gyrase subunit to which the gyramides bind, we anticipated that overexpression of GyrA would reduce the susceptibility of cells to ciprofloxacin.

We hypothesized that the results of the target-multicopy suppression experiment we observed for ciprofloxacin and gyramide D might be due to the requirement of an excess of the DNA gyrase holoenzyme to titrate the effect of the drug. To test whether the DNA gyrase complex suppressed the biological activity of ciprofloxacin and gyramide D, we cloned *gyrA* and *gyrB* into compatible vectors to simultaneously overexpress GyrA and GyrB in *E. coli* cells. To confirm the overexpression of GyrA and GyrB and the formation of the functional DNA gyrase holoenzyme, we performed controls using *E. coli* mutant strains containing temperature sensitive GyrA or GyrB (Figure S3). Simultaneous overexpression of GyrA and GyrB did not suppress the biological activity of ciprofloxacin or gyramide D (Table 3). The results for ciprofloxacin are different from recent studies in which overexpression of DNA gyrase increased the susceptibility of *E. coli* cells to ciprofloxacin from 9 ng/mL to 2 ng/mL, which is attributed to a drug-bound DNA gyrase creating additional DNA damage rather than conferring drug resistance [28]. Our experiments using a single concentration of IPTG for GyrA and GyrB induction from different plasmids and a different nutrient media—from that reported in Palmer and Kishony (2014) [28]— yielded an MIC of 2 ng/mL. Small differences in MICs may be due to differences between the two studies: e.g., growth conditions, strains, and methods for performing measurements. Our results similarly showed that overexpression of DNA gyrase subunits in *E. coli* cells did not reduce their susceptibility to the gyramides toxicity. If the gyramides inhibit DNA gyrase partway through its catalytic cycle as demonstrated for ciprofloxacin [4, 28], overexpression of DNA gyrase subunits may exacerbate cellular toxicity.

DISCUSSION

DNA gyrase inhibitors are one of the most successful classes of clinical antibiotics currently used [29]. Nevertheless, the success of these therapeutic agents has been compromised by the development of drug tolerance and resistance among clinical strains of bacteria [30]. We report the characterization of three new analogs of the gyramides, a family of synthetic small molecules that inhibit bacterial DNA gyrase. Compounds gyramide D and gyramide F both contain a 3-cyano group on the benzenesulfonamide ring (and are identical with the exception of a 6-methyl group on the benzenesulfonamide ring in gyramide F), display narrow spectrum activity against Gram-negative bacteria, and are only active against ~30% of the Gram-negative strains that we tested. The effectiveness of gyramide E against both Gram-negative and Gram-positive bacteria is likely due to the inclusion of the trifluoromethyl group at the 3-position on the benzenesulfonamide ring. It is tempting to point out that gyramide E also differs from gyramide D and gyramide F by incorporation of an arylisopropylether at the other end of the molecule (compared to a phenyl group in gyramide D and gyramide F); however, this difference has no obvious effect on gyramide efflux. We support this hypothesis with the observation that gyramide A is very similar in structure to gyramide E with the exception of a 3-fluoro group (in gyramide A) compared to a 3-trifluoromethyl group (in gyramide E), and yet the compounds have extremely different efflux profiles from a comparison of their MICs against *E. coli* BW25113 and JW5503. It may also be possible that gyramide E also targets DNA gyrase from different organisms effectively.

Although we do not yet understand the structural and biochemical basis for the

difference in the sensitivity of DNA gyrase from different organisms (i.e., Gram-negative versus Gram-positive bacteria), previous studies of quinolones suggested that the extended α4-helix domain of *S. aureus* GyrA is partially responsible for the increased resistance of *S. aureus* DNA gyrase to quinolones compared to *E. coli* DNA gyrase, and the higher concentration of potassium glutamate in the cytoplasm of *S. aureus* modulates this effect [31]. The differences in the activity that we observed for the gyramide analogs against different organisms could similarly connect back to the DNA-DNA gyrase-gyramide ternary complex, the intracellular environment in which these compounds are active, or a combination of these factors.

Many antibiotics are transported out of Gram-negative organisms by a bacterial efflux transporter in the resistance-nodulation-division (RND) protein family that spans the cell envelope [32, 33]; specifically, the AcrAB-TolC tripartite pump is found in *E. coli*, *Salmonella* spp., and *Shigella* spp. and contributes to multidrug resistance [33-35]. Our observation that gyramide D-F are most active against strains of the Gram-negative bacteria *E. coli*, S. *enterica* Typhimurium, and *S. flexneri*—and very potent against strains harboring the Δ*tolC* mutation—supports the hypothesis that the cyano and trifluoromethyl modifications in the 3-position of the benzenesulfonamide ring reduce drug efflux against this family of drug pumps.

Five efflux drug pump families [ATP binding cassette (ABC), major facilitator superfamily (MFS), multidrug and toxin extrusion (MATE), RND, and small multidrug resistance (SMR)] pump antibiotics out of Gram-positive cells [36]. Surprisingly, gyramide E—and not gyramide D and F—is also active against Gram-positive bacteria, suggesting that the trifluoromethyl modification to the benzenesulfonamide ring may play a unique role in reducing its specificity for pumping by these five efflux protein

families. Lacking a definitive set of molecular design rules for drug reducing efflux by bacteria, and taking into consideration that many clinical antibiotics contain an arylfluoro group (e.g., the entire family of fluoroquinolones), replacing this group with a trifluoromethyl moiety may reduce efflux further, expand the activity of drugs to Gram-positive organisms, contribute to understanding bacterial efflux mechanisms, and contribute to antibiotic development.

Importantly, the gyramides are still effective against *E. coli* strains resistant to the known DNA gyrase inhibitors ciprofloxacin and novobiocin, indicating no cross-resistance when bacteria with altered susceptibility to ciprofloxacin or novobiocin are treated with gyramide D-F. Our results imply that the mutations that confer resistance to ciprofloxacin and novobiocin occur in a region of DNA gyrase that does not affect the binding of gyramides to DNA gyrase. Further structural biology data can provide insight into the region of DNA gyrase to which the gyramides bind. We observed that two of the Nov^R mutants are resistant to ciprofloxacin, which may arise from uncharacterized mutations.

Gyramide D and F are more potent inhibitors of the in vitro DNA supercoiling activity of *E. coli* DNA gyrase than ciprofloxacin, novobiocin, gyramide E, and the gyramide analogs that we reported previously [14]. Importantly, we previously demonstrated that the gyramides do not affect the activity of other type II topoisomerases [17]. When testing the inhibition of the ATPase activity of DNA gyrase, we observed gyramide D-F precipitate at a concentration >100 μM and therefore obfuscate absorbance measurement, which previously led to the incorrect conclusion that gyramide A competitively inhibited the ATPase activity of DNA gyrase at millimolar concentrations [17]. We do not currently have an explanation for the

reduction in the activity of gyramide E (3-trifluoromethyl modification) against *E. coli* DNA gyrase compared to gyramide D and F (3-cyano modification).

Our investigation of the inhibition of ATPase activity and overexpression studies of different DNA gyrase subunits suggests that gyramide D does not compete directly for the ATP binding site. Unlike novobiocin, gyramide D did not inhibit the ATPase activity of DNA gyrase and overexpression of GyrB did not promote resistance to gyramide D. Overexpression of both GyrA and GyrB in the same cell did not affect the antibacterial activity of either ciprofloxacin or gyramide D. However, it has been recently demonstrated that simultaneous overexpression of GyrA and GyrB exacerbates the antibacterial activity of ciprofloxacin. This effect could be caused by an increase in the amount of DNA gyrase-DNA bound complexes and covalent attachment of ciprofloxacin to the complexes [28]. Gyramide D may also create DNA gyrase-DNA bound complexes that are toxic to cells and overexpression of GyrA and GyrB may not reduce susceptibility to the compound. We have previously shown that the mutations conferring resistance to gyramides do not map to the same region as mutations conferring resistance to quinolones [14].

Our previous and current data support the hypothesis that the gyramides may bind to a new site on DNA gyrase and operate through a new mechanism of inhibiting DNA replication and, consequently, bacterial cell growth. We hypothesize that gyramides inhibit DNA gyrase during its catalytic cycle, resulting in stalled DNA-bound DNA gyrase. To test this hypothesis, we are currently working on the structural biology of the gyramide-DNA gyrase complex and on the synthesis of gyramide analog probes containing chemical modifications that can be used in photo-induced crosslinking studies.

CONCLUSIONS

We report new potent analogs of the gyramides that display broad spectrum and specific antibacterial activity. The observation that *E. coli* strains resistant to ciprofloxacin and novobiocin are not resistant to gyramides supports the hypothesis that the gyramides bind to a new site on DNA gyrase and exhibit a novel mechanism of inhibiting DNA replication and cell division. It is possible that gyramides inhibit DNA gyrase partway through its catalytic cycle resulting in stalled DNA-bound DNA gyrase.

ACKNOWLEDGEMENTS

We acknowledge materials from Anthony Maxwell (*E. coli* HB101, CC5, CC7, and LE316), Kenneth Kreuzer (*E. coli* KNK453), Sean Brady (*E. coli* BAS849), and Rodney Welch (*E. coli* UPEC). This research was supported by the National Institutes of Health (1DP2OD008735, D.B.W.), the Human Frontiers Science Program (RGY0076/2013, D.B.W.), and partially supported by Venture Catalyst in the UC Davis Office of Research through a Science Translation and Innovative Research (STAIRTM, J.T.S.) Grant.

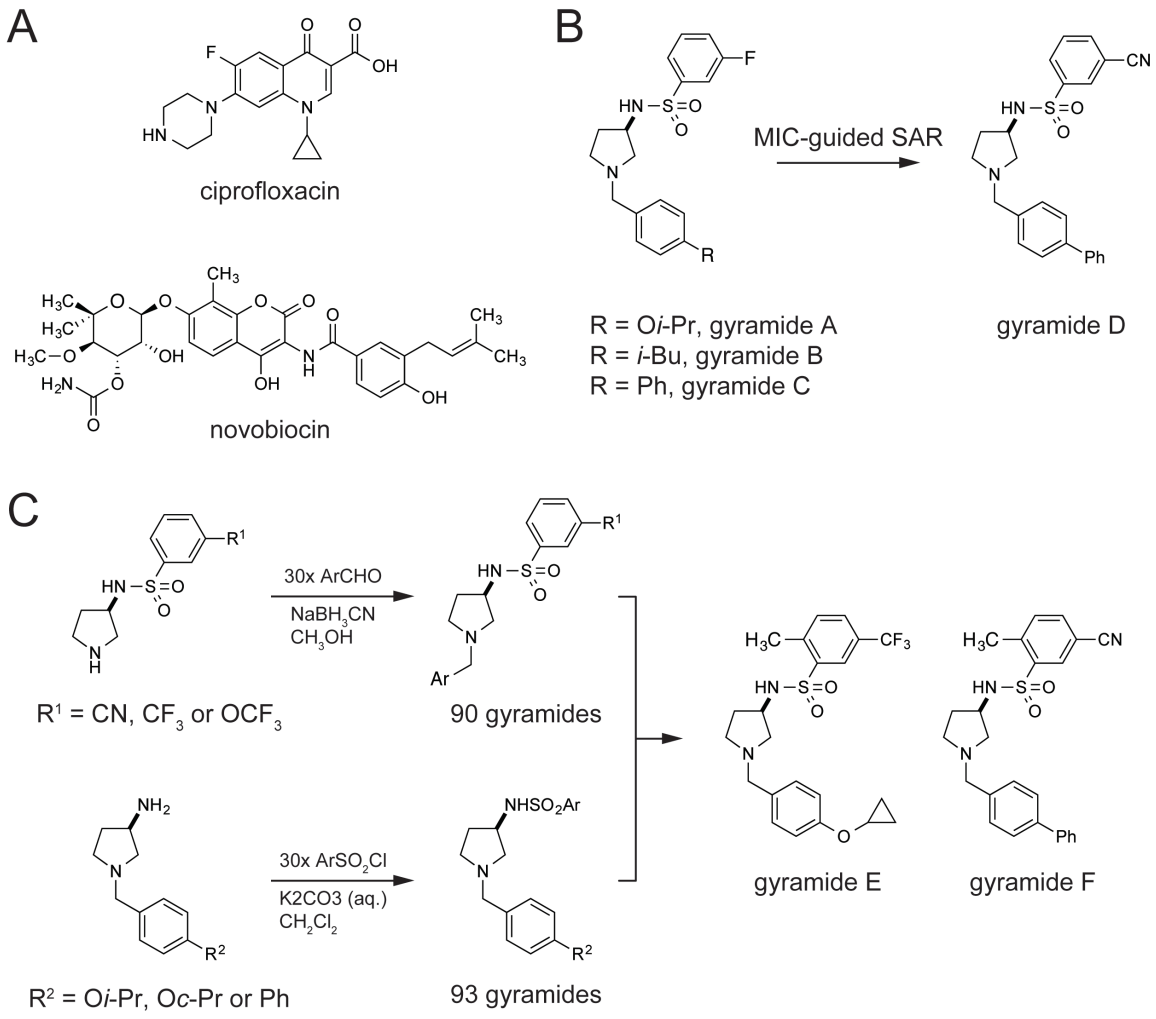

Figure 1. Chemical structure of compounds used in this study and library design of gyramide analogs.

(A) The chemical structures of ciprofloxacin and novobiocin.

(B) The chemical structures of gyramide D. Gyramide D was created from a MIC-guided structure-activity relationship study of gyramide A-C and was used as a lead structure for further analog design and synthesis.

(C) Design of a chemical library of 183 gyramide analogs. Two reactions were performed with 30 aldehydes (and 3 arylsulfonamides) and 31 sulfonyl chlorides (and 3 arylamines) to create 183 gyramide analogs (Figure S1).

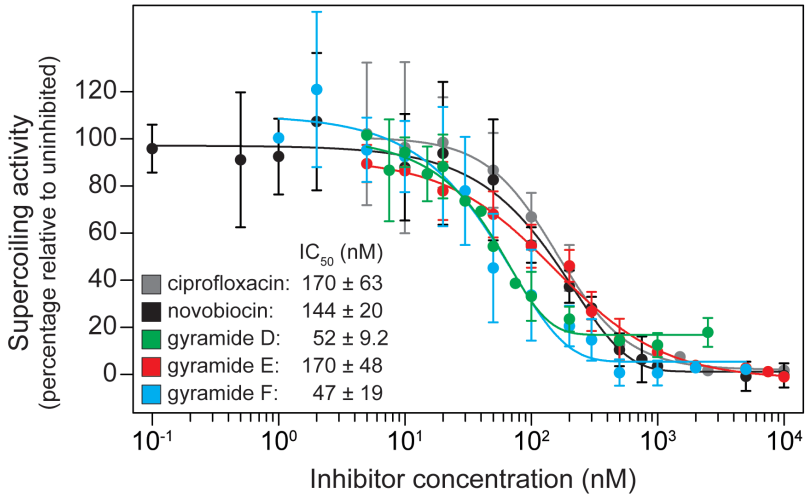

Figure 2. Dose-response curves for DNA gyrase-dependent supercoiling activity in the presence of ciprofloxacin, novobiocin, gyramide D, gyramide E, or gyramide F.

We performed DNA supercoiling reactions with *E. coli* DNA gyrase, relaxed pUC19 plasmid substrate, and various concentrations of ciprofloxacin, novobiocin, gyramide D, gyramide E, or gyramide F. Reactions were run for 30 min and the DNA was separated on a 0.8% (w/v) agarose gel for 3 h. We stained the DNA by immersing the gel in a solution of 0.5 μg/mL ethidium bromide for 1 h. The fluorescence intensity of the supercoiled DNA band was normalized to the DMSO solvent control and plotted for each concentration of compound tested (Figure S3). Each reaction was performed in triplicate. Error bars indicate the standard deviation.

Table 1. MICs of gyramide D, gyramide E, and gyramide F against Gram-negative and Gram-positive bacterial strains.

Bacterial strains	**Compound (μg/mL)**		
	Gyramide D	**Gyramide E**	**Gyramide F**
E. coli BW25113	16	8	8
E. coli JW5503	0.1	0.4	0.1
E. coli MC4100	8	16	8
E. coli BAS849 [a]	1	1	0.5
E. coli UPEC *	16	>16	>16
Acinetobacter baumannii *	>16	>16	>16
Edwardsiella tarda *	16	8	8
Enterobacter aerogenes *	>16	>16	>16
Klebsiella pneumoniae	>16	>16	>16
Morganella morganii *	>16	>16	>16
Pseudomonas aeruginosa	>16	>16	>16
Salmonella enterica Typhimurium	2	4	2
Shigella flexneri	8	4	4
Bacillus cereus	>16	8	>16
Bacillus subtilis	>16	8	>16
Enterococcus faecalis	>16	16	>16
Enterococcus faecium	>16	8	>16
Staphylococcus aureus *	>16	8	>16
Staphylococcus epidermidis *	>16	8	>16
Staphylococcus saprophyticus *	>16	8	>16
Streptococcus agalactiae	>16	8	>16
Streptococcus pyogenes	>16	4	>16

[a] This is a hyperpermeable *E. coli* strain derivative of *E. coli* MC4100.

* Denotes clinical isolates.

Table 2. MIC of ciprofloxacin, novobiocin, gyramide D, gyramide E, and gyramide F against *E. coli* and resistant mutants.

Bacterial strains [a]	**Compound**				
	Ciprofloxacin (ng/mL)	**Novobiocin (μg/mL)**	**Gyramide D (μg/mL)**	**Gyramide E (μg/mL)**	**Gyramide F (μg/mL)**
E. coli JW5503	1.6	0.8	0.1	0.4	0.1
Gyr^R *E. coli*					
GyrA – Pro35Thr	1.6	0.8	10	11	5.4
GyrA – Phe96Leu	3.2	0.8	10	11	2.7
GyrA – Ser97Pro	1.6	0.8	>10	22	22
GyrA – His45Tyr	3.2	0.8	10	22	22
GyrB – Thr508Met	3.2	0.8	10	5.5	1.3
Cip^R *E. coli* [b]					
GyrA – Ser83Leu	6.4	0.8	0.2	0.4	0.2
GyrA – Asp87Gly	16	0.8	0.4	0.8	0.2
GyrA – Asp87Gly	32	0.8	0.4	0.2	0.1
GyrB – Ser464Phe	16	0.8	0.2	1.6	0.4
E. coli HB101	1.6	>100	>16	4	1
E. coli HB101 (+ 100 μM PAβN)	1.6	3.2	0.1	0.1	0.1
Nov^R *E. coli* [c]					
GyrB – Arg136His (CC5)	13	102	0.2	0.4	0.2
GyrB – Arg136Ser (CC7)	3.2	6.4	0.1	0.2	0.1
GyrB – Arg136Val (LE316)	26	12.8	0.2	0.2	0.2

[a] All the Gyr^R and Cip^R mutants are derived from *E. coli* JW5503 ([14] and this study), while Nov^R mutants are derived from *E. coli* HB101 [23].

[b] We isolated the Cip^R strains from a spontaneous resistant mutant screen and

determined that 3 of the 4 mutations in *gyrA* that conferred resistance to ciprofloxacin have been confirmed in other studies [37, 38].

[c] The MIC determination for Nov^R strains was performed in LB broth supplemented with the efflux pump inhibitor, phenylalanine arginine β-naphthylamide (PAβN). We used PAβN because these strains contain an intact *tolC* gene.

Table 3. Target overexpression confers resistance to novobiocin, but not to ciprofloxacin or gyramide D.

Overexpression condition		Compound		
(*gyrA*/*gyrB*)	Induction	Ciprofloxacin (ng/mL)	Novobiocin (μg/mL)	Gyramide D (μg/mL)
(–/–)	+	2.1	0.4	0.2
	–	2.1	0.4	0.2
(+/–)	+	2.1	0.8	0.1
	–	2.1	0.8	0.2
(–/+)	+	2.1	6.3	0.1
	–	2.1	0.8	0.2
(+/+)	+	2.1	3.2	0.1
	–	2.1	0.4	0.2

SUPPLEMENTARY INFORMATION

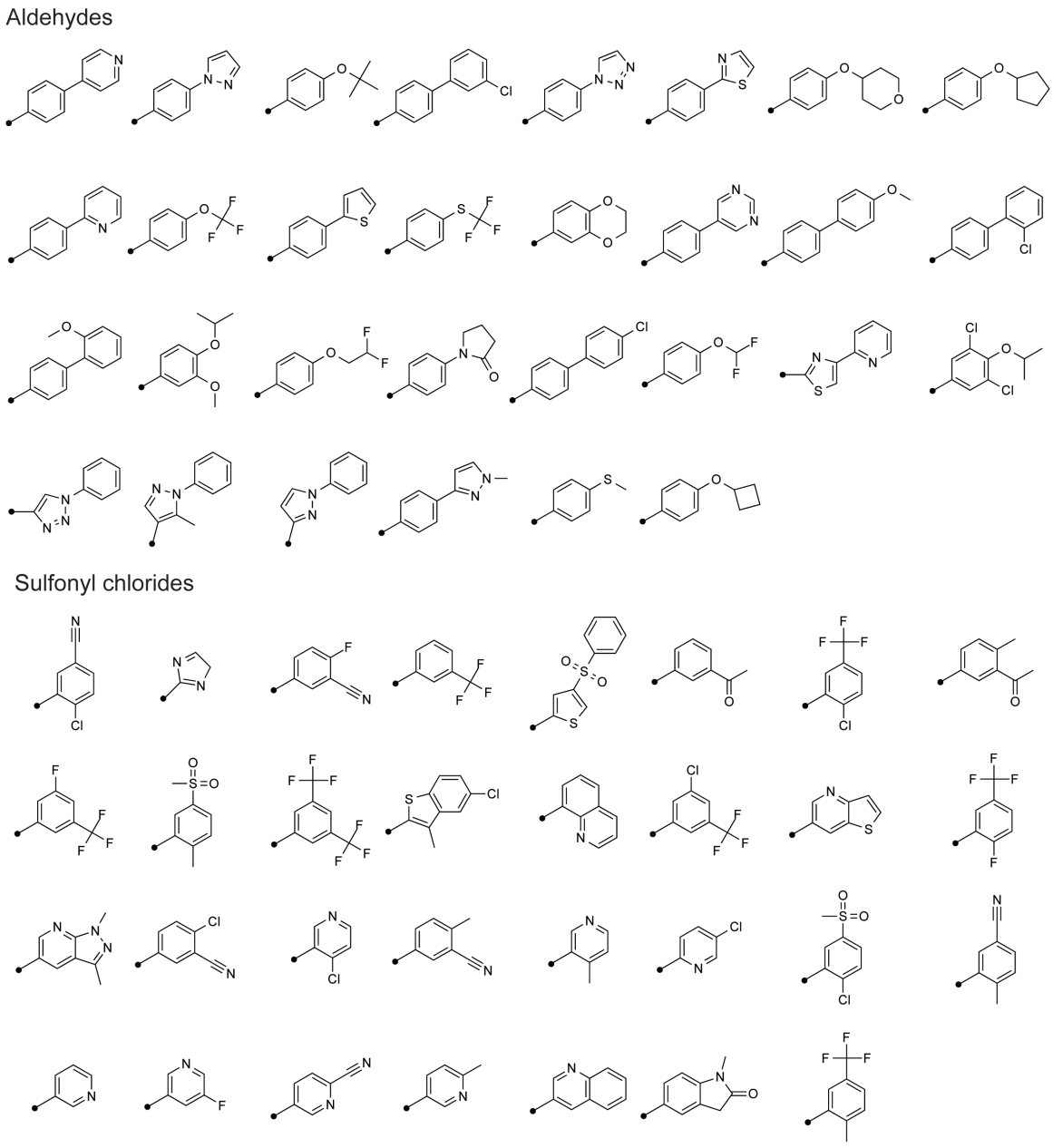

Figure S1. The starting materials used to synthesize all 183 gyramide analogs.

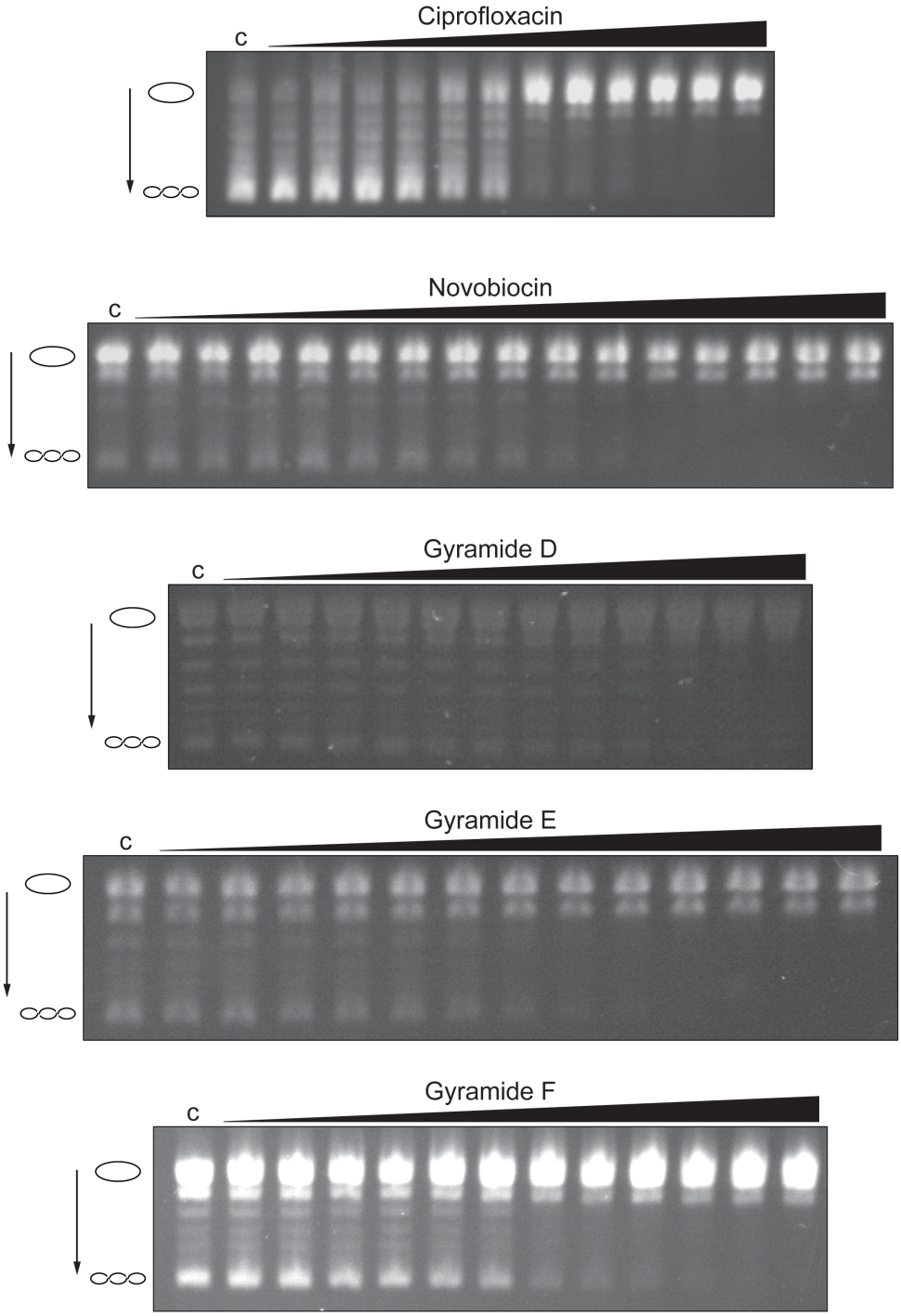

Figure S2. Inhibition of DNA gyrase supercoiling activity by ciprofloxacin, novobiocin, gyramide D, gyramide E, and gyramide F.

A representative gel obtained for the analysis of the inhibition of DNA gyrase supercoiling activity for each compound. The open circle graphic represents relaxed closed circular DNA (plasmid pUC19), the coiled graphic represents supercoiled DNA, and the arrow shows the direction of increased mobility of supercoiled DNA states. Lane "c" indicates the reaction correspondent to the solvent control (no compound added to the supercoiling reaction). The other lanes on the gel show increasing concentrations of compound.

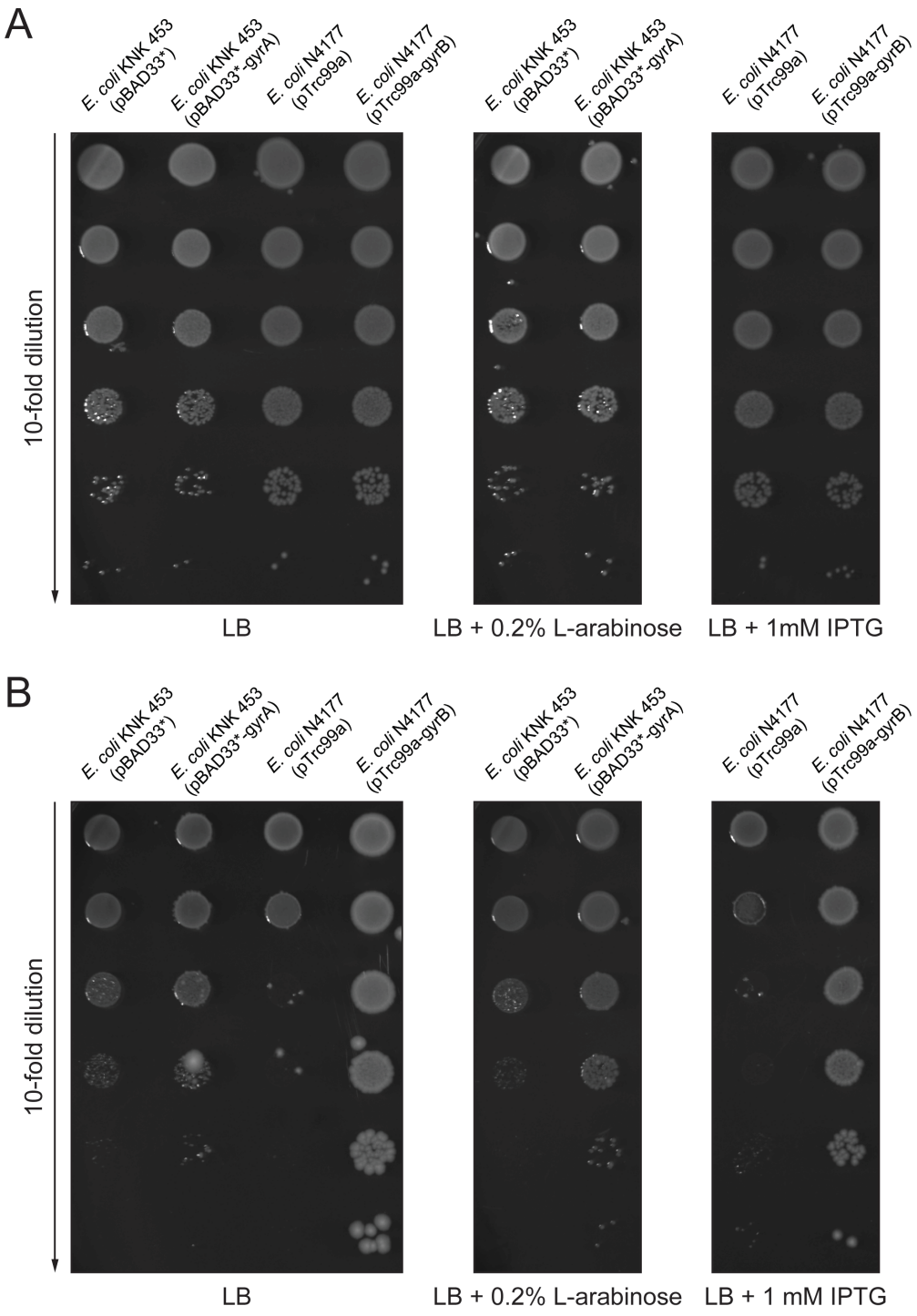

Figure S3. Growth assay of *E. coli* mutant strains containing temperature sensitive GyrA (*E. coli* KNK453) or GyrB (*E. coli* N4177).

The plates were incubated at 30°C (permissive temperature, A) or at 42°C (non-permissive temperature, B) for 16 h. Aliquots of 10-fold serial dilutions (5 μL, ~10^7-10^2 c.f.u./mL) from induced cultures were spotted on LB agar, LB agar supplemented with ampicillin (50 μg/mL) and 1 μM IPTG, or chloramphenicol (25 μg/mL) and 0.2% L-arabinose.

Table S1. Bacterial strains and plasmids used in this study.

Designation	Genotype or description	Source or reference
Bacterial strains		
E. coli BAS849	MC4100 *imp*-4213	[21]
E. coli CC5	GC→AT transition, position 407 of *gyrB* (Arg136→His), Nov^R	[23]
E. coli CC7	CG→AT transversion, position 406 of *gyrB* (Arg136→Ser), Nov^R	[23]
E. coli Cip^R (1)	CG→TA transition, position 248 of *gyrA* (Ser83→Leu), Cip^R	This study
E. coli Cip^R (2)	AT→GC transition, position 260 of *gyrA* (Asp87→Gly), Cip^R	This study
E. coli Cip^R (3)	GC→TA transversion, position 259 of *gyrA* (Asp87→Tyr), Cip^R	This study
E. coli Cip^R (4)	CG→TA transition, position 1,391 of *gyrB* (Ser464→Phe), Cip^R	This study
E. coli DH5α	F^- Δ(*argF-lac)169* ϕ80d*lacZ*(M15) Δ*phoA8 glnV44*(AS) λ^- *deoR481 rfbC1*? *gyrA96*(NalR) *recA1 endA1 thiE1 hsdR17*	CGSC #12384 [a]
E. coli Gyr^K (1)	CG→AT transversion, position 103 of *gyrA* (Pro35→Thr), Gyr^K	[14]
E. coli Gyr^K (2)	TA→CG transition, position 289 of *gyrA* (Ser97→Pro), Gyr^K	[14]
E. coli Gyr^R (3)	TA→CG transition, position 286 of *gyrA* (Phe96→Leu), Gyr^R	[14]
E. coli Gyr^K (4)	CG→TA transition, position 133 of *gyrA* (His45→Tyr)	[14]
E. coli Gyr^K (5)	CG→TA transition, position 1,523 of *gyrB* (Thr508→Met)	[14]
E. coli HB101	F^- *mcrB mrr hsdS20*(rB^- mB^-) *recA13 leuB6 ara-14 proA2 lacY1 galK2 xyl-5 mtl-1 rpsL20*(Sm^R) *glnV44* λ^-	[23]
E. coli JW5503	BW25113, Δ*tolC732*::*kan* [b]	Keio collection [39]
E. coli KNK453	It contains a temperature sensitive mutation in the gene *gyrA*, [*gyrA43*(ts)]	CGSC #6972 [40]
E. coli LE316	GC→TA transversion, position 491 of *gyrB* (Gly164→Val), Nov^R	[41]
E. coli MC4100	F^- $[araD139]_{B/r}$ Δ(*argF-lac)169* λ^- *e14- flhD5301* Δ(*fruK-*	CGSC #6152

	yeiR)*725*(*fruA25*) *relA1 rpsL150*(strR) *rbsR22* Δ(*fimB-fimE*)*632*(*::IS1*) *deoC1*	
E. coli MG1655	$F^- \lambda^-$ *rph−1*	CGSC #6300
E. coli N4177	It contains a temperature sensitive mutation in the gene *gyrB*, [*gyrB203*(ts)]	CGSC #6462 [42]
Acinetobacter baumannii	Isolated from urine	ATCC 19606 [c]
Bacillus cereus	Origin unavailable	ATCC 14579
Edwardsiella tarda	Isolated from human feces	ATCC 15947
Enterobacter aerogenes	Isolated from sputum collected at South Carolina Department of Health and Environmental Control	ATCC 13048
Enterococcus faecalis	Origin unavailable	ATCC 19433
Enterococcus faecium	Origin unavailable	ATCC 19434
Klebsiella pneumoniae subsp. *pneumoniae*	Origin unavailable	ATCC 13883
Morganella morganii subsp. *morganii*	Isolated from patient with summer diarrhea	ATCC 25830
Pseudomonas aeruginosa	Origin unavailable	ATCC 10145
Shigella flexneri	Origin unavailable	ATCC 29903
Salmonella enterica subsp. *enterica* serovar Typhimurium	Origin unavailable	ATCC 29630

Staphylococcus aureus subsp. *aureus*	Isolated from pleural fluid	ATCC 12600
Staphylococcus epidermidis	Isolated from a nose	ATCC 14990
Staphylococcus saprophyticus subsp. *saprophyticus*	Isolated from urine	ATCC 15305
Streptococcus agalactiae	Origin unavailable	ATCC 13813
Streptococcus pyogenes	Origin unavailable	ATCC 12344
Plasmids [d]		
pBAD33* [e]	Cm^R, P_{ara} promoter, pBAD33 containing *araC*-C280* mutation	[43]
pBAD33*-gyrA	Encodes GyrA regulated by an arabinose-inducible promoter	This study
pTrc99a	Amp^K, P_{trc} promoter, a derivative of pBR322	Amersham Pharmacia
pTrc99a-gyrB	Encodes GyrB regulated by a lactose-inducible promoter	This study
pCA24N	Cm^K, P_{lac} promoter, a derivative of pGEX-2TK	[19]
pCA24N-gyrA	Encodes GyrA regulated by a lactose-inducible promoter	[19]
pCA24N-gyrB	Encodes GyrB regulated by a lactose-inducible promoter	[19]

[a] CGSC, Coli Genetic Stock Center, Yale University, New Haven, Connecticut.

[b] Allele numbers as indicated in the CGSC.

[c] ATCC, American Type Culture Collection, Manassas, Virginia.

[d] Plasmids expressing genes in an operon are described using the convention "backbone-gene".

[e] The *araC*-C280* mutation enables more efficiently compatible co-induction of IPTG-inducible and arabinose-inducible promoter systems [43].

Abbreviation: Amp, ampicillin; Cip, ciprofloxacin; Cm, chloramphenicol; Gyr, gyramide; Nov, novobiocin; R, resistance.

Table S2. Primers used in this study.

Primer [a]	**Sequence (5′–3′)** [b]	**Reference**
gyrA-F	GGGCTAGCGAATTC**GAGCTC**AGGAAGGTGCCTT**ATG**AGCGACCT TGC	This study
gyrA-R	GCAGGTCGAC**TCTAGA*TTA***TTCTTCTTCTGGCTCGTCGTCAACGTC CACTTCCGG	This study
gyrB-F	ACAGACCATG**GAATTC**AGGAAGGTGCCTT**ATG**TCGAATTCTTATG	This study
gyrB-R	CGACTCTAGA**GGATCC*TTA***AATATCGATATTCGCCGCTTTCAGG	This study
pBAD33*-F	GTCACACTTTGCTATGCCATA	[43]
pBAD33*-R	CTGCGTTCTGATTTAATCTGT	[43]
pTrc99a-F	AGCGGATAACAATTTCACACAGG	[44]
pTrc99a-R	GATTTAATCTGTATCAGG	[44]

[a] Oligonucleotide primers were from Integrated DNA technology, IDT (Coraville, IA). Primer names correspond to the gene that the primer amplifies; F, forward primer; R, reverse primer.

[b] The restriction sites used for cloning are in bold. Ribosomal binding site (RBS) are underlined. Start codons are in bold and underlined. Stop codons are italicized and bold.

Table S3. The minimum inhibitory concentration (MIC) of ciprofloxacin, novobiocin, and gyramide D against *E. coli* JW5503 overexpressing GyrA or GyrB.

Bacterial strain	**IPTG (μM)**	**Compound**		
		Ciprofloxacin (ng/mL)	**Novobiocin (μg/mL)**	**Gyramide D (μg/mL)**
E. coli JW5503	0	2.1	0.8	0.1
	10	2.1	0.8	0.1
	100	2.1	0.8	0.1
	1,000	2.1	0.8	0.1
E. coli JW5503 (pCA24N)	0	2.1	0.8	0.1
	10	2.1	0.8	0.1
	100	2.1	0.8	0.1
	1,000	2.1	0.8	0.1
E. coli JW5503 (pCA24N-gyrA)	0	2.1	0.4	0.1
	10	2.1	0.4	0.1
	100	2.1	0.4	0.1
	1,000	2.1	0.4	0.1
E. coli JW5503 (pCA24N-gyrB)	0	2.1	0.4	0.1
	10	2.1	0.8	0.1
	100	1.0	51	0.1
	1,000	1.0	51	0.1

REFERENCES

1. Sanyal G, Doig P. Bacterial DNA replication enzymes as targets for antibacterial drug discovery. *Exp Op Drug Disc*. 2012; 7: 327-39.
2. Bush NG, Evans-Roberts K, Maxwell A. DNA Topoisomerases. *EcoSal Plus*. 2015; 6: ESP-0010-0014.
3. Gubaev A, Klostermeier D. The mechanism of negative DNA supercoiling: A cascade of DNA-induced conformational changes prepares gyrase for strand passage. *DNA Repair* (Amst). 2014; 16: 23-34.
4. Bax BD, Chan PF, Eggleston DS, Fosberry A, Gentry DR, Gorrec F, et al. Type IIA topoisomerase inhibition by a new class of antibacterial agents. *Nature*. 2010; 466: 935-40.
5. Schroder W, Goerke C, Wolz C. Opposing effects of aminocoumarins and fluoroquinolones on the SOS response and adaptability in *Staphylococcus aureus*. *J Antimicrob Chemother*. 2013; 68: 529-38.
6. Maxwell A. The interaction between coumarin drugs and DNA gyrase. *Mol Microbiol*. 1993; 9: 681-6.
7. Lamour V, Hoermann L, Jeltsch JM, Oudet P, Moras D. An open conformation of the *Thermus thermophilus* gyrase B ATP-binding domain. *J Biol Chem*. 2002; 277: 18947-53.
8. Nonejuie P, Burkart M, Pogliano K, Pogliano J. Bacterial cytological profiling rapidly identifies the cellular pathways targeted by antibacterial molecules. *Proc Natl Acad Sci U S A*. 2013; 110: 16169-74.
9. Khodursky AB, Zechiedrich EL, Cozzarelli NR. Topoisomerase IV is a target of quinolones in *Escherichia coli*. *Proc Natl Acad Sci U S A*. 1995; 92: 11801-5.
10. Hardy CD, Cozzarelli NR. Alteration of *Escherichia coli* topoisomerase IV to novobiocin resistance. *Antimicrob Agents Chemother*. 2003; 47: 941-7.
11. Alt S, Mitchenall LA, Maxwell A, Heide L. Inhibition of DNA gyrase and DNA topoisomerase IV of *Staphylococcus aureus* and *Escherichia coli* by aminocoumarin antibiotics. *J Antimicrob Chemother*. 2011; 66: 2061-9.
12. Bredberg A, Brant M, Jaszyk M. Ciprofloxacin-induced inhibition of topoisomerase II in human lymphoblastoid cells. *Antimicrob Agents Chemother*. 1991; 35: 448-50.
13. Mukherjee S, Robinson CA, Howe AG, Mazor T, Wood PA, Urgaonkar S, et al. N-Benzyl-3-sulfonamidopyrrolidines as novel inhibitors of cell division in *E. coli*. *Bioorg Med Chem Lett*. 2007; 17: 6651-5.
14. Foss MH, Hurley KA, Sorto N, Lackner LL, Thornton KM, Shaw JT, et al. N-benzyl-3-sulfonamidopyrrolidines are a new class of bacterial DNA gyrase inhibitors. *ACS Med Chem Lett*. 2011; 2: 289-92.

15. Edwards MJ, Flatman RH, Mitchenall LA, Stevenson CE, Le TB, Clarke TA, et al. A crystal structure of the bifunctional antibiotic simocyclinone D8, bound to DNA gyrase. *Science*. 2009; 326: 1415-8.

16. Black MT, Stachyra T, Platel D, Girard AM, Claudon M, Bruneau JM, et al. Mechanism of action of the antibiotic NXL101, a novel nonfluoroquinolone inhibitor of bacterial type II topoisomerases. *Antimicrob Agents Chemother*. 2008; 52: 3339-49.

17. Rajendram M, Hurley KA, Foss MH, Thornton KM, Moore JT, Shaw JT, et al. Gyramides prevent bacterial growth by inhibiting DNA gyrase and altering chromosome topology. *ACS Chem Biol*. 2014; 9: 1312-9.

18. O'Shea R, Moser HE. Physicochemical properties of antibacterial compounds: implications for drug discovery. *J Med Chem*. 2008; 51: 2871-8.

19. Kitagawa M, Ara T, Arifuzzaman M, Ioka-Nakamichi T, Inamoto E, Toyonaga H, et al. Complete set of ORF clones of *Escherichia coli* ASKA library (a complete set of *E. coli* K-12 ORF archive): Unique resources for biological research. *DNA Res*. 2005; 12: 291-9.

20. Nikaido H. Prevention of drug access to bacterial targets: Permeability barriers and active efflux. *Science*. 1994; 264: 382-8.

21. Sampson BA, Misra R, Benson SA. Identification and characterization of a new gene of *Escherichia coli* K-12 involved in outer membrane permeability. *Genetics*. 1989; 122: 491-501.

22. Eggert US, Ruiz N, Falcone BV, Branstrom AA, Goldman RC, Silhavy TJ, et al. Genetic basis for activity differences between vancomycin and glycolipid derivatives of vancomycin. *Science*. 2001; 294: 361-4.

23. Contreras A, Maxwell A. *gyrB* mutations which confer coumarin resistance also affect DNA supercoiling and ATP hydrolysis by *Escherichia coli* DNA gyrase. *Mol Microbiol*. 1992; 6: 1617-24.

24. Augustus AM, Celaya T, Husain F, Humbard M, Misra R. Antibiotic-sensitive TolC mutants and their suppressors. *J Bacteriol*. 2004; 186: 1851-60.

25. Howard BM, Pinney RJ, Smith JT. Studies on mutational cross-resistance between ciprofloxacin, novobiocin and coumermycin in *Escherichia coli* and *Staphylococcus warneri*. *Microbios*. 1993; 75: 185-95.

26. Shapiro AB, Andrews B. Allosteric inhibition of the DNA-dependent ATPase activity of *Escherichia coli* DNA gyrase by a representative of a novel class of inhibitors. *Biochem Pharmacol*. 2012; 84: 900-4.

27. Maxwell A. DNA gyrase as a drug target. *Trends Microbiol*. 1997; 5: 102-9.

28. Palmer AC, Kishony R. Opposing effects of target overexpression reveal drug mechanisms. *Nat Commun*. 2014; 5: 4296.

29. Lewis K. Platforms for antibiotic discovery. *Nat Rev Drug Discov*. 2013; 12: 371-87.

30. Jacoby GA. Mechanisms of resistance to quinolones. *Clin Infect Dis*. 2005; 41 Suppl 2: S120-6.

31. Strahilevitz J, Robicsek A, Hooper DC. Role of the extended alpha4 domain of *Staphylococcus aureus* gyrase A protein in determining low sensitivity to quinolones. *Antimicrob Agents Chemother*. 2006; 50: 600-6.

32. Nikaido H, Pages JM. Broad-specificity efflux pumps and their role in multidrug resistance of Gram-negative bacteria. *FEMS Microbiol Rev*. 2012; 36: 340-63.

33. Anes J, McCusker MP, Fanning S, Martins M. The ins and outs of RND efflux pumps in *Escherichia coli*. *Front Microbiol*. 2015; 6: 587.

34. Giraud E, Baucheron S, Cloeckaert A. Resistance to fluoroquinolones in *Salmonella*: Emerging mechanisms and resistance prevention strategies. *Microbes Infect*. 2006; 8: 1937-44.

35. Yang H, Duan G, Zhu J, Lv R, Xi Y, Zhang W, et al. The AcrAB-TolC pump is involved in multidrug resistance in clinical *Shigella flexneri* isolates. *Microb Drug Resist*. 2008; 14: 245-9.

36. Schindler BD, Kaatz GW. Multidrug efflux pumps of Gram-positive bacteria. *Drug Resist Updat*. 2016; 27: 1-13.

37. Heisig P, Tschorny R. Characterization of fluoroquinolone-resistant mutants of *Escherichia coli* selected in vitro. *Antimicrob Agents Chemother*. 1994; 38: 1284-91.

38. Morgan-Linnell SK, Becnel Boyd L, Steffen D, Zechiedrich L. Mechanisms accounting for fluoroquinolone resistance in *Escherichia coli* clinical isolates. *Antimicrob Agents Chemother*. 2009; 53: 235-41.

39. Baba T, Ara T, Hasegawa M, Takai Y, Okumura Y, Baba M, et al. Construction of *Escherichia coli* K-12 in-frame, single-gene knockout mutants: The Keio collection. *Mol Syst Biol*. 2006; 2: 2006 0008.

40. Kreuzer KN, Cozzarelli NR. *Escherichia coli* mutants thermosensitive for deoxyribonucleic acid gyrase subunit A: Effects on deoxyribonucleic acid replication, transcription, and bacteriophage growth. *J Bacteriol*. 1979; 140: 424-35.

41. Orr E, Fairweather NF, Holland IB, Pritchard RH. Isolation and characterisation of a strain carrying a conditional lethal mutation in the *cou* gene of *Escherichia coli* K12. *Mol Gen Genet*. 1979; 177: 103-12.

42. Hansen FG, von Meyenburg K. Characterization of the *dnaA*, *gyrB* and other genes in the *dnaA* region of the *Escherichia coli* chromosome on specialized transducing phages lambda *tna*. *Mol Gen Genet*. 1979; 175: 135-44.

43. Lee SK, Chou HH, Pfleger BF, Newman JD, Yoshikuni Y, Keasling JD. Directed evolution of AraC for improved compatibility of arabinose- and lactose-inducible promoters. *Appl Environ Microbiol*. 2007; 73: 5711-5.

44. Santos TM, Lin TY, Rajendran M, Anderson SM, Weibel DB. Polar localization of *Escherichia coli* chemoreceptors requires an intact Tol-Pal complex. *Mol Microbiol*. 2014; 92: 985-1004.

CHAPTER 5

Conclusions

The absence of sophisticated endomembrane systems is one of the most distinctive features of prokaryotic cells. This apparent structural simplicity shaped the traditional notion that bacteria are "bags of enzymes" lacking dedicated mechanisms of spatial organization. For many years, this simplistic description of bacterial cells remained unquestioned and concealed several aspects of their biology. The transformation in the field began with the observation that some bacterial proteins have an asymmetric distribution that is critical for the metabolic and structural properties of the cell. It is now widely recognized that intracellular organization of proteins and other biomolecules is a widespread phenomenon amongst bacteria. Drawing parallels to eukaryotes, these mechanisms compartmentalize biochemical processes and influence cell morphology, growth, and survival. This dissertation explores several aspects of bacterial physiology with an emphasis on the mechanisms for intracellular organization and negative physiological outcomes associated with malfunctioning systems. Our motivation for these studies is to explore these mechanisms used for intracellular organization in bacteria to design new approaches to tackle unconventional antibacterial targets. We used a combination of genetic and chemical tools to uncover new aspects of mechanisms regulating cell motility, chemotaxis, and division.

The canonical example of protein localization in bacteria is the chemoreceptor family of proteins. Chemoreceptors mediate bacterial chemotaxis [1, 2] and play a central role in pathogen virulence [3] and in symbiotic relationships between bacteria and plants [4]. These inner membrane receptors form large arrays that are predominantly concentrated at the cell poles in rod-shaped bacteria [5-7]. In chapter 2, we use a set of techniques from genetics, biochemistry, and materials science to characterize the molecular mechanisms controlling polar localization of chemoreceptors

in the model bacterium *Escherichia coli*. We compared the localization profile of chemoreceptors in wild-type *E. coli* and in various mutants lacking anionic phospholipids or structural components of the cell envelope. This approach revealed that the Tol-Pal complex, a multiprotein complex conserved in Gram-negative bacteria [8], is required to maintain the polar localization of chemoreceptor clusters. Co-immunoprecipitation analyses confirmed that components of the Tol-Pal complex interact with chemoreceptors and we proposed that this interaction mediates polar positioning of chemoreceptors by restricting cluster mobility at the cell poles. Interestingly, deletion of the Tol-Pal complex did not affect the localization of all polar proteins, suggesting that the interactions between the Tol-Pal proteins and the chemoreceptors may be specific for localization of the chemosensory machinery.

Physical barriers to the free diffusion of cytoplasmic membrane constituents (e.g., proteins and lipids) play an important role in generating functional domains in the membrane of eukaryotes [9, 10]. Transmembrane and membrane-associated protein complexes are commonly responsible for the formation of these physical barriers that accounts for the poor mobility of some eukaryotic proteins [9]. Movement of proteins with restricted mobility is further reduced as a result of association with intracellular components (e.g., the cortical actin cytoskeleton intimately associated with the cytoplasmic membrane [11]) or the extracellular matrix [12]. It is likely that bacteria have developed analogous strategies (i.e., placement of physical barriers) to regulate intracellular organization of molecular machineries that are asymmetrically distributed inside the cell. The Tol-Pal complex might function as a physical barrier restricting mobility of polar inner membrane proteins that form large arrays such as chemoreceptors. Several lines of evidence support this prediction: (1) Tol-Pal forms a

trans-envelope complex and its components are positioned in all three layers of the cell envelope; (2) the lipoprotein Pal interacts with the peptidoglycan layer [13]; and (3) Pal is significantly enriched at the cell poles [14, 15].

The Tol-Pal complex is also an important component of the division machinery of Gram-negative bacteria and is responsible for outer membrane invagination during cell constriction [16]. Our model suggests that Tol-Pal-dependent polar localization of chemoreceptors is a bacterial strategy to coordinate cell division and segregation of the chemosensory machinery. In support of our model and the proposed role of the Tol-Pal complex in bacterial intracellular organization, it has been recently demonstrated that an intact Tol-Pal complex is required for cytokinesis-dependent polar localization of TipN in *Caulobacter crescentus* [17]. Importantly, the spatiotemporal dynamics of TipN during the *C. crescentus* cell cycle is connected to cell division [18, 19]. Finally, we show that some of the phenotypic alterations that accompany deletion of the Tol-Pal complex include motility and chemotaxis defects, reinforcing the connection between protein subcellular localization and function. The long-term impact of our findings will guide studies of localization and regulation of integral membrane proteins in other biomedically relevant microbes and in eukaryotic organelles (e.g., mitochondria) in which understanding of spatial control is virtually unknown.

Assembly and function of the divisome during bacterial division is another essential cellular event that depends on precise protein localization. The spatiotemporal dynamics of the bacterial divisome are regulated in response to several cellular [20-24] and environmental signals [25-29]. Recent studies in our laboratory demonstrated that divin, a synthetic small molecule identified in a high-throughput screen for inhibitors of bacterial cell division, blocks late stages of constriction [30, 31]. However, the

mechanism of action of divin and its chemical analogs was not characterized in detail. In chapter 3, we show that divin is a potent iron chelator that perturbs iron homeostasis in bacteria and halts division. Iron is an essential nutrient for virtually all forms of life and, therefore, iron-poor environments pose a major challenge to bacterial survival. Not surprisingly, a universal strategy in human innate defense capitalizes on the low abundance of free iron to protect the host against bacterial infections [32, 33]. We explored the essentiality of iron and the concept of nutritional immunity to study whether bacterial iron homeostasis offers a suitable target for antibiotic research.

We used divin and other structurally unrelated families of iron chelators as chemical tools to investigate the effect of iron starvation on cell division in diverse bacterial groups. Cells treated with an inhibitory concentration of iron chelators fail to complete constriction during division. Fluorescence microscopy revealed that iron deprivation prevents assembly of the divisome and consequently leads to division arrest. The phenotypic alterations that accompany iron deprivation are not similar to the changes observed for classes of clinical antibiotics that block cell division by arresting general biosynthetic processes [34]. This finding suggests that iron chelators have a unique mechanism for blocking bacterial division. Gene expression and multi-copy suppression analyses indicated that the expression of some proteins involved in cell division is significantly reduced following treatment with iron chelators. Our results suggest the existence of iron-dependent cellular checkpoints in the bacterial cell cycle. This regulatory feature has remarkable similarities with the eukaryotic cell cycle, in which the connection between iron availability and expression of cell-cycle regulators has been previously characterized [35-37]. Although the antibacterial potential of small molecule iron chelators has been long acknowledged [38-40], the clinical use of

chelators is limited to the treatment of human diseases that require removing iron from the body. Our findings provide insights into the mechanisms by which iron homeostasis and cell division are coordinated in bacteria, and suggest potential strategies for antibiotic development.

Bacterial cell division is precisely coordinated with DNA replication and segregation [41-44]. DNA replication is an essential process that depends on conserved enzymes widespread amongst bacteria [45, 46]. One such component is the type II topoisomerase DNA gyrase, responsible for catalyzing the ATP-dependent negative supercoiling of double-stranded closed-circular DNA to alleviate topological stresses generated during replication, transcription, recombination, and repair [46, 47]. Inhibitors of DNA gyrase are one of the most successful classes of clinical antibiotics currently used [48]. However, development of drug tolerance and resistance among bacterial pathogens has compromised the success of these antibacterial agents. Our group has previously introduced gyramides as a new family of synthetic small molecules that inhibit the activity of DNA gyrase [49, 50]. In chapter 4, we report the characterization of three new structural analogs of the gyramides that are active against pathogenic strains of diverse bacteria. These new compounds are potent inhibitors of the supercoiling activity of DNA gyrase and active against *E. coli* strains resistant to the known DNA gyrase inhibitors ciprofloxacin and novobiocin. Similarly, resistance to gyramides does not confer resistance to ciprofloxacin or novobiocin. We demonstrate that target multi-copy suppression does not alter the inhibitory activity of gyramides, suggesting that gyramides induce toxic reactions that cannot be alleviated by overexpression of DNA gyrase. Instead, it is likely that target overexpression exacerbates the toxicity of gyramides. These results provide insights into the

mechanism of action of this new family of DNA gyrase inhibitors. We propose that the gyramides bind to a new site of DNA gyrase and display a unique mechanism of inhibiting DNA metabolism.

Bacteria have evolved several mechanisms to maintain spatial intracellular compartmentalization. Comprehensive understanding of spatiotemporal organization in bacteria and the underlying regulatory mechanisms is relevant to both fundamental and applied biology. Of particular interest are: (1) an expanded picture of the bacterial "localizome" and the types of mechanisms available; (2) the advance of research programs directed at targeting the disruption of biomolecule localization as a strategy for antibiotic development; and (3) the search for parallels with eukaryotic systems, which may shed insights into the connection between some organelle dysfunction and human diseases. To reach these goals, we will need to understand (1) the diversity and conservancy of the bacterial mechanisms for spatiotemporal organization; (2) how these mechanisms overlap to maintain cellular homeostasis; and (3) how environmental factors modulate these mechanisms. The research described in this dissertation addresses some of these points and provides a small degree of progress toward these goals.

REFERENCES

1. Hazelbauer GL, Falke JJ, Parkinson JS. Bacterial chemoreceptors: High-performance signaling in networked arrays. *Trends Biochem Sci*. 2008; 33: 9-19.
2. Wadhams GH, Armitage JP. Making sense of it all: Bacterial chemotaxis. *Nat Rev Mol Cell Biol*. 2004; 5: 1024-37.
3. Garvis S, Munder A, Ball G, de Bentzmann S, Wiehlmann L, Ewbank JJ, et al. *Caenorhabditis elegans* semi-automated liquid screen reveals a specialized role for the chemotaxis gene *cheB2* in *Pseudomonas aeruginosa* virulence. *PLoS Pathog*. 2009; 5: e1000540.
4. Miller LD, Yost CK, Hynes MF, Alexandre G. The major chemotaxis gene cluster of *Rhizobium leguminosarum* bv. *viciae* is essential for competitive nodulation. *Mol Microbiol*. 2007; 63: 348-62.
5. Alley MR, Maddock JR, Shapiro L. Polar localization of a bacterial chemoreceptor. *Genes Dev*. 1992; 6: 825-36.
6. Maddock JR, Shapiro L. Polar location of the chemoreceptor complex in the *Escherichia coli* cell. 1993; 259: 1717-23.
7. Briegel A, Ding HJ, Li Z, Werner J, Gitai Z, Dias DP, et al. Location and architecture of the *Caulobacter crescentus* chemoreceptor array. *Mol Microbiol*. 2008; 69: 30-41.
8. Sturgis JN. Organisation and evolution of the *tol-pal* gene cluster. *J Mol Microbiol Biotechnol*. 2001; 3: 113-22.
9. Nakada C, Ritchie K, Oba Y, Nakamura M, Hotta Y, Iino R, et al. Accumulation of anchored proteins forms membrane diffusion barriers during neuronal polarization. *Nat Cell Biol*. 2003; 5: 626-32.
10. Trimble WS, Grinstein S. Barriers to the free diffusion of proteins and lipids in the plasma membrane. *J Cell Biol*. 2015; 208: 259-71.
11. Goswami D, Gowrishankar K, Bilgrami S, Ghosh S, Raghupathy R, Chadda R, et al. Nanoclusters of GPI-anchored proteins are formed by cortical actin-driven activity. *Cell*. 2008; 135: 1085-97.
12. Paszek MJ, DuFort CC, Rossier O, Bainer R, Mouw JK, Godula K, et al. The cancer glycocalyx mechanically primes integrin-mediated growth and survival. *Nature*. 2014; 511: 319-25.
13. Bouveret E, Benedetti H, Rigal A, Loret E, Lazdunski C. In vitro characterization of peptidoglycan-associated lipoprotein (PAL)-peptidoglycan and PAL-TolB interactions. *J Bacteriol*. 1999; 181: 6306-11.
14. Lai EM, Nair U, Phadke ND, Maddock JR. Proteomic screening and identification of differentially distributed membrane proteins in *Escherichia coli*. *Mol Microbiol*. 2004; 52: 1029-44.

15. Li G, Young KD. Isolation and identification of new inner membrane-associated proteins that localize to cell poles in *Escherichia coli*. *Mol Microbiol*. 2012; 84: 276-95.

16. Gerding MA, Ogata Y, Pecora ND, Niki H, de Boer PA. The trans-envelope Tol-Pal complex is part of the cell division machinery and required for proper outer-membrane invagination during cell constriction in *E. coli*. *Mol Microbiol*. 2007; 63: 1008-25.

17. Yeh YC, Comolli LR, Downing KH, Shapiro L, McAdams HH. The *Caulobacter* Tol-Pal complex is essential for outer membrane integrity and the positioning of a polar localization factor. *J Bacteriol*. 2010; 192: 4847-58.

18. Lam H, Schofield WB, Jacobs-Wagner C. A landmark protein essential for establishing and perpetuating the polarity of a bacterial cell. *Cell*. 2006; 124: 1011-23.

19. Huitema E, Pritchard S, Matteson D, Radhakrishnan SK, Viollier PH. Bacterial birth scar proteins mark future flagellum assembly site. *Cell*. 2006; 124: 1025-37.

20. Raskin DM, de Boer PA. Rapid pole-to-pole oscillation of a protein required for directing division to the middle of *Escherichia coli*. *Proc Natl Acad Sci U S A*. 1999; 96: 4971-6.

21. Wu LJ, Errington J. Coordination of cell division and chromosome segregation by a nucleoid occlusion protein in *Bacillus subtilis*. *Cell*. 2004; 117: 915-25.

22. Bernhardt TG, de Boer PA. SlmA, a nucleoid-associated, FtsZ binding protein required for blocking septal ring assembly over chromosomes in *E. coli*. *Mol Cell*. 2005; 18: 555-64.

23. Thanbichler M, Shapiro L. MipZ, a spatial regulator coordinating chromosome segregation with cell division in *Caulobacter*. *Cell*. 2006; 126: 147-62.

24. Fleurie A, Lesterlin C, Manuse S, Zhao C, Cluzel C, Lavergne JP, et al. MapZ marks the division sites and positions FtsZ rings in *Streptococcus pneumoniae*. *Nature*. 2014; 516: 259-62.

25. Weart RB, Lee AH, Chien AC, Haeusser DP, Hill NS, Levin PA. A metabolic sensor governing cell size in bacteria. *Cell*. 2007; 130: 335-47.

26. Dong G, Yang Q, Wang Q, Kim YI, Wood TL, Osteryoung KW, et al. Elevated ATPase activity of KaiC applies a circadian checkpoint on cell division in *Synechococcus elongatus*. *Cell*. 2010; 140: 529-39.

27. Modell JW, Hopkins AC, Laub MT. A DNA damage checkpoint in *Caulobacter crescentus* inhibits cell division through a direct interaction with FtsW. *Genes Dev*. 2011; 25: 1328-43.

28. Modell JW, Kambara TK, Perchuk BS, Laub MT. A DNA damage-induced, SOS-independent checkpoint regulates cell division in *Caulobacter crescentus*. *PLoS Biol*. 2014; 12: e1001977.

29. Beaufay F, Coppine J, Mayard A, Laloux G, De Bolle X, Hallez R. A NAD-dependent glutamate dehydrogenase coordinates metabolism with cell division in *Caulobacter crescentus*. *EMBO J*. 2015; 34: 1786-800.

30. Eun YJ, Zhou M, Kiekebusch D, Schlimpert S, Trivedi RR, Bakshi S, et al. Divin: A small molecule inhibitor of bacterial divisome assembly. *J Am Chem Soc*. 2013; 135: 9768-76.

31. Zhou M, Eun YJ, Guzei IA, Weibel DB. Structure-activity studies of divin: An inhibitor of bacterial cell division. *ACS Med Chem Lett*. 2013; 4: 880-5.

32. Skaar EP. The battle for iron between bacterial pathogens and their vertebrate hosts. *PLoS Pathog*. 2010; 6: e1000949.

33. Hood MI, Skaar EP. Nutritional immunity: Transition metals at the pathogen-host interface. *Nat Rev Microbiol*. 2012; 10: 525-37.

34. Nonejuie P, Burkart M, Pogliano K, Pogliano J. Bacterial cytological profiling rapidly identifies the cellular pathways targeted by antibacterial molecules. *Proc Natl Acad Sci U S A*. 2013; 110: 16169-74.

35. Kulp KS, Green SL, Vulliet PR. Iron deprivation inhibits cyclin-dependent kinase activity and decreases cyclin D/CDK4 protein levels in asynchronous MDA-MB-453 human breast cancer cells. *Exp Cell Res*. 1996; 229: 60-8.

36. Chaston TB, Lovejoy DB, Watts RN, Richardson DR. Examination of the antiproliferative activity of iron chelators: Multiple cellular targets and the different mechanism of action of triapine compared with desferrioxamine and the potent pyridoxal isonicotinoyl hydrazone analogue 311. *Clin Cancer Res*. 2003; 9: 402-14.

37. Yu Y, Kovacevic Z, Richardson DR. Tuning cell cycle regulation with an iron key. *Cell Cycle*. 2007; 6: 1982-94.

38. Jones RL, Peterson CM, Grady RW, Kumbaraci T, Cerami A, Graziano JH. Effects of iron chelators and iron overload on *Salmonella* infection. *Nature*. 1977; 267: 63-5.

39. Thompson MG, Corey BW, Si Y, Craft DW, Zurawski DV. Antibacterial activities of iron chelators against common nosocomial pathogens. *Antimicrob Agents Chemother*. 2012; 56: 5419-21.

40. Tatano Y, Kanehiro Y, Sano C, Shimizu T, Tomioka H. ATP exhibits antimicrobial action by inhibiting bacterial utilization of ferric ions. *Sci Rep*. 2015; 5: 8610.

41. Den Blaauwen T, Buddelmeijer N, Aarsman ME, Hameete CM, Nanninga N. Timing of FtsZ assembly in *Escherichia coli*. *J Bacteriol*. 1999; 181: 5167-75.

42. Regamey A, Harry EJ, Wake RG. Mid-cell Z ring assembly in the absence of entry into the elongation phase of the round of replication in bacteria: Co-ordinating chromosome replication with cell division. *Mol Microbiol*. 2000; 38: 423-34.

43. Quardokus EM, Brun YV. DNA replication initiation is required for mid-cell positioning of FtsZ rings in *Caulobacter crescentus*. *Mol Microbiol*. 2002; 45: 605-16.

44. Wang JD, Levin PA. Metabolism, cell growth and the bacterial cell cycle. *Nat Rev Microbiol*. 2009; 7: 822-7.

45. Robinson A, Causer RJ, Dixon NE. Architecture and conservation of the bacterial DNA replication machinery, an underexploited drug target. *Curr Drug Targets*. 2012; 13: 352-72.

46. Bush NG, Evans-Roberts K, Maxwell A. DNA Topoisomerases. *EcoSal Plus*. 2015; 6: ESP-0010-0014.

47. Gellert M, Mizuuchi K, O'Dea MH, Nash HA. DNA gyrase: An enzyme that introduces superhelical turns into DNA. *Proc Natl Acad Sci U S A*. 1976; 73: 3872-6.

48. Lewis K. Platforms for antibiotic discovery. *Nat Rev Drug Discov*. 2013; 12: 371-87.

49. Foss MH, Hurley KA, Sorto N, Lackner LL, Thornton KM, Shaw JT, et al. N-Benzyl-3-sulfonamidopyrrolidines are a new class of bacterial DNA gyrase inhibitors. *ACS Med Chem Lett*. 2011; 2: 289-92.

50. Rajendram M, Hurley KA, Foss MH, Thornton KM, Moore JT, Shaw JT, et al. Gyramides prevent bacterial growth by inhibiting DNA gyrase and altering chromosome topology. *ACS Chem Biol*. 2014; 9: 1312-9.

APPENDIX

Future Directions

During the course of the studies reported in this dissertation, we made several interesting observations that offer opportunities for future research. Some of these observations and the unanswered questions that accompany these remarks are highlighted here.

Protein localization mediated by the Tol-Pal complex

The Tol-Pal complex has been extensively studied for its role in maintaining cell envelope stability and facilitating phage infection and colicin uptake in Gram-negative bacteria [1-10]. More recently, it was proposed that this trans-envelope complex is also an important component of the divisome and, more specifically, plays a role in outer membrane invagination during constriction [11-13]. Consistent with this function in division, the Tol and Pal proteins seem to localize dynamically during the cell cycle, similarly to the cell division proteins: their distribution in the cell envelope is initially disperse, with some isoforms enriched at the poles [14, 15], and they accumulate at the division site during early stages of septation [11-13].

An emerging hypothesis suggests that components of the Tol-Pal complex are also important for polar localization of some proteins, such as TipN in *Caulobacter crescentus* [12] and chemoreceptor clusters in *Escherichia coli* [16]. The proposed model posits that the Tol-Pal complex functions as a barrier preventing protein diffusion from the cell poles. This model is consistent with the observations that TipN localizes at the newer cell pole (i.e., the pole generated following the previous round of division) in the beginning of the cell cycle and moves to the division site as the *C. crescentus* divisome starts to assemble [17, 18]. Similarly, as proposed by the stochastic nucleation model for chemoreceptor clustering and positioning, in an *E. coli* cell with large clusters at both

poles, new clusters will preferentially form at the mid-cell, which is the location furthest from both poles [19-21]. We proposed that the *E. coli* Tol-Pal complex may restrict the diffusion of polar and mid-cell chemoreceptor clusters [16].

These observations raise the question of whether *E. coli* and *C. crescentus* utilize this mechanism for localization of other proteins. To partially address this question, we showed that TnaA and IcsA localize to the *E. coli* cell poles in the absence of Tol-Pal [16]. However, it is possible that the Tol-Pal complex influences the localization of other proteins in *E. coli* and *C. crescentus*; particularly, proteins that have a cell cycle-dependent pattern of localization and accumulate at the cell poles and/or the division site. To further explore this possibility, one could take advantage of fluorescently-labelled protein libraries available for both bacterial groups [22, 23]. One experiment that we propose is to use these fluorescently-labelled protein libraries to create mutants lacking individual or multiple components of the Tol-Pal complex and study the effect of these deletions on the subcellular localization of the entire proteome of *E. coli* and *C. crescentus*. Crosslinking and immunoprecipitation studies could be used to confirm direct and indirect interactions between polarly-localized proteins and components of the Tol-Pal complex. Site-directed mutagenesis will enable characterization of amino acids that are critical for these interactions.

Previous bioinformatics studies have shown that the Tol-Pal complex is widely conserved among Gram-negative bacteria, including biomedically-relevant pathogens such as *Pseudomonas aeruginosa*, *Vibrio cholerae*, *Helicobacter pylori*, *Campylobacter jejuni, Haemophilus influenzae,* and *Chlamydia trachomatis* [24]. These findings point to the possibility that the Tol-Pal complex might play a role in protein localization in several other bacterial groups. To explore this area, one could revisit these comparative studies

and use a combination of biochemical (e.g., in vivo crosslinking and co-immunoprecipitation) and genetic (e.g., gene deletion and complementation) approaches to characterize the organizational role of the Tol-Pal complex in these biomedically-relevant pathogens. We propose the use of in vivo crosslinking and immunoprecipitation to confirm potential interactions between polarly-localized proteins and components of the Tol-Pal complex. Another experiment that we suggest is the construction of mutants lacking an intact Tol-Pal complex and the use of time-lapse microscopy and image analysis to confirm the participation of Tol-Pal in protein localization. One could assess the spatiotemporal pattern of polarly-localized fluorescently-labelled proteins of interest in wild-type cells and in Tol-Pal mutants, and perform complementation experiments to restore the normal localization pattern of the protein of interest. Further studies in this area will uncover new patterns of protein localization in non-model bacteria and guide future antibiotic discovery efforts.

Other outstanding questions in this area include: (1) what is the ultimate positional information regulating the spatiotemporal dynamics of the Tol-Pal complex during the cell cycle?; and (2) what intrinsic features of the complex allow these proteins to function as molecular landmarks for localization of other proteins? The components of the Tol-Pal complex display disperse distribution in the cell envelope and accumulate at the division site to drive outer membrane constriction during division [11, 12]. The Tol and Pal proteins localize to the division site in the absence of each other, suggesting that they are recruited independently and, not necessarily, as a complex. Components of the divisome are obvious candidates for recruitment of the Tol-Pal complex to the division site. In *E. coli* cells, accumulation of Tol-Pal complex at the division site requires the cell division protein FtsN [11]. However, direct or indirect

interactions between the Tol-Pal complex and FtsN have yet not been demonstrated. In contrast, recruitment of Tol-Pal complexes to the divisome in *C. crescentus* occurs independently of FtsN.

To address the first question, we propose the use of co-immunoprecipitation experiments to identify binding partners that affect the localization of the Tol-Pal complex. One could use native components of the Tol-Pal complex or variants containing affinity tags (e.g, a FLAG epitope or a polyhistidine tag) to preform co-immunoprecipitation followed by gel extraction, protein digestion, and mass spectrometry. These experiments will confirm the necessity of FtsN for localization of the Tol-Pal complex in *E. coli* and reveal additional binding partners that might influence the spatiotemporal dynamics of Tol and Pal proteins. To investigate the intrinsic features of the Tol-Pal complex that allow these proteins to function as molecular landmarks for localization of other proteins, we propose the use of site-directed mutagenesis to characterize the binding sites and map the residues involved in protein-protein interaction.

Protein localization mediated by Lpp

The lipoprotein Lpp (Braun's lipoprotein) interacts with the peptidoglycan [25-27] and, similarly to the Tol-Pal complex, contributes to the structural and functional integrity of the cell envelope [28-30]. Bacterial cells lacking Lpp exhibit increased permeability to small molecules, leakage of periplasmic content, and production of outer membrane vesicles [28-30]. Lpp exists in two distinct forms: a "free-form" and a "bound-form", which is covalently bound to the peptidoglycan layer [25, 31, 32]. It was

recently demonstrated that free-form Lpp spans the outer membrane and is surface-exposed, whereas the peptidoglycan-bound Lpp resides in the periplasm [27].

During our studies of chemoreceptor localization in *E. coli*, we found that some *lpp* mutations lead to mislocalization of chemoreceptor clusters [16]. Lpp can be chemically crosslinked with TolB in vivo [33], suggesting that it is able to interact with components of the Tol-Pal complex. These observations raise the possibility that Lpp may play a role in spatiotemporal control of proteins and this function could be in concert with the Tol-Pal complex. It would be interesting to test whether deletion of Lpp affects the localization of other proteins in *E. coli* and other bacteria. To explore this topic, one could use fluorescently-labelled protein libraries [22, 23], create *lpp* deletion mutants, and measure the effect of the deletion on the subcellular localization of an entire bacterial proteome. Interactions between Lpp and proteins of interest could be confirmed by in vivo crosslinking and immunoprecipitation experiments. In addition, site-directed mutagenesis could be used to characterize amino acids that are critical for these interactions.

Finally, it is worth noting that the Tol-Pal complex appears to be essential only in bacteria that lack Lpp or an Lpp homolog (e.g., *C. crescentus* [12]). It would be interesting to test whether Lpp and the Tol-Pal complex form synthetic lethal pairs in bacteria that contain both cellular components, such as *E. coli*. To verify this prediction, we propose the construction of mutants lacking Lpp and the Tol-Pal complex. To allow construction of mutants, we recommend deleting the *tol-pal* operon, transforming the *tol-pal* mutant with a plasmid encoding the *lpp* gene under the control of a lactose-inducible promoter, inducing the expression of *lpp* with isopropyl β-D-1-thiogalactopyranoside (IPTG), and deleting the chromosomal copy of *lpp*. The absence

of *lpp*/*tol-pal* deletion mutants after the final selection might indicate a synthetic lethality relationship between Lpp and the Tol-Pal complex.

Motility performance of Lpp mutants

As we described in chapter 2, mutations in *lpp* affect the polar localization of chemoreceptors in *E. coli* [16]. To study the consequences of these mutations on *E. coli* swimming motility, we compared swimming behavior of wild-type and *lpp* mutants and found that the *lpp* mutants *E. coli* UE49, *E. coli* UE51 and *E. coli* UE53 form significantly larger ($P < 0.05$) swimming colonies (Figure 1). It is still unclear why these mutants form larger colonies on swimming agar. One possibility is that these *lpp* mutants contain more flagella than wild-type cells.

The bacterial flagellum is a rotatory motor that propels cells through liquid and across surfaces. This organelle is important for bacterial pathogenesis and biofilm formation [34-36]. The morphogenetic pathway of the bacterial flagella is a highly-regulated process and bacteria have developed robust mechanisms to ensure that flagellar assembly follows a defined path [37]. Connections between Lpp and flagellar assembly/function are just starting to emerge. A recent study showed that mutations in the *Salmonella lppA* gene—the equivalent of *E. coli lpp*—increased swim rate of these *Salmonella* mutants by 10% [38].

To investigate the possibility that *lpp* mutants contain more flagella than wild-type cells, we propose to revisit the motility (swimming and swarming) experiments to confirm the observed phenotype (e.g., increased motility). To substantiate the observations, we suggest cloning *lpp* and mutated versions of *lpp* under the regulation of an arabinose-inducible promoter in a plasmid and perform complementation studies

to restore the wild-type phenotype. In addition, we propose the use of quantitative western blot and flagella immunostaining with anti-flagellin (anti-FliC) antibody to measure the number and arrangement of flagella, respectively. To complement these studies, one could also use cryo-electron microscopy to investigate number and flagellar morphology of *E. coli lpp* mutants. Results from these studies will strengthen the connections between Lpp and flagellar assembly/function and potentially reveal additional roles for Lpp in bacteria.

The effect of long-term exposure to iron chelators on the cell division machinery

As we showed in chapter 3, *E. coli* cells are able to grow in the presence of inhibitory concentrations of divin or bipyridine (bipy) if iron is supplemented in the medium [39]. Interestingly, the cell length distribution of the population treated with these iron chelators is bimodal. We hypothesize that the population of shorter cells completed division, were at early pre-divisional stages during drug treatment, and have a normal phenotype; the other cell population was undergoing division prior to treatment, are susceptible to the iron chelators, and display the cell division phenotype. To test this hypothesis, we propose a series of experiments. First, we recommend the use of fluorescence-activated cell sorting (FACS) to separate the two subpopulations of cells that we identified and use the sorted populations as inoculum in dose-response assays to verify the antagonistic effect of iron, cobalt, and copper on cell growth and division following treatment with divin or bipy. Next, we propose the use of fluorescence microscopy to study divisome assembly in these cell populations. One could transform *E. coli* cells with functional, fluorescently-labeled cell division proteins, treat the cells with inhibitory concentrations of divin or bipy for 16 h, sort the two

populations using FACS, and perform time-lapse microscopy to observe the spatiotemporal assembly of the divisome following long-term (>16 h) exposure to iron chelators.

We performed time-lapse experiments to investigate how an increase in iron availability following long-term (>16 h) exposure to divin or bipy affects division in arrested cells. We treated wild-type *C. crescentus* CB15N cells for 16 h with 2× MIC of divin or bipy, harvested the cells to remove the inhibitor, added medium supplemented with 100 μM of $FeSO_4$, incubated the cultures for 2 h in the supplemented medium, and imaged the cells for 4 h. Surprisingly, we found a group of cells that is unable to resume growth and divide even after 2 h of recovery in iron-replete conditions (Figure 2, red arrows). Interestingly, another group of cells starts dividing at the cell quartile and never completes constriction at the primary, arrested division site at mid-cell (Figure 2, yellow arrow). These results indicate that the cellular injuries caused by long-term iron deprivation may cause permanent damage to the division machinery.

It remains to be investigated whether components of the divisome maintain mid-cell localization in chelator-treated cells when division resumes at the cell quartiles (Figure 2, yellow arrow). The characteristic arrested constriction observed at mid-cell in these cells that escape cytokinetic arrest and start dividing at the cell quartiles indicate that components of the divisome or a complete, non-functional divisome are stalled at mid-cell. Combined with our results presented in chapter 3, we suggest that iron-dependent cellular checkpoints in bacterial cell division may exist. A comprehensive understanding of the divisome dynamics in these arrested cells is of particular interest because it will provide new insights into the temporal order of divisome assembly and reveal the potential iron-dependent step of the process. We propose the use of super-

resolution and single-molecule fluorescence microscopy to obtain detailed information of structural changes associated with cell-cycle progression in iron-depleted cells. For example, one could use structured-illumination microscopy (SIM) to characterize the divisome at the constricted region in arrested cells. Additionally, we propose transforming *E. coli* with plasmids encoding cell division proteins labeled with fluorescent proteins (e.g., mEos2, Dendra2, or PAmCherry), and using imaging techniques such as photoactivated localization microscopy (PALM) to study the dynamics of cell division proteins during conditions of iron starvation. These experiments will provide insights on the cellular requirements necessary for constriction at the future division sites (i.e., the cell quartiles).

The mode of action of gyramides

In chapter 4, we presented evidence supporting the hypothesis that the gyramides have a unique binding site on DNA gyrase and exhibit a novel mechanism that is distinct from other known DNA gyrase inhibitors such as ciprofloxacin and novobiocin. However, we still lack detailed information about the chemical interactions between the gyramides and DNA gyrase. This information will provide biochemical insights into the reaction catalyzed by DNA gyrase, facilitate establishing gyramides as chemical tools for cell biological studies, and guide our current medicinal chemistry efforts. To explore the details regarding binding site and mode of action of the gyramides, we propose the synthesis of analog probes containing chemical modifications (e.g., azide, diazirine, benzophenone) that can be used in photo-induced crosslinking studies. In this approach, purified DNA gyrase and the chemical probe are combined and crosslinked by UV light. DNA gyrase-probe complexes can be

enzymatically digested with trypsin, for example, and the fragments generated can be analyzed by mass spectrometry to map the binding site of gyramides. An additional approach to acquire information on the biochemistry and mode of action of the gyramides is crystallography. One of the major challenges of crystallography is to produce suitable crystals of the ternary complex DNA-DNA gyrase-gyramide.

Despite the improved potency of the new gyramide analogs we characterized, this family of compounds is still subject to active efflux by bacterial multidrug efflux pumps such as the *E. coli* AcrAB-TolC system [40]. The scarcity of information that can help illuminate specific aspects of drug efflux is a fundamental roadblock in antibiotic development platforms. One of the next steps towards advancing the gyramides into the antibiotic development pipeline is to investigate chemical modifications that increase gyramides accumulation inside the cells. According to a recent study, small molecules that contain an amine group, are amphiphilic and rigid, and have low globularity are more likely to accumulate in Gram-negative bacteria [41]. We propose the use of these predictive rules to guide structure-activity relationship studies of new gyramide analogs with increased capacity to accumulate in bacteria.

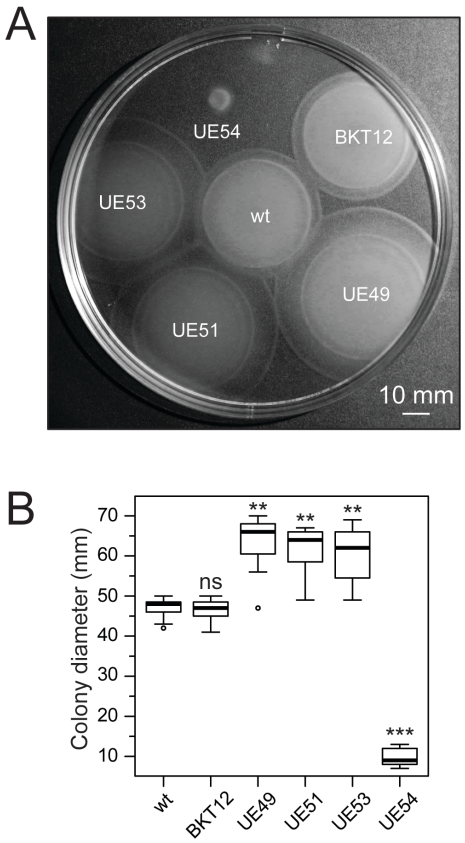

Figure 1. *E. coli lpp* mutants form larger swimming colonies than wild-type *E. coli* MG1655.

(A) Representative image of swimming colonies of wild-type (wt) *E. coli* MG1655, *E. coli* MG1655 BKT12 (cardiolipin deficient) and various *E. coli* UE strains (*lpp* mutants) after 14.5 h of incubation at 30°C on swimming motility agar. Scale bar = 10 mm.

(B) Box-and-whisker plots depicting the size of the migrating colonies ($n = 20$) measured for wild-type (wt) *E. coli* MG1655, *E. coli* MG1655 BKT12 (cardiolipin deficient), and various *E. coli* UE strains (*lpp* mutants). The extent of the box encompasses the interquartile range (IQR) of the diameter (in mm) and the black line within each box represents the median. The upper whisker extends to the maximum data value, or 1.5 of the IQR, whichever is the smaller. The lower whisker extends to the maximum data value, or 1.5 of the IQR, whichever is the larger. Outliers are represented as open black circles. Statistical analysis was performed using two-way ANOVA followed by Tukey's multiple-comparison post-hoc test. ns, non-significant; **, $P < 0.01$; ***, $P < 0.001$ compared to the wild-type phenotype. Plots represent the combination of at least two independent experiments.

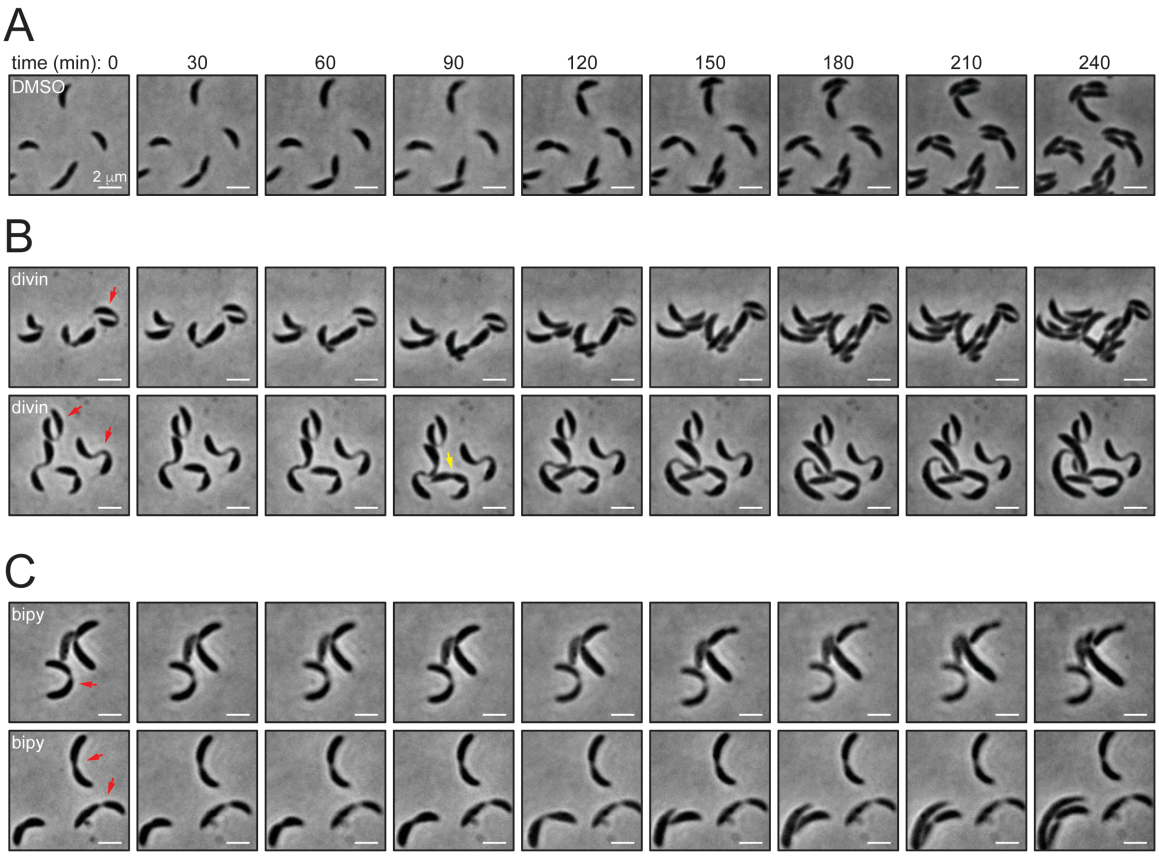

Figure S11. Long-term exposure to iron chelators causes permanent cell division arrest.

Bright field microscopy images from time-lapse experiments showing the morphological changes of *C. crescentus* CB15N cells grown for 4 h at 30°C in PYE agar pads. Prior to each time lapse, cells were grown for 16 h at 30°C in PYE broth containing (A) DMSO, (B) 2× MIC of divin (25 μM), or (C) 2× MIC of bipy (400 μM). Following this initial treatment, cells were harvested, washed and grown for additional 2 h in fresh PYE broth supplemented with 100 μM $FeSO_4$ to allow recovery. Red arrows indicate cells that fail to divide for the duration of the experiment (4 h). Yellow arrow indicates a cell that develops a second division site and completes division at this new site prior to completing division at the primary site. Scale bars = 2 μm.

REFERENCES

1. Hill C, Holland IB. Genetic basis of colicin E susceptibility in *Escherichia coli*. I. Isolation and properties of refractory mutants and the preliminary mapping of their mutations. *J Bacteriol*. 1967; 94: 677-86.
2. Nagel de Zwaig R, Luria SE. Genetics and physiology of colicin-tolerant mutants of *Escherichia coli*. *J Bacteriol*. 1967; 94: 1112-23.
3. Nomura M, Witten C. Interaction of colicins with bacterial cells. 3. Colicin-tolerant mutations in *Escherichia coli*. *J Bacteriol*. 1967; 94: 1093-111.
4. Sun TP, Webster RE. *fii*, a bacterial locus required for filamentous phage infection and its relation to colicin-tolerant *tolA* and *tolB*. *J Bacteriol*. 1986; 165: 107-15.
5. Sun TP, Webster RE. Nucleotide sequence of a gene cluster involved in entry of E colicins and single-stranded DNA of infecting filamentous bacteriophages into *Escherichia coli*. *J Bacteriol*. 1987; 169: 2667-74.
6. Russel M, Whirlow H, Sun TP, Webster RE. Low-frequency infection of F-bacteria by transducing particles of filamentous bacteriophages. *J Bacteriol*. 1988; 170: 5312-6.
7. Levengood SK, Beyer WF, Jr., Webster RE. TolA: A membrane protein involved in colicin uptake contains an extended helical region. *Proc Natl Acad Sci U S A*. 1991; 88: 5939-43.
8. Lazzaroni JC, Portalier R. The *excC* gene of *Escherichia coli* K-12 required for cell envelope integrity encodes the peptidoglycan-associated lipoprotein (PAL). *Mol Microbiol*. 1992; 6: 735-42.
9. Click EM, Webster RE. Filamentous phage infection: Required interactions with the TolA protein. *J Bacteriol*. 1997; 179: 6464-71.
10. Bernadac A, Gavioli M, Lazzaroni JC, Raina S, Lloubes R. *Escherichia coli tol-pal* mutants form outer membrane vesicles. *J Bacteriol*. 1998; 180: 4872-8.
11. Gerding MA, Ogata Y, Pecora ND, Niki H, de Boer PA. The trans-envelope Tol-Pal complex is part of the cell division machinery and required for proper outer-membrane invagination during cell constriction in *E. coli*. *Mol Microbiol*. 2007; 63: 1008-25.
12. Yeh YC, Comolli LR, Downing KH, Shapiro L, McAdams HH. The *Caulobacter* Tol-Pal complex is essential for outer membrane integrity and the positioning of a polar localization factor. *J Bacteriol*. 2010; 192: 4847-58.
13. Gray AN, Egan AJ, Van't Veer IL, Verheul J, Colavin A, Koumoutsi A, et al. Coordination of peptidoglycan synthesis and outer membrane constriction during *Escherichia coli* cell division. *Elife*. 2015; 4: 2839-45.
14. Lai EM, Nair U, Phadke ND, Maddock JR. Proteomic screening and identification of differentially distributed membrane proteins in *Escherichia coli*. *Mol Microbiol*. 2004; 52: 1029-44.

15. Li G, Young KD. Isolation and identification of new inner membrane-associated proteins that localize to cell poles in *Escherichia coli*. *Mol Microbiol*. 2012; 84: 276-95.

16. Santos TM, Lin TY, Rajendran M, Anderson SM, Weibel DB. Polar localization of *Escherichia coli* chemoreceptors requires an intact Tol-Pal complex. *Mol Microbiol*. 2014; 92: 985-1004.

17. Lam H, Schofield WB, Jacobs-Wagner C. A landmark protein essential for establishing and perpetuating the polarity of a bacterial cell. *Cell*. 2006; 124: 1011-23.

18. Huitema E, Pritchard S, Matteson D, Radhakrishnan SK, Viollier PH. Bacterial birth scar proteins mark future flagellum assembly site. *Cell*. 2006; 124: 1025-37.

19. Thiem S, Kentner D, Sourjik V. Positioning of chemosensory clusters in *E. coli* and its relation to cell division. *EMBO J*. 2007; 26: 1615-23.

20. Thiem S, Sourjik V. Stochastic assembly of chemoreceptor clusters in *Escherichia coli*. *Mol Microbiol*. 2008; 68: 1228-36.

21. Greenfield D, McEvoy AL, Shroff H, Crooks GE, Wingreen NS, Betzig E, et al. Self-organization of the *Escherichia coli* chemotaxis network imaged with super-resolution light microscopy. *PLoS Biol*. 2009; 7: e1000137.

22. Kitagawa M, Ara T, Arifuzzaman M, Ioka-Nakamichi T, Inamoto E, Toyonaga H, et al. Complete set of ORF clones of *Escherichia coli* ASKA library (a complete set of *E. coli* K-12 ORF archive): Unique resources for biological research. *DNA Res*. 2005; 12: 291-9.

23. Werner JN, Chen EY, Guberman JM, Zippilli AR, Irgon JJ, Gitai Z. Quantitative genome-scale analysis of protein localization in an asymmetric bacterium. *Proc Natl Acad Sci U S A*. 2009; 106: 7858-63.

24. Sturgis JN. Organisation and evolution of the *tol-pal* gene cluster. *J Mol Microbiol Biotechnol*. 2001; 3: 113-22.

25. Inouye M, Shaw J, Shen C. The assembly of a structural lipoprotein in the envelope of *Escherichia coli*. *J Biol Chem*. 1972; 247: 8154-9.

26. Braun V. Covalent lipoprotein from the outer membrane of *Escherichia coli*. *Biochim Biophys Acta*. 1975; 415: 335-77.

27. Cowles CE, Li Y, Semmelhack MF, Cristea IM, Silhavy TJ. The free and bound forms of Lpp occupy distinct subcellular locations in *Escherichia coli*. *Mol Microbiol*. 2011; 79: 1168-81.

28. Hirota Y, Suzuki H, Nishimura Y, Yasuda S. On the process of cellular division in *Escherichia coli*: A mutant of *E. coli* lacking a murein-lipoprotein. *Proc Natl Acad Sci U S A*. 1977; 74: 1417-20.

29. Yem DW, Wu HC. Physiological characterization of an *Escherichia coli* mutant altered in the structure of murein lipoprotein. *J Bacteriol*. 1978; 133: 1419-26.

30. Suzuki H, Nishimura Y, Yasuda S, Nishimura A, Yamada M, Hirota Y. Murein-lipoprotein of *Escherichia coli*: A protein involved in the stabilization of bacterial cell envelope. *Mol Gen Genet*. 1978; 167: 1-9.

31. Braun V, Rehn K. Chemical characterization, spatial distribution and function of a lipoprotein (murein-lipoprotein) of the *E. coli* cell wall. The specific effect of trypsin on the membrane structure. *Eur J Biochem*. 1969; 10: 426-38.

32. Braun V, Bosch V. Sequence of the murein-lipoprotein and the attachment site of the lipid. *Eur J Biochem*. 1972; 28: 51-69.

33. Clavel T, Germon P, Vianney A, Portalier R, Lazzaroni JC. TolB protein of *Escherichia coli* K-12 interacts with the outer membrane peptidoglycan-associated proteins Pal, Lpp and OmpA. *Mol Microbiol*. 1998; 29: 359-67.

34. Feldman M, Bryan R, Rajan S, Scheffler L, Brunnert S, Tang H, et al. Role of flagella in pathogenesis of *Pseudomonas aeruginosa* pulmonary infection. *Infect Immun*. 1998; 66: 43-51.

35. O'Neil HS, Marquis H. *Listeria monocytogenes* flagella are used for motility, not as adhesins, to increase host cell invasion. *Infect Immun*. 2006; 74: 6675-81.

36. Serra DO, Richter AM, Klauck G, Mika F, Hengge R. Microanatomy at cellular resolution and spatial order of physiological differentiation in a bacterial biofilm. *MBio*. 2013; 4: e00103-13.

37. Macnab RM. How bacteria assemble flagella. *Annu Rev Microbiol*. 2003; 57: 77-100.

38. Cohen EJ, Ferreira JL, Ladinsky MS, Beeby M, Hughes KT. Nanoscale-length control of the flagellar driveshaft requires hitting the tethered outer membrane. *Science*. 2017; 356: 197-200.

39. Santos TMA, Lammers MG, Zhou M, Sparks IL, Rajendran M, Fang D, De Jesus CLY, Carneiro GFR, Cui Q, Weibel DB. Small molecule chelators reveal that iron starvation inhibits late stages of bacterial cytokinesis. (*Submitted*)

40. Hurley KA, Santos TMA, Fensterwald MR, Rajendran M, Moore JT, Balmond EI, et al. Targeting quinolone- and aminocoumarin-resistant bacteria with new gyramide analogs that inhibit DNA gyrase. *Med Chem Commun*. 2017; 8: 942-51.

41. Richter MF, Drown BS, Riley AP, Garcia A, Shirai T, Svec RL, et al. Predictive compound accumulation rules yield a broad-spectrum antibiotic. *Nature*. 2017; 545: 299-304.